The use of in-situ ion-irradiation/TEM techniques to study radiation damage in SiC

Christopher Pawley

Materials and Physics Research Centre
School of Computing, Science and Engineering
University of Salford, Salford, UK

Submitted in partial fulfillment of the requirements of
the degree of Doctor of Philosophy

August 2014

Contents

List of Figures

List of Tables

List of Important Equations

Acknowledgments

Embarking on a Ph.D program is an exciting personal journey; I would like to thank some of the individuals who have supported me.

The most significant of these is my Ph.D supervisor Steve Donnelly. Without him this work would have taken far longer, been less scientifically sound and been much less enjoyable. Thank you Steve — I hope you enjoyed this research as much as I did. Thanks go to Steve, and to Jonathan Hinks for their extensive feedback during the writing of my thesis.

To the rest of the research group (Graeme Greaves, Francis Sweeney and Kerry Abrams), I also have to say thank you, for fixing the things that I broke or just laughing at me for breaking them in the first place. I would also like to thank Graeme for writing the code needed to simulate bubble overlap.

To the other members of academic staff who have supervised my Ph.D at one time or another — Sue Kilcoyne, Jaap van den Berg and Ian Morrison — thanks for helping me progress this far. Finally, thanks to my collaborators; Erwan Oliviero, Marie-France Beaufort and Jean-Francois Barbot.

Without the solid support of my family this would have been a significantly more taxing period of my life; thanks to my mum and brother.

I would also like to extend my gratitude to my friends Alice Bailey, Tim Ashcroft and Tom Walsh for providing card games, dinner and good company when it was needed. Respite was provided by holidaying with Ben Hunwicks, Chris Yates and Mark Lewis — so, thanks to them for providing some time to reflect on my research. Thank you to those who I shared my office with, for making tea and providing ample procrastination opportunities especially Helen Christie, Lisa Simmons and Rhiannon Forrest.

This research was partially funded through the GTA scheme at Salford University - I am grateful for the opportunity that this presented. Thank you to Jaye McIsaac for welcoming me into GTA life and my initial training. Thanks also to my GTA colleagues for taking an interest in my research and supporting me — particularly Lucy Burnett, Tom Hughes-Roberts and David Roberts.

Thanks to colleagues at VATUK; notably Kieran Hardern, Robert Simmons, Barrie Joplin, Kris Thompson, Simon Irvine and Gunnar Lindahl. Finally, thanks to Julian and all my collegues at Premiere Handling for their support during my time there.

Declaration

The research described within is the work of the named author with the exception of *ex-situ* ion-irradiation described in Section 3.4.2. This work was conducted by staff at Institut Pprime at Université de Poitiers under direction of Marie-France Beaufort. Some of the specimens used for experimental work at the JANNuS facility, the results of which are described in Chapter 5, were prepared by the research group at Université de Poitiers.

Some of the *in-situ* experiments at the MIAMI facility were conducted in collaboration with Jonathan Hinks or Graeme Greaves who operated the microscope or ion-beam systems. At the JANNuS facility the microscope was operated by Erwan Oliviero. For this assistance during these experiments I am grateful to those involved.

In order to explore the results further, the modelling of electron and ion-irradiation reported within Chapters 5 and 6 was complemented with work performed by Roger Webb at the University of Surrey. Where relevant, this work is referenced. The simulated images used to assess the degree of bubble overlap were generated by code written and developed by Greaeme Greaves which was written specifically for this purpose. Analysis and interpretation of these images was performed by the author.

List of Abbreviations and Acronyms

AES Auger Electron Spectroscopy

AFM Atomic Force Microscopy

APFIM Atom Probe Field-Ion Microscopy

BCA Binary Collision Approximation

CCD Charge Coupled Device

CVD Chemical Vapour Deposition

DEMO DEMOnstration Power Plant

DFT Density Functional Theory

DLTS Deep Level Transient Spectroscopy

DMS Dilute Magnetic Semiconductor

DPA Displacements Per Atom

EDS Energy-Dispersive X-Ray Spectroscopy

EELS Electron Energy Loss Spectroscopy

EFTEM Energy Filtered Transmission Electron Microscopy

EPMA Electron Probe X-Ray Microanalysis

EPSRC Engineering and Physical Sciences Research Council

ERDA Elastic Recoil Detection Analysis

FEG Field Emission Gun

FIB Focused Ion Beam

GT-MHR Gas Turbine Modular Helium Reactor

HiPER High-Power laser Energy Research facility

HRTEM High Resolution Transmission Electron Microscopy

HTR-10 10 MW High Temperature gas-cooled Reactor

HTTR High Temperature engineering Test Reactor

IBIC Ion Beam Induced Crystallisation

IBIEC Ion Beam Induced Epitaxial Crystallisation

IR Infrared

ITER International Thermonuclear Experimental Reactor

JANNuS Joint-Accelerators for Nano-science and Nuclear Simulation

JET Joint European Torus

LED Light Emitting Diode

LLNL Lawrence Livermore National Laboratory

LTPL Low Temperature PhotoLuminescence

MD Molecular Dynamics

MEMS MicroElectroMechanical Systems

MIAMI Microscope and Ion Accelerator for Material Investigations

MOS Metal-Oxide-Semiconductor

MOSFET Metal Oxide Semiconductor Field Effect Transistor

NBD Nanobeam Diffraction

NIF National Ignition Facility

NRA Nuclear Reaction Analysis

OAS Optical Absorption Spectroscopy

PAC Perturbed Angular Correlation Spectroscopy

PAS Positron Annihilation Spectroscopy

PENELOPE Penetration and Energy Loss of Positrons and Electrons

PIPS Precision Ion Polishing System

PKA Primary Knock-on Atom

PLS Photoluminescence Spectroscopy

PVT Physical Vapour Transport

RBPM Rotating Beam Profile Monitor

RBS Rutherford Backscattering Spectrometry

RPM Revolutions Per Minute

SACT Small Angle Cleavage Technique

SAD Selected Area Diffraction

SEM Scanning Electron Microscopy

SiC Silicon Carbide

SIMS Secondary Ion Mass Spectrometry

SRIM Stopping and Range of Ions in Matter

STEM Scanning Transmission Electron Microscopy

TEM Transmission Electron Microscopy

THDS Thermal Helium Desorption Spectroscopy

TRISO TRIstructure-ISOtropic

UHV Ultra-High Vacuum

UV Ultra Violet

VHTR Very High Temperature Reactor

WBDF Weak-Beam Dark-Field

XPS X-Ray Photoelectron Spectroscopy

XRD X-Ray Diffraction

XTEM Cross-Sectional Transmission Electron Microscopy

List of Nomenclature

α_0	Divergence (semi-) angle
ϵ	Charge of one electron
ϵ_T	Reduced PKA energy
γ	Surface tension
λ	Wavelength
λ_d	Mean free path between ion and target atoms
Ω	Scattering solid angle
ρ	Density
σ	Single atom scattering cross-section
θ	Scattering semi-angle
d_0	Diameter of the electron source
$F(\theta)$	Structure factor
$f(\theta)$	Atomic structure factor
i_e	Cathode emission current
N	Number of atoms in a unit cell
x, y, z	Atomic coordinates in a unit cell
$(h\,k\,l)$	Miller indicies of a crystal plane
A	Area
a_0	Bohr radius of a hydrogen atom
B	Magnetic field strength
d	Distance between plates

d	Interplanar seperation
D_{eff}	Effective diffusion coefficient
E	Electric field
E_d	Energy required to displace an atom from its lattice site
F	Force
L	Path difference between scattered waves
M	Mass (of ion or substrate)
m	Ion mass
N	Number of atoms
N_A	Avagadro's number
P	Pressure
Q	Fusion energy gain factor
q	Ion charge
R	Ion range
r	Radius
R_P	Ion projected range
T	PKA energy
V	Voltage
V	Volume
v	Velocity
Z	Atomic number

Abstract

SiC is a material currently under consideration to be used in future generations of fission and fusion reactors where it will be subjected to high temperatures and significant fluxes of energetic neutrons. The work reported in this thesis aims to answer some outstanding issues of the behaviour of SiC at high temperature during irradiation by high-energy neutrons in combination with a build-up of helium (from both transmutation reactions and by direct implantation). These processes have been simulated by in-situ ion-irradiation / TEM at the MIAMI and JANNuS facilities.

This thesis contains the results of experiments which investigated the nucleation and growth of helium bubbles in SiC and the behaviour of these helium bubbles under high energy heavy ion-irradiation. Our conclusions are that helium bubbles in SiC are extremely stable at high temperatures and during high-energy ion-irradiation. However, we have discovered that there is a significant effect on the bubbles attributable to either electron beam irradiation alone or the synergistic effect of the electron beam and ion-irradiation which causes helium bubbles to shrink.

For my Dad

Chapter 1

Introduction

First documented in 1824 [1], SiC has evolved to become a material of intense research interest for a variety of applications. Driven by a motivation for improved electronic devices, the material properties of SiC have been researched and a significant amount of literature has been published. This has been reviewed in chapter 2. One aspect that makes SiC particularly interesting is the existence of many polytypes, with more than 200 discovered to date [2]; each of these has a different stacking sequence along the c-axis [1, 2]. There are a large number of rhombohedral polytypes (15R-, 21R-, 27R- etc.), many hexagonal types (2H-, 4H-, 6H- etc.) and a single cubic polytype (3C-). The major polytypes have been heavily researched and their fundamental properties are well understood [3, 4]. Some polytypes have a particularly useful combination of properties which promote their use for some specific roles, such as crystal growth substrates [5].

This chapter provides a brief history of SiC followed by an outline of the major contemporary applications and in particular its use in the nuclear industry. The second part of this chapter describes the motivation for this research and concludes with details of the work undertaken during the project and reported in this thesis.

1.1 History

SiC was first reported in a paper by Berzelius in 1824 [1], but at the time he only hypothesised about the presence of a silicon-carbon bond. It was not until the 1850s that silica and coke were deliberately combined in a furnace to produce the first SiC compound [1]. In 1893, the polytypic properties were

reported, followed by investigations of its suitability as an electrical device. The first SiC Light Emitting Diode (LED) was reported in 1907 which sparked interest in SiC as a semiconductor [1, 6].

The invention of the Lely method in 1955 allowed the creation of single crystal SiC [1, 7, 8]. The Lely method uses a crucible with a source of SiC at the top and bottom. Using thermal processes, the SiC sublimates and small hexagonal crystallites grow on the walls of the crucible. However, poor impurity control and small crystallite size meant these crystals were not particularly useful for industrial research purposes [8]. 1978 saw the invention of seeded sublimation growth of SiC by Tairov and Tsvetkov [7, 9]. This transformed SiC research as it allowed the growth of large, high purity, single crystal SiC wafers.

Creating large wafers for research use has stimulated a significant scientific community surrounding SiC. In the late 1980s, further refinements to the crystal growth process [10] led to the founding of Cree inc. [1, 11]. This company specialises in wafer manufacture and has brought a number of SiC-based electronic devices to market [12].

1.2 Applications

SiC has a number of applications. As a hard ceramic semiconductor with exceptional radiation hardness, high thermal conductivity and low coefficient of thermal expansion, it has diverse attributes which can be exploited for a number of purposes. These include graphene production [13], electronics and sensor development [14] as well as nuclear applications [15].

The ceramic properties of SiC have been used for both cutting [16] and abrasive polishing of materials [17]. SiC is particularly suited for this as it has a Mohs hardness of nine [18]. The use of SiC-based composites has been investigated for industrial scale cutting and has been found to be superior to other ceramic materials used for this purpose (for example, tungsten carbide) [16]. SiC-composite aircraft brake-systems have been studied in recent years as a replacement for current carbon or steel brakes [19–21]. Carbon/SiC composite brake materials have excellent braking performance, lower wear and suffer a lower reduction in brake power at high temperatures than current materials [19, 20]. Composite materials made of metal and SiC have worse performance, with wear rates significantly higher than the brake material

currently used [21].

Information about the use of SiC for electrical devices, in astronomy as mirrors, graphene production and as a nuclear material is presented in sections 1.2.1 to 1.2.4.

1.2.1 Electronic Devices

Rapid improvement of SiC wafer growth and processing has resulted in a large amount of interest in using SiC as a semiconductor [1, 14]. It has a wide bandgap [14, 22, 23] of 3.26 eV (for 4H-SiC, see table 2.1 for other polytypes) which allows it to be used in high-temperature environments. SiC has a high thermal conductivity [14, 22, 24], large (saturation) drift velocity [24] and is radiation hard [14, 22]. These properties are highly favourable for devices designed to operate in high temperature, frequency or power environments [22, 23].

There is significant interest in using SiC as a material for the creation of MicroElectroMechanical Systems (MEMS) [14, 18]. To date, only relatively simple electronics have been manufactured from SiC [14]. There is potential for devices of a more novel nature to be manufactured in the near future [14]. It has taken several decades to establish commercially-viable SiC-based devices [1, 22]. However, the early 21st century has seen the production of high-temperature SiC-based Metal Oxide Semiconductor Field Effect Transistors (MOSFETs) [25, 26] and Schottky diodes [23, 24, 27].

Some polytypes lend themselves better to electronic applications. For example the cubic (3C-) polytype is the only one that can be epitaxially grown on a silicon substrate [5]. This is particularly interesting because it reduces the cost of SiC wafer development by combining it with the well understood and low-cost industry which manufactures silicon wafers [14, 28]. The disadvantage to this solution is the introduction of additional (or non-stochiometric) silicon which undermines some of the favourable SiC properties — especially the high temperature performance [28].

1.2.2 Astronomy

Due to its high reflectivity in the Ultra Violet (UV) and Infrared (IR) bands, SiC has been used as mirrors in telescopes on satellites [29–31]. Optical systems

used in these satellites have been made to be exceptionally lightweight using porous SiC as a structural material and thin elements of SiC as mirrors [31]. These telescopes are operated at cryogenic temperatures and surface profiles of SiC have been shown to be stable when operating at the low temperatures [31]. A proposed design for a new, extremely-large telescope (100 m in diameter) has led to some research using sintered SiC mirrors for this purpose [32]. This is promising because of its high Young's modulus and high thermal stability [32]. SiC remains a proposed material to enable manufacturing of lightweight extraterrestrial or earth-based telescopes [32]. Weight is a particularly important factor to consider when launching equipment into space, as it directly impacts on launch cost.

1.2.3 Graphene Production

The production of large scale graphene wafers is regarded as one of the bottlenecks in the development and adoption of this 'super' material as part of the electronics industry [33–35]. Heating of SiC wafers has been shown to be a viable method of production and has resulted in a significant amount of interest in SiC for this purpose [36–38]. Above temperatures of 1050°C, silicon within SiC is able to sublimate from the crystal resulting in graphitisation of the surfaces of SiC [39–49]. Several research groups have investigated this phenomenon with a view to producing high quality graphene. It is now possible to control the parameters of this process with such fine control that a known number of high quality, single crystal graphene sheets can be grown consistently on a SiC substrate [36–38].

The use of SiC as a substrate may create a pathway to efficient commercial production of graphene [35]. However it needs further work in order to be implemented on an industrial scale — specifically addressing the repeatability of growth [13]. Growth of graphene on a SiC substrate needs investigation in order to determine the effect of the interface on the grown material [13]. Theoretical work has shown that the bonding between SiC and graphene is significant [50]. Should the retail value of graphene remain as high as current levels, the use of SiC wafers in this way could be a viable commercial manufacturing process [51].

1.2.4 Nuclear Applications

Energy is considered to be one of the (if not the most) important issues for the 21st century [52]. There is an increasing emphasis on producing more electricity with a lower environmental impact and for greater financial gain [53]. The desire to move away from reliance on mined fuels is also clear and the increase in research on nuclear fusion technologies demonstrates how important this area is for modern scientific and engineering development [53, 54].

As mentioned in section 1.2.1, one of the key properties of SiC is its radiation hardness. This has potential to be exploited, not only in electronic and astronomical applications, but also by the nuclear industry [15, 55, 56]. In order to facilitate this, there is still a significant amount of research to be conducted into SiC both as a composite and as crystalline wafers [57]. In the form of SiC fibre matrix composites, its properties are improved when compared to bulk SiC. These composites consist of a series of SiC fibres embedded in bulk SiC.

SiC has been used to address some contemporary nuclear problems and it is expected that SiC composites will be employed as structural materials in the next generation (Generation IV) of fission reactors and in the future generations of fusion reactor design [15, 55].

SiC is used as part of the TRIstructure-ISOtropic (TRISO) fuel pellet structure to add strength and combat the stresses associated with fission gas release during fuel use [58, 59]. The TRISO fuel pellet is used in Generation III+ reactors and in one of the Generation IV reactor designs. It consists of a uranium dioxide centre surrounded by a layer of porous carbon. The porous carbon layer is then surrounded by a layer of dense carbon, and a layer of SiC. Finally an outer layer of dense carbon is added to complete the fuel pellet [58, 60, 61]. Figure 1.1 shows an schematic of a TRISO fuel pellet. SiC is also used in the pebble bed reactor (one of the Generation IV reactor designs) as a fire proofing layer [61].

SiC is of interest as a nuclear material for the future, both for the next generation of fission nuclear reactors [15] and for fusion reactor development [15, 55, 56, 62, 63]. Primarily, the applications in which SiC will be employed are expected to be structural, though recent improvement in SiC composite materials has reignited the interest in SiC for use in fuel cladding applications [15].

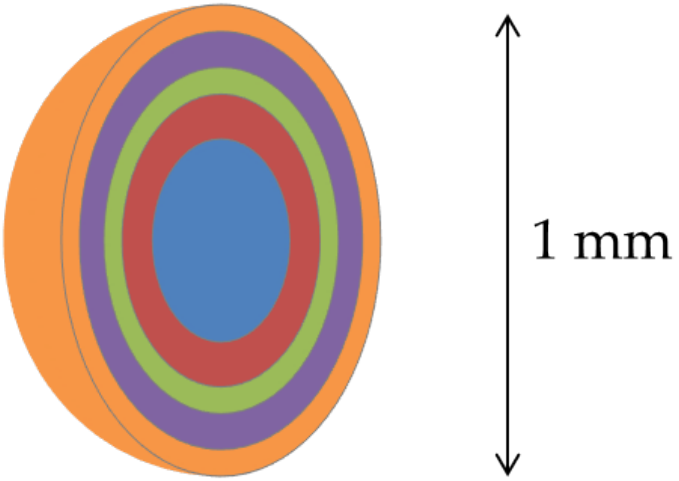

Figure 1.1: Cross-section of a TRISO fuel pellet showing the fuel kernel, the porous carbon buffer layer, the inner pyrolytic carbon layer, the SiC layer and the outer pyrolytic carbon layer based on [60].

1.2.4.1 Nuclear Fuel Cladding

TRISO fuel cladding is used, or is proposed to be used, in two Very High Temperature Reactor (VHTR) designs, namely the pebble bed module reactor [59, 61] and the Gas Turbine Modular Helium Reactor (GT-MHR) [64, 65]. Currently, TRISO fuel is used in two experimental reactors. These are the 10 MW High Temperature gas-cooled Reactor (HTR-10) [66, 67] (a pebble bed modular reactor) and the High Temperature engineering Test Reactor (HTTR) (a GT-MHR) [68, 69].

TRISO fuel is a layered structure, with the nuclear fuel located in the centre (described in section 1.2.4). SiC in TRISO fuel is used to contain gaseous and metallic fission products [59, 65, 70] and to add strength to the fuel pellet [58, 59]. SiC is suited to its role in TRISO fuel, because of its radiation hardness and stability at the high temperatures at which these reactors operate. Additionally, a low thermal expansion coefficient is required, as well as minimal swelling during its lifetime in the reactor. These are required in order to ensure that the fuel pellet remains structurally sound to keep the fuel safe [71, 72].

Chemical Vapour Deposition (CVD) SiC is used in TRISO fuel kernels. The chemical environment in which CVD is performed has been studied with a view to reducing grains to nanometer size in order to improve the mechanical and radiation resistant properties [72]. In addition, an investigation on

deposition temperature has also been performed [73].

The failure mechanism of the SiC layer in TRISO fuels has been studied. This is attributed to the shrinking of both pyrolytic carbon layers. This causes the inner layer to pull away from, and the outer layer to push into, the SiC layer [71]. The shear strength at the interface is therefore critical in determining failure of TRISO fuel pellets [74]. A handbook summarising the behaviour of SiC in TRISO fuel has recently been completed by Snead and colleagues [75].

1.2.4.2 Future Nuclear Uses

SiC has been proposed as a first wall material for some types of fusion reactor [76, 77]. The first wall is the plasma-facing surface in a magnetic confinement fusion reactor. SiC-based materials are also under consideration for blankets which absorb thermal energy from the reactor and will breed tritium as a result of interaction with neutrons [57, 78, 79]. Several proposed fusion reactor designs suggest using SiC [55, 79], but ten years ago SiC composites were not considered to have properties which matched the expected requirements [55]. Since then, there has been a significant amount of research into improving the properties of SiC for applications in fusion reactors.

Many of the properties of SiC discussed in the earlier parts of this chapter make SiC suitable for use in fusion reactors. High temperature strength and low induced radioactivity are already well understood for SiC and its composites [56]. The mechanical properties of SiC composites have been shown to be stable to tens of Displacements Per Atom (DPA) at temperatures above 700°C [78].

Research on the properties of SiC, and investigation of radiation damage of SiC including SiC-composites, continues to be relevant [80, 81] and it remains an important material for nuclear applications. As well as fusion applications, a number of future fission reactor applications have been summarised in a recent review by Katoh [15].

1.3 Fusion Reactor Development

Fusion as an energy source has many promises; it is energy dense, proliferation resistant and produces a small amount of radioactive waste. In addition, much of the fuel is readily available [82]. Fusion reactors would generate power

by using the excess mass-energy generated when two nuclei fuse together to form a heavier element. Excess energy is created because the nucleus created has a mass slightly lower than the total mass of the two elements used to create it. This energy will be used to generate steam, much in the same way that current power plants work. In order to generate a sufficient density of fusion events a plasma is created of hydrogen, deuterium and/or tritium nuclei which must then be confined in some manner. There are two potential methods of confinement, either inertial or magnetic. The energy required to create conditions suitable for fusion is significant. The overall efficiency of the process is labelled Q, which is energy output divided by energy input. The current goal is to achieve an experiment with a Q factor of 1 (or greater) for sustained periods of time.

Fusion is considered to be safer than the fission reactor designs that can lead to accidents as occurred, for example, at Fukushima [53]. Fusion plants would be proliferation resistant [82] and have significantly lower nuclear waste levels when compared to current nuclear reactors [83]. There have been significant studies detailing the economic viability of fusion research and development projects leading to operating power plants — these are, understandably, high-risk due to the unproven nature of a significant amount of the required technology [83]. In order to share the high cost of these projects, European and World-wide projects have been established which aim to culminate in the demonstration of an operational fusion-based power plant in the next 20 years.

There are two parallel projects which aim to investigate the confinement options. Confinement is used to retain the high temperature and pressure plasma required for fusion within the reactor. The first is a well defined development plan operating in Europe using magnetic confinement [53]. Three experimental facilities have been or will be constructed; in order these are: Joint European Torus (JET), International Thermonuclear Experimental Reactor (ITER) and DEMOnstration Power Plant (DEMO) [53].

The alternative is a less coordinated plan which is in progress using a laser based system using inertial confinement. Two linked facilities are under development, the first is the National Ignition Facility (NIF) [84], which will be followed by High-Power laser Energy Research facility (HiPER) [85].

1.3.1 Joint European Torus (JET) (1983 – present)

Following a five-year construction period at the Culham Laboratories near Oxford, UK, the Joint European Torus (JET) became operational in the middle of 1983. A 15 m diameter tokamak; JET was designed to develop a full understanding of the plasma process and the way in which it interacts with the first wall [86]. A significant amount of research output has come from the JET team since 1985. Some of this has included enhancing fundamental understanding of the erosion of vessel walls [87] by the plasma. Investigations using Rutherford Backscattering Spectrometry (RBS), Nuclear Reaction Analysis (NRA) and Elastic Recoil Detection Analysis (ERDA) found that around 15% of the material sputtered from the inner walls was redeposited on the outer walls of the tokamak [87]. The other 85% of sputtered material was concluded to have been redeposited within the limiters or the diveror plates. This was observed following three months in JET, during which it was subjected to approximately 22500 seconds of plasma discharge with a density of $2 - 9 \times 10^{19}$ m^{-3} [87]. In the late 1990s the role of JET was adjusted in order to begin to provide relevent information on plasma behaviour for the ITER experiment [88]. Gibson and the rest of the JET team demonstrated some significant results in their work [89] including the absence of mass scaling between deuterium-deuterium and deuterium-tritium discharges. (That is, energy output is independent of whether tritium is used in the plasma or not.) The report also claims evidence of α-particle heating as well as providing a significant level of detail for optimisation of the fusion yield. More recent publications [88, 90] demonstrate that the project is continuing to produce excellent information primarily in plasma optimisation, control and shape.

1.3.2 National Ignition Facility (NIF) (2009 – present)

Built at the Lawrence Livermore National Laboratory (LLNL) in California, USA, the National Ignition Facility (NIF) [84] is a 192-beam ultraviolet laser system with a 10 m diameter target chamber. This facility is designed to be a demonstration of inertial confinement of fusion plasma which will allow researchers to investigate the behaviour of hydrogen fuel at high density and pressure [91]. Beryllium ignition capsules measuring just 2 mm outer diameter are filled with cryogenic deuterium-tritium fuel which is then the target for this high-energy laser system [92, 93]. While designing the materials for the first

wall of this experiment, LLNL workers performed ablation experiments on various materials to understand the relevant properties for introduction in the NIF. SiC featured in these results, but the thermal shock which was observed reduced the likely usefulness of this material in the NIF [94]. The design parameters for NIF have been selected to ensure precision and accuracy at every level in order to extract the highest possible scientific output from the experiments [93]. NIF was exceptionally goal-centred in its design — refusing to be confined to the technology of the time — it has, however, like many projects, been superseded by newer ideas of fast-ignition systems. Workers at NIF intend to modify the experiment to suit the needs of the scientific community. It will, however, not be the final developmental step between experiment and power plant [92].

1.3.3 International Thermonuclear Experimental Reactor (ITER) (2019–)

Collaboration among the EU, the USA, Russia and Japan has led to the design of the International Thermonuclear Experimental Reactor (ITER) [95]. Construction began in Cadarache, France in 2009. The design goal is to achieve ignition of deuterium-tritium plasma and upscale the work performed at JET to a level where power generation can be demonstrated. To confine the plasma, superconducting magnets will be utilised to generate the high magnetic fields required. Though the project has suffered some financial setbacks [96] the design goals remain clear: to establish plasma conditions with $Q \geq 10$ [97], to demonstrate the required technology is both available and can be used, and to demonstrate that a tritium breeding concept can lead to self-sufficiency in the future. Material considerations for ITER are key to ensuring that the reactor is successful and have been extensively detailed [98, 99]. SiC, in the form of fibre reinforcement of other materials, has been considered for inclusion in the project as a heat-sink material [100]. Following recently completed work at JET in 2012, the first wall at ITER will be manufactured using a combination of tungsten and beryllium [101]. SiC has been suggested for other roles at ITER such as in the diverter [102], in the blankets [103] and other plasma-facing components [104].

Currently this project is in its infancy [99], but already there is a requirement for some key research questions and experiments to be performed in the

development of materials for this project [99, 100].

1.3.4 High-Power laser Energy Research facility (HiPER) (2030–)

The High-Power laser Energy Research facility (HiPER) project is aimed at demonstrating fast-ignition by a multi-laser beam array. The project has been designed to bridge the gap between the NIF and future plans for an inertial confinement fusion energy demonstration reactor [85]. (A demonstration reactor aims to show that the power generation concept can be realised on an economic and geographic scale which signifies the moment that the transfer of technology from the scientific community to the commercialisation community can begin.) The key difference at HiPER is that it will operate on a pulsed system rather than the single-shot system employed at NIF. The target for the project is intended to be tungsten based. There are, however, issues with helium bubble formation as well as sputtering and cratering on the surface of tungsten. Significant work [85] has been performed on the behaviour of tungsten under equivalent conditions. Though the project is in its early stages, there has been research on the cryogenic system required [105], the beamline [106] and sample chamber [85].

1.3.5 DEMOnstration Power Plant (DEMO) (2033–)

Building on the work undertaken at ITER, the DEMOnstration Power Plant will show that commercial generation of power from a fusion reactor is possible and both economically and environmentally viable [107]. The construction of such a power plant is scheduled to begin sometime in the next decade. Power generation is expected sometime in the 2030s. This, it is hoped, will lead to the commercial uptake of fusion reactors around 2050 [107]. The big upscale between ITER and DEMO will be in the efficiency factor, Q, which will be scaled from 10 to 40. Significant studies have been undertaken [108, 109] describing five concepts under consideration for design and construction in the DEMO project. The connected nature of the magnetic confinement programme means that key information required for decision making about the design requirements for DEMO are not yet known [109]. Key planning decisions are awaiting information from the ITER project. This

may place DEMO at a disadvantage compared to other fusion projects from a completion timescale perspective, though the body of knowledge which will be complete by the time construction begins on DEMO should offset any delay incurred during construction and operations at ITER [108].

Material research is ongoing for inclusion in both the ITER and DEMO projects. SiC/SiC composites are clearly a crucial component for the success of these [81, 110]. One of the areas of concern is the behaviour of the material under irradiation [110]. Additionally, the ability to manufacture sufficient quantities of radiation resistant composites [110] will influence the design criteria for DEMO [111]. Several publications state SiC/SiC composites should be investigated for this purpose as a priority [111, 112].

1.4 Motivation

Understanding the behaviour of SiC under irradiation is essential for the design of Generation IV nuclear reactors because of its promising properties as a structural material in a nuclear environment. This will allow designs to be implemented which can be employed within power plants across the world, in order to ensure safe and efficient power generation with a smaller environmental cost in comparison to present systems. Within the UK alone, the World Nuclear Association [113], EDF energy (the operator of the majority of the reactors) [114] and the UK's office of nuclear regulation [115] report that nine of the 16 nuclear reactors are scheduled to be shut down over the next 11 years. Although the lifetime of current reactors is expected to be extended worldwide [116–118] including in the UK, the design and construction of new nuclear reactors is essential in order to meet future energy demands globally. The motivation for this research is to provide some of the much-needed information on SiC for the nuclear community, in order to ensure that efficient and contemporary nuclear stations designs are available for construction when, and if, a decision regarding the building of Generation IV (and beyond) nuclear power stations is made by the UK government.

Research into SiC has shown that it has attractive properties for nuclear applications, specifically its radiation hardness and strength characteristics [56]. The use of fibre composites as a structural material in reactors is considered to be the most promising application for SiC in the nuclear industry [15, 55]. (Further information on the use of SiC in the nuclear industry is

provided in section 1.2.4.) Despite the promising outlook, a recent review by Riccardi [57] concluded that there are still some critical issues to explore for this material. It is in order to address one of the outstanding issues — that of radiation stability — that the work contained within this thesis has been conducted.

One of the considerations when introducing materials to a nuclear environment is how they perform following prolonged exposure to the harsh conditions. In both current and future nuclear applications, a significant amount of helium is introduced to the material either by direct implantation of by-products from the nuclear reaction or as a result of nuclear transmutation reactions taking place in the material itself. Helium is, usually, able to diffuse rapidly and combine with other helium nuclei and vacancies to form helium bubbles within the material. The creation of helium bubbles leads to a significant degradation of the material properties (often the same properties which were favourable for the extreme conditions in the first place). This includes decreased toughness, cracking (particularly at grain boundaries), increased creep and irradiation induced swelling of the material [57, 119, 120].

1.5 Work Undertaken

The primary focus of the work reported within this thesis has been to gain a fundamental understanding of helium bubbles in SiC. An investigation in to helium bubble nucleation and growth in SiC and the behaviour of helium bubbles in SiC under high-energy heavy-ion-irradiation has been performed. Helium bubbles have been grown by helium ion-irradiation of SiC. All of the ion-irradiation in this work has been performed exclusively at *in-situ* ion-irradiation/TEM facilities. Observations of the dynamic irradiation effects on the nanoscale in real-time have been possible and have enabled the unique nature of many of the results reported in this thesis.

This work is the first *in-situ* ion-irradiation/TEM investigation of helium bubbles in SiC and it provides new insight in to the behaviour of this material under these conditions. The conclusions of this work provide important information for both the nuclear industry and those conducting research in this area.

Chapter 2

Literature Review

This chapter contains a review of relevant literature for the experimental results presented in following chapters. It consists of several sections, covering fundamental properties of SiC, ion-irradiation of solids, defects in solid materials, Transmission Electron Microscopy (TEM), irradiation of SiC by a variety of particles, diffusion in SiC and thermal effects in SiC. The literature review is intended to highlight the important publications in order to contextualise the research in this thesis.

2.1 Silicon Carbide

As a material, SiC has many interesting properties and not least of these is the extensive polytypism exhibited. There have to date been over 250 polytypes characterised [2]. This is a result of the basic component of SiC which is the Si and C bonded together into a tetragonal building block. When these are combined, they form sheets of atoms. The layers are often labeled either A, B or C, which can be stacked with many different combinations. Three crystal structures exist within the polytypes; cubic (denoted C), hexagonal (denoted H) and rhombohedral (denoted R) [121]. Each polytype comes with a number defining the number of layers before repetition in the layer. The most common polytypes are 3C-, 4H- and 6H-SiC. Table 2.1 details the fundamental properties of each of these main polytypes.

The key limitation for the development of SiC both for electronic and material research has been the availability of high quality, large, single-crystal wafers. Many semiconductor growth processes rely on the ability to form the crystal from a melt or a solution. The fundamental properties of SiC do not allow

Material Property	Polytype 3C (α)	4H	6H (β)
Density (g.cm^{-3}) [121]	3.21	3.21	3.21
Lattice Parameters (Å) [122]	a=3.083 b=7.551	a=3.081 b=10.084	a=3.081 b=15.12
Space Group [3]	T_d^2(F43m)	C_{6V}^4(P6$_3$mc)	C_{6V}^4(P6$_3$mc)
Thermal Conductivity (W.cm^{-1}.K^{-1}) [121]	4.9	4.9	4.9
Bulk Modulus (10^{-3} Bar)	2.22 [123]	2.23 [123]	2.04 [124]
Band Gap (eV) [23]	2.40	3.26	3.02
Coefficient of Thermal Expansion ($\times 10^{-6}$ K^{-1})	2.74 (at RT) [125]	$\bar{a}_{11}$=4.47 $\bar{a}_{33}$=4.06 [126]	4.25 [127]

Table 2.1: Fundamental properties of common silicon carbide polytypes

crystals to be easily grown in this manner. Referring to the phase diagram in figure 2.1, it can be observed that above 2800°C the crystal will undergo a phase change resulting in non-stoichiometric melting of SiC. The conditions for stoichiometric melting are described in reference [10] and indicate how unfeasible this methodology would be in the creation of SiC wafers.

During the latter part of the last century, a viable technique for the creation of SiC wafers was developed — that of Physical Vapour Transport (PVT). Described by Tairov and Tsvetkov [7], the technique relies on the use of a graphite-walled crucible containing a seed on which the crystal can grow, a source of SiC in the bottom of the crucible and a furnace capable of raising the temperature of the crucible to above 2000°C. A schematic of PVT is shown in figure 2.2.

Polytype control is a key consideration when using PVT as a small variation of conditions can result in different polytypes. This is a result of the low stacking fault energy in SiC [10, 129]. The primary control mechanism is the provision of the appropriate seed on which the crystal can nucleate. This can be assisted by the introduction of catalysts to enhance or inhibit specific phase transitions [7]. Other parameters can be adjusted to control the polytype such as whether the growth is on the carbon or silicon face of the seed crystal [130, 131], temperature [132] or the system pressure [9].

An understanding and a minimisation of defects while growing PVT crystals of SiC is a crucial component for production of high-quality wafers for research in this field. There is a variety of types of defects which have been observed to occur including micropipes [133], growth spirals [134], dislocations [135],

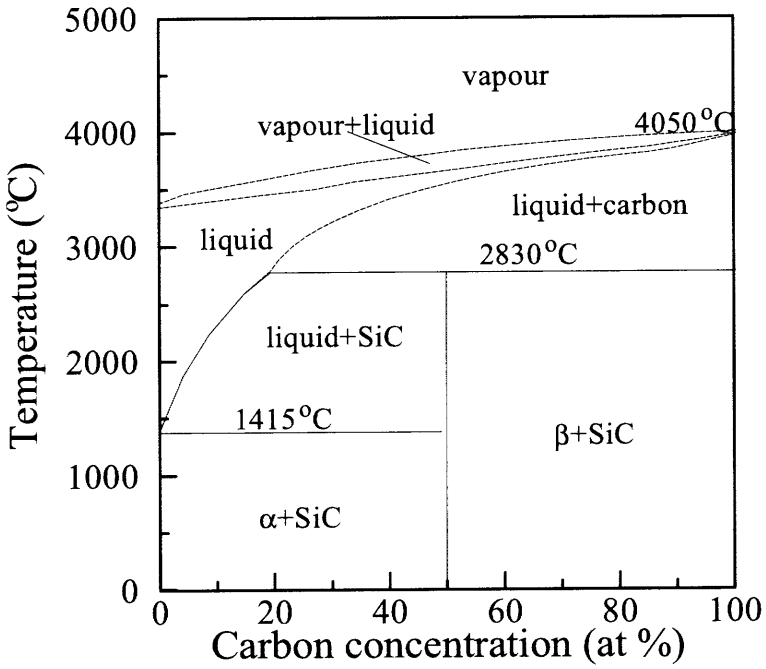

Figure 2.1: SiC phase diagram showing SiC phase composition for different temperature and carbon content taken from [128]. The phases labeled α and β are a solid solution of carbon in silicon and a solid solution of silicon in carbon respectively.

grains (and areas within grains which have a low ($< 10°$) misorientation from the main grain called sub-grains) [136] and hexagonal pits [136, 137] (see section 2.3 for more details on defect types). A number of research groups have made progress with producing wafers which contain very few defects (they report them as "essentially defect free") [138]. However, their wafers are extremely thin and are not viable for most research or electrical applications. In recent times, the micropipe has been all but eliminated as a defect in SiC, but the reduction and elimination of other defects, such as dislocations, is seen as a requirement for further development in this field [139].

In addition to PVT, the CVD method is available for the manufacture of SiC wafers. This also requires a high temperature, reportedly as low as 800°C [140] but reported predominantly in the range 1500–1600°C [141–144]. The majority of modern CVD SiC is manufactured using a combination of silane (SiH_4) and propane (C_3H_8), though much of the early work [142] utilised methyltrichlorosilane (CH_3SiCl_3). The growth pressure is commonly reported in the 50–500 Torr range [140, 142, 144] though there has been successful growth reported at both atmospheric pressure [143, 145] as well as at lower

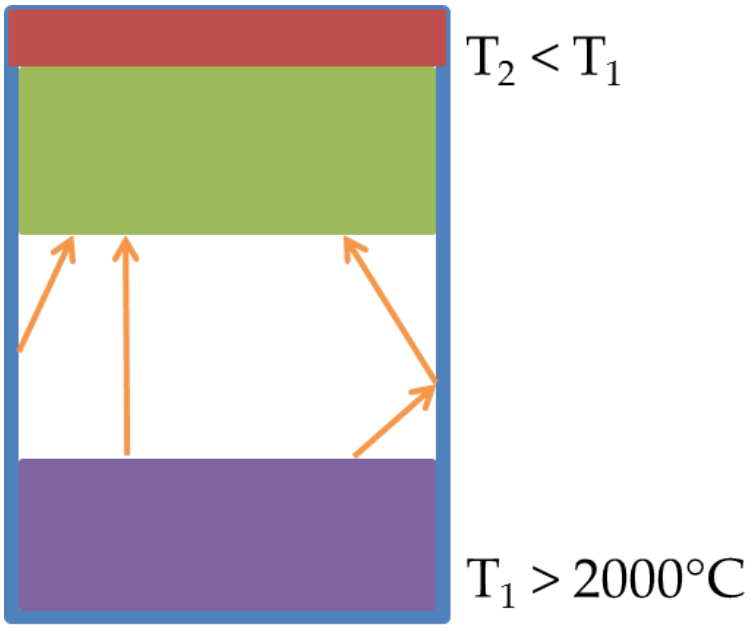

Figure 2.2: PVT schematic based on [1, 8]. The figure shows the graphite crucible, the SiC seed crystal, the growing SiC ingot, the SiC charge and the potential routes for molecules to take from the charge material to the ingot. The potential routes are direct evaporation of SiC, evaporation of graphite from the crucible and a two stage process where an evaporated molecule collides with the crucible before condensing on the ingot.

pressures of 0.15 Torr [146] and 10^{-7} Torr [147]. Some research has reported significant macroscopic defects such as triangular pits [141, 143] as well as screw dislocations and micropipes [143, 144, 148]. (For more details on defects, see section 2.3.) Using CVD, researchers have been able to create both single crystal [145–147] and polycrystalline [142, 149, 150] deposits of SiC.

2.2 Ion-Irradiation of Solids

Ion-irradiation of solids is of interest to material scientists as it is possible to facilitate changes in material properties by this process. Ion-irradiation of solid materials has applications for electronics research as well as providing information for the nuclear and aerospace industries. The following section details some of the core findings of research conducted in this area and is relevant for the work reported in this thesis.

2.2.1 Energy-Loss Mechanisms

When an energetic ion enters a solid it may undergo a series of collisions within the system. These can be categorised as interactions with the cores of the atoms within the solid (described as nuclear stopping) and as interactions with the electrons surrounding the nuclei (described as electronic stopping) [151, 152]. The significance of each mechanism is highly dependent on ion energy and target mass. For example, nuclear stopping is the dominant process when low energy ions are incident on a target with a high atomic number, whereas electronic stopping is most significant collisions between ions with a high energy with a target with a low atomic number [151]. The total energy lost by an incident ion in a target is the sum of the nuclear energy loss and the electronic energy loss.

2.2.1.1 Nuclear Stopping

Nuclear stopping of ions is the result of collisions with the cores of atoms within the target. Nuclear stopping transfers energy from the incident ion to the target atoms through almost elastic collisions. (This process is not necessarily truly elastic as there is some excitation of electrons of the target atoms.) The incident ion scatters as a result of the collision with the target atom, the degree to which the ion is scattering (compared to its original trajectory) is proportional to the energy transferred to the target atom [152]. If the energy transferred to the target atom by the incident ion during the collision exceeds the energy required to displace it from its lattice site then the ion-irradiation will cause displacements to the target atom and thus cause damage to the specimen [152]. The energy required to displace a single atom from its lattice site will vary, but each material has an average value, E_d.

2.2.1.2 Electronic Stopping

Electronic stopping is a more complicated process than nuclear stopping though the interaction can be shown to be mostly dependent on the ion velocity and the charge on the ion and on the target atom [151]. Where the ion is moving slower than the velocity of atomic electrons (when $v < v_0 \, Z_1^{2/3}$) it readily captures an electron and neutralises [151]. In this energy range, electronic energy loss is proportional to ion velocity or $E^{1/2}$. If the ion is moving at higher velocities (when $v \geq v_0 \, Z_1^{2/3}$) it is not possible for the ion

to capture electrons. Instead the electrons are stripped from the incident ion and it becomes a point charge moving much faster than orbital electrons [151]. Electronic energy loss in this energy range is proportional to Z_{ion}/v^2 [151].

In both cases, as the ion moves through the target material, electron clouds on each atom (or in the case of metals, the quasi free electron cloud) provides a drag force on the incident ion, causing it to slow as it travels through the specimen. The energy lost by the ion causes excitation of the electrons.

2.2.2 Range

The range of an incident ion is linked directly to the energy loss process described above. The path of incident ions within the target is defined by scattering by atoms in the target. As a result of this the path travelled is not always parallel to the entry path of the incident ion. Many properties are defined for incident ions. Two important properties are range (R) and projected range (R_P). Range is the total path the ion has travelled within the solid. Projected ion range is the distance the ion has travelled in a direction parallel to the incident ion [151]. Calculating R and R_P can be performed using scattering cross-sections to find the probability of nuclear collisions taking place and factoring in the energy lost during each nuclear collision. An additional calculation is then performed which takes into account the energy lost through electronic interactions as a function of distance through the specimen [152].

Each incident ion has a statistical chance of collision as it passes through the target. It is likely that no two incident ions will undergo the same sequence of collisions in the target and so they come to rest at different depths within the target [152]. The result of this is a statistical distribution of ranges which is characteristic of the incident ion and the target solid. Statistical information relating to the spread of the projected ranges, R_P, is available by using the variance, σ^2. In cases where the target is made from a single element, the variance can be calculated [151] to be approximately:

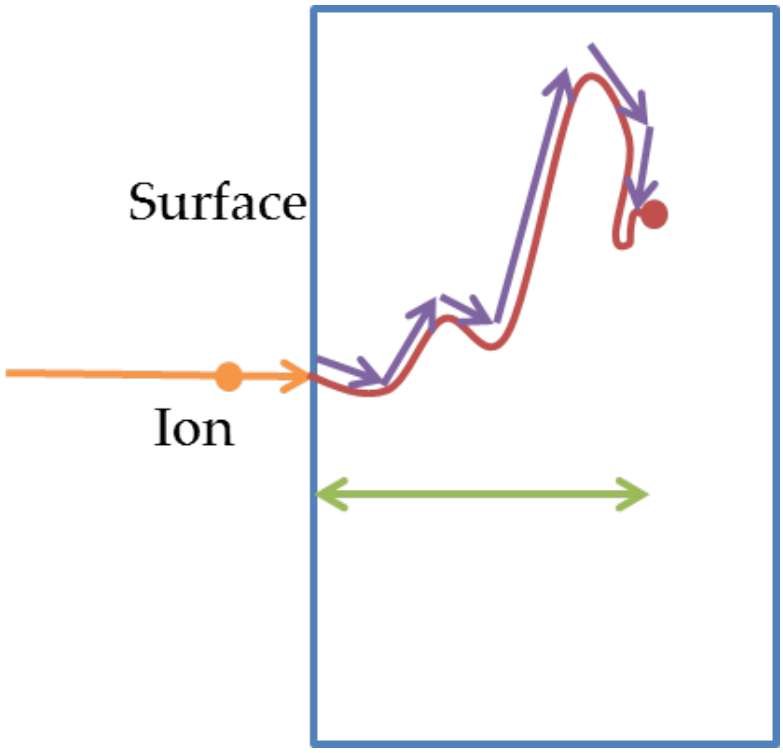

Figure 2.3: Schematic of range concepts during ion implantation. Based on [120]. The difference between R_p and R for an incident ion can be seen. This is due to the ion path in the material not being parallel to the incident ion

$$2.5\Delta R_p \approx 1.1 R_p \left[\frac{2(M_1 M_2)^{\frac{1}{2}}}{M_1 + M_2}\right]$$

$$\Delta R_p \approx \frac{R_p}{2.5} \tag{2.1}$$

2.2.3 Channelling

Channelling in crystal structures is a consideration when performing ion implantation because it can significantly alter the range of implanted species [151]. This is particularly important during depth dependent doping of semiconductors. The nature of crystalline structures, with regularly spaced planes of atoms means it is easy to steer energetic ions into the less resistive paths

in the crystal [153]. This can occur accidentally or can be exploited if it is desired. This technique, known as channelling results in a significantly deeper ion range than in cases where chanelling does not occur.

Simonton and Tasch [153] detailed two mechanisms which contribute to increased ion channelling. The first is an ion inserted between planes with low Miller index directions with a velocity such that it travels between these planes. The atomic potentials of each successive atom in the target steer the ion along the channel within the crystal. This process can continue for long distances through the crystal (compared to the range of ions in the non-channelling case), greatly increasing the range of the incident ions. Electronic stopping is the primary mechanism for stopping of channelled ions, as a result, the total number of atom displacements will be reduced. The second mechanism is that of planar channelling where the incident ion enters the crystal with a small angle to a low Miller index plane. It then undergoes collisions with the channel wall, similar to the total internal reflectance principle in optical systems [151]. Both mechanisms are highly angle-dependent with a critical angle for channelling defined by the energy and element of the incident ions as well as the crystal structure of the target. Figure 2.4 demonstrates three ion paths through the crystal, including both of the channelling principles and non-channelling examples.

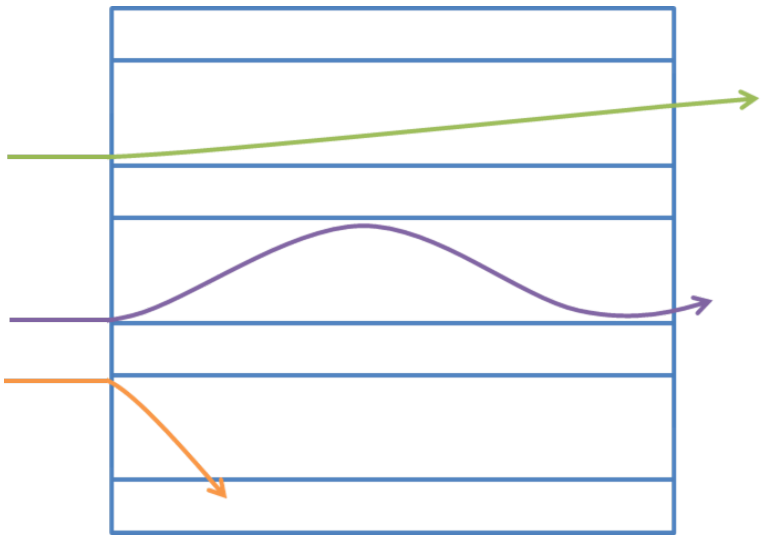

Figure 2.4: Schematic demonstrating channelling within crystal planes based on [151]. This figure shows well channelled ions which remain channelled for long distances, ions with a large oscillation during channelling and will likely be de-channelled and ions which feel no channelling effect.

If experimenters wish to avoid channelling in single crystal targets there is an obvious solution which is to reorient the crystal or the ion beam so that the major channelling directions are not in the same direction as the ion trajectory. This is not a simple task, given the multiple channelling orientations that exist in many crystalline systems. The potential number of chanelling directions in a crystalline material means that the tilt angle (the angle between the ions beam and the normal to the surface of the target) as well as the azimuthal angle (around the axis normal to the surface of the target) need to be considered [153]. Additionally, there are also issues of flexing of the wafer due to sample heating and cooling during irradiation. Reproducibility is a further concern; the measurements of the angles needs to be accurate enough to provide consistent results between irradiated batches [153].

Alternative techniques are available, such as growing an oxide on the surface of the material. This can be desirable as it protects the implanted wafer from surface contamination from the specimen chamber during the implantation process [153]. The oxide on the surface is an amorphous material which causes the incident ion beam to scatter into a relatively wide cone, which drastically reduces the opportunity for the ions to enter the crystalline part of the target in a manner which encourages channelling [153]. Another technique which reduces channelling in crystals is radiation damage in the crystal. As the amount of damage increases in a specimen, it is less likely that a plane of the appropriate orientation will remain to guide the ion. As more atoms become removed from their original sites then channelling tends to be less likely to occur and the effect becomes reduced [151].

2.2.3.1 Channelling in SiC

Morvan *et al* [154] investigated the channelling behaviour of SiC by comparing implantation with 'random' orientation to implantation performed with 0° tilt with respect to a $\langle 0\,0\,0\,1 \rangle$ axis. Implantations performed with channelling conditions demonstrated an R_P of approximately twice that of unchannelled ions. Peak dopant levels were measured by Secondary Ion Mass Spectrometry (SIMS) to be approximately one order of magnitude lower in the channelled case than in the non-channelled case. Additionally the depth of the damage was 2.5 times further into the wafer than was measured in specimens where channelling was avoided [154]. Theoretical calculations based on the Binary Collision Approximation (BCA) [155] have corroborated the experimental

work by Morvan, showing the channelling can occur in the $\langle 0\,0\,0\,1 \rangle$ and $\langle 1\,1\,\bar{2}\,3 \rangle$ directions.

2.2.4 Radiation Damage

As described in section 2.2.1.1, the implantation of ions into a solid target will usually result in damage [151]. The initial interaction with the target generates a Primary Knock-on Atom (PKA) as a result of a nuclear collision with the incident ion. The PKA disperses its energy in the same way as the incident ion, through nuclear and electronic losses [156]. The reduced PKA energy can be calculated from equation 2.2 taken from [120]:

$$\epsilon_T = \frac{T}{2Z^2\epsilon^2/a} \tag{2.2}$$

Where a is given by:

$$a = \frac{0.8853a_0}{Z^{\frac{1}{3}}}$$

Where ϵ_T is a reduced PKA energy (a measure of how energetic the collision is and how close the ion gets to the nucleus), Z is the atomic number, ϵ is the unit charge, T is the PKA energy, a_0 is the Bohr radius of a hydrogen atom.

2.2.4.1 Cascades

Each PKA is generated by a collision between an incident ion and a target atom so long as the atom is displaced from its lattice site. If the energy given to the atom by the ion is $\geq$ E_d then a Frenkel pair is created (a vacancy and an interstital); if the energy is less than E_d, the atom will not leave its lattice site [151, 156]. Every atom which is displaced from the lattice goes on to have further collisions until its energy descreases to the stage where it comes to rest within the target. As each ion can create multiple PKAs and each of those can have further collisions in the lattice, each incident ion can create a cascade of collisions within the target. With sufficiently high energy ions, the PKA damage paths leave behind a trail of Frenkel defects. These damage paths will be well seperated at low fluences, but begin to overlap with increasing fluence

[156].

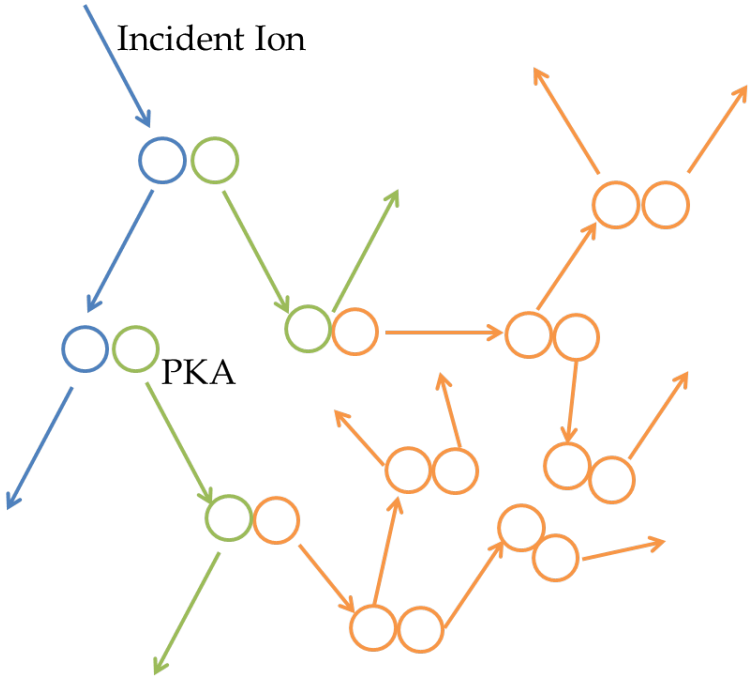

Figure 2.5: Schematic of PKAs and cascades created by an incident ion based on [151]. The incident ion continues to create PKAs until coming to rest or leaving the specimen. PKAs continue to create cascades within the target until their energy has been dissipated.

Figure 2.5 shows a typical displacement cascade. The cascade density increases rapidly towards the end of its range. As ion energy decreases, the scattering cross-section increases and the cascade becomes more dense due to the high probability of collision with nearby atoms. The volume of a cascade is determined by the energy distribution in both the transverse and longitudinal directions [120]. At higher energies, the displacements become distributed in a series of smaller sub-cascades which have a long(er) distance between each sub-cascade [120]. This is because the mean free path between collisions is higher. Channelling can also alter cascade behaviour as ions or PKAs will travel further between collisions and where they de-channel they will lose energy and form subcascades [120].

2.2.4.2 Spikes

If the properties of the irradiating particle and the target result in collision distances with an average seperation of close to the distance between atoms within the target then the phenomenon of spike-type behaviour is observed.

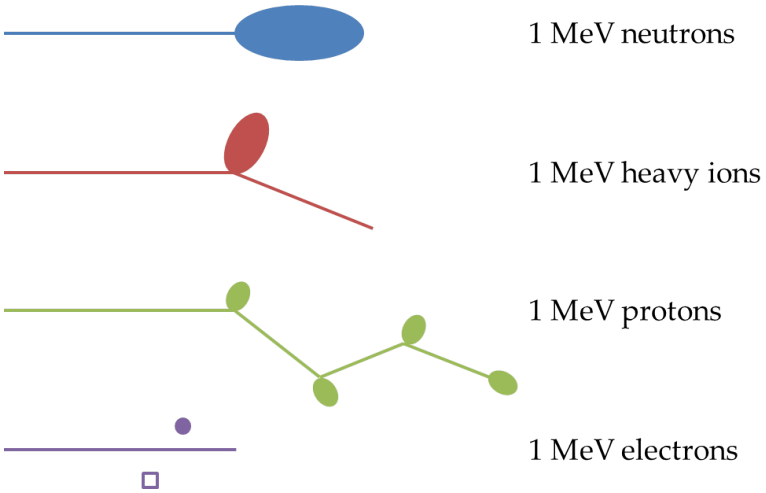

Figure 2.6: Differences between cascade volumes for different species based on [120]

A spike can be described as a small volume in the target in which the majority of atoms will be in motion simultaneously [151, 156].

2.2.4.2.1 Displacement Spikes

During displacement spikes many atoms in a small volume are displaced away from their lattice site [120, 151]. This creates many intersitial vacancy pairs and has been described by Brinkman as a highly-damaged region consisting of a core of vacancies surrounded by a shell of a high concentration of interstitial atoms [120]. This volume is the remnant of a displacement spike. Figure 2.7 shows a schematic of a displacement spike.

2.2.4.2.2 Thermal Spikes

As the incident ion or PKA comes to rest, each collision is no longer able to displace further atoms in the target. The energy is transferred to the surrounding atoms in the form of thermal energy and is dissipated through lattice vibrations with nearby neighbours. This raises the temperature of the lattice locally which can last for a few picoseconds, depending on the thermal conductivity of the target [151].

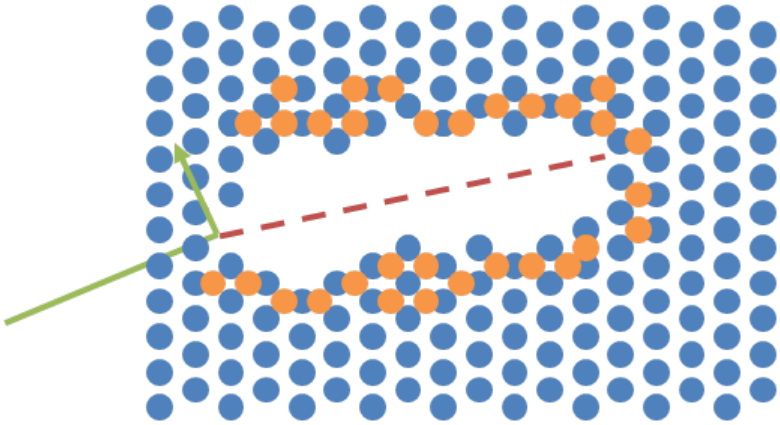

Figure 2.7: Schematic of a displacement spike based on [151]. The schematic shows atoms on lattice sites, interstitial atoms, path of incoming particle and path of the PKAs

2.2.4.3 Amorphisation

Disordering of a crystalline material can be achieved by ion-irradiation. Users can simulate the intended ion-irradiation conditions in order to achieve a damage profile in their target suitable for amorphisation. Through the diffusion of intersititals or vacancies, damaged materials can recover. This may require thermal annealing depending on the material. Where irradiation is performed at low temperatures it is possible to 'freeze in' damage generated by ion collisions with the target atoms [157]. Alternatively, amorphisation can be avoided entirely in materials susceptible to amorphisation by raising the temperature sufficiently to allow displaced ions to return to lattice sites [120]. There are two commonly proposed mechanisms for the crystalline to amorphous transition, which are material dependent. Firstly, some materials show a gradual transition towards amorphisation which is directly proportional to dose. The second observed mechanism is that of a slow transition during early damage accumulation followed by a rapid collapse of the lattice into an amorphous state. When amorphisation is driven by this mechanism it can be more difficult to predict [157].

2.2.5 Simulation of Ion-Irradiation in Solids

Simulation of ion-irradiation has been extensively utilised during this research, both in order to establish appropriate experimental conditions for this work, but also in order to to interpret the results of ion-irradiation. For this reason, it

is important to understand the current research in simulation of ion-irradiation of solids.

Computer simulation of ion collisions with solids is important for calculations of range, energy deposition and damage creation. There are two predominant simulation techniques to achieve this.

In order to perform simulations of the interaction of ions with solids, a very computationally-efficient technique is to use the BCA. This considers each collision between atoms to be isolated to just the two colliding atoms. It assumed that the contribution to collision mechanics by the many-body interactions is minimal. This approximation is remarkably good at simulating collisions [120]. During these simulations, atoms with an energy below a defined threshold (where it is assumed they no longer have energy to cause displacements) are ignored meaning these simulations are relatively efficient and can be performed reasonably quickly. BCA simulations of cascades work most accurately at ion energies significantly above the average atomic displacement energy. Closer to or below this threshold, other phenomena such as replacement collisions can be well simulated using the BCA [120]. The BCA is valid as long as the incident ion-irradiation undergoes discrete individual cascades (when the mean free path of the collisions is greater than the interatomic spacing) rather than spike-type behaviour. The BCA only applies for collisions between a single incident ion and the target, if information is required outside of this limitation then the BCA cannot be used. Monte Carlo methods can be used in combination with the BCA method described above. This method relies on the generation of random numbers and utilising these to generate statistically representative data by performing a high number of iterations. These programs follow a large number of incident ions, monitoring their position, direction and energy. In these simulations, the target is considered to be an amorphous material with atoms at random locations, but with an average distance between the atoms equal to that of the modelled system. Alternatively, some software allows users to input crystal structure and uses this information when performing the simulations. Collisions are then modelled, with the nuclear and electronic stopping components calculated independently. One of the most refined pieces of software for this purpose is SRIM [152, 158], more details are provided in section 3.4.3.

Molecular Dynamics (MD) can be used to perform simulations of ion-irradiations in solids, though this is generally computationally intense when simulations involve a large number of target atoms or many incident ions. The energy and force on each atom is continually and repeatedly calculated using appropriate interatomic potentials between each atom and all of the other atoms in the simulation [120]. The simulation then applies Newtonian equations of motion for each atom in the simulation. When the calculation for every atom is complete, the time step is increased by a very small amount (on the order of 10^{-15} s) and everything is recalculated. Computing power restricts what can be achieved by MD simulations. Often this results in simulations restricted in either the total number of atoms simulated or time scales that can be covered. This technique is particularly useful for simulating a small interaction volume, for example, a single cascade in exceptional detail, but can also be used to simulate larger volumes (at higher computational cost) [120].

2.2.6 Sputtering

Sputtering is an important consideration during ion-irradiation research. The introduction of an energetical particle to a solid material can sputter material from the surface. For *in-situ* ion-irradiation and TEM, it is particularly important because of the thin samples required, which mean that the sample has a higher surface-to-volume ratio than in other ion-irradiation studies.

The nature of the collision mechanics described above leads to a simple model for sputtering behaviour. Collisions that occur with the atoms in the near surface can provide sufficient momentum to remove a target atom from the specimen. From an ion implantation perspective, it is necessary to understand the sputtering performance of the ion/target combination. Sputtering yield (the number of atoms emitted per incident particle) can be calculated for single-element targets [151, 159]. For more complex targets the calculation is more difficult, but the sputtering yield is known to be proportional to the number of displaced atoms close to the surface [151].

Sputtering is used for specimen preparation. It is used to provide final thinning of specimens for TEM [160] or to deposit thin films [161, 162]. See section 3.2.3 for details on the use of sputtering to prepare samples for this work.

2.2.6.1 Sputtering of SiC

Sputtering of SiC has been investigated using a variety of ions and energies. For light ions, early work by Roth and co-workers in the keV energy range showed sputtering in the range 10^{-2} to 10^{-3} atoms/ion [163], and has since been corroborated by Sone *et al* [164]. More recent work has been conducted on sputtering yields of SiC in Focused Ion Beam (FIB) systems showing a sputtering yield of 1 to 10 atoms/ion [165, 166]. SRIM is capable of producing sputtering figures during its simulations. The accuracy of these figures is sometimes questioned [167]. In the case of SiC in those papers comparing their findings to SRIM there is very good reported correlation [165, 168].

2.3 Defect Types

This section describes crystallographic defects observed in crystal structures. These range from simple, point defects through to large scale extended defects within the lattice. They are commonly generated by ion-irradiation and can have a significant impact on the response of a material to these conditions. For nuclear materials, commonly, it is the defects which determine whether this material is suitable for performing its role within the environment it is designed for.

Defect control, calculation and investigation are important considerations for semiconductor development and materials research. Some defects and impurities can be as rare as one part per million or billion, though others are significantly more common than this. Imperfect crystals can have significant levels of strain within the lattice due to the incorporated defects [169, 170].

An electrically active defect is described as shallow or deep, depending where its electronic state is relative to the edge of the conduction or valance-band [169]. Shallow defects are within tens of meV of the band edge whereas deep defects are defined as being much further in the band gap. In addition, the defect can be described as intrinsic or extrinsic. Intrinsic defects involve only the atoms of the material. Extrinsic defects are those which involve an atom of a foreign species such as an impurity or atoms introduced through doping [171]. The exposure of a crystal to damaging events such as ion-irradiation for doping leads to the introduction of impurities and defects within the target.

2.3.1 Point Defects

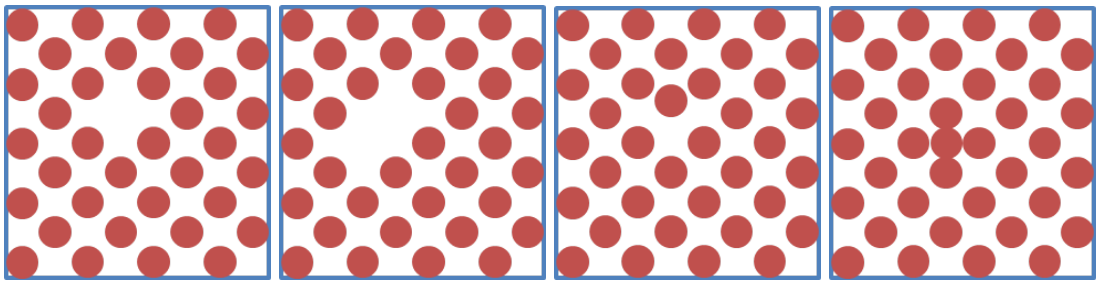

(a) Vacancy **(b)** Divacancy **(c)** Interstitial-vacancy pair **(d)** Interstitial

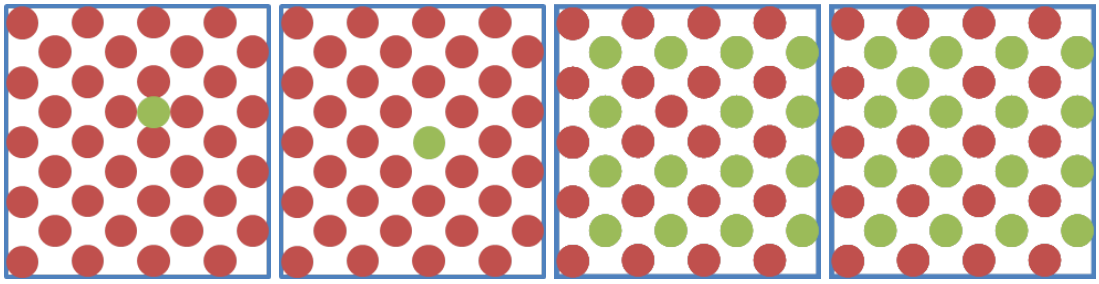

(e) Interstitial impurity **(f)** Substitutional impurity **(g)** A anti-site defect **(h)** B anti-site defect

Figure 2.8: Schematic of different types of point defects

Defect name	Nomenclature	Defect name	Nomenclature
Vacancy (in species A)	V_A	Substitutional (C on A site)	C_A
Intersitial (of species A)	I_A	A anti-site defect	A_B
Interstitial impurity (species C)	I_C	B anti-site defect	B_A

Table 2.2: Point defect nomenclature

In elemental materials there are two types of point defect. In materials with more than a single element the number of point defects increases significantly. Figure 2.8 shows eight different types of point defects within a crystal. The simplest defects are the vacancy, which is the lack of an atom on a lattice site, and the interstitial, an atom located within the crystal on a site which is not on the lattice [172]. Where two vacancies are situated on adjacent lattice sites these are called divacancies. Similarly, two interstitials sharing the same site are called di-interstitials. A slightly more complex defect is the Frenkel pair (or Frenkel defect) which is an interstitial-vacancy pair which

often results from ion-irradiation [172]. For materials containing more than one element additional defects are possible. The anti-site defect is where an atom of element A sits on a site which should contain element B [151]. Finally, impurities which may be introduced to the lattice intentionally or otherwise will be sited on either lattice sites or interstitial sites in the material [151].

2.3.1.1 Vacancies

A vacancy can be introduced or removed from a crystal lattice via a variety of sources and sinks. For example, these can be surfaces, grain boundaries or dislocations [170]. Vacancies are created when an atom moves from its lattice site to create an interstitial, though this is more energetically unfavorable than the vacancy alone due to the necessity to position the interstitial in the lattice.

In SiC, vacancies are known to be stable to 800°C [173]. Similar investigations of the divacancy show it is stable to at least 2015°C [174]. MD simulation of vacancy behaviour in SiC shows that the migration energy for V_{Si} is 2.35 eV and 4.10 eV for V_C [175]. Vacancy migration occurs at a lower temperature compared to interstitial migration in samples which have been irradiated. This is indicative of a lower migration energy for vacancies compared to interstitials in SiC [173, 176].

2.3.1.2 Interstitial

As briefly outlined above, the introduction of an interstitial defect to a lattice requires significantly more energy than the production of a vacancy alone. This makes it less likely to form than the vacancy. To consider them as two separate defects is a slightly simplistic viewpoint as the creation of a vacancy results in an interstitial. Interstitials are likely to diffuse from within an interstice to annihilate through combination with a vacancy. When diffusing the defect may either jump to a second interstitial site or, alternatively, move to a lattice site, displacing another atom to the interstitial position as it does so [170]. Crystallographically anisotropic systems will promote transportation of interstitials in certain directions. Some systems (for example, graphite) form planes of very strongly bonded atoms. This makes it far more likely that interstitials will be transported between the planes rather than passing between these sheets of strongly bonded atoms [170].

In SiC the mechanism for interstitial diffusion depends on the element in

question. Carbon diffuses to the nearest or next nearest neighbour site [175], whereas the silicon interstitial migrates using only other silicon atoms in the lattice to form a di-interstitial [175]. The migration energy has been established using MD simulations and it is reported that for I_C the migration energy is 0.74 eV and for I_{Si} it is 1.53 eV [175]. These energies can be correlated to temperatures where observable lattice recovery follows low temperature irradiation. As the temperature increases, interstitials are able to move within the lattice, which allows them to occupy vacancies, leading to lattice recovery.

2.3.1.3 Anti-Site

The anti-site is a defect which can occur only where there is more than a single element in the crystal. Here, an atom of element A sits on the site of element B (or vice-versa). Where the two elements have a similar size, the distortion of the lattice is minimal. However, where there is a size mismatch, the anti-site can have a significant strain effect on the crystallographic structure.

One intrinsic defect in SiC wafer growth is the anti-site [177]. In SiC the size of the elements is not particularly different, though there is a higher electronegativity for carbon [177]. The anti-site pair (that is both carbon on a silicon site and silicon on a carbon site) is known to be stable up to 1700°C [178]. One example where the anti-site has been reported is in rapidly-grown CVD SiC. Here, the anti-site pair has been observed by Photoluminescence Spectroscopy (PLS) [178]. An increase in the number of carbon atoms available during crystal growth reduces the likelihood of formation. This indicates that carbon is unlikely to sit on silicon sites, but silicon will readily sit on carbon sites.

2.3.1.4 Interstitial-Vacancy Pairs

As described in section 2.2.4, the irradiation of a material results in the transfer of energy through collisions. Often this results in the displacement of atoms from lattice sites. This creates an interstitial-vacancy pair known as a Frenkel defect or Frenkel pair. Recombination of the Frenkel pair is possible due to mobility of either the interstitial or the vacancy.

In SiC, Frenkel pairs have been shown to be a driving force for amorphisation [179]. By raising the temperature to allow sufficient recombination of pairs, amorphisation can be avoided. Molecular Dynamics (MD) simulations of

recombination of Frenkel pairs shows that recombination occurs for ≈40% of created pairs almost immediately due to the short distance between them [180]. For the remaining pairs, Density Functional Theory (DFT) and MD simulations indicate activation energies for diffusion (and therefore recombination) in the range of 0.22 eV (for carbon I-V pairs) and 1.84 eV (for the silicon I-V pair) [180, 181].

2.3.2 Dislocations

Dislocations are linear defects along which the crystallographic regularity of the crystal is missing. There are two distinct types of dislocation. The naming of these two types comes from the positioning of the atoms around the dislocation. The 'edge' dislocation is the insertion or removal of an extra partial-plane of atoms. The 'screw' dislocation forms at the boundary between a slipped part of the crystal and the unslipped part [172]. The screw dislocation can be thought of as a cut part way through a plane of atoms. The plane is then shifted in a direction parallel to the edge of the cut in the lattice [172]. Most dislocations in 'real' materials have a mixture of edge and screw components and are called 'mixed' [170]. Edge and screw dislocations are shown in figure 2.9.

The Burgers vector of a dislocation defines the lattice vector which would return the lattice to its perfect form. To find the Burgers vector, a closed vector circuit is made around a suspected dislocation. This is made by moving from one lattice point to another. If, when mapped onto the perfect lattice the same vector circuit fails to close, then a dislocation is concluded to exist in the real crystal. The lattice vector which closes the vector circuit on the perfect crystal is the Burgers vector of the dislocation [170]. A convention for the sign of this vector is known as the Finish-Start/Right-Hand (FS/RH) convention. The Burgers circuit should be assigned such that it has a right-hand screw relationship to the dislocation line (the RH part of the convention). Following this, the Burgers vector should be mapped from finish to start of the Burgers circuit (the FS part of the convention) [170].

2.3.2.1 Edge Dislocations

Edge dislocations can be described as a partial plane inserted into the crystal lattice. In general, dislocations form closed loops or pass from one surface to

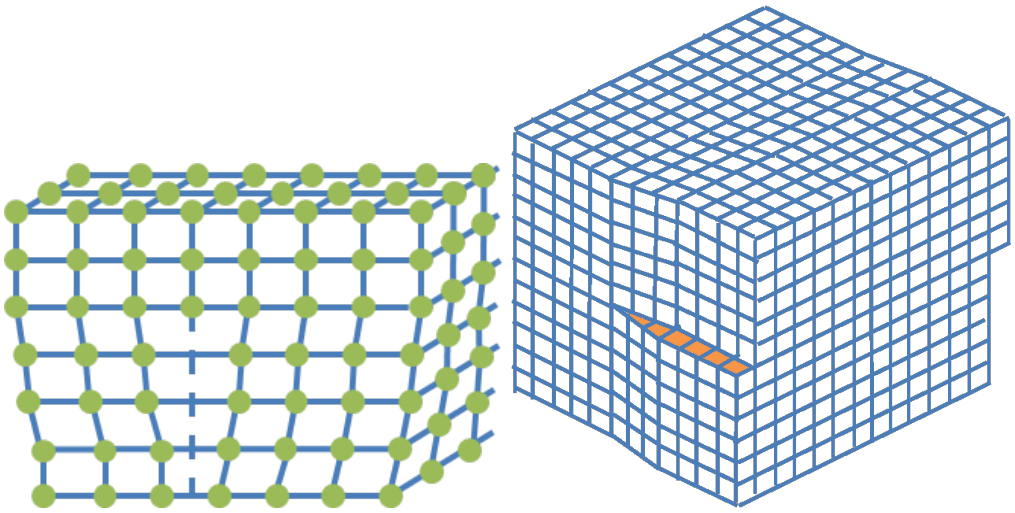

(a) Edge Dislocation **(b)** Screw Dislocation

Figure 2.9: Schematic showing differences between edge and screw type dislocations based on [172]. Lines indicating the planes are shown in both cases. Atom positions are shown in the edge dislocation only.

another in order to exist stably in the crystal. There have been a number of investigations of dislocation loops in SiC under a variety of ion-irradiation conditions. They have been seen to form following helium ion-irradiation [182], aluminium ion-irradiation [183] and neutron irradiation [184, 185].

Many workers have attempted to induce recovery of dislocation loops in SiC using annealing. For aluminium irradiated SiC, Persson and co-workers [183] were able to anneal out most of the resulting dislocation loops by heating to 1700°C for 30 minutes. Hallen and colleagues observed fewer, larger loops [186] following annealing but the total amount of the sample which is contained within the loops remained approximately constant both before and after annealing.

During helium irradiation it has been shown that dislocation loops pin helium platelets in place and that these platelets grow during annealing experiments [182]. (Platelets are bubbles which are contracted in one direction resulting in a plate-like shape.)

2.3.2.2 Screw Dislocations

Screw dislocations can occur as a result of slip within the crystal due to external stresses but can also be the result of the growth process [170]. In SiC the screw dislocations occur at the growth phase rather than through

slip [187, 188]. They are attributed to basal plane dislocations and have been observed to form during incorporation of inclusions within the crystal growth process [187]. (The basal plane is the plane perpendicular to the primary axis, the primary axis is the axis which has the highest rotational symmetry. In 4H-SiC this is often labelled as the c-axis and is in the $(0\,0\,0\,1)$ direction.) Many dislocations are observed to be parallel to the $[0\,0\,0\,1]$ axis [134] and result in growth spirals on the $\{0\,0\,0\,1\}$ surfaces during crystal growth [189]. When crystal growth takes place on the $\{1\,\bar{1}\,0\,0\}$ faces the spiral growth and dislocation behaviour do not occur, resulting in a superior crystal [188].

2.3.3 Other Defects

Where several linear defects form in the same region of a sample during thermally activated processes such as crystal growth or recrystallisation, the effect can be to create a planar defect of one type or another. Planar defects generally result in continued crystal growth but with a different orientation, polytype or stacking sequence. Most uses of semiconductors rely on a high quality, single crystal as a starting material — the inclusion of planar defects will reduce this quality — ultimately changing the fundamental properties of the material [1]. There are two main types of planar defect:

Stacking faults occur where the plane stacking sequences, for example ABCABCABC, becomes interrupted and amended, for example ABCBBCABC. The polytype does not change here because the erroneous sequence is not repeated, there is simply a mistake in a single layer [170, 172]. These often occur during recrystallisation following ion-irradiation, where the crystal structure does not sequence together correctly [120, 190].

The other main type of planar defect is the grain boundary, which is where the lattice changes from one orientation to another, resulting in a polycrystalline material [170, 172]. It is common that the lattice itself is unchanged, so cubic material remains cubic, it is rotated at the grain boundary and retains the new orientation until the next grain boundary.

2.3.3.1 Stacking Faults

Stacking faults have been identified as a limiting aspect to SiC electronic devices [1, 173]. Saddow reports that the presence of stacking faults stands between SiC and commercial success [1]. The reason for this concern is that

SiC crystals with stacking faults have a lower band-gap than those without due to a local potential fluctuation [173] around the defect. This fluctuation attracts carriers and allows recombination [1, 173].

Stacking faults in SiC have been shown to occur in the basal plane. The layered natural crystal structure results in a very low activation energy for stacking faults to form [191]. Stacking faults are a problem when creating wafers which are doped in the growth process. Research has been conducted following doping of SiC to a high fluence (10^{19} cm^{-2}) with nitrogen (during the growth process) and annealing to 1150°C. The samples of 4H-SiC have been observed to exhibit extensive stacking faults [192–194]. Faults are attributed to the annealing process as they are not present prior to annealing [193].

2.3.3.2 Grain (and Sub-Grain) Growth

Grain growth is an important consideration during crystal growth. Without a seed it is likely that crystals will grow in a polycrystalline manner as multiple zones will crystallise at the same energy and therefore temperature [1, 7]. These areas expand in all directions, acting as seeds for their own single crystal growth until they reach the adjacent crystal. Where this occurs the crystals will form a grain boundary [170]. In SiC recrystallisation of amorphous material has been shown to occur at 900°C [195, 196]. This temperature can be lowered through simultaneous ion-irradiation to 500°C [197].

2.3.3.3 Micropipes

Hollow core dislocations are referred to as micropipes [173]. These defects can run through the entire crystal, are perpendicular to the surface of the wafer and are parallel to the crystallographic c-axis. These have been shown to nucleate on impurities within the crystal [187, 198], but have also been shown to grow due to stacking faults and screw dislocations on polytype boundaries [199]. In SiC, micropipes are considered to be the most important defect for producing SiC-based electrical devices [1]. Kuhr *et al* [199] believe the introduction of a void between the seed crystal and the growing crystal causes dislocations to line up along its path, providing the corners of the void with a hexagonal shape, and thus the micropipe itself. There has been extensive research on how to avoid micropipe propagation through the entire crystal. It has been proposed to force the growth of the crystal in such a way that

the c-axis is not perpendicular to the direction of growth by growing in the $[0\,3\,\bar{3}\,8]$ direction [1]. The Lely method (where SiC is evaporated and passed through a porous graphite layer which then acts as nucleation source for small SiC crystals) has been reported to avoid the inclusion of micropipes, but it is not widely believed to be capable of producing large, commercial scale wafers [198].

2.3.3.4 Bubbles

Bubbles form as the result of agglomeration of vacancies and impurity atoms, often as the result of ion-irradiation or nuclear transmutation [120]. In many materials, the incorporation of bubbles results in volumetric swelling [120, 200]. There are several mechanisms which compete during the bubble growth phase. Ghoniem and colleagues summarised the mechanisms as follows [200]. During ion-irradiation there is a competition between irradiation induced interstitials and incident ions to absorb the vacancies. Some ions (such as helium) bond very strongly with vacancies. Calculations have been performed that shown that helium bubbles readily absorb thermally activated vacancies as well as the irradiation induced vacancies [200]. The final consideration is that the incident ion can collide with the bubble and displace gas atoms from within the bubble. It is claimed by some workers in this field that bubbles grow at equilibrium pressures, with a bias to absorb interstitials or vacancies for under- and over-pressurised bubbles, respectively [201]. However, others such as Mansur [202] claim bubbles grow as under-pressurised voids until a critical radius, beyond which equilibrium growth occurs.

Silicon carbide has been investigated extensively under irradiation from ion species which give rise to bubble formation. These include hydrogen [203], helium [182, 204, 205], nitrogen [206] and neon [206]. They have been shown to form preferentially along the grain boundaries in polycrystalline material [204]. It has been shown that this causes swelling [207–210] in SiC and modifies the mechanical properties [211]. Neutron irradiation induced voids in SiC have also been demonstrated [184, 212].

2.4 Transmission Electron Microscopy

Transmission electron microscopy (TEM) is a powerful technique which can be used to characterise materials of many different types [213]. TEM is a particularly effective way to assess the response of semi-conductors to ion-irradiation. This section discusses the available sample preparation and microscopy techniques used in the study of SiC reported in the literature. This is important for this research because all of the experimental data was gathered using this technique. It is important to be able to understand and recognise whether the observed effects are as a result of ion-irradiation or another artifact, such as sample preparation, imaging conditions or an effect of the electron beam.

2.4.1 Sample Preparation

There are a variety of techniques for the preparation of semiconductors for TEM [160]. These include mechanical polishing [214], FIB [215–217] and Small Angle Cleavage Technique (SACT) [218]. By far the most common technique reported is (mechanical) tripod polishing [205, 207, 208, 219–224] followed by sputtering by low energy, glancing angle argon ion-irradiation in a Precision Ion Polishing System (PIPS) [190, 205, 207, 212, 219, 221, 222, 225–227]. The impact of radiation damage in SiC is discussed in section 2.5. However, the low energy and glancing angle results in relatively little radiation damage introduction to the specimens [160, 228] especially in samples as resistant to radiation damage as SiC.

FIB has been used to create samples [216, 217] of SiC for radiation damage studies [229, 230]. Radiation damage studies can be compromised by damage introduced by the sample preparation phase. There are limitations to samples prepared using FIB such as orientation and maximum sample area.

2.4.2 TEM for Investigation of Radiation Damage

TEM can be used to investigate material behaviour under irradiation from energetic particles. This is because the use of TEMs to observe radiation-induced defects provides an excellent insight into the nature of these defects [213]. TEM is a useful tool to image both linear and planar defects (see section

2.3) as these can cause significant amounts of strain onto the surrounding lattice which creates contrast within the image (see section 3.3.3.3). Several facilities have been constructed to perform *in-situ* ion-irradiation with TEM, for the observation of damage development [231]. More information on *in-situ* facilities is available in section 2.4.5.

2.4.3 TEM of Silicon Carbide

Various TEM techniques have been performed on radiation damaged SiC. These include bright field imaging [182, 208, 210, 230, 232–241], weak-beam dark-field imaging [208, 210, 229, 232, 242, 243], diffraction [229, 232, 236, 241, 243], EELS [242] as well as using high energy electron irradiation to study defect creation and amorphisation [243, 244]. High Resolution Transmission Electron Microscopy (HRTEM) has also been performed [232, 234, 235, 237].

TEM has been used to characterise implanted SiC. Amorphous layers or zones are observed by TEM following room or low temperature implantation [229, 232–237, 243]. Recrystallisation of amorphous layers has been observed during *in-situ* heating within the microscope [232, 233, 236]. Other defects such as stacking faults [236, 237] and dislocation loops [210, 241] have been observed in SiC using TEM. Helium bubbles and platelets ranging in size from 3 to 100 nm have been observed by TEM in samples of SiC which have been helium ion-irradiated [182, 230, 238, 239, 241]. Radiation damage is evident in some studies in the form of interstitial clusters which have been observed in work reported in several publications [208, 240, 241, 245].

Weak-beam dark-field imaging of SiC has been utilised in order to image the distortion of the lattice due to sub-nanometer defects which are below the resolution of the microscope [242]. In some cases, the strain in the SiC lattice is high enough that it can be detected using bright-field techniques. This occurs when the lattice is distorted into or out of Bragg conditions, where the electrons are strongly diffracted.

These publications demonstrate that TEM is a suitable technique for the investigation of radiation damage processes in SiC, which occur as a result of irradiation with a variety of particles.

2.4.4 Electron Beam Effects

Information has been provided on the electron beam irradiation effects in SiC in section 2.5.2. Broadly speaking, it is well understood that minimal heating is introduced during electron irradiation at energies below 1 MeV at moderate electron fluxes. Electron densities required to perform conventional TEM techniques are thought to avoid heating in SiC [213, 244].

Irradiation of SiC by electrons under a variety of conditions is discussed in section 2.5.2. Though displacement of atoms from the lattice can occur at electron energies commonly used for TEM and ultimately result in damage and amorphisation. By raising the temperature of the sample, the defects can be recombined and the damage can be repaired [246]. At higher energies, defects increase in complexity and number which would raise concerns for users working with microscopes operating above 800 keV.

2.4.5 *In-Situ* Ion-Irradiation with TEM

The use of *in-situ* ion-irradiation with TEM to study the material response to radiation damage has become more prevalent in the last thirty years [231, 247]. Dynamic effects can be easily observed by this technique and it is especially useful during competing processes where a short-term effect is superimposed on a long-term trend [248]. An example of this would be the irradiation-induced structural changes to MAX phase alloys (Metal-aluminium-carbides/nitrides) which gives them favourable properties for the nuclear industry. Two general designs of *in-situ* ion-irradiation facility have been introduced. Firstly, there is the addition of (small) ion guns directly attached to the microscope. The second design is the use of large free-standing accelerators with multiple irradiation chambers, where a microscope is one of the chambers and is usually added to the facility at a later date [231]. Dosimetry is a particular area of concern due to the geometry around the sample position giving rise to technical difficulties. It is difficult to provide accurate dosimetry without altering the experiment [231, 248]. A variety of systems have been implemented to combat this involving deflecting the beam on to a current measuring device just before the sample position [231, 247, 249], *in-situ* ion detection elements on specimen rods [231] or through the use of retractable ion detection elements [250]. There are currently 12 facilities offering *in-situ* ion-irradiation with TEM. A recent review [247] details 11 of

these with a recently completed facility at Sandia National Laboratory [251] being the twelfth.

2.5 Radiation Effects

This section contains information on radiation damage as a result of irradiating particles in SiC. It is important to provide a broad review at this stage because the research we have conducted is concerned with electrons, neutrons and a variety of heavy and light ions. We are attempting to simulate the behaviour of neutrons in SiC through the use of high-energy heavy-ion irradiation and we are observing this through the use of high-energy electron irradiation. We implant bubbles into the material using low-energy, light-ion irradiation. Therefore, a wide range of literature is presented in order to place this work in to perspective.

2.5.1 Summary of Radiation Effects

Radiation effects in SiC can be divided into groups of energy and species combinations where similar effects occur.

Sputtering occurs below threshold displacement energies for lattice atoms in the bulk as atoms near to the surface require less energy to be removed than atoms within the lattice [151]. In SiC there is an energy range for preferential sputtering of carbon from the lattice. This occurs during very low energy, light ion-irradiation and has been observed for $\leq$100 eV hydrogen and deuterium [252–254]. For 3 keV tritium ion-irradiation the opposite is observed — silicon atoms are preferentially sputtered from the target. The authors believed that their findings demonstrate that the bound state of the carbon atoms plays a role in sputtering [164].

Within the lattice, the defect which occurs with the lowest creation energy is the vacancy. In SiC, irradiation experiments (using a variety of techniques for the detection of defects) have shown that the carbon vacancy forms at lower energies than the silicon vacancy. For electrons, carbon vacancies occur under irradiation above 116 keV [255–257]. 1 keV hydrogen ion-irradiation [258] or 1.3 keV helium ion-irradiation has been shown to displace carbon from its lattice site [259]. For the generation of silicon vacancies, a threshold energy

of 250 keV for electron beam irradiation has been reported [257, 260]. Silicon vacancies form following 300 keV proton irradiation [261].

Amorphisation occurs in SiC at energies below the threshold to displace silicon from its lattice site. For example, this has been observed following irradiation by 180 keV electrons at low temperatures [244, 262] and 200 keV for room temperature irradiation [262]. Amorphisation occurs following irradiation by fast neutrons (>1 MeV) [226, 227, 263] and by 12 keV helium ion-irradiation [264–266]. At higher energies, amorphous layers or platelets are observed to form depending on irradiation conditions [267].

Heavy ion-irradiation has been shown to also result in amorphisation. In particular, aluminium implantation below room temperature [268–270] as well as implantation using argon [271], titanium [272], germanium [233, 273, 274], iodine [59, 275], xenon [276] or caesium [277] ions at room temperature has been observed to cause amorphisation in SiC.

Clusters of defects (both vacancies and interstitials) occur at higher energies than isolated defects. For electrons this is observed following irradiation by 800 keV electrons [278–280]. The preferential displacement of carbon from the lattice results in a preference for these clusters to contain carbon interstitials. For proton irradiation, clusters form following irradiation by a beam of 2 MeV particles [281].

The silicon anti-site (Si_C) defect occurs more regularly in SiC than the carbon anti-site [281]. This is presumably due to the higher number of carbon vacancies on which the silicon can become sited. Silicon anti-sites have been seen to be created following irradiation of SiC by 2 MeV (or greater) electrons [282], 2 MeV proton irradiation [281] or fast neutron (>0.1 MeV) irradiation [283, 284].

Divacancies occur above irradiation energy thresholds required for the silicon anti-site (Si_C) defect to form. For helium ion-irradiation, the ion energy required is 1.7 MeV [285] which increases to 3 MeV for electrons [286, 287] and 6.5 MeV [287] for proton ion-irradiation. For heavier ions, the divacancy is not widely reported in the literature — though there are reports of divacancy formation following implantation of SiC by 200 keV phosphorus [288]. The lack of reports is probably a result of larger observable effects in the irradiated material, the divacancies occur, but are not included in the publication.

The formation of dislocation loops occurs at high temperatures (>500°C)

during 180 keV (and higher) neutron irradiation [184, 289] or 50 keV helium ion-irradiation in SiC [207]. For neon ion-irradiation, dislocations are seen to occur following 200 keV implantation [290].

The agglomeration of vacancies forms voids in a material. These can contain gas atoms which would then be defined as a bubble. This has been shown to occur following ion-irradiation by light gaseous ions, including 10 keV hydrogen [291, 292], 10 keV helium [293, 294], 20 keV neon [206] or 180 keV oxygen ion-irradiation in SiC [237]. Following neutron irradiation (energy > 0.18 MeV), the formation of faceted voids has been observed when irradiated above 1000°C [184, 289]. In polycrystalline material there is a preference for bubbles to grow on or near to grain boundaries [119, 295]. Close to boundaries there is often a denuded zone in the grain [119, 296].

Following ion-irradiation by species which are heavier than boron, it has been shown that various phases form in the SiC crystal. These include graphite and diamond following carbon ion-irradiation [297], various phases of SiC and nitrogen following high dose nitrogen implantation [298, 299] and silicon oxide layers as a result of oxygen implantation [237]. Tungsten carbide and hafnium compounds are shown to form following tungsten [300, 301] and hafnium [302] ion-irradiation, respectively. Precipitates are observed following implantation of metallic ions in SiC including aluminium [303, 304], cobalt [305], titanium [272], copper [306], silver [306] and gold [306]. Semi-insulating layers have been seen to form as a result of implantation using tungsten [307] or platinum ions [308].

2.5.2 Electrons

Understanding the response of SiC to electron irradiation is important for TEM of SiC. Electron irradiation is relatively easy to perform, with many materials science departments owning equipment capable of generating high-energy coherent electrons. Electron sources are highly tunable to a specific energy which allows threshold energies to be accurately determined.

2.5.2.1 80 – 160 keV

Low electron-energy irradiation (in the range 80 – 160 keV) has been shown to cause carbon displacements within the lattice [255, 256] above a threshold of 116 keV. This was determined by Deep Level Transient Spectroscopy (DLTS)

of samples irradiated by electrons at between 80 and 400 keV. This creates I_C and V_C [257]. Annealing the samples following electron irradiation creates more complex defects including C_{Si} [255]. Danno and co-workers claim the carbon interstitial has high mobility and as a result will form complex defects rapidly [255, 309]. Silicon vacancies have not been observed following electron irradiation below 160 keV for 4H- and 6H-SiC [260]. It has been shown [310] that irradiation with 160 keV electrons extends the lifetime of carriers within the specimen by introducing defects within the specimen.

2.5.2.2 180 – 300 keV

Electron irradiation above approximately 180 keV amorphises thin TEM foils of SiC at low temperatures (-173°C) [244, 262]. At room temperature, amorphisation is observed when using an intense beam ($\geq 10^{21}$ e.cm^{-2}.s^{-1}) of 200 keV electrons [262]. Recovery has been shown to be inhibited or supressed using temperature control [244]. This process must be dominated by the displacement of carbon atoms as the threshold electron energy for electron-induced silicon displacements in the lattice is reported to be 250 – 260 keV [257, 260]. Investigations by PLS and DLTS techniques show that silicon Frenkel pairs form above this 250 keV threshold [260, 309, 311]. Other work [312] claims silicon vacancies cannot be detected following irradiation with 300 keV electrons. However, it is possible that the annealing treatment used in this work caused Frenkel pair recombination. Electron irradiation of SiC at room temperature has been shown to cause swelling as a result of radiation damage by the electron beam. Work by Matsunga correlated swelling to amorphisation, both of which are caused by electron beam induced radiation damage [313].

It has been shown by Aihara and colleagues [292] that irradiation by 200 keV electrons can stimulate bubble growth in hydrogen- and deuterium-implanted SiC. The specimens were amorphous following room temperature ion implantation. Sample thickness and ion species both play a role in determining bubble growth rate and final bubble size. It is speculated (by the authors) that electron irradiation stimulates mobility of hydrogen to form bubbles [292].

2.5.2.3 800 keV – 1.7 MeV

Higher energy electron irradiation introduces more complicated defects (than at lower energies) within the SiC structure. Clusters of both vacancies [278, 279] and interstitials [280] are shown to form following irradiation with electrons of between 800 keV and 1 MeV. DLTS has been used to explore the nature of the silicon vacancies generated as a result of 1.7 MeV irradiation. When compared to silicon vacancies generated with 300 keV electrons [314] they are shown to be of a deeper level and have a more complex structure [279]. Chen and co-workers [312] described the defects as similar in terms of structure but on different sites within the lattice.

The displacement model discussed for lower incident electron energies has been shown to apply for higher energies at temperatures both above [242] and below [243] the critical temperature for electron beam induced amorphisation at 1 – 1.25 MeV (flux 1.8×10^{20} e.cm^{-2}.s^{-1}). Preferential displacement of carbon leads to direct silicon-silicon bonding. Any displaced silicon atoms have a variety of fates. They can become a self-interstitials, form anti-site defects or form small clusters within the lattice [242].

2.5.2.4 2 – 2.5 MeV

Silicon vacancy-related complexes are the dominant defect created by 2 MeV electron irradiation [261, 315]. There are two recovery temperatures reported at 750°C and 1300°C [316]. Aside from vacancies, 2 MeV electron irradiation has been shown to create anti-site defects when carried out at -270°C [282]. Electron induced amorphisation in SiC — and of other ceramics at electron energies of up to 2 MeV — has been shown to be linked to the phase diagram of the material [317], with the likelihood for amorphisation governed by the proximity to the liquid phase. The electrical performance of SiC diodes has been shown to reduce as a result of electron irradiation in this energy range, mostly due to defects within the crystal creating electron traps [318].

Work by Dannefaer, with electron irradiation performed at 2.2 MeV, demonstrated that the silicon vacancy complex exists with a nearby interstitial. The authors were unable to determine whether the interstitial was carbon or silicon. An observed transition to $V_C C_{Si}$ implies that this was carbon [319]. Earlier work by Son *et al* using 2.5 MeV electrons to irradiate 3C-SiC showed a similar complex vacancy defect. The work contained insufficient information

to make conclusions about the exact nature of the defect [320–322]. In p-type SiC the vacancy behaviour is not observed, presumably due to the dopant(s) occupying a high percentage of the vacancy sites [323].

2.5.2.5 3 – 10 MeV

For 3 MeV (and higher) electron irradiation, divacancies are reported [286, 287] as well as I-V pairs which have a large separation. It is proposed that pairs with a short separation distance undergo irradiation-enhanced recombination. This is more prevalent at higher irradiation doses [286]. High energy electron irradiation has been shown to reduce the number of available acceptors in doped SiC; this is due to the movement of the dopant from lattice sites to interstitial positions [324]. At 10 MeV, the bias for producing carbon vacancies ceases and silicon and carbon vacancies are produced in equal numbers [323]. Positron Annihilation Spectroscopy (PAS) results provide further evidence of isolated vacancies [319] with the interstitials and vacancies separated sufficiently to be considered 'remote' Frenkel pairs.

2.5.3 Neutrons

Neutron irradiation of materials for the nuclear industry is often simulated using ions and electrons. In order to be able to use ions and electrons to substitute for neutron irradiation, some comparitive investigations are necessary to ensure suitable energy, fluence and flux are chosen. Ions and electrons are used because they are easier to generate and manipulate and they have a well defined energy. There is also a benefit from both shielding and radioactivity perspectives.

Neutron irradiation of materials for the nuclear industry is essential to compare observed effects from other particles (such as ions or protons). Neutrons are generated with a spectrum of energies depending on the instrument used. Spallation neutron sources rely on a high flux of protons which collide with a target and generate neutrons [325]. Alternatively, research nuclear reactors can be used to generate a flux of neutrons which are then manipulated through a beamline, in order for neutron irradiation experiments to be performed [326]

2.5.3.1 ≥0.1 MeV

Irradiation by fast neutrons (energy $\geq$ 0.1 MeV) has been shown to cause amorphisation of SiC below the critical temperature of 650°C [226, 227, 263] at a flux of 10^{15} n.cm^{-2}.s^{-1}. This amorphisation leads to the material becoming less dense and hardness decreasing [226, 227]. A more detailed study of defects following neutron irradiation in this energy range showed evidence of vacancies (of both species) and the $C_{Si}V_C$ complex [283, 284]. Local compositional changes are likely due to the higher likelihood of displacing carbon over silicon [263].

Swelling behaviour of CVD SiC has been studied across a range of temperatures. Swelling is minimal above 1100°C and significant below 800°C [327]. This is due to defect creation and recombination during the neutron irradiation. This behaviour has also been studied in sintered SiC which swells due to irradiation by neutrons of energy $\geq$ 0.1 MeV at 500°C [328] and has a reduced coefficient of thermal expansion following irradiation [329]. Interstitials are shown to agglomerate to form loops due to them having a higher mobility compared to vacancies. Swelling is largely attributed to the behaviour of the interstitials due to their ability to cause an increase in loop density and size [328].

Similar studies on SiC/SiC composite fibres show that there is significant strength reduction [330] due to shrinkage of the fibre when neutron irradiated at room temperature. (SiC/SiC composites are SiC fibres embedded in an SiC mold or cast. The aim of these is to improve the mechanical properties by combining the favourable properties of both the fibre and the bulk material.) At 100°C and 500°C shrinkage is observed which causes the composite to disintegrate. Density is shown to decrease as described above, as well as elastic modulus reduction by up to 20% [331]. High temperature (800°C) irradiation of fibres shows no major changes to mechanical properties following irradiation to high levels (up to 12 DPA) of damage [78, 332]. (1 Displacements Per Atom (DPA) means that each atom has on average been displaced from its lattice site once.)

2.5.3.2 ≥0.18 MeV

Irradiation of SiC with neutrons of energies above 0.18 MeV at temperatures above 500°C created interstitial-type dislocation loops [184, 289]. At higher

temperatures (above 1000°C) faceted voids are created, either triangular or hexagonal in shape [184, 289]. Following annealing (1800 °C for one hour), these become circular in nature [184]. Swelling is observed in bulk irradiations [333, 334], with a damage/recovery equilibrium reached at 5×10^{20} n.cm^{-2}. However, higher temperature and fluences have shown that slow continuous expansion occurs [333].

2.5.3.3 $\geq$1 MeV

Similar to the work described in the previous two sections, irradiating with 1 MeV neutrons results in the degradation of the mechanical properties of SiC. Several investigations have reported that both fracture strength [76, 335] and Young's modulus [335] are reduced as the result of the irradiation. For SiC fibres (both amorphous and monocrystalline) the opposite effect has been reported in work performed by Okamura, where the Young's modulus increases with neutron irradiation fluence [336, 337]. Okamura [337] also reports a highly temperature-dependent disordering reponse in monocrystalline SiC fibres.

Clusters of dislocation loops have been observed by TEM in samples irradiated by >1 MeV neutrons at 200°C irradiated to 1.2×10^{21} n.cm^{-2}. In specimens irradiated under the same neutron irradiation conditions at 1100°C the dislocations are no longer seen. Instead small black spots are observed in the specimen which the authors conclude are much smaller 'collapsed' dislocation loops within the sample [338]. Isotropic swelling in SiC has been reported following 1 MeV neutron irradiation [335]. Defects in SiC diodes have been identified during irradiation from >1 MeV neutrons. These cause significant defects deeper than $\approx$ 17 μm in the target. Importantly 90% of the damage is observed to be annealed out at 350°C which offers good prospects for high temperature operation [339]. A similar lack of degredation in radiation detectors has been reported [340] showing that detector efficiency is unimpaired for irradiated devices.

Samples containing boron as a result of the manufacturing process have been shown to form helium bubbles during neutron irradiation [341]. The bubbles formed on or very near to the grain boundaries. Helium is formed in the specimen as a result of transmutation reactions induced by incident neutrons in boron in the sample. Helium is also released from the crystal during this process [341].

2.5.4 Ions

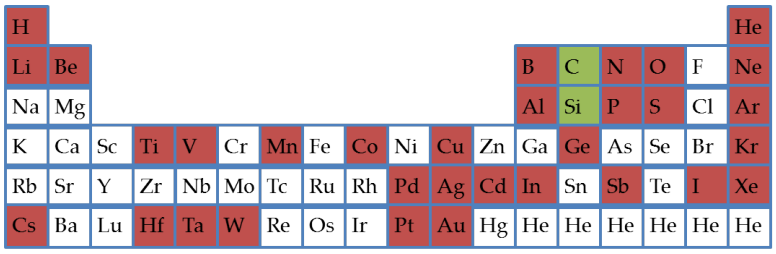

Figure 2.10: Periodic table showing the elements used in ion-irradiation of SiC

2.5.4.1 Hydrogen (H_2^+)

Hydrogen ion-irradiation (proton irradiation) tends to generate a defect density one order of magnitude higher than that generated by electrons at the same energy with the same flux [287].

2.5.4.1.1 ≤100 eV – 1.75 keV

Low energy (≤ 100 eV) hydrogen ion-irradiation of SiC causes surface modification to the target. At energies below the threshold to perform atomic displacements in the bulk there is evidence of sputtering of silicon and carbon from the surface [252].

Amorphous SiC prepared by laser ablation was hydrogen irradiated by Leblanc and co-workers [342]. For energies of 250 eV – 1.75 keV depth analysis was perfomed using ERDA. Compared to the SRIM code available at the time (versions -95 and -SP) the hydrogen depth profile was shallower than expected. Using a different stopping potential (mainly focussed on electronic stopping) yields a correct first order result, but second order statistics (such as straggle and kurtosis) were still erroneous. (Kurtosis is the measure of how peaked a statistical distribution is.) Irradiation results in an enriched carbon layer within the specimen due to preferential displacement of carbon atoms away from the implanted surface and into the specimen and a silicon enriched layer near to the surface [258].

2.5.4.1.2 2 – 10 keV

Unlike the lower energy range results, at slightly higher energies (2 keV and 5 keV) there is evidence of a preferential sputtering of silicon atoms [343–345]. SiC subjected to 10 keV hydrogen irradiation has been shown to form bubbles when the sample is subsequently irradiated with electrons [291, 292]. This has been shown to occur even in amorphous SiC. Annealing the specimen between hydrogen irradiation and electron irradiation prevents bubble formation. The authors suggest this is due to the liberation of hydrogen atoms within amorphous material by the thermal treatment allowing the hydrogen to diffuse through the specimen rather than forming bubbles [291].

2.5.4.1.3 15 – 150 keV

At 15 keV, hydrogen has been shown to amorphise SiC at room temperature [266], an amorphous state is observed (by TEM) to be formed following irradiation to fluences above 1.8×10^{16} ions.cm^{-2} over the thickness of a TEM specimen (100 nm). The pre-implantation of hydrogen enhances helium bubble growth when helium is subsequently implanted [264]. At higher energies (100 keV), significant disorder is introduced to the lattice when irradiated below room temperature [346]. Most of this disorder can be rapidly recovered during heating back to room temperature. Above 10^{17} ions.cm^{-2} only a small recovery occurs following thermal treatment to 500°C. If annealing is performed in appropriate conditions (one example is 800°C and 20 minutes) then blistering forms on the surface centred around the R_P [346]. Irradiation by 150 keV hydrogen ions of doped SiC wafers causes no alteration to dopant concentration [347] — though there is evidence (from DLTS) of electron trapping on proton irradiation-induced defects.

2.5.4.1.4 300 keV

Irradiation by 300 keV hydrogen at room temperature generates a number of defects in the SiC lattice. There is evidence to suggest that different types of carbon vacancy defects are created together with silicon vacancies. Additionally, the interstitial hydrogen has been shown not to interact with silicon vacancies even during thermal treatment up to 800°C [261].

2.5.4.1.5 1.2 – 2 MeV

When irradiated with 1.2 MeV hydrogen ions and compared with electrons causing similar levels of damage, Alfieri *et al* [348] identified three new defects following irradiation and annealing. These are thought to be a combination of hydrogen atom(s) and vacancies within the crystal. 2 MeV hydrogen ion-irradiation is reported to result in single carbon interstitials and clusters of silicon interstitials within the lattice, as well as some silicon filling carbon vacancies to form an anti-site defect [281].

2.5.4.1.6 2.5 – 6.5 MeV

Irradiation by hydrogen ions at energies of both 2.5 MeV and 2.9 MeV at room temperature has been shown to induce many defects in SiC which are easily annealed out. Following annealing to 125°C, many of these are annihilated and a few stable defects remain [349]. There is some discussion about whether these defects are divancancies or impurity/vacancy complexes. The work by David *et al*, however, fails to draw firm conclusions as to the nature of these defects [349]. Irradiation by 4 MeV hydrogen ions produces only a small disordering effect on the crystal [350].

An increase in energy to 6.5 MeV results in the introduction of divacancies and other complicated defects [287] alongside I-V pairs within the crystal. 8 MeV has been extensively selected as an energy for proton irradiation into SiC by a research group at the Russian Academy of Sciences, St Petersberg [347, 351–355]. Their publications indicate there are stable divacancies, lone V_C as well as other, unclassified defects [354, 355] created during hydrogen ion-irradiation. There is evidence for the formation of layers of SiC with a higher resistance in bulk SiC following hydrogen ion-irradiation at this energy at room temperature [347, 355].

There is no evidence of irradiation enhanced diffusion of boron during irradiation by 2.5 MeV hydrogen ions in the temperature range 500°C to 850°C [356]. This is due to the high activation energy ($\geq$ 3.5 eV) which cannot be overcome despite the combined high temperature and irradiation [356].

2.5.4.1.7 12 – 65 MeV

12 MeV hydrogen ion-irradiation creates silicon monovacancies in both hexagonal and cubic sites as well as divacancies (as observed at lower energies) [278, 357, 358]; the silicon vacancy concentration is lower than predicted by SRIM simulations. The authors believed this is due to recombination effects [357].

Conductivity studies of 17 MeV hydrogen ion-irradiated SiC has shown [359] that radiation induced conductivity is four times higher in the hydrogen ion-irradiation case when compared to the reactor case (both specimens having recieved the same ionising fluence). The authors consider this to be caused by ionisation effects within the material [359].

Electrical devices such as diodes [360, 361], Schottky rectifiers [362] and Metal-Oxide-Semiconductor (MOS) capacitors [360] made from SiC have been irradiated with high energy (40 – 65 MeV) hydrogen ions. Broadly, the devices investigated respond well to hydrogen ion-irradiation. Some properties of the devices are degraded including an increase in recombination centres and electron traps due to defect creation. There are some improvements in the devices, for example, the reverse leakage current is reduced. The conclusions of the work on these devices indicate that the design and manufacture of SiC based electronic components for harsh environments (for example, extra-terrestrial or nuclear applications) is likely to result in successful operation of electronic devices despite a high flux of energetic particles irradiating the device throughout its lifetime.

2.5.4.1.8 100 MeV – 24 GeV

Calculations of defect creation by considering the division of recoil energy to atoms in the target have been performed to establish displacement energies of silicon and carbon from the SiC lattice as a result of irradiation by hydrogen ions of energies of between 100 MeV and 10 GeV. The results of these calculations corroborate the displacement energies reported elsewhere in the literature (of 20 eV for carbon and 35 eV for silicon) [363].

A small amount of work has been performed on the development of semi-insulating layers in SiC using 1 GeV hydrogen ion-irradiation. This irradiation results in an increase in donor concentration [347]. It is thought that this work

will lead to the creation of devices which rely on the creation of regions of high resistance within SiC without the need to raise the temperature. This is important for the manufacturing of devices where only a small thermal budget is available.

The vast majority of the high-energy ion-irradiation has been performed on electronic devices; mostly diodes [364–366] and radiation detectors [367, 368]. The overwhelming conclusion of this work is the favourable response of the targets to hydrogen ion-irradiation. The diodes investigated show no significant change in their characteristics following irradiation with 203 MeV hydrogen ions [364, 365]. Following irradiation by 24 GeV hydrogen ions, the diode function was shown not to be critically impaired and the radiation response was quite low. Following irradiation to the highest fluence the device was considered intrinsic [366]. The authors conclude that this is due to the dopant effect being offset by the damaging effect of the radiation.

Schottky diodes used for radiation detection suffer significantly more (compared to the diodes investigated in the paragraph above) from side effects of damage during irradiation [367, 368]. There is evidence for effective carrier transport during low fluence irradiation (10^{15} cm^{-2}) using 1 GeV hydrogen ions [367], though irradiation beyond this causes a reduction in the reverse current, and an increase in the potential barrier height of the diodes [368]. As the fluence increases, the material properties begin to alter significantly [368] which reduces the effectiveness of the device. It should be noted that this is only observed at the very highest hydrogen ion-energies reported (24 GeV) and, generally, the radiation response of SiC-based devices is favourable, especially at lower energies.

2.5.4.2 Deuterium

2.5.4.2.1 10 – 100 eV

At energies below 100 eV, similar effects as reported for hydrogen are observed with deuterium. A silicon-rich surface layer is created due to preferential chemical erosion of carbon from the surface [254, 369]. This occurs at temperatures below 225°C. From 225 to 525°C neither physical nor chemical sputtering dominates. Above 525 °C, physical sputtering dominates and there is preferential removal of carbon from the lattice [253, 254].

2.5.4.2.2 150 – 500 eV

Above 100 eV chemical erosion ceases to dominate at lower temperatures and sputtering is the prevalent process [253, 254]. This results in the production of volatile compounds due to chemical bonding between deuterium and carbon or silicon. Significant surface roughness is observed during deuterium irradiation at 400 eV in addition to the observation of a porous structure which forms bubble-like structures at a fluence of 10^{21} ions.cm^{-2} [370]. Blistering of the surface is not observed during irradiation at these energies during irradiaton at 700°C [370].

2.5.4.2.3 4 – 10 keV

4 keV deuterium has been shown to displace hydrogen when irradiating SiC containing hydrogen [371]. Deuterium has a slightly higher saturation concentration (0.75 compared to 0.70 for hydrogen). (Saturation concentration is the maximum number of deuterium atoms per unit volume divided by the number of atoms of the specimen per unit volume. Beyond a certain concentration, no net additional ions come to rest in that area, instead displacing another implanted atom from its site.) Room temperature irradiation of SiC by 7 keV deuterium results in significant surface blistering at low fluences which evolved to cause sputtering of the specimen at high fluences. The resulting surface contained a significant level of pitting [372]. Mohri, Kato and colleagues observed evidence of both physical and chemical sputtering following 10 keV irradiation of SiC [373, 374].

2.5.4.2.4 300 keV

The defects created by electron irradiation and 300 keV deuterium irradiation of SiC have been investigated. Carbon vacancy complexes are evident, probably containing an impurity at their cores. Silicon monovacancies are also created during the deuterium irradiation [261].

2.5.4.3 Tritium

2.5.4.3.1 3 keV

3 keV tritium irradiation has been performed and subsequent Auger Electron Spectroscopy (AES) and Electron Probe X-Ray Microanalysis (EPMA) showed no significant surface morphology changes are observed during this, despite significant erosion of the surface [164]. There is a bias towards sputtering of silicon atoms, leaving a carbon rich surface in originally stochiometric specimens [164]. The work also reports that stochiometric SiC has a lower sputtering yield when compared to carbon and silicon rich targets [164].

2.5.4.4 Helium

2.5.4.4.1 $\leq$ 1 keV

Irradiation of SiC by helium at energies lower than 1 keV results in a ratio of retained helium to implanted helium of almost one [375]. The small amount of helium which does not remain in the specimen is assumed to be backscattered. Two groups of defects have been explored using Thermal Helium Desorption Spectroscopy (THDS) which showed the presence of interstitial helium and helium clusters [375]. Annealing above 950°C has been shown to cause helium de-trapping from bubble-type helium-vacancy clusters [375].

2.5.4.4.2 1.3 – 10 keV

Pre-implantation of 1.3 keV helium has been shown to improve the retention of deuterium during implantation [259]. It is supposed that helium displaces carbon at these energies and occupies the resulting vacancies. Reportedly, the displaced carbon diffuses to surfaces during heating and significant recovery of Si-C bonds is observed during annealing [259]. As with irradiation at energies below 1 keV, Oliviero [375] reported complete trapping in the case of helium ion-irradiation 1.5 – 3 keV. Pre-irradiation with deuterium followed by 8 keV helium results in de-trapping of deuterium, a reduction of carbon and an increase in C-C bonds near the surface [376].

In-situ ion-irradiation/TEM of SiC by 10 keV helium has been shown to form bubbles at both room and elevated temperature (1000°C) [293, 294]. The former results in the creation of an amorphous specimen with high fluence

(1×10^{16} ions.cm^{-2}) irradiation resulting in bubble formation [294]. Preferential nucleation of bubbles has been observed (by TEM) to occur preferentially along the basal planes following implantation at 1000°C [293, 294]. At higher fluences, the number of bubbles increased, and their position became more random within the lattice.

2.5.4.4.3 12 – 30 keV

Irradiation by 12 keV helium causes amorphisation below the critical temperature (of 650°C) above a fluence of 6×10^{14} He.cm^{-2} [264–266]. Pre-implantation by hydrogen results in enhanced helium bubble growth [264]. Bubbles have been reported during irradiation at both room temperature [264, 266] and -250°C [265]. Recrystallisation of specimens amorphised by ion-irradiation occurs above 900°C [265]. Helium irradiation at 19 keV has been shown to create blisters [377]. The skin of the blisters is amorphous and contains a high density of bubbles. 30 keV irradiation forms defect clusters and bubbles which are observed (by TEM) to lie in the basal plane [230, 293, 378]. At higher fluences the preferential nucleation and growth ceases, bubbles grow and nucleate homogeneously through the lattice. Amorphisation occurs at 7×10^{15} ions.cm^{-2} in orientations which avoid ion channelling effects. Recrystallisation has been seen to occur following annealing above 725°C which creates a high number of small crystallites [294].

2.5.4.4.4 50 keV

Below the critical temperature for amorphisation, irradiation of SiC by 50 keV helium to a fluence of 10^{16} He.cm^{-2} causes a buried amorphous layer to be formed within the sample [205, 207, 211, 241]. Evidence for damage accumulation in the carbon sublattice has been observed due to the lower energy required to displace carbon [379]. Swelling is observed due to amorphisation which increases linearly with increased fluence up to 10^{16} ions.cm^{-2}[205, 241]. A decrease in sample hardness has been observed following irradiation to fluences above 10^{16} He.cm^{-2}. At 10^{17} He.cm^{-2} the hardness is approximately 50% of the virgin specimen [211, 241].

Irradiation above 300°C results in a buried layer of bubbles within crystalline SiC [205, 207, 241, 380] (i.e. amorphisation is avoided). Annealing promotes bubble growth and results in stacking faults within the bubble layer [207, 241,

380] as well as dislocation loops and partial dislocations in the basal planes [207]. Swelling occurs, which cannot be explained by the bubble growth alone and it is concluded that defects between the bubble layer and the surface must contribute to swelling [380].

2.5.4.4.5 140 – 160 keV

Irradiation by 140 keV helium ions of SiC at high temperatures forms helium bubbles. Annealing for longer periods causes void and platelet formation due to agglomeration of vacancy clusters [267]. Both of these contribute to swelling in the target. Annealing results in large bubbles or platelets as well as dislocation loops in the basal planes [221, 241].

2.5.4.4.6 390 – 400 keV

Analysis (using RBS) of SiC subjected to irradiation by 390 keV helium at low temperature indicates that defect concentration increases with decreasing sample temperature [381]. Complete amorphisation is reported as possible using helium at low temperature (-100°C) using 390 keV ions [382]. Partial recovery of lattice damage is possible when returning the specimen to room temperature. It is thought that complete damage recovery is not possible due to helium atoms occupying lattice sites [381–383]. 390 keV helium irradiation of SiC was performed by Jiang and colleagues at -80°C [384]. Displacement of atoms from the silicon sublattice was determined using RBS. The displacement energy was concluded to be around 35 eV.

Bubbles form following 400 keV irradiation in short lines with alignment parallel to the basal planes. TEM of specimens implanted at room temperature show an amorphous zone is formed slightly deeper than the peak damage depth. The authors suggest that helium atoms play a role in induced amorphisation rather than solely causing damage leading to amorphisation [385].

2.5.4.4.7 550 keV – 1 MeV

AES performed on specimens irradiated by 600 keV helium ions has been used to observe the surface behaviour [386]. The primary effect observed is blistering of the specimen which evolves to flaking of the surface.

Sputtering yields were reportedly difficult to measure, though a figure of $\approx$ 0.15 atoms/ion was reported [386]. Irradiation at 1 MeV forms bubbles at 1000°C with an increase in bubble number with higher temperature. At 1000°C the majority of bubbles form near grain boundaries. At 1300°C, bubbles are observed both within the grains and at the boundaries. Bubbles which form near to the grain boundary are shown to be of a larger size when compared to those within the grain interior [295].

2.5.4.4.8 1.6 – 2 MeV

Implantation by 1.6 MeV helium ions at room temperature creates similar effects to those reported in the previous sections at lower energies. A buried amorphous layer is observed between two crystalline layers. At high fluences (10^{17} ions.cm^{-2}) small bubbles are observed in part of the amorphous layer [190, 222, 387]. Slight recovery is observed following annealing to 800°C [190]. Annealing to 1500°C results in recrystallisation of the amorphous layer [190, 387] and growth of bubbles to much larger sizes which are faceted in some cases [190].

Several defects (which act as electron traps) have been identified by DLTS following 1.7 MeV helium irradiation. There is evidence of divacancies as well as both silicon and carbon vacancies [285]. 1.7 MeV He irradiation of SiC/SiC composites in a graphite matrix was performed by Nogami and co-workers [388] at 800°C and 950°C. Importantly, neither amorphisation nor helium bubble growth is observed for these conditions. Axial shrinkage of the fibres was observed — though no modification to grains was observed [388]. Hua and co-workers reported irradiation by 2 MeV to cause similar effects as implanting at a lower energy (140 keV) and annealing. 2 MeV irradiation forms a network of voids and platelets at the interface between the crystalline and highly damaged regions in the specimen [267].

2.5.4.4.9 3 MeV

The behaviour of SiC/SiC composites under irradiation from 3 MeV helium has been investigated [119, 389]. Helium bubbles have been observed (by TEM) to grow within the fibres when irradiated at this energy and during subsequent annealing to 1400°C. Bubbles preferentially grow on grain boundaries and a denuded zone was observered near the graphite binder between fibres [119].

Helium was only released (measured by mass spectrometry) from the fibre at temperatures above 1300°C — otherwise it remains relatively stable in small clusters within the specimen [389].

Room temperature irradiation of 6H-SiC wafers by Sasase and colleagues [390] showed that at a fluence of 10^{17} ions.cm^{-2}, 3 MeV helium does not cause an amorphous layer as reported at lower energies by Beaufort and Oliviero [190, 222, 387]. Helium bubbles were observed using TEM and the damaged region is considered 'defective crystalline' SiC [390].

2.5.4.4.10 3.5 MeV

Rovner's study [386] of sputtering of SiC as reported in section 2.5.4.4.7 was also performed at 3.5 MeV. This shows a much higher ($\approx$ 75 atoms/ion) sputtering yield than at lower energies and the sputtering was stochiometric. No blistering was observed (by Scanning Electron Microscopy (SEM)) at this energy — but flaking did occur at higher fluences [386]. Kháhn investigated the radiation damage caused by 3.5 MeV helium during RBS experiments. The work concluded that in the early stages, RBS-detected damage increases almost linearly with increased fluence [391]. In the high fluence regime ($\geq$ 3 $\times 10^{17}$ ions.cm^{-2}), RBS is no longer capable of detecting higher damage levels, though the sample continues to be damaged until amorphisation is reached [391]. The authors believe this is due to high levels of disorder causing significant amounts of scattering during RBS. Damage levels continue to increase beyond 3 $\times 10^{17}$ ions.cm^{-2} as observed by step-height measurements.

2.5.4.4.11 $>$ 15 MeV

Irradiation of SiC was performed by a 15.7 MeV helium beam which was energy attenuated by aluminium foils of various thicknesses to provide a profile of energies up to 15.7 MeV. Samples implanted at room temperature and annealed to 1100 °C were observed (by TEM) to contain bubbles at grain boundaries and within the grain interior [296]. A denuded zone around grain boundaries was observed. Discs of bubbles are the predominent defect inside grains orientated along the basal planes [296].

A similar technique has been used by researchers working at Institut für Festkörperforschung (IFF) in Jülich, Germany, where a 26.3 MeV helium beam was attenuated to give a homogeneous distribution of helium within

the specimen [182, 238, 392]. Experiments have been performed at room temperature and at 1000°C. In SiC/C composite material no bubbles form at grain boundaries where one of the grains at the boundary is made of graphite, this is thought to be an encouraging result as it leads to improved mechanical properties of the material. However, where SiC/SiC grains meet, there is a high density of bubbles which ultimately degrades the material [238]. In polycrystalline SiC, bubble behaviour is the same as has been reported at lower energies. Bubbles nucleate preferentially on grain boundaries and far from grain boundaries within the grain interior. Depleted zones near to the edge of grains are observed by TEM [392]. Bubbles have been observed to be faceted on $(0\,0\,0\,1)$ and either $(0\,1\,\bar{1}\,2)$ (for 4H-SiC) or $(0\,1\,\bar{1}\,3)$ (for 6H-SiC). Interstitial-type dislocation loops and helium platelets are observed which grow during thermal treatments [182, 392].

Using aluminium degrader foils, a 36 MeV helium beam has been attenuated to create a uniform profile of helium in an SiC target. This has been used to investigate SiC/SiC composites [393, 394]. Bending strength is shown to decrease when compared to an unirradiated specimen [393] with little or no surface modification observed due to irradiation. Implantation with helium with a uniform profile using an attenuated 36 MeV ion beam and subsequently irradiated by neutrons ($E \geq 0.1$ MeV) has shown no modification to properties when compared to composites exposed to neutron irradiation alone. This includes hardness, fracture strength and elastic modulus [394].

Finally, an investigation on the behaviour of SiC/SiC composites (at 900°C) under irradiation by 39 MeV helium beams which were attenuated by the technique described above has been performed. The authors [210] observe that swelling is increased in comparison to similar levels of neutron damage at the same temperature. The mechanism for this is assumed to be the inhibition by helium of defect annihilation, presumably by the same mechanism as at lower energies, that is, helium occupying vacancies, and preventing interstitials returning to these sites.

2.5.4.5 Lithium

8 MeV lithium has been used to cause radiation damage in 21R-SiC at room temperature [395]. The sample was found (using RBS) to be amorphised at the end of the ion range (12.3 μm) with some evidence for localised heating causing a small amount of lattice recovery. Ion channelling effects

were investigated using RBS and the authors have found and reported appropriate parameters to avoid channelling in 21R-SiC. The authors of the paper concluded that these results are difficult to relate to the other polytypes of SiC.

2.5.4.6 Beryllium

Beryllium is an important p-type dopant for SiC [396–398]. It is an alternative to the more commonly used aluminium ion due to a longer range within SiC (for the same energy) and the ready availability of gaseous sources for ion beam creation [396]. It has been shown that beryllium-doped diodes perform better than boron-doped equivalents [396]. Irradiation by beryllium at energies of between 50 and 590 keV to create a uniform profile within the specimen, has been shown to match the theoretical profile predicted by SRIM [397, 398]. There is rapid diffusion (measured by SIMS) towards the surface of irradiated specimens following annealing processes [397]. Defects created using this profile have been shown to consist of two carbon atoms sharing the same silicon vacancy. This implies the introduction of the beryllium atom allows a di-interstitial to be accepted on the lattice site [398, 399]. There was no evidence of a V_{Si}-V_C divacancy as reported in other irradiation studies [399].

2.5.4.7 Boron

Boron is an important impurity for SiC electronics as it dopes the crystal structure to modify electrical behaviour [400–404]. Implantation depth of dopants is important in order to control and develop efficient electronic structures. The implantation depth of boron has been studied by SIMS [270, 405]. The reported depths of boron irradiation, including those where multiple energies are used, were found to match the SRIM calculations [270, 405]. Boron implantation at 350 keV has been investigated by Low Temperature PhotoLuminescence (LTPL) which shows that there are specific defects generated by boron implantation, which are concluded to incorporate the boron as part of the defect centre [406].

Uniform profiles of boron have been implanted into SiC in order to dope the structure and achieve p-type conductivity in the crystal [401–404, 407]. These have then been subjected to thermal treatments to modify the profile. Implanted boron has a reportedly low activation (less than 50% after

annealing) [401, 402, 405] and as a result it would seem unlikely that boron will be used to achieve p-type doping in SiC in the future. There are reports of high temperature annealing leading to higher activation percentages (90%) [404, 407]. Despite the potentially low activation, doping of SiC with boron has resulted in devices with lower leakage current, higher breakdown voltage and higher electron-hole mobility than other p-type dopants [401, 402, 407].

2.5.4.8 Carbon

Carbon implantation has been used to promote recovery of the carbon sublattice [408, 409] which will inevitably be damaged by the introduction of dopants via ion-irradiation [151]. Recovery processes have been shown [408, 409] to be assisted by implantation of carbon into a shallow surface layer. There is evidence that this process gives beneficial doping conditions due to the inhibition of deep, electrically degrading defects [409]. The position and width of carbon-carbon signals generated by Raman spectroscopy has been shown to correlate linearly with ion fluence during irradiation by 30 keV carbon ions. For small increases of carbon to silicon ratio, the bandgap increases significantly. However, this sharply drops off beyond a ratio of approximately 6:4 [410]. High fluence (10^{18} ions.cm^{-2}) 60 keV carbon irradiation in SiC has also been shown to form graphite and diamond phases during annealing to 600°C and 900°C, respectively [297].

2.5.4.9 Nitrogen

Nitrogen is an n-type dopant in SiC [411–413]. An understanding of irradiation by nitrogen is, therefore, important for its role in the semiconductor industry.

Kimoto has shown that implantation of nitrogen with a box shaped profile (using a combination of ion energies of between 30 and 140 keV) at 800°C and annealing at 1500°C results in suppression of amorphisation and a reduced damage profile within the lattice [411]. A high breakdown voltage and low leakage current were noted following this implantation and thermal treatment [411]. Ions implanted to form a box profile using multiple energies between 15 and 180 keV of nitrogen has been shown to have good thermal stability within SiC [413]. Although this implantation was conducted at 700°C it is claimed that implantation at room temperature would have achieved the same electrical efficiencies as the work conducted by Kimoto [413].

High dose nitrogen implantation to SiC has been shown to form phases of α-$Si_{1.5}C_{1.5}N_4$ following 100 keV implantation [414], a-SiC_xN_Y [298] following 180 keV implantation and β-Si_3N_4 [299] using 50 keV irradiation. The inclusion of these phases in the silicon carbide crystal causes significant property changes. This includes increased hardness [414], amorphous and nano-crystalline layers [298, 299] as well as blister formation [299]. Nitrogen doping (p-type) has been shown to improve electron mobility following implantation with 2.5 and 5 keV nitrogen [415] as well as much improved reverse-bias leakage when implanted with a box shaped profile [416] when compared other p-type dopants.

2.5.4.10 Oxygen

180 keV oxygen irradiation of SiC has been investigated using TEM [237, 417] and RBS [417]. Irradiation at 650°C avoids amorphisation up to 10^{17} ions.cm^{-2} but there is evidence of an amorphous layer at higher fluences (5×10^{17} ions.cm^{-2}) [417]. Oxygen bubbles are observed to form in the amorphous layers [237]. Extended defects are observed at the amorphous/crystalline interface with evidence of a silicon oxide layer forming due to a deficiency of carbon atoms around the R_P [237].

2.5.4.11 Neon

SiC thin-films have been amorphised under 20 keV [418] and 2.3 MeV [419] neon irradiation at room temperature and were observed to recrystallise during annealing [418, 419]. Samples have been shown to have increased hardness during early irradiation, which rapidly falls as the samples approach amorphisation [419]. Neon implanted with a uniform profile into SiC and annealed up to 1750°C, has been shown to create clusters of point defects [290]. In some cases these evolve into extrinsic dislocation loops in the basal planes. The defect densities match the calculated profile of damage and it is believed by the authors that the same behaviour occurs for all light elements [290].

2.5.4.12 Aluminium

Aluminium implantation causes p-type doping within SiC and has been shown to cause significant changes to carrier concentration [269, 420]. This is

mainly due to the formation of high hole concentrations during implantation and annealing [421]. The combination of high dose aluminium radiation with a box shaped profile (energy 50 – 450 keV) followed by Ion Beam Induced Crystallisation (IBIC) has been shown to form layers of low resistivity in SiC [420].

Irradiation carried out below room temperature causes amorphisation due to the high disordering rate of the carbon sub-lattice [268–270]. This has been shown using 1.1 MeV ions [268], using multiple energy implants up to 120 keV to form a box profile [269] and using 40, 90 and 190 keV aluminium ion-irradiation to form a box shaped profile [270]. Recovery is possible using thermal treatments which have been shown to remove almost all significant defects [269]. High temperatures also help to electrically activate the aluminium within SiC following implantation of box shaped profiles using energies between 15 and 180 keV [413] and between 30 and 360 keV [401]. DLTS has shown a complex series of defects as the result of the implantation of a box shaped profile of aluminium [422].

Above a critical concentration of approximately 10-atomic-%, aluminium precipitates have been observed (by TEM and AES) to form following both 350 keV ion-irradiation [303, 304] and multiple energy (50 – 450 keV box shaped profiles) ion-irradiation [423]. Preferential occupation of aluminium on silicon sites is observed (by SIMS and AES) [303, 304] which leads to the formation of aluminium carbide precipitates as well as small precipitates of silicon in the silicon carbide lattice [303, 304]. This effect is not observed (by TEM, RBS or SIMS) in poly- or nano- crystalline SiC due to diffusion of aluminum at the grain boundaries [423].

2.5.4.13 Phosphorus

Phosphorus doping of SiC gives rise to n-type regions in SiC [405]. Nitrogen is a more favourable n-type dopant for low fluence doping because its low mass results in a deeper implantation depth at the same energy and its low ionization energy increases the concentration of mobile carriers. At higher fluences, the activation of nitrogen dopant is poor in comparison to phosphorus. Therefore, for high fluence n-type doping of SiC, phosporus is a more efficiently activated dopant [424–426].

Removal of irradiation-induced defects is essential to ensuring high electrical efficiency [427]. The amount of potential lattice recovery has been shown to

be closely linked to fluence following multiple energy ion-irradiation between 10 and 280 keV [427]. Samples implanted by various box profiles (50 keV – 4 MeV [405], 10 – 280 keV [427] and 10 – 360 keV [426]) to concentrations less than 3×10^{18} cm^{-3} can be almost entirely recovered by thermal processes [405, 426, 427]. Beyond 2×10^{20} cm^{-3}, significant recovery cannot be stimulated up to 1700°C [424, 427]. Room temperature irradiation by 200 keV phosphorus has been shown to form divacancies and vacancy clusters within SiC [288]. Dopant atoms are shown to occupy both cubic and hexagonal interstitial sites following ion-irradiation using 70 keV – 2 MeV energy ions to create a box shaped profile [428].

2.5.4.14 Sulphur

The study of sulphur as an n-type dopant in SiC stems from its use as a dopant in silicon [429]. Irradiation studies using multiple energies to create a box profile in all three major polytypes (3C, 4H and 6H) show that sulphur occupies lattice sites within SiC and forms double donors when incorporated into the lattice [429]. There is no indication (so far) as to which position on the lattice, if any, sulphur occupies [429].

2.5.4.15 Argon

Argon ion implantation has been used to modify electrical properties of SiC [430, 431], to induce amorphisation [271] and in TEM sample preparation (see section 2.4.1). Implantation of 30 keV argon ions causes the formation of high resistivity layers within the specimen and can be used to create a high breakdown voltage or a reduced leakage current within SiC based electrical devices [430, 431]. Room temperature irradiation of SiC has been shown to cause amorphisation when irradiated with 150 keV argon ions [271].

2.5.4.16 Titanium

Titanium implantation using 175 or 190 keV ions has been performed on SiC to create phases of TiC within the SiC target [272, 432]. Low fluence amorphisation is documented at room temperature following 175 keV implantation [272]. Annealing introduces further complicated SiC-Ti complexes such as Ti_3SiC_2 [272]. Titanium implantation using 190 keV ions causes a reduction of sample hardness and swelling within SiC [432].

2.5.4.17 Vanadium

Semi-insulating layers in SiC can be formed by 300 and 400 keV vanadium ion-irradiation [433] and require a lower fluence than oxygen implantation to achieve the same levels of resistivity [433]. There are very small amounts of vanadium diffusion during annealing processes, but surface morphology modifications [434] are observed by Atomic Force Microscopy (AFM) after 2.1 MeV vanadium irradiation and annealing to 1650°C, probably due to evaporation of silicon from the specimen (see section 2.7.3).

2.5.4.18 Manganese

The introduction of manganese to SiC can form Dilute Magnetic Semiconductors (DMSs). Implantation using 350 keV ion-irradiation at 800°C avoids amorphisation [435, 436]. Two phases (3C-(Si,Mn)C and Mn_5Si_2:C) exist simultaneously following Mn doping of SiC [436]. The samples exhibit a strong preference for ferromagnetic ordering (over anti-ferromagnetic) [435, 436].

2.5.4.19 Cobalt

A FIB system has been used to implant 35 keV cobalt ions in SiC [305]. At room temperature, a variety of cobalt silicide precipitates are formed within the SiC crystal. At higher temperatures, the regions of cobalt silicide agglomerate into larger isolated regions within the specimen [305].

2.5.4.20 Copper

Nanoclusters of copper have been formed during implantation by 2 MeV copper ions in SiC [306]. Post-implantation annealing or high temperature implantation (500°C) anneals out the damage caused by implantation which enhanced the formation of copper nanocrystals within the specimen (as observed by Optical Absorption Spectroscopy (OAS)) [306].

2.5.4.21 Germanium

The implantation of 200 keV germanium ions into the SiC lattice causes amorphisation during irradiation at room temperature [233, 273] and has also

been observed following room temperature implantation of either 250 keV or 800 keV followed by 500 keV germanium ion-irradiation [274]. The amorphous areas can be recrystallised by annealing. For implantation performed at 700°C, amorphisation is avoided [274, 437] with germanium occupying interstitial sites in SiC. Annealing above 1600°C results in the formation of germanium nano-crystals which were observed using TEM [274, 437]. It has been reported that the formation of germanium precipitates after annealing can be avoided by adjusting the thermal treatment. For example, annealing above 1450°C for 10 minutes after irradiation by 50 and 140 keV germanium ions resulted in the formation of a silicon carbide/germanium alloy structure [438]. Deep level vacancy-type defects have been identified (using PAS) as a result of 200 keV germanium ion-implantation into SiC [273].

2.5.4.22 Krypton

5 MeV krypton ion implantation into SiC at room temperature causes an increase in the hardness of SiC when compared to unimplanted SiC. Hardness increases during annealing up to approximately 600°C, with hardness falling beyond this temperature [439]. X-Ray Diffraction (XRD) investigations show that strain increases during implantation and decreases following annealing of the specimen [439].

2.5.4.23 Palladium

Palladium implantation in SiC is of particular interest as SiC irradiated by palladium can be used in devices for hydrogen sensing [440]. When irradiating with a variety of energies between 30 and 130 keV to form a box profile, an optimum fluence of 10^{15} ions.cm^{-2} is concluded due to the compromise between sufficient doping and radiation-induced damage due to ion-irradiation [440]. The device is expected to be stable up to 800°C. The authors claim that attempting to recover damage using thermal processes will cause device damage due to silicon and carbon evaporation [440].

2.5.4.24 Silver

Silver nanocrystals have been shown to form during 2 MeV ion implantation at room temperature [306]. The quality of these crystals is improved by implantation at 500°C [306]. The formation of an amorphous layer together

with silver precipitates within the specimen have been observed by TEM [441, 442] following irradiation by 93 or 161 MeV silver ions. Minimal migration of silver during annealing was observed by X-Ray Photoelectron Spectroscopy (XPS) [441, 442]. Vacancy clusters have been shown to be caused by 360 keV silver ion-irradiation in SiC at lower temperatures [443]. Higher temperatures cause a reduction in these defects with only point defects created during irradiation between 325 and 600 °C [443].

2.5.4.25 Cadmium

60 keV cadmium ions have been implanted into SiC [302]. These implanted ions have been shown to sit interstitially within the basal plane of the target, as well as to induce a vacancy, a divacancy or an interstitial [302].

2.5.4.26 Indium

Indium implantation has been carried out using 400 keV ions resulting in the formation of complexes where indium combines with a vacancy [302]. This has been observed by Perturbed Angular Correlation Spectroscopy (PAC). The number of indium atoms incorporated in this way increases during thermal treatments up to 1300°C and is stable on these sites at 1700°C.

2.5.4.27 Antimony

80 keV implantation of antimony in SiC at 800°C and subsequent RBS measurements have shown that there is a low solubility limit of antimony in SiC [444]. There is a small amount of damage resulting from implantation at this temperature and there is significant out-diffusion measured by SIMS of antimony during post-irradiation thermal treatments [444].

2.5.4.28 Iodine

Work by Audren has claimed to detect amorphisation using RBS as a result of room temperature 400 or 700 keV iodine ion implantation [59, 275] of SiC at a dose of approximately 0.3 DPA [275]. The implanted profile (as measured by RBS) is stable up to 1000°C. Elevated temperatures reduce the level of disorder within the specimen (and thus prevent amorphisation) [275].

2.5.4.29 Xenon

The electrical and material properties of SiC have been investigated following room temperature irradiation by 5.5 GeV xenon ions or by ions implanted at energies between 3.3 and 8 MeV to form a uniform box profile [276, 445]. Point defect creation has been observed by high resolution XRD as a result of this high-energy heavy ion-irradiation [276, 445]. Amorphisation is ultimately detected by XRD in these specimens. Hardness increases during defect accumulation (with increasing fluence of the box shaped profile) and drops significantly at the amorphisation threshold [276]. Using van der Pauw's method, hole mobility was measured to decrease with increasing fluence of 5.5 GeV xenon ions whereas carrier concentration was measured to increase initially and slowly decreased at higher fluence irradiation [445].

2.5.4.30 Caesium

Implantation of 360 keV caesium results in an amorphous layer, as measured by RBS, within the specimen when performed at room temperature [277]. A highly disordered (but not amorphous) layer is reported to be created during implantation at 350°C. This temperature, close to the critical temperature for amorphisation is significantly higher than has been reported previously [277]. Above 600°C the crystal structure is retained during irradiation.

2.5.4.31 Hafnium

Stable hafnium complexes have been created following 160 keV hafnium ion implantation and annealing. The hafnium has been shown to be stable in the basal planes of SiC, the concentration of hafnium in basal planes increases during annealing to 1500°C [302]. Defects due to ion-irradiation are detected using PAC. These are concluded to be interstitials, vacancies or divacancies [302].

2.5.4.32 Tantalum

DLTS of tantalum-implanted SiC has been performed following implantation by various energies between 1 and 6.2 MeV resulting in a box profile [446]. A number of defects exist following implantation, with the number of defects being reduced following annealing post-irradiation [446]. The authors claim

that 100% of incident tantalum ions form deep level defects which has been shown to have donor-like properties within the specimen [446].

2.5.4.33 Tungsten

Field emission properties of SiC can be improved by implantation of 70 keV tungsten ions [300]. A variety of workers have shown that irradiation by 70 or 200 keV tungsten forms crystalline W_2C in an amorphous mix of W_xSi_y [300, 301]. The introduction of tungsten to SiC causes modification of the band gap structure. The deep acceptor level of tungsten generates semi-insulating SiC layers where sufficient levels of tungsten are introduced to the specimen [307] by multiple energy ion-irradiation at energies between 1 and 6.2 MeV. Significant surface modification is reported due to the formation of small tungsten carbide structures near the surface [300].

2.5.4.34 Iridium

Iridium doping of SiC using 5 – 6 MeV ion-irradiation results in the introduction of single atoms forming p-type doped areas in the lattice [308] observed using DLTS. This implantation causes some deep level defects within the specimen, these are attributed to the iridium substitutional defect. There is some evidence that iridium sits on silicon vacancy sites [308].

2.5.4.35 Platinum

Platinum has been shown to create a double acceptor state within SiC following irradiation by 5 – 6 MeV ions [308]. Platinum has also been shown to be the second deepest acceptor state in SiC (after vanadium) [308]. This is used to form semi-insulating layers in SiC. Surface modification of SiC during 13 keV platinum ion-irradiation is a concern for electrical devices [447]. 13 keV platinum ion implantation at room temperature and 500°C has been observed by AFM to cause a high degree of surface roughening which implies radiation damage to this region is significant [447]. Samples irradiated at higher temperature have less observed damage and are considered more suitable for fabrication of electrical devices.

2.5.4.36 Gold

Irradiation of SiC at low temperature (-120°C) by 4 MeV gold has been performed in order to investigate disorder of the silicon and carbon sublattices [448, 449]. Recovery has been observed using RBS and NRA at room temperature for low fluence irradiation [448, 449]. At 300°C the lattice is not observed to recover from the damage caused by high fluences of gold irradiation. There is more disorder observed within the carbon sublattice than the silicon sublattice [448] and there is some evidence from the NRA and RBS results to suggest that many defects are well aligned with the $\langle 0\,0\,0\,1 \rangle$ axis [448] in 4H and 6H-SiC and the $\langle 1\,1\,0 \rangle$ axis in 3C-SiC [449]. Elevated temperature implantation of 2 MeV gold in SiC results in the formation of nanoclusters of gold within the crystal as with copper and silver (see sections 2.5.4.20 and 2.5.4.24) [306].

2.5.4.37 Multi-Beam Ion-Irradiation

There has been significant use of multiple beams to create a variety of conditions including nuclear reactor relevant conditions for the study of SiC. There have been two main techniques used in multi-beam ion-irradiation. Both use helium ion beams. The first technique uses a combination of helium and silicon ion beams [229, 239, 338, 450–453]. The second technique reported is the use of a helium ion beam in combination with a heavy ion beam [229, 452, 454]. There are some reports combining two light ion beams (hydrogen and helium) [264, 266].

Simultaneous implantation of 15 keV hydrogen ions and 12 keV helium ions has shown significantly different effects, when compared to consecutive implantation by the two ion beams [264]. Pre-implantation of hydrogen enhances bubble growth, whereas simultaneous implantation causes almost no modification to bubble growth [264]. Hydrogen co-implantation with helium has been shown to cause amorphisation of SiC at a lower fluence as well as a transition to silicon rich zones at lower fluences [266].

Implantation by 5.1 MeV silicon ions and energy-degraded 1 MeV helium ions have been used to investigate swelling in SiC [229, 452]. The contribution to swelling by helium has been identified as significant below 800°C but negligible above 1000°C [452]. Swelling of between 1% and 10% is reported for a variety of temperatures [229, 452]. Cavities formed as a result of 650 keV

or 1 MeV helium and 5.1 or 6 MeV silicon ion-irradiation (with and without 340 keV hydrogen ion-irradiation) have been observed. These are seen to nucleate preferentially on grain boundaries [239, 450, 451] and are larger and more numerous when irradiation is performed at high temperatures [450]. TEM observations show that more cavities are formed during irradiation by additional ions of 1 MeV helium and 340 keV hydrogen [450, 451]. Swelling caused by cavities has been shown to be about 0.3% at 100 DPA [239] this has been linked to the implantation of 1 MeV helium ions [450].

Simultaneous irradiation by 2 MeV gold ions and 50 keV helium ions has been shown to introduce disorder to the silicon and carbon sublattices [454]. Recovery is possible using annealing processes with a residual disorder of approximately 10% of atoms remaining in interstitial sites. This is attributed to defect clusters within the specimen as well as amorphous zones within the specimen [454].

2.6 Diffusion in SiC

Diffusion is important for these experiments, as it partially determines to how bubbles nucleate. It is well established that one property of SiC is a very low diffusion coefficient [455–457] for all species. There is an extensive body of research on the diffusive behaviour of a variety of elements in SiC including self interstitials. A full understanding of the diffusive behaviour in any material is essential for ion-irradiation investigations, because this can have a significant impact on that material response.

2.6.1 Self Diffusion

Self diffusion in SiC has been measured by introducing additional quantities of isotopes C^{14} and Si^{31} into the crystal. In order to stimulate sufficient diffusion these experiments are conducted at high temperature. Rüschenschmidt *et al* [458] performed their work at 2200°C, while other work has been performed at a range of temperatures from 1600°C [459] to 2300°C [460]. The more recent studies of Rüschenschmidt [458] and Linnarsson [461] indicate that the diffusion coefficients measured in earlier work [459, 460] were an order of magnitude too high. The studies by Rüschenschmidt [458] and Linnarsson [461] found that the silicon and the carbon diffusion coefficients are much

closer to each other than previously reported [458]. The study by Hong [460] shows carbon diffusion that is quicker than silicon whereas work by Gostagore [459] indicates the opposite. The latter admits that the research does not provide a viable explanation for this behaviour. Preferential diffusion of carbon out of SiC has been used to create a silicon layer in SiC. This results in a thin film of SiC on a silicon substrate. The stoichiometry of the films is maintained as excess carbon diffuses preferentially, providing a pathway to the manufacture of high-quality SiC thin films [462].

2.6.2 Hydrogen

Hydrogen permeability through SiC has been shown to be up to three orders of magnitude lower than for hydrogen diffusion in refractory metals [463]. Activation energies of between 1 eV and 1.12 eV have been reported [464] for hydrogen diffusion at temperatures below 350°C. Experiments and simulations of diffusion of interstitial hydrogen show that activation energies are significantly higher for boron and aluminium doped SiC at 2.5 eV and 1.6 eV, respectively [465, 466]. The simulations also showed significant trapping of hydrogen on silicon vacancies within the lattice [466].

2.6.3 Helium

Jung *et al* [467] irradiated SiC with helium at high temperature (1100°C) and monitored helium release using mass spectrometry. They deduced an activation energy for diffusion of between 1.0 eV and 1.8 eV for helium in SiC. Pramono and colleagues [468] report an activation energy of 0.9 eV at temperatures between 750°C and 1060°C for neutron irradiated SiC. Zhang and colleagues [230] working on the formation of cavities in SiC report an activation energy for helium diffusion in SiC of 1.1 eV.

A modified interstitial diffusion mechanism has been reported to operate for helium diffusion in SiC [468]. This mechanism is called the dissociative mechanism where the impurity atom moves interstitially, unable to dislodge atoms from their lattice sites. If the impurity atom moves into a vacancy it becomes trapped and becomes immobile. There is a significant reduction in diffusion rates above 1260°C, it is claimed that this occurs due to the migration of vacancies which then traps the helium [468].

2.6.4 Lithium

Two studies have been performed on lithium diffusion in SiC, one theoretical [469] and the other experimental [470]. Car-Parrinello calculations by Bernholc led the authors to conclude that lithium diffuses interstitially and is a fast diffuser (compared to other elements in SiC) [469]. There are reported activation energies of 0.85 eV [469] and 2.1 eV [470]. The higher energy, reported as a result of SIMS by Linnarsson [470], is claimed to be caused by trapping on the boron dopant.

2.6.5 Beryllium

Beryllium diffusion in SiC was investigated by Henkel using SIMS [471]. The sample was annealed at high temperature (from 1300°C through to 2100°C). At the high end of the temperature range, effective diffusion (D_{eff}) of beryllium was found to be 5.7×10^{-9} $cm^2.s^{-1}$. The work concludes that the activation energy for diffusion of beryllium in SiC is 3.1 eV and beryllium is reported to undergo interstitial diffusion.

2.6.6 Boron

An extensive amount of work has been carried out on the diffusion of boron in SiC. This is because the implantation of boron leads to the generation of p-type crystals, which are useful for Schottky diode manufacture [472]. The majority of the work was performed via high temperature annealing. Most of this is between 1700°C and 2100°C [180, 472–476]. However, there is a single study at a lower temperature of 1250°C [477]. The majority of the papers which detail activation energies give a reasonably uniform range of results from 4.6 eV to 6.0 eV [180, 473, 478]. One paper differs significantly from this range. Atabaev and colleagues performed secondary ion mass spectrometry and report a D_{eff} of between 5.5×10^{-11} and 5×10^{-10} $cm^2.s^{-1}$ resulting in an activation energy of approximately 1 eV [477].

2.6.7 Nitrogen

Similar to the work discussed in the previous sections, diffusion of nitrogen in SiC has been calculated following experiments perfomed at high temperature.

The work of Tian *et al* [479] has been performed with the assistance of laser ablation, which results in temperatures of over 2500°C. Kroko and co-workers [480] achieved similarly high temperatures of 2600°C, while a more recent study by Phelps annealed at a lower temperature of 1600°C [481]. The higher temperature studies note that there is evaporation of Si from the samples resulting in graphitisation (for more details see section 2.7.3). As in the boron case, there are two groups of values for activation energy of nitrogen diffusion in SiC. Tian's publication [479] reports activation energies of between 2.3 eV and 3.4 eV, while Kroko and colleagues [480] measured significantly higher activation energies of between 7.6 eV and 9.4 eV. Kroko and co-workers [480] concluded that in their experiments the diffusion of nitrogen is inhibited by the presence of aluminium in the lattice. Work by Phelps [481] indicates that the presence of boron in the lattice enhances diffusion of nitrogen.

2.6.8 Aluminium

Linnarsson and colleagues [476] investigated aluminium diffusion in the study mentioned in section 2.6.6. Samples were implanted and annealed up to 2000°C. Diffusion has been investigated by SIMS. A TEM study was also performed which shows that aluminum diffuses through the lattice to form precipates of Al_4C_3 and Al_4SiC_4. The solubility is concluded as 10^{20} Al/cm^3 at 1700°C.

2.6.9 Vanadium

Vanadium-implanted SiC has been investigated by SIMS [434]. The samples were annealed to 1650°C and also characterised using AFM. No significant diffusion of vanadium in SiC was observed following annealing to this temperature.

2.7 Thermal Effects

Thermal effects should be considered when performing ion-irradiation studies, as they can influence whether a material remains crystalline or not, or whether it undergoes a change of structure. In the context of this research, it is important to know whether the effects we observe are in response to the

thermal treatment or ion-irradiation. We also need to ensure that SiC will avoid both amorphisation and graphitisation during the experiments.

2.7.1 (Re) Crystallisation

Recrystallisation of amorphous silicon carbide has been reported to occur across a range of temperatures. Two stages of recrystallisation are reported. The first is slow, nucleated growth which begins to take place at 700°C and continues until reaching 900°C [226, 482–484]. Nucleated growth is the random diffusion of atoms in amorphous material such that they form a small amount of crystalline material. This nucleation is then a seed for further growth. Nucleated growth has no orientation preference. These small crystallites may later form the seeds for other types of crystal growth. The second stage of recrystallisation is epitaxial regrowth which takes place above 900°C [196, 206, 226, 236, 265, 482–485]. Epitaxial growth is where the crystal grows layer by layer on top of an existing crystal. The growth is in a particular orientation, which is defined by the crystal which acts as a template for epitaxial growth. It has been shown that columnar regrowth also occurs in this temperature range, usually as a transition from epitaxial growth into columnar [190, 196]. This columnar growth includes inclusion of the 3C-SiC polytype when recrystallising amorphous (formerly 6H-SiC) targets [190, 196, 233, 236, 485]. Columnar growth builds from a seed in the same way as epitaxial growth. However it grows as partial layers, forming columns with different orientations or polytypes.

2.7.1.1 Ion Beam Induced Epitaxial Crystallisation

High-energy heavy-projectile induced cascades which lead to thermal spikes have been shown to create sufficiently high localised temperatures for recrystallisation in ceramics [313]. In SiC, there have been several reports [197, 209, 378] of recrystallisation below threshold temperatures when an ion-beam is introduced to the specimen during annealing. This technique (known as IBIEC) has been demonstrated at room temperature with 827 MeV lead ions [209], 500°C with 300 keV silicon irradiation [197] and 725 °C with 30 keV helium ions [378].

2.7.2 Amorphisation Resistance

Avoidance of amorphisation during irradiation by energetic particles is important for the introduction of dopants to silicon carbide for electronic purposes [1]. From a nuclear industry perspective, understanding temperature dependence of amorphisation during irradiation is important as it determines the response of SiC in an irradiating environment [486].

A critical temperature can be determined for the avoidance of amorphisation. This is the temperature which allows sufficient diffusion of irradiation-induced defects to allow recovery of the lattice. The critical temperature for amorphisation has been shown to vary depending on irradiating species and energy [486]. In SiC, it has been shown that disordering of the carbon sub-lattice is the driving factor for amorphisation and as such is considered the limiting factor. This is due to a lower threshold energy to create carbon vacancies [487].

Critical temperatures have been reported as between 100°C and 300°C depending on the irradiation conditions. Electron irradiation causes amorphisation when irradiating below 100°C [262, 487] with electron energies above 100 keV. For incident electrons with energies below 100 keV there is insufficient energy to displace carbon from the lattice [262]. For light ion-irradiation below 120°C and damage levels above 1 DPA, amorphisation has been reported [56, 226, 488]. For high-energy heavy-ion-irradiation, amorphisation can be avoided by raising the temperature to between 250°C (for 1.5 MeV xenon ions [486] and 560 keV silicon ions [226]) and 300°C (230 keV galium and 300 keV antimony [489]). For neutrons, amorphisation is avoided above 150°C with damage levels above 1 DPA [226, 227].

2.7.3 Graphitisation

Graphitisation has been shown to occur in silicon carbide when heated above 1050°C under Ultra-High Vacuum (UHV) conditions [39–49]. In higher pressure environments graphitisation can still occur though this requires higher temperatures of up to 1600°C [490, 491]. There have also been studies of graphitisation in a nitrogen atmosphere [492]. The graphene grown on SiC has historically been of low quality, and important recent work has been performed to improve the quality [36] and to create more intricate graphene structures such as nanoribbons [493, 494] grown on a SiC substrate. In order

to produce the highest quality graphene on SiC, the sample is prepared by a chemical treatment [42–44, 46, 47, 490, 491, 495] or exposure to a silicon flux [39–41, 45]. The silicon flux is achieved by heating a silicon wafer to 900°C and placing it near to the SiC wafer. The mechanism for graphene formation is silicon evaporation from the SiC lattice which results in the tetragonal SiC system collapsing into the graphene structure [36, 39, 41, 48, 493, 496].

Chapter 3

Experimental Methods

The use of Transmission Electron Microscopy (TEM), invented by Ruska and Knoll [497], as a tool for material scientists has provided a significant level of information for investigations into material structure. TEM is particularly suited for the study of radiation effects in materials. The use of TEM often requires specific additional equipment, skills as an operator and preparation techniques. This section details these as well as the ion-irradiation facilities used during this research.

3.1 Bulk Material

Silicon carbide wafers of the 4H (four-hexagonal) polytype were acquired from Cree Scientific (USA). The wafers are three inches (7.62 cm) in diameter, have an approximate thickness of 350 μm and a resistivity (as specified by the manufacturer) of 0.021 Ω.cm. The primary flat, a cut along one side defining a crystallographic plane, is a $\{1\,0\,\bar{1}\,0\}$ plane with the flat face parallel to a $\langle 1\,1\,\bar{2}\,0\rangle$ direction. The crystal is grown 8° off-axis $(0\,0\,0\,1)$ towards the $[1\,1\,\bar{2}\,0]$ direction to minimise ion-channelling effects. See figure 3.1 which shows the directions in the grown crystal.

3.2 Sample Preparation

TEM sample preparation was undertaken using a combination of the tripod polishing method [214] and ion-beam milling. A diamond wire saw was used to cut the wafer into 3 mm x 1 mm pieces. These were mechanically

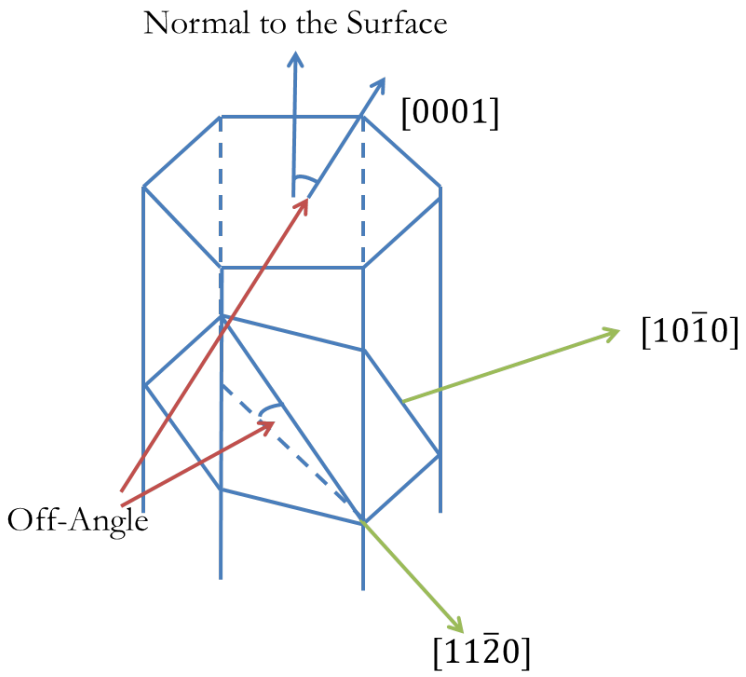

Figure 3.1: Image showing crystallographic directions in 4H-SiC including the off-angle, and directions that the sample was cut in order to make samples.

polished using a tripod polisher and glued onto molybdenum washers (often called grids). The final thinning was performed using low energy Ar^+ ions to produce areas sufficiently thin so as to be transparent to a 200 keV electron beam.

3.2.1 Cutting of Bulk Material

In order to create samples of suitable size for the TEM, the single crystal wafer of 4H-SiC supplied by Cree was cut, using a Well 3241 diamond wire saw and 0.3 mm wire. The wafer was cut along the $[1\,0\,\bar{1}\,0]$ and $[1\,1\,\bar{2}\,0]$ directions. Figures 3.1 and 3.2 show how the wafer was typically cut prior to polishing.

3.2.2 Tripod Polishing

Following the cutting stage, the sample was mounted for tripod polishing. The polisher consists of a Pyrex stub in a jig held in place by two screws. The legs of the tripod can be adjusted to provide the required angle for polishing — in

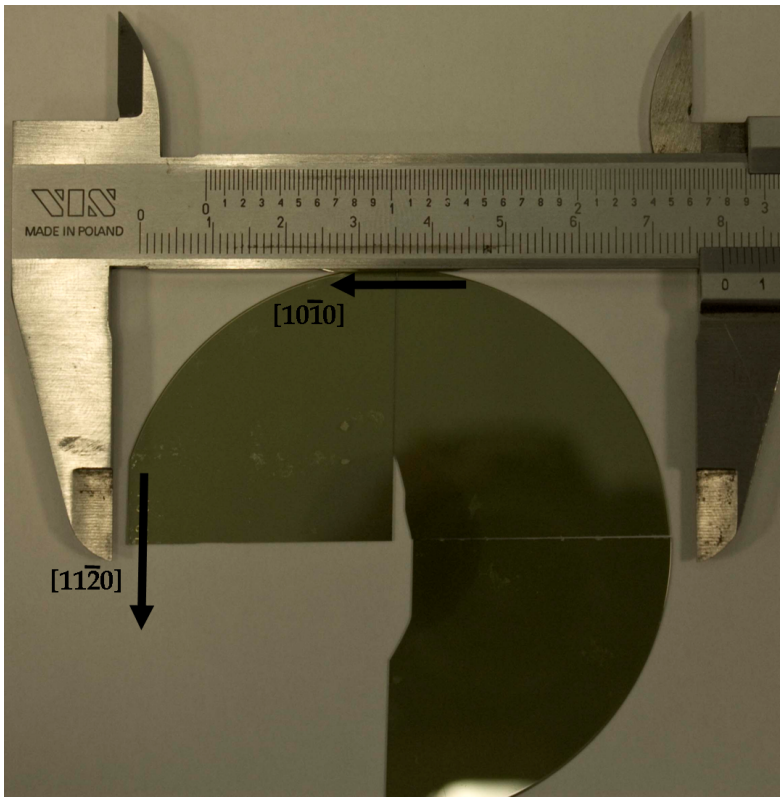

Figure 3.2: Image showing part of the SiC wafer and the directions it is cut in order to make samples for the TEM.

the current work the angle was close to 0°. Figure 3.3 (below) shows the tripod and stub.

The sample was mounted on the Pyrex stub using low temperature wax. The aim of the polishing stage was to reduce the thickness of the entire sample to approximately 10 μm while minimising the damage caused to the surface of the sample. The polishing wheel used was an Escil ESC300 GTL. Plastic discs with embedded diamonds of various sizes were stuck to the glass plate on the polishing wheel using surface tension of water. Water was also used to wash polished material from the polishing disc to retain sample quality during preparation. As the sample became thinner the disc was changed successively for one with smaller sized diamond particles. This removes material from the specimen reasonably quickly while ensuring that the surface roughness of the sample is minimised when the polishing process is complete. Table 3.1 (below) shows the disc used for various thicknesses of sample.

During the process of tripod polishing the thickness of the sample was measured using a Cooke, Troughton and Simms traveling microscope which

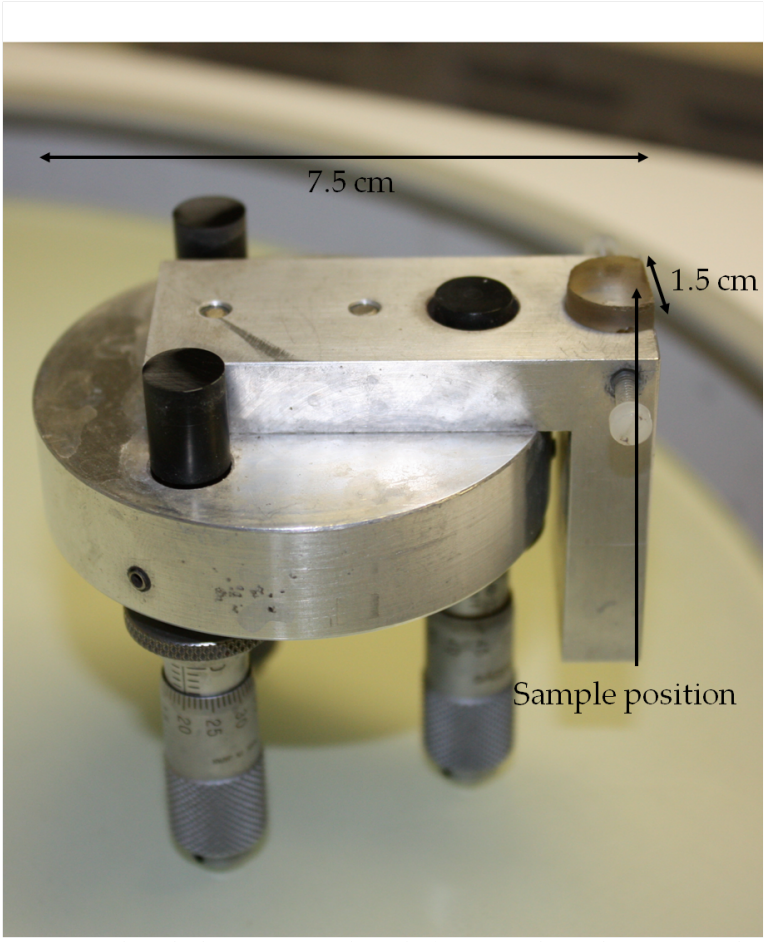

Figure 3.3: Tripod polishing jig and stub (inverted to show sample position).

has an approximate precision of ± 1 μm. Once the sample was thinned sufficiently it was removed from the Pyrex stub using acetone. The sample was then mounted on a molybdenum grid. The grids (supplied by Agar Scientific) are 3.05 mm in diameter, with a 2 mm x 1 mm hole. Figure 3.4 (below) shows the design of grid used.

The sample was glued using Gatan G1 epoxy such that the longest length of sample sat across the 1 mm gap in the grid. Following this, the glue was cured in a low temperature oven at between 60°C and 80°C for two hours in an air atmosphere. The sample was then removed from the oven and cooled ready for further sample preparation.

Particle Size (μm)	Sample Thickness (μm)	Wheel Speed (RPM)
15	< 80	15
9	80 – 50	10
6	50 – 25	6
3	25 – 15	3
1	15 – 10	1

Table 3.1: Size of diamonds on polishing disc for various thicknesses.

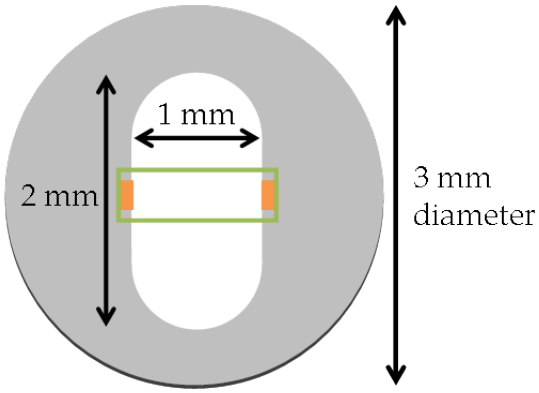

Figure 3.4: Molybdenum grid as used to mount samples for TEM showing dimensions, specimen position and glued areas.

3.2.3 Ion-Beam Thinning

The final stage of thinning is designed to reduce the thickness of the material to obtain a large electron-transparent area. For the TEMs utilised in this project, samples of thickness of $\leq$100 nm were required. Samples containing heavier elements (or with a higher density) must be thinner due to increased electron scattering. The thinning was performed using a Gatan model 691 PIPS by low energy Ar^+ ions striking the sample at glancing angles. This sputters material away from the sample in a controlled manner which results in a consistent and efficient sample preparation process. The equipment can be adjusted to provide optimum parameters for thinning a variety of materials and this allows the user to adjust thinning rates to improve the quality of the finished sample. Figure 3.5 shows the geometry of the polishing system and the parameters that are adjustable.

The samples were then screened using TEM to ensure suitability for experimental work, and stored in air for use at a later date.

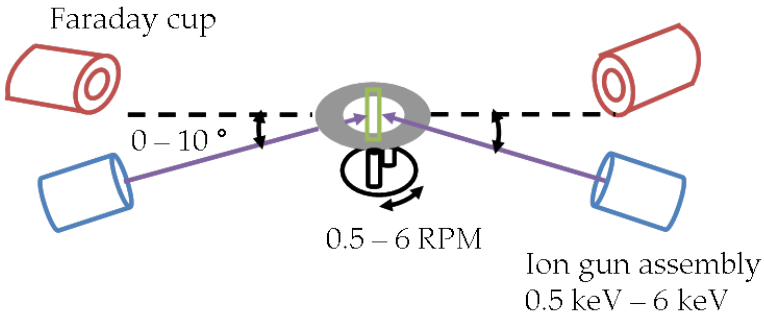

Figure 3.5: Geometry in Gatan PIPS showing ion guns, path of the ion beams, sample position and ion detection elements.

3.2.4 Pre-Implanted Samples

Some samples were implanted *ex-situ* in order to develop a bubble distribution which contains fewer, larger bubbles than can be created *in-situ*. Single crystal 4H-SiC (as described in section 3.1) was irradiated at the Institut Pprime at Université de Poitiers. Full details are available in section 3.4.2. Samples were then prepared using a Cross-Sectional Transmission Electron Microscopy (XTEM) method. Samples were cut using the Well diamond wire saw (described above) and glued so that the faces that had been irradiated were face to face (see figure 3.6). The samples were then cut into thin sections for polishing. The samples were tripod polished and ion-beam thinned as described in sections 3.2.2 and 3.2.3. This geometry protects the irradiated material from being milled away during the sample preparation process.

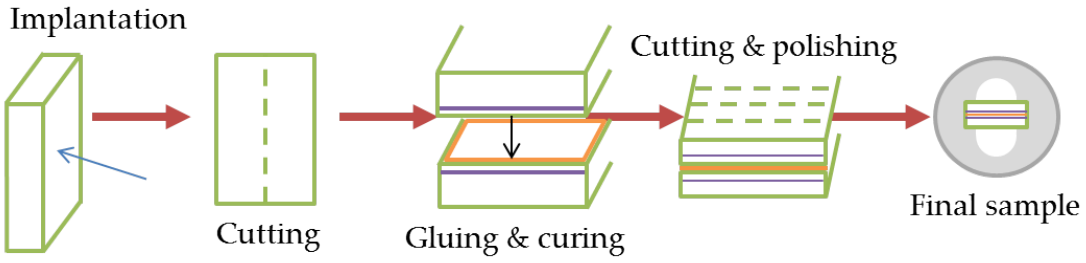

Figure 3.6: Sample preparation process for ex-situ irradiated samples showing the irradiated wafer together with implanted region, glued faces and the final sample orientation on the grid.

3.3 Transmission Electron Microscopy (TEM)

A transmission electron microscope (TEM) is an instrument which is designed to generate and control electrons for the purposes of imaging and analysing materials. This section highlights the operating principles, functions, and techniques of the TEMs that were used in this project. All of the TEMs used during this project have predominantly identical features, any differences between specific models will be highlighted in section 3.3.4.

3.3.1 Electron Scattering

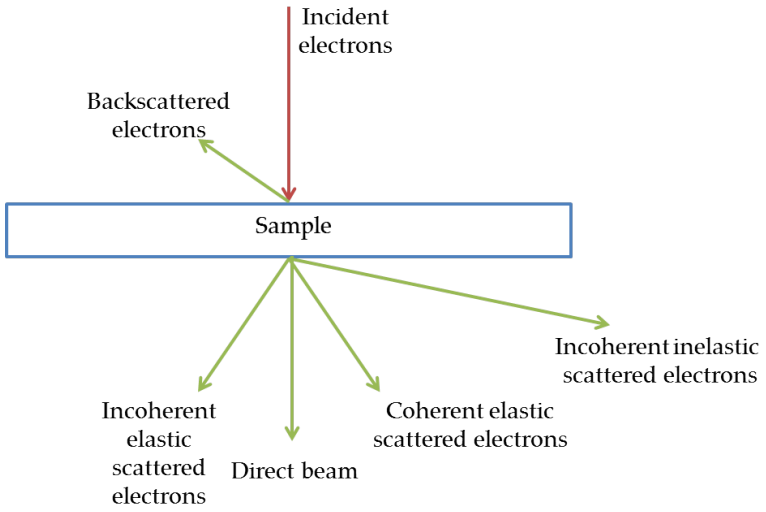

Figure 3.7: Types of scattering of electron beam when interacting with a thin sample. Based on [213]

Electron scattering is a fundamental principle in electron microscopes of all types. Just as detection of visible objects is only possible as a result of some interaction with visible wavelengths of light, in electron microscopy, users are unable to 'see' anything unless there is some interaction between incident electrons and the sample. Interaction with the sample does not necessarily mean that electrons will appear in the appropriate point in the image of the sample. It is possible that elastically scattered electrons are visible elsewhere in the image because they satisfy the forbidden reflection criteria. Transmission electron microscopists are usually interested in the electrons which are not scattered very far from the incident trajectory — these electrons contain the most important information about internal construction. Some techniques,

such as high-angle annular dark-field imaging require images to be formed only from the very high-angle incoherently scattered electrons.

If a scattering event causes no loss of energy to the incident electron it is described as 'elastic'. Electrons that have an energy shift as a result of a scattering event are described as 'inelastically scattered'. A separate property of scattered electrons is their coherence. If a phase change occurs as a result of a scattering event, it can be described as incoherent; if the incident and scattered electron are in phase, they are considered as coherent. This property results from the wave-like nature of an electron. We consider incident electrons to be monochromatic. In reality, an energy spread (full-width half-maximum) of 2 eV for a 100 keV beam using a LaB_6 filament is typical. This is such a small range that chromatic abberation is not a significant factor for image resolution considerations.

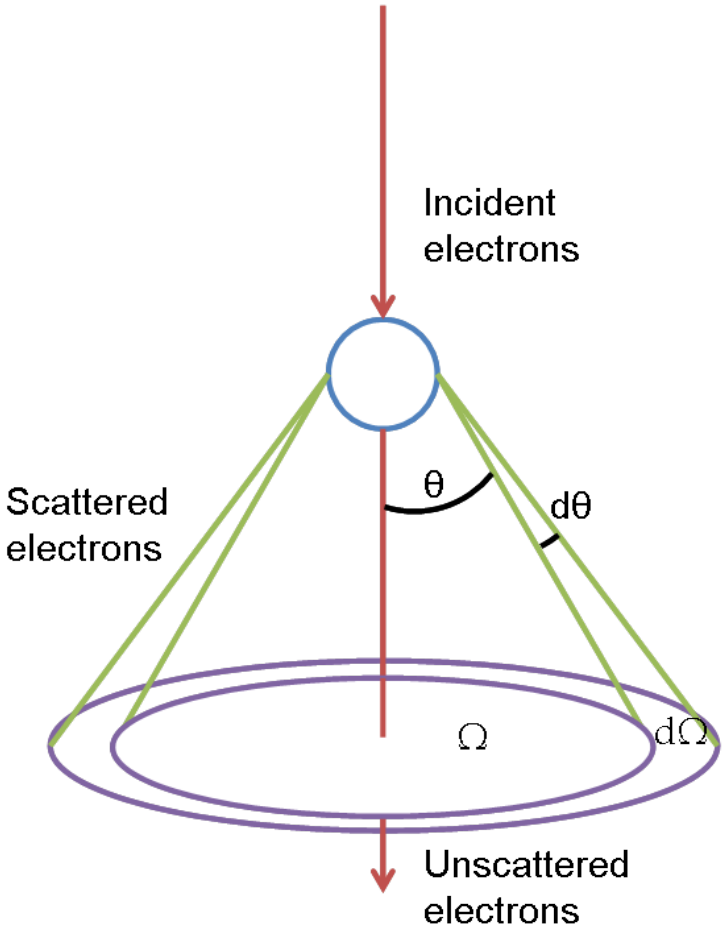

Figure 3.8: Electron scattering from an individual atom. Incident electrons are scattered through an angle θ into a solid angle Ω. A small change of angle, $d\theta$, results in a change of solid angle, $d\Omega$. Based on [213].

When an electron interacts with an isolated atom, it may be scattered through an angle (θ) into a solid angle (Ω) (see figure 3.8). The outcomes of this event are strongly related to the electron properties (such as energy) and the atomic properties of the specimen (such as its atomic number (Z)). The scattering cross-section, σ, gives the probability of a scattering event taking place. Elastic and inelastic events will each have a different probability. For scattering through a specific angle the scattering cross-section function, ($\sigma(\theta)$), gives the probability of an incident electron being scattered through angle θ.

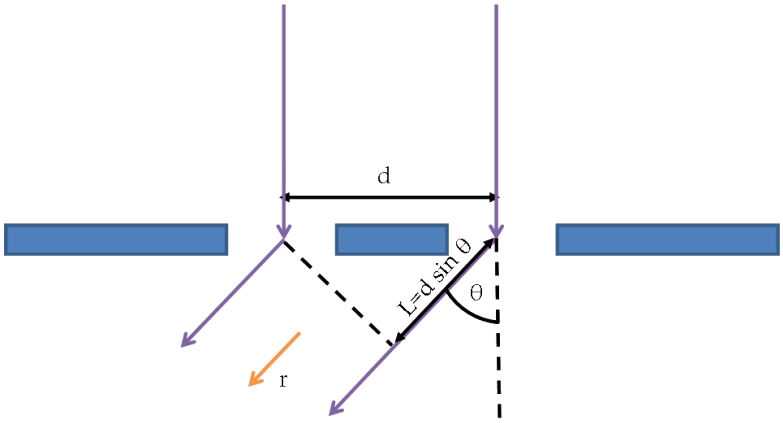

Figure 3.9: Schematic of the Young's slit experiment showing wavelet path, grating and the direction of the wave. Based on [213].

Electron diffraction is the most informative scattering phenomenon within TEM for materials scientists. It can be explained by the Young's slit experiment in which an incident wave travels through two slits distance (d) apart. The incident wave is scattered through all angles with diffraction occurring when the scattered waves are in phase. The waves will remain in phase so long as the path difference (L) is equal to an integer number of wavelengths of the original wave (λ). Figure 3.9 shows this concept.

From figure 3.9:

$$L = 2\,d\,Sin\,\theta$$

$$\therefore n\,\lambda = 2\,d\,Sin\,\theta \tag{3.1}$$

These equations enable us to determine whether scattered waves remain in phase or not. This also determines whether the scattering is considered to be

coherent or incoherent.

3.3.1.1 Elastic Scattering

At the energies used in TEM, elastically scattered electrons are closely associated with scattering at moderate angles of a few mRad. These electrons are important for materials analysis because elastically scattered electrons are responsible for a large proportion of contrast in imaging mode, as well as contributing to diffraction information. To explain the mechanisms of elastic scattering, this section will consider both the principles of electron scattering from a single atom as well as from the multiple atom case which we encounter in our specimens.

In the single atom case, the high energy incident electron is repelled by electrons in a cloud around an atom in the sample. This repulsion is strong and in the case of a direct hit results in complete 180° backscattering (similar to that observed by Rutherford [498]). The higher the angle of scattering, the higher the likelihood of some part of that interaction causing some loss of energy. However, this section will ignore these cases.

The probability of an electron being scattered by an atom through an angle θ is $\sigma(\theta)$ which can be differentiated with respect to the solid angle Ω and can be related to the atomic structure factor, $f(\theta)$. $\sigma(\theta)$ is highly dependent on scattering angle, electron energy (wavelength) and mass of the nucleus of the scattering atom, Z.

$$\frac{d\sigma(\theta)}{d\Omega} = |f(\theta)|^2$$

The amplitude of the wave of an electron scattered by an individual atom is given by $f(\theta)$. The intensity is given by squaring to give $|f(\theta)|^2$. As individual atom scattering is not characteristic of realistic electron/specimen interaction we use the structure factor, $F(\theta)$. This is the sum of the individual atomic scattering factors of each atom in the unit cell multiplied by a phase factor. The phase factor resolves the phase differences for waves scattered from different planes atoms given by Miller indices $(h\,k\,l)$. For N atoms in a unit cell with coordinates x_i, y_i and z_i the structure factor is given by equation 3.2:

$$F(\theta) = \sum_{i=1}^{i=N} f_i \, e^{2\pi i (hx_i + ky_i + lz_i)} \tag{3.2}$$

Where θ is the angle between scattered and incident electron beams. All of the elastic coherent scattering information is governed by this equation, thus diffraction is influenced by the types of atoms the electrons are interacting with, the positions of that atoms in the unit cell, and the atomic planes of the unit cell.

Originally posited by von Laue in 1913, the understanding of diffraction from crystal places was based upon the well-known understanding of optical diffraction. It is understood that diffracted waves are in phase if the path difference caused by two adjacent scattering sites is equal to an integer number of wavelengths.

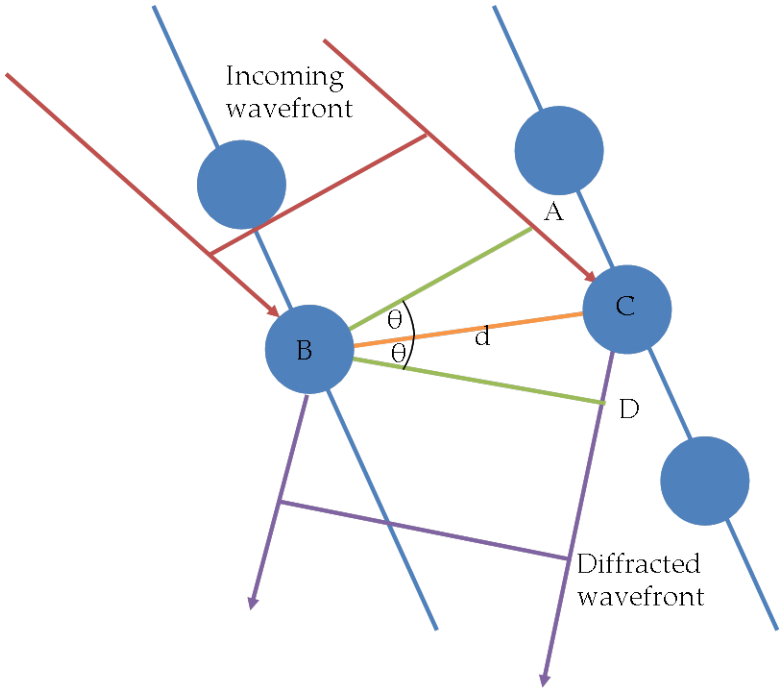

Figure 3.10: Diffraction by atomic planes separated by distance d, showing incident and diffracted waves and the angle of diffraction, θ.

Figure 3.10 shows our scattering sites, B and C, separated by a distance of d. The incident wave (with wavelength λ) strikes the plane and is scattered through an angle θ.

The von Laue scattering equations were later simplified by William Lawrence Bragg and William Henry Bragg to describe the waves as reflected from atomic planes and their understanding of reflected electrons is still used today — as the result of their work is correct — despite their understanding not accurately describing the physical phenomena. From figure 3.10 and equation 3.1 the relationship between wavelength (λ) and Bragg angle (θ_B) is given by:

$$n\lambda = 2dsin\theta_B$$

$$AC + CD = L = n\lambda = 2dsin\theta_B \tag{3.3}$$

Where n is an integer, λ is the wavelength, d is interatomic spacing and θ_B is the Bragg angle

The inversely proportional relationship shows that the closer together the atomic scattering sites, the larger the Bragg angle for diffraction. In bright-field imaging mode, electron waves will destructively interfere when scattered through θ_B. Where the electrons are scattered in this way the image will have low brightness. By tilting by a few degrees from this angle, the image will have high contrast where darker regions correspond to bending of a non-uniform specimen into the Bragg conditions. Depending on what is of interest in the specimen, the sample may be tilted into or out of Bragg conditions to obtain images as appropriate.

3.3.1.2 Inelastic Scattering

Inelastic scattering occurs during a variety of interactions of electrons with the atoms in the specimen. There is a higher likelihood of inelastic scattering during interactions closer to the nucleus of the atom. Inelastic scattering is an essential analytical tool, since considerable information is available from these interactions. One important inelastic process is ionisation. Incoming electrons collide with electrons within the specimen, providing sufficient momentum for both the electron in the specimen to be ejected, as well as for the incident electron to continue through the specimen. Another electron falls from a higher energy level to fill the vacated level resulting in the emission of an X-ray. The energy of the X-rays are characteristic of the element(s) that the

sample is made from. Analysis of either the X-rays or the energy loss caused to the incident electron can be conducted using either Energy-Dispersive X-Ray Spectroscopy (EDS) or Electron Energy Loss Spectroscopy (EELS), respectively. Further information is available in the sections on EDS (3.3.3.4.1) and EELS (3.3.3.4.2).

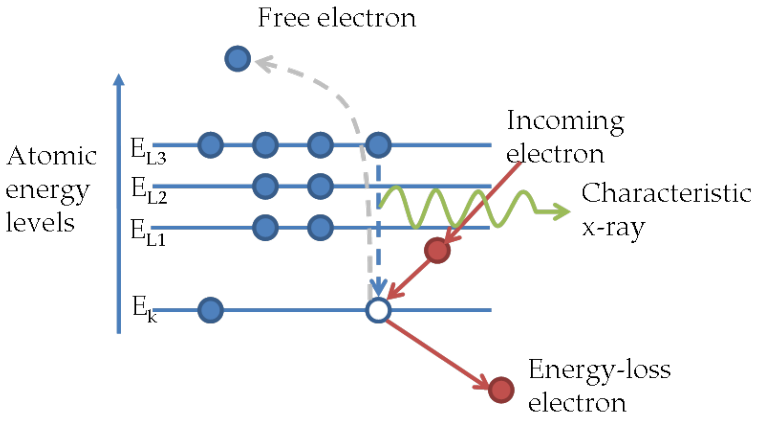

Figure 3.11: The ionisation process in TEM samples. Incoming electrons provide energy to electrons within the sample resulting in characteristic X-Ray emission. Based on [213].

Inelastic collisions within the sample can also give rise to electron beam damage to the specimens. This can be understood as three separate processes. The first is the breaking of chemical bonds within polymers and other materials (such as alkali metal halides). The second process can be described as classical billiard-ball type collisions which causes atomic displacements within a material causing Frenkel pairs to be formed. If this occurs within a few atomic layers of the surface of a specimen then sputtering type behaviour can occur. The final damage mechanism is heating of the specimen by electron irradiation through the generation of phonons. This is mainly of concern when investigating biological specimens or polymers. Some experiments are designed to simulate radiation damage using these displacements using high energy electron beams [499]. In general, however, it can be said that electron beam damage in a TEM is best avoided, and extensive studies have been performed, so as to ascertain which electron beam conditions avoid beam damage in various samples [500, 501]. The exact behaviour is highly sample specific and is known to be complicated, involving both electron-electron interactions and interactions with nuclei within the sample [213].

3.3.1.3 Sample Heating

While sample heating is often difficult to quantify, because of the several often unknown parameters such as sample thickness and properties of the thermal contact between specimen, grid and sample holder, the use of electrons in conventional *transmission* electron microscopy usually leads to heating of $< 10^{\circ}C$ [213, 502]. As a rule, good conductors under standard TEM conditions have negligible heating (by standard we mean not HRTEM). Lower thermal conductivity can lead to considerable sample heating, but only under relatively high electron fluxes where the region under electron irradiation is thermally isolated [213]. Hobbs [502] provided significant information for microscopists, comparing thermal conductivity, beam current and temperature change. For the work discussed in subsequent chapters, the effect of sample heating is expected to be of a few $^{\circ}C$, with the low electron flux and high thermal conductivity of SiC working in combination to minimise heating.

3.3.2 Construction and Equipment

The construction of all TEMs is broadly similar. Though the latest designs look considerably different to the equipment utilised in this project, the basic components are identical. In order to generate and manipulate electrons, a series of electromagnetic lenses and deflectors allow a high quality image of the sample to be produced. Modern machines include abberation correctors, monochromators and image filters in order to perform HRTEM or Energy Filtered Transmission Electron Microscopy (EFTEM).

3.3.2.1 Electron Sources

There are two methods of electron generation in TEMs. Each uses a different physical phenomenon and it is not easy to convert a TEM from one electron source type to the other. The type of electron source can have a significant impact on image quality as well as the performance of the microscope.

3.3.2.1.1 Thermionic Sources

Thermionic sources use tungsten filaments or, more commonly nowadays, lanthanum hexaboride (LaB_6) crystals. The filament is heated to provide

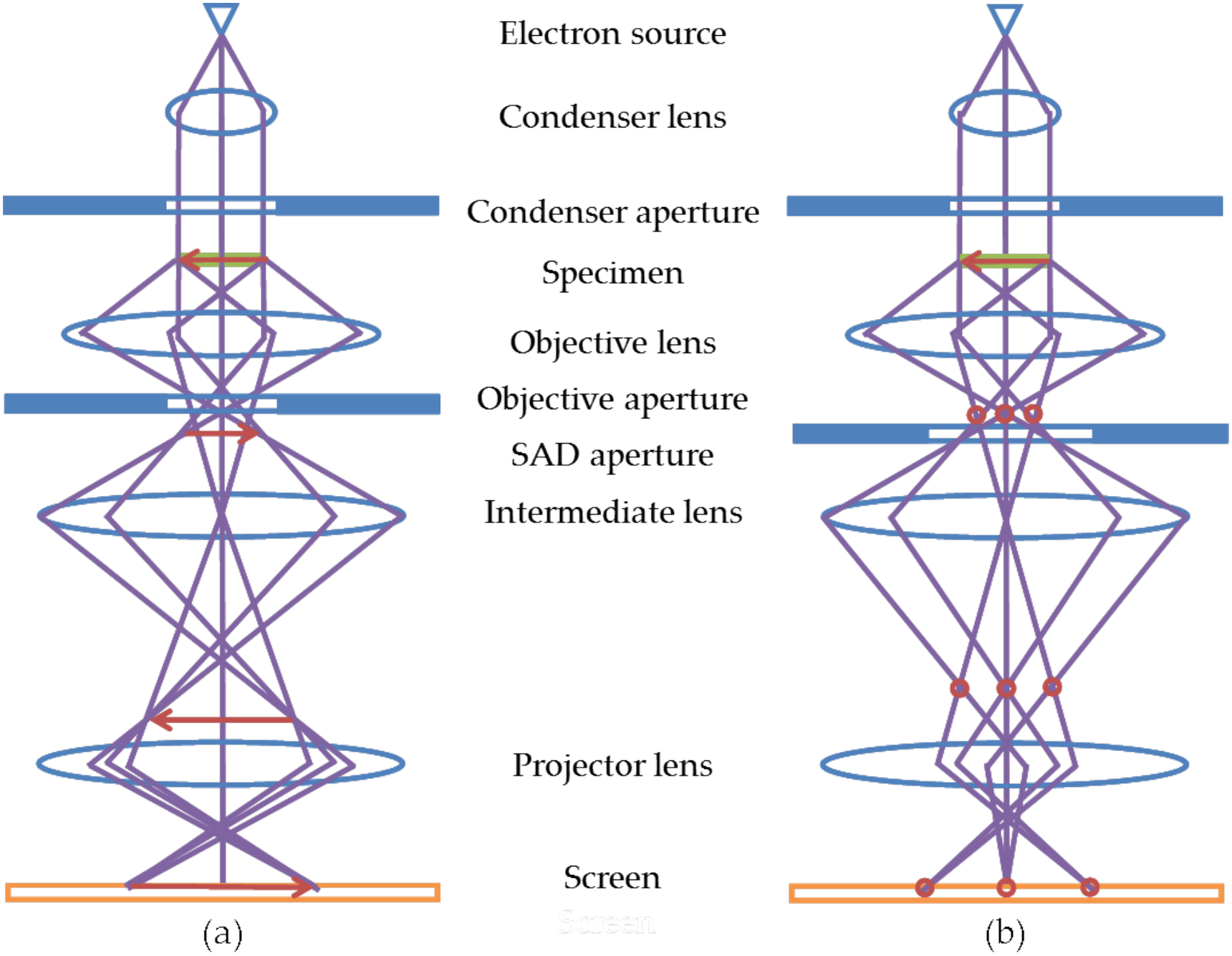

(a) **(b)** **(c)**

Figure 3.12: Ray diagrams and equipment overview of a TEM operating in imaging mode (a) and diffraction mode (b).

electrons with sufficient energy to overcome the work function. A potential is applied within the gun, between the filament or crystal (which acts as a cathode) and the anode in order to extract the electrons from the source. The elecrons are then accelerated by a high voltage potential which defines the energy of the electrons in the microscope; this forms one of the limitations for microscopy. These include a reduction of incoherency of the electrons due to the source size or stability. This can reduce image or diffraction pattern quality, or degrade spectroscopic measurements such as EELS. The thermionic source is surrounded by a Wehnelt cup, which is a simple electrostatic lens and serves to focus the electrons as they are emitted and accelerated. Figure 3.13 shows a schematic arrangement for a thermionic emission source, as well as fundamental parameters for the electron source; divergence (semi-) angle, α_0 , crossover diameter, d_0, and emission current, i_e.

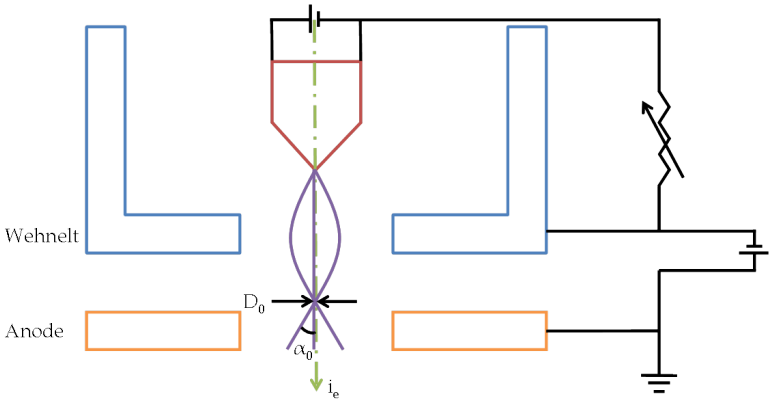

Figure 3.13: Thermionic emission electron gun for a TEM. Voltage is applied between the filament and anode. The electrons are focused by a Wehnelt which causes the electrons to crossover at diameter d_0 on the optical axis. Based on [213].

3.3.2.1.2 Field-Emission Sources

The Field Emission Gun (FEG) is based around the extraction of electrons through the application of a strong electric field. The strength of the electric field, E, is related to the voltage applied and radius of curvature of the electron source (shown by equation 3.4). The electric field is increased in a source with a sharper radius when the same voltage is applied.

$$E = \frac{V}{r} \tag{3.4}$$

Where E is electric field, V is voltage and r is radius of curvature of the source. The increase in popularity of Atom Probe Field-Ion Microscopy (APFIM) has resulted in an increase in availability of tips suitable for use in field-emission sources. As such, tungsten wire tips with a radius of <0.1 μm are now readily available. Applying equation 3.4 above allows us to see that even a 1 kV potential applied to a 0.1 μm radius tip gives an electric field of 10^{10} V/m. This electric field reduces the work function in the tungsten tip and increases the likelihood of electrons tunnelling through the barrier.

To complete the FEG, the tip is made a cathode with respect to a pair of anodes. The first of these provides the extraction voltage, the intense electric field which enables electrons to tunnel out of the tip. The second anode provides the acceleration voltage to the electrons to the higher energies required for TEM (of the order of 100s of kV).

3.3.2.2 Lenses

There are four main lenses within the TEM; the condenser lens, the objective lens, the intermediate lens and the projector lens (see figure 3.12 for their locations). Electron lenses consist of two components, firstly a soft magnetic material such as iron is manufactured into a symmetrical core with a hole bored through the centre. The soft iron is referred to as the polepiece. Many modern objective lenses are split into two with an upper and lower polepiece. This opens up manufacturing options, allowing the iron core to be made as one piece or two separate elements. The second component is inside the lens. A coil of copper wire is wound around each iron core and current is passed through the copper wire which creates an approximately axially symmetric magnetic field in the centre of the polepiece. Figure 3.15 shows a cross-section of a typical lens and the electron path through the polepiece. For all but the lowest energy TEMs, heating of the coils — due to their resistive properties — results in having to cool the lens continuously using a refrigerated recirculating water system.

3.3.2.2.1 Types of Objective Lens

The objective lens is much stronger than the other lenses. It comes in a variety of types depending on the specific operational requirements of the

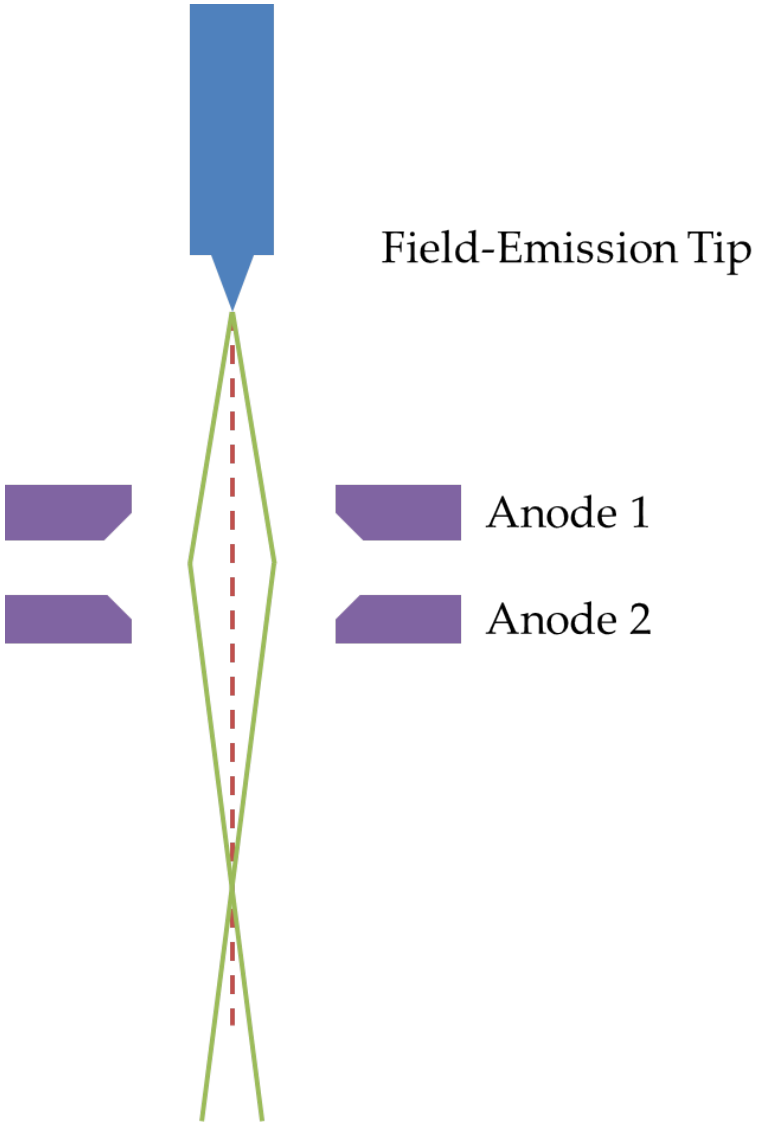

Figure 3.14: Field emission electron gun (FEG) for a TEM. Voltage is applied between the filament and anodes. The first anode extracts the electrons from the tip. The second anode provides the acceleration voltage. Based on [213].

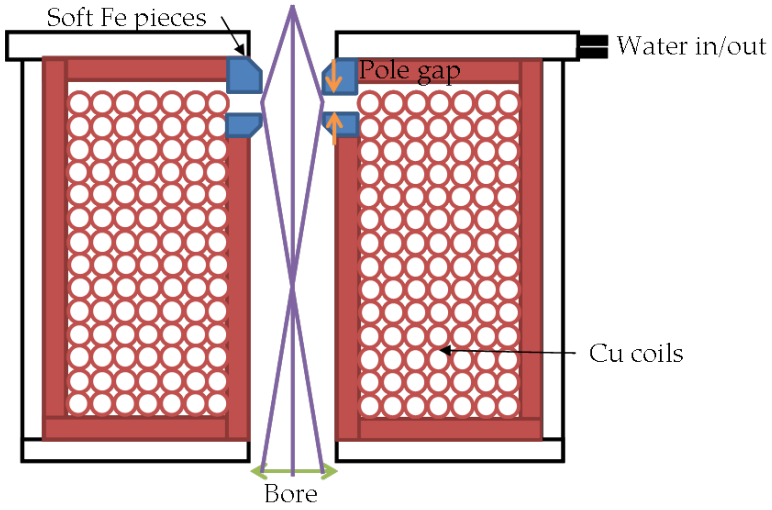

Figure 3.15: Typical lens arrangement in a TEM showing the polepieces, pole-gap, bore, copper coils and electron path though the lens. Based on [213].

TEM. Flexibility is achieved by splitting the upper and lower elements of the polepiece (each with their own windings) allowing a larger (a few cm wide) polepiece gap in which to insert specimen rods (for example, capable of heating, cooling, tilting, rotating or straining) and apertures of a variety of sizes. Other analytical components such as X-ray detectors are positioned above the objective lens in a position to have direct line-of-sight to the sample position. This polepiece gap also facilitates the entry of ion beams for *in-situ* ion-irradiation; this is of particular interest because of its utilisation during this project.

3.3.2.3 Deflectors

Deflectors exist throughout the microscope for the purpose of tilting and shifting the beam. Their construction is relatively simple in comparison to some of the components within the microscope. A deflector consists of a pair of magnetic poles orientated perpendicular to each other, such that the magnetic field is uniform across the microscope bore. Deflectors work in orthogonal pairs (to tilt and shift in both x- and y- directions) which are also often doubled up to allow beam tilting without shifting and vice-versa.

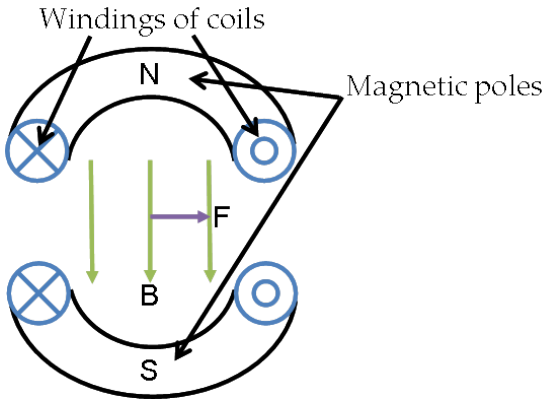

Figure 3.16: Top-down schematic arrangement of deflectors in a TEM. Arrows indicated magnetic field lines and direction of the force applied to the electrons. Based on [503].

3.3.2.4 Stigmators

Stigmators in TEMs are designed to minimise and combat astigmatism caused by a non-uniform magnetic field from the lenses. This occurs because the soft iron pole pieces cannot be manufactured to perfect cylindrical symmetry. There are stigmators in both the illumination and imaging systems. The stigmators in modern TEMs consist of a pair of magnetic six-pole lenses rotated by 30°. Astigmatic correction can be one of the most difficult alignment procedures for a TEM operator as three different adjustments are required simultaneously. This correction is especially important for HRTEM as the images depend on the phases of the beams and thus the cylindrical symmetry of the magnetic field applied.

3.3.2.5 Apertures

Apertures are the holes made in discs or strips of refractory metals (the discs or strips are called diaphragms), these are often constructed in such a way to exist along one piece of metal called an aperture strip with a variety of hole sizes. These range from a few μm up to several hundred μm in diameter.

In section 3.3.2.2, we mentioned placing diaphragms into our lenses within the microscope, in order to control many of the fundamental properties of the images that the microscope creates by limiting the collection angle, β (see image 3.17 for more details). In reality, there are several options for positioning of apertures with respect to the lenses in the microscope. The

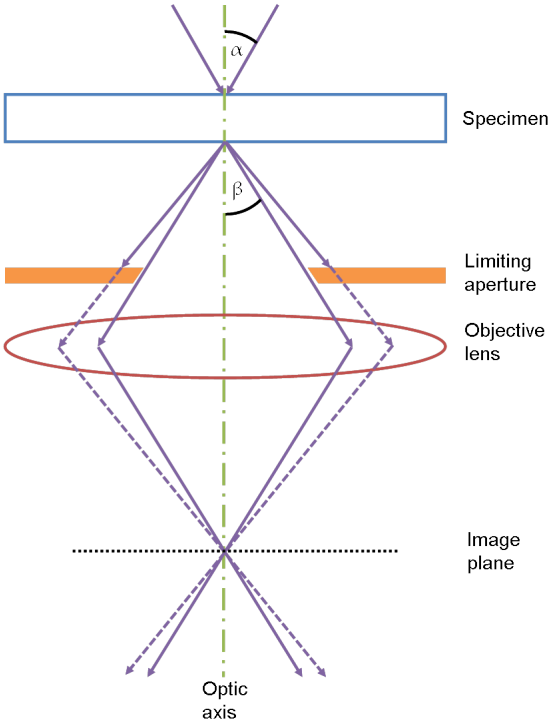

Figure 3.17: Schematic of a typical arrangement of an objective lens and objective aperture showing the specimen, aperture, lens position and electron path. Fundamental angles α and β are also shown. Based on [213].

.

particular geometry of each aperture depends on its function, but this will be appropriately designed for each aperture.

3.3.2.6 Sample Holders

A variety of types of TEM holder allow users to perform an array of experiments *in-situ* in the TEM. TEM holders have been developed to allow tilt in two axes (in order to align various crystallographic directions with the electron beam) as well as holders capable of heating (typically through conductive heating from a nearby filament), cooling, rotation and straining. Less complicated but more practical holders, such as quick exchange or multiple specimen holders, allow users to engage with a large number of specimens in a short period of time, ideal for screening specimens.

3.3.2.7 Image Capture

Electrons strike a fluorescent screen in the base of the TEM which allows users to observe the electrons in the form of green light (wavelength of ≈550 nm) (a result of the emission spectra of doped ZnS which is commonly used as the coating on the screen). This is close to the wavelength for peak sensitivity for human eyes. Such screens are useful, especially for alignment of the microscope. In modern machines, the fluorescent screen is removed entirely and instead users rely on Charge Coupled Device (CCD)-based solutions for image capture. In addition many older microscopes have been retrofitted with a CCD camera to capture images. The use of electronic image capture has allowed TEM to evolve from dark rooms and wet photography into a modern technique which allows users to share images quickly on site (many users can observe the images on screens simultaneously) as well as externally (image distribution becomes very rapid). Images can be captured and analysed in real time and processing these takes considerably less time. There is an additional advantage which is the provision for microscopes to be operated remotely, further improving potential image quality. This isolates the microscope from external vibration or interference from control systems by placing the operator and associated systems in separate accommodation, remote from the TEM.

CCD-based cameras are fast becoming the norm for TEM image and diffraction pattern capture. CCDs are particularly advantageous over other modern imaging solutions (such as imaging plates) because of low noise characteristics (typically a few electrons per pixel [504]) and rapid image capture. They consist of an array of several million pixels — each pixel behaving like an electrically isolated capacitor — which accumulates charge in proportion to the irradiation intensity. Each pixel is typically subdivided into gates, which collect charge in individual potential wells until the end of the exposure, and it is collected by varying the voltage across the gates allowing the collected charge to flow towards an output amplifier and onwards to be displayed on a computer screen.

3.3.2.8 Considerations when using TEM

The strengths of TEM are apparent. However there are some areas which require some consideration when utilising this technique. These are usually classified into four areas, which are discussed below.

There is a need to have thin specimens (how thin depends on the electron energy, density of the specimen, elemental composition and technique used). In many cases, this means samples must be less than 100 nm in thickness. In order to create usable specimens of the material of interest, a variety of mechanical, chemical, electrochemical or ion beam thinning techniques are utilised.

There are some materials which are difficult to make into TEM samples. These may be hard or particularly fragile materials. Creating samples of materials which are difficult to image such as those with magnetic properties may also be a challenge when using TEM. Having created a sample, the next consideration is to limit the damage caused by electrons. If this is unavoidable, the user should be aware of the effect and take this into account when interpreting the images that are captured.

One clear consideration to TEM is the small volume of material which can be sampled during a given session. The high resolution nature of the technique and thickness of each specimen means a very small amount of material is observed from each sample. It may, therefore, be essential that users understand and interpret data from other techniques so as to form a full(er) understanding of the results, depending on what information is desired.

Interpretation of images in projection is something which needs careful consideration by TEM operators. When we capture an image, the 3-D specimen is captured in a 2-D image. This has the effect that every defect spread through the thickness of the sample appears in same plane of the image. It may be possible to tilt the sample or perform an advanced technique to establish the precise seperation between features and thus to gain a better understanding of the specimen.

3.3.3 Techniques

TEM is an extremely useful tool for the investigation of materials in a variety of contexts.

This section details some of the techniques that the microscope is used for and how these can be applied within a material context.

3.3.3.1 Diffraction

Diffraction patterns are formed by setting the lenses so that the back focal plane of the objective lens is used as the object plane in the intermediate lens (see figure 3.12 for position of the lenses in the microscope and ray diagram). If diffraction information is required from only a specific part of the specimen, then the appropriate part of the specimen can be chosen using the selected-area aperture. This technique is often called Selected Area Diffraction (SAD). Alternatively Nanobeam Diffraction (NBD) can be used to focus a very narrow beam onto a small area of the sample using the condenser lens.

3.3.3.2 Imaging

The second basic operating mode is imaging mode whereby the image that forms in the imaging plane of the objective lens is magnified by the intermediate lens. Predominantly TEM is performed in one of two modes — 'bright-field' and 'dark-field' — depending on the information desired. The main principles of these modes are detailed below.

3.3.3.2.1 Bright-Field Imaging

The majority of the work performed in this project involved capturing images in conditions known as 'bright-field'. This is achieved through the use of the objective aperture which is used to select only the central diffraction spot (i.e. the undiffracted beam).

3.3.3.2.2 Dark-Field Imaging

Dark-field imaging uses one of the beams of diffracted electrons in order to form the image. This allows users to gain insight into crystallographic direction dependent features within the specimen but often results in a darker image. (Due to the exclusion of much of the electron beam intensity by the objective diaphragm.) In order to minimise astigmatism and abberations within the microscope the beam is tilted above the specimen (see figure 3.19) to allow it to continue down the optical axis of the microscope, as well as ensuring the correct part of the beam passes through the aperture. Figure 3.20 shows an example of how this technique works.

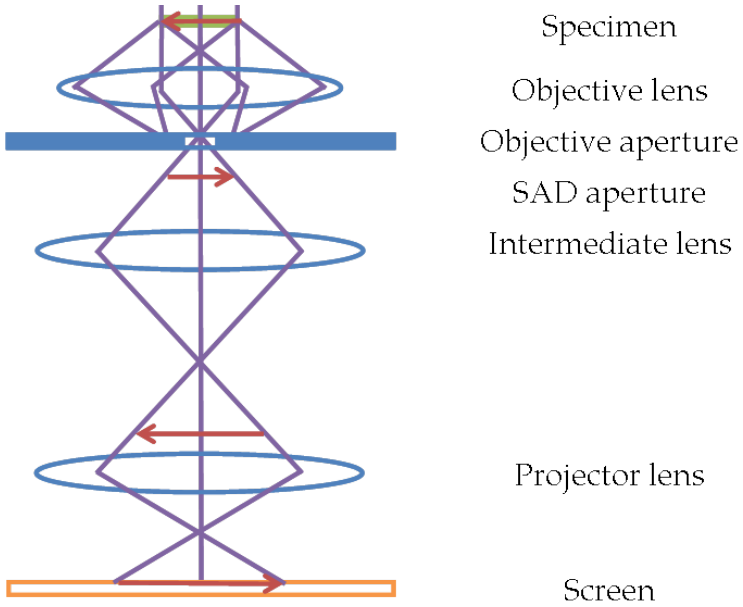

Figure 3.18: Schematic diagram illustrating bright-field. The objective diaphragm excludes all but the undiffracted beam to produce the image.

3.3.3.2.3 Down-Zone

Down-zone conditions involve aligning the sample such that one low-index crystallographic direction is aligned parallel to the electron beam. The sample will then satisfy the Bragg conditions and give a uniformly dark image in bright-field. The structure factor equation (see equation 3.2) defines which diffraction spots will be available while in down-zone conditions. Additional spots may be visible due to double diffraction.

3.3.3.3 Contrast Mechanisms

Imaging within the microscope relies on electron interaction with the specimen. Contrast is generated when different regions cause particular electron behaviours as a result of different material properties within these areas of the sample. This section discusses the three principal contrast mechanisms observed during imaging within this work.

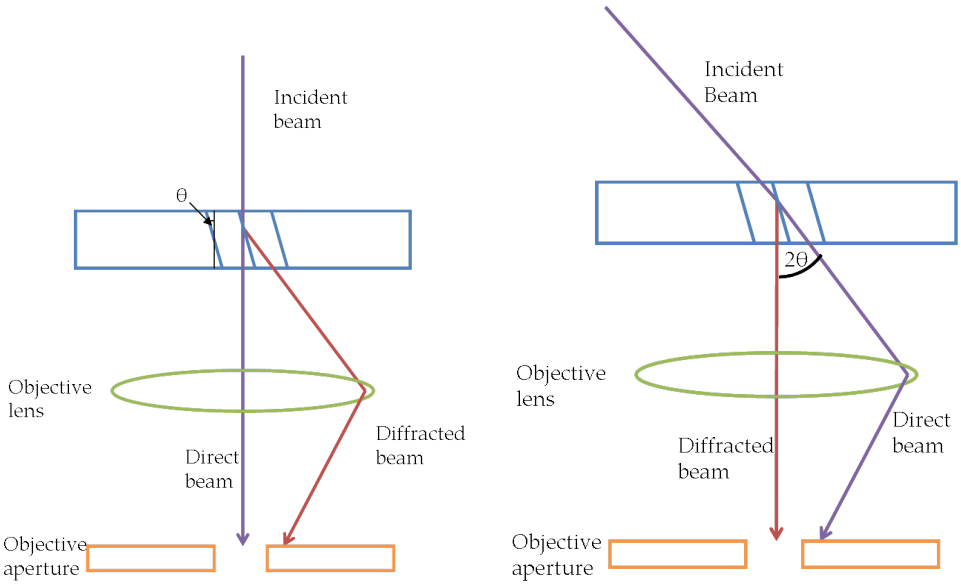

(a) Bright-field **(b)** Dark-field

Figure 3.19: Schematic of the use of beam shift and tilt to switch from bright-field (a) to dark-field (b).

3.3.3.3.1 Diffraction Contrast

The bending of crystallographic planes causes a change of contrast of the image captured. In the vicinity of defects lattice strain can be significant as it incorporates the flaw into the lattice. Contrast is generated by the bending of planes into or out of Bragg conditions. This allows the imaging of defects below the resolution limit of TEM due to strain effects generated by small defects. Imaging strain-fields can be achieved by using Weak-Beam Dark-Field (WBDF) by orienting the sample so that the area of interest does not satisfy Bragg conditions. The effect of the defect on the surroundings can then be detected by observing electrons which are scattered by planes which are bent back into Bragg conditions over a short distance near to the defect.

3.3.3.3.2 Fresnel Contrast

Fresnel contrast is generated at any sharp interface between two regions of the specimen of different inner potential. The imaging of bubbles or holes that are enclosed within a specimen can be achieved by defocussing the image and observing the phase contrast generated by the bubble. This provides a useful contrast mechanism even when there is no strain field associated with a bubble. These can be imaged regardless of the content of the bubble, whether this is gas, liquid, solid or empty (a void). (If the material in the

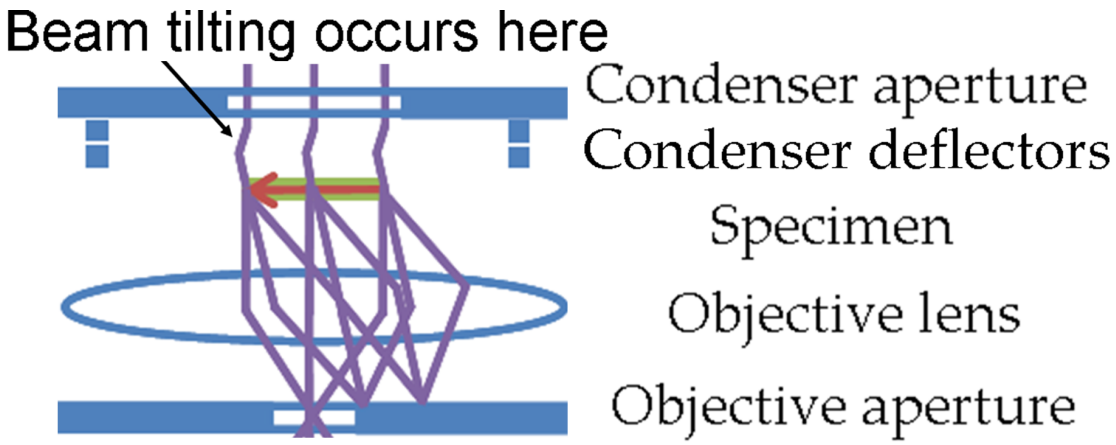

Figure 3.20: Figure showing ray diagram of dark-field. The beam is tilted by the condenser deflectors after leaving the condenser lens. This results in the direct beam hitting the diaphragm of the objective aperture and the diffracted beam passing through and forming an image.

bubble has the same inner potential as the substrate then there will be no contrast in the image caused by the bubble.) The image shows Fresnel contrast whenever the objective lens is not focused on the specimen (i.e. is in over- or under- focus conditions). This allows the imaging of cavities as small as 1 nm and generates a dark fringe in underfocus conditions and a bright fringe in overfocus conditions. The interior of the bubble or cavity depends on the relative inner potential of the bubble and the substrate. The contrast is generated due to the sharp interface between two areas. This generates Fresnel fringes due to the interference between the planar unscattered waves with the curved waves created during scattering from the sharp interface in the specimen. The wavelength of the electron means that these are below the resolution limit of the microscope until the image is placed over- or under-focus (by roughly 1000 nm) because the fringes in the focused image are too narrow to observe.

3.3.3.3.3 Mass-Thickness Contrast

Mass-thickness contrast occurs due to incoherent elastic scattering. This is strongly related to atomic number (Z), density (ρ) and thickness. Images formed by electrons scattered through angles of less than 5° are dominated

by mass-thickness contrast, often in combination with Bragg contrast. Mass-thickness contrast is particularly important for investigations into non-crystalline materials such as biological specimens. Almost all specimens show some evidence of mass-thickness contrast due to the difficulty in preparing specimens with a uniform thickness.

3.3.3.4 Spectrometry

3.3.3.4.1 Energy-Dispersive X-Ray Spectroscopy

Energy-Dispersive X-Ray Spectroscopy (EDS) is the observation of a secondary effect (partially discussed in section 3.3.1.2) caused by the ionisation of the samples within the TEM. The removal of a core electron from the specimen leaves an instability in the atom. As a result of this, an electron within the sample falls from a higher energy state into the vacant lower-energy state. In doing so it loses the equivalent energy difference between the levels and emits an X-ray which is characteristic of that element. Detection of these X-rays, and measurement of their energies and intensity allows quantitative elemental analysis to be performed. When coupled with Scanning Transmission Electron Microscopy (STEM) mode (rastering of a small electron beam across the surface of the specimen in perpendicular directions) elemental mapping may be performed to understand the distribution of an element throughout a sample.

EDS uses a lithium-doped silicon detector to absorb the incoming X-rays. This generates electron-hole pairs, the electrons have an energy characteristic of the X-ray (and thus the atom in the sample). A bias is applied to the detector to separate the electron and hole allowing detection of the electron energy, which are then analysed by a computer. The detectors are often separated from the TEM by a window which forms a vacuum seal, though windowless systems are now common. This is a necessity as the detector is kept at cryogenic temperatures (to reduce electrical noise and prevent lithium diffusion) and residual water in the microscope column would condense on the detector. The window material is chosen to be transparent to incoming X-rays and is usually constructed of beryllium or a similar material.

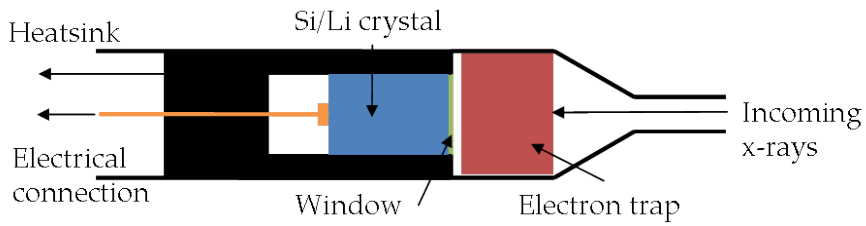

(a) Schematic for EDS system fitted to the column of a TEM including electron trap, window, detector and electrode and electrical connections.

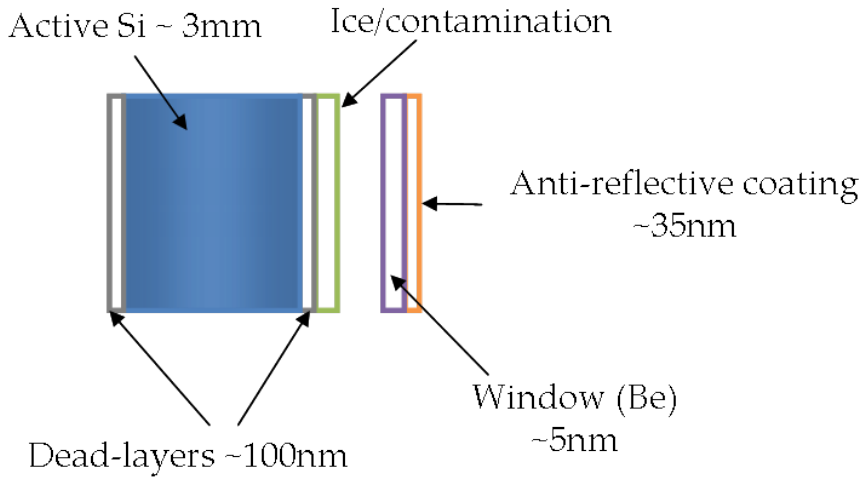

(b) Schematic for an EDS Lithium-doped Silicon detector including anti-reflective coating, window, ice layer and dead layers.

Figure 3.21: Schematic of an EDS detector (a) and the silicon detector in an EDS system (b). Based on [213]

3.3.3.4.2 Electron Energy Loss Spectroscopy

Electron Energy Loss Spectroscopy (EELS) is analysis of the energy of electrons which have passed through a specimen. Many of these electrons will have suffered no energy-loss at all. However, the small number that do will have lost an amount of energy which is characteristic of the element the electron has interacted with and its chemical bonding state. Other information, including specimen thickness, bandgap and free-electron density is readily available through analysis of appropriate signals. This technique can be used to form EFTEM images, which is where images are formed using only the electrons of a certain energy, this allows high resolution elemental mapping to be completed — not just on a single elemental scale — but also providing information on bonding.

To perform EFTEM or EELS, the electrons must be energy-dispersed and

detected. For EELS this dispersion is performed by a magnetic prism which is situated below the viewing screen in the microscope. Many EFTEM systems perform the dispersion using a filter within the column of the microscope. This prism brings electrons with the same energy to the same position on the detector regardless of where they enter the magnetic prism. The electron beam and the detector must be aligned prior to each use because the EELS lens has similar aberration and astigmatic characteristics as the lenses within the microscope. Aberration and astigmatism should be minimised for optimal spectrometer performance.

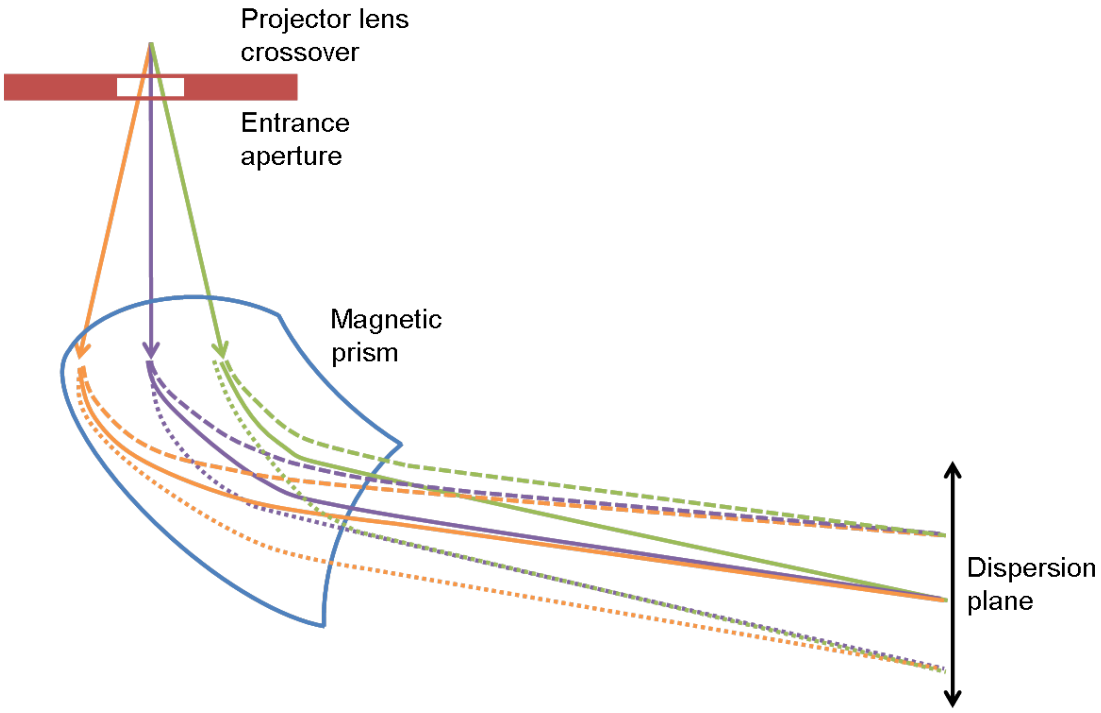

Figure 3.22: Schematic for magnetic prism EELS system fitted below the viewing screen of a TEM. Shown are the entrance aperture, as well as energy selection of the electrons (dotted, solid and dashed lines indicate equivalent energies) despite the electrons entering the prism at different location. Based on [213].

EELS and EDS perform similar but different roles. EELS is capable of analysis of bonding states and plasmons. It is possible to perform elemental analysis to a better spatial resolution when using EELS and EFTEM. Sensitivity to lighter elements is better when using EELS, though when comparing two adjacent elements in the periodic table EDS is a superior technique.

3.3.4 Application

TEM was carried out at the MIAMI facility (at the University of Salford and the University of Huddersfield) on a JEOL JEM-2000FX microscope operated at 200 keV using a thermionic tungsten filament. In addition a JEOL JEM-3010 using a LaB_6 thermionic filament operating at 300 keV was used for post-irradiation analysis for many samples. At JANNuS we utilised a Technai G^2 operating at 80 keV and 200 keV. This instrument also uses a LaB_6 filament. On all three microscopes, images and continuous video was captured using a CCD. The CCDs had been previously calibrated in order to provide an accurate scale on the images.

3.4 Ion-Beam Irradiation

3.4.1 In-Situ

The majority of irradiation carried out during this project was performed *in-situ* in the TEM. The advantages of using this technique are detailed in section 2.4.5. The following sections discuss the facilities used. These were the MIAMI facility at the University of Huddersfield and the JANNuS facility at CSNSM, Orsay, Paris.

3.4.1.1 MIAMI Facility at University of Huddersfield

The MIAMI facility at the University of Huddersfield is a purpose-built ion accelerator which works in combination with a TEM in order to perform *in-situ* ion-irradiation within the TEM. The design and construction of the facility was performed in-house at the University of Salford under funding from the Engineering and Physical Sciences Research Council (EPSRC). In 2011 the entire facility, as well as support equipment, transferred to the University of Huddersfield. Details of the facility have been provided by Hinks *et al* [250]. This section will cover the design of the equipment as well as the operating principles. The system consists of a JEOL JEM-2000FX microscope in combination with an ion beam system which is based around a Colutron model G-2 ion gun system. It is capable of applying an accelerating voltage of between 2 kV and 100 kV to ion beams consisting of most elements. The angle between ion and electron beams was initially 25°, latterly 30°. The setup of the

orientations and trajectories around the sample position is illustrated in figure 3.24.

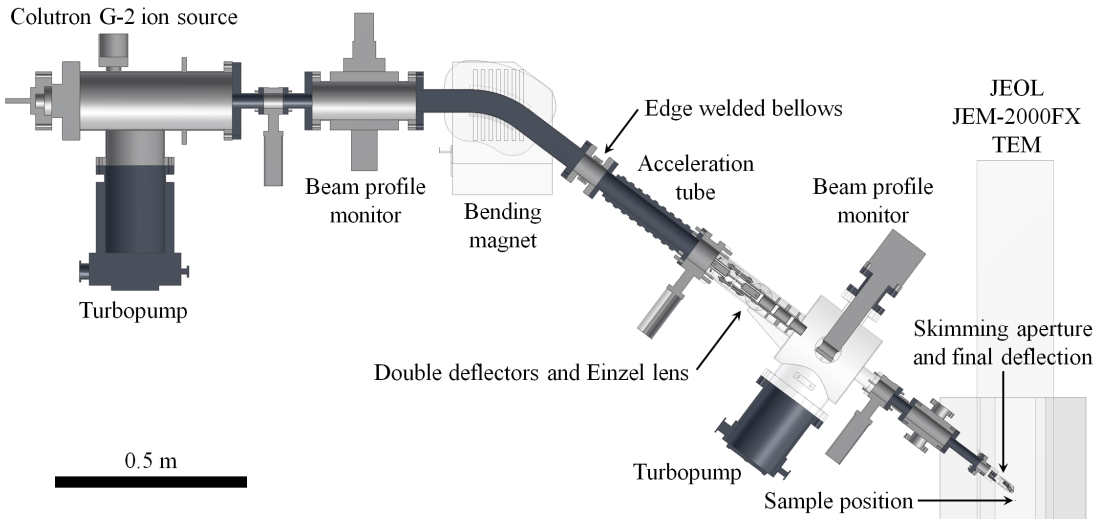

Figure 3.23: CAD image showing beamline from ion source to sample position in the MIAMI facility. Taken from [505].

3.4.1.1.1 Ion Source

The Colutron ion source system generates ion beams by ionising a gas. Ionisation occurs by bombardment from electrons generated by a tungsten filament heated electrically by applying between 12 and 15 V (giving currents of between 14 and 18 A). Electrons are extracted using an anode which has a voltage of between 100 and 125 V (current limited to 0.20 A) with respect to the filament. Ions are extracted from the source by applying a voltage of up to 10 kV which provides an initial acceleration down the beamline. Ions can then be accelerated to higher energies by floating the entire gun assembly and associated equipment to higher voltages. The ions are then accelerated in steps as they pass down the acceleration lens (see figure 3.23).

The ionising chamber and gas inlet tube are constructed from quartz (SiO_2). The filament and anode are made of tungsten. The ionising chamber is capped at both ends by boron nitride components which holds the source together and encourages heat flow from the chamber to the heat sink. The remaining components are constructed from stainless steel and molybdenum.

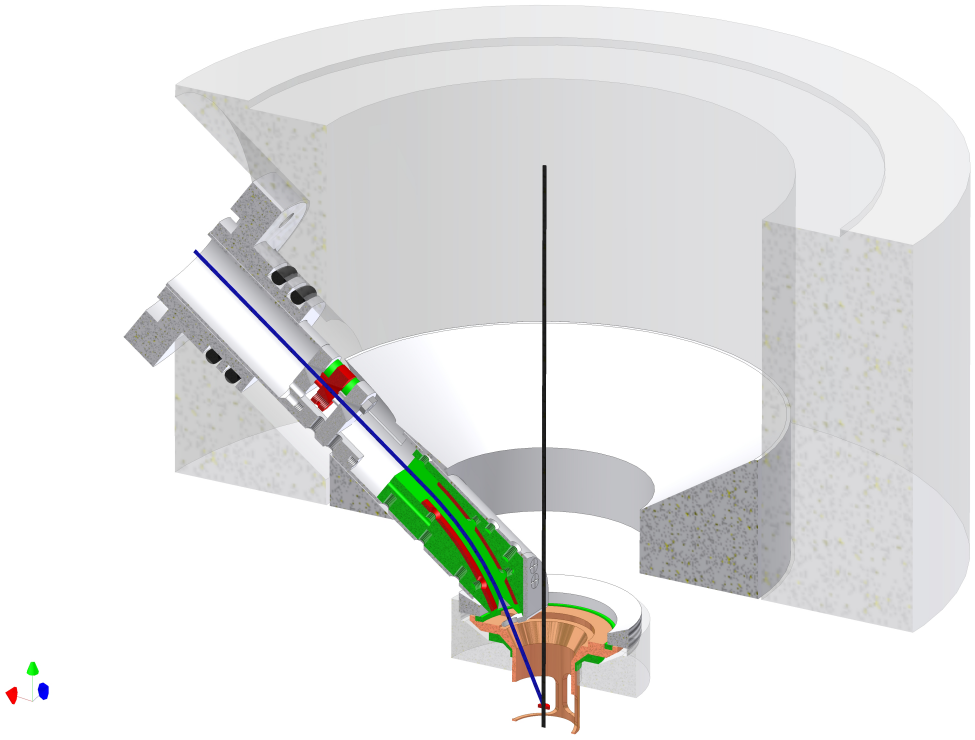

Figure 3.24: Sample position geometry in the MIAMI facility. Ion beam path, final deflection plates and electron beams are shown. The electron beam, ion beam and sample position all intersect towards the bottom of the image. Taken from [247].

3.4.1.1.2 Focusing Elements

There are two lenses in the MIAMI facility for the purpose of focusing the ion beam. One focusing element is installed immediately following the ion source assembly and a second is located in the beamline section before the second Rotating Beam Profile Monitor (RBPM). The focus at the ion source is provided as part of the Colutron G-2 components, the second is designed and built in-house although they both operate using the same principle. It should be noted that many of the other components in the beamline will have a slight focusing effect on the ion beam. The ion beam will be slightly off-centre in each component and the part of the ion beam away from the centre will be deflected towards the zero potential line in these components. However, their primary function is to shift, tilt or modify the ion beam, their secondary effects are of minor consequence.

The focusing elements are based on a design known as an Einzel lens; this comprises three metal cylinders situated sequentially along the beamline. The

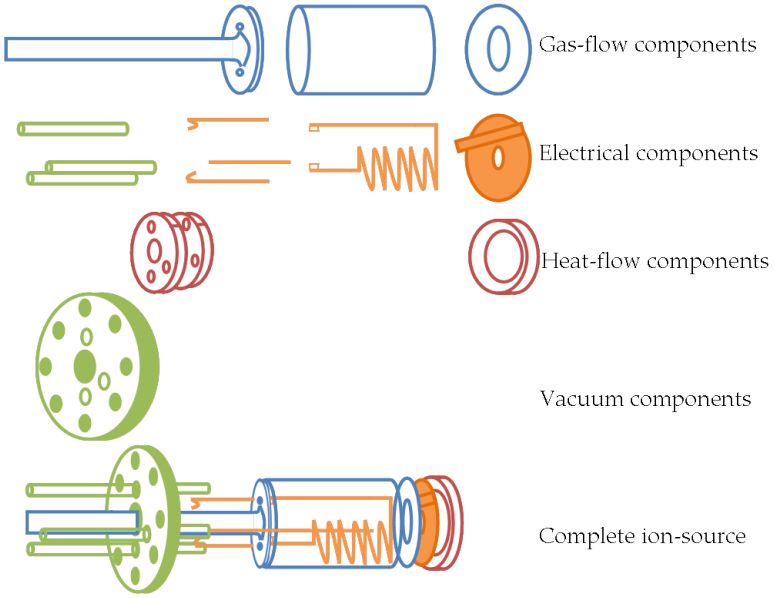

Figure 3.25: Schematic diagram showing expanded ion source components including quartz components for gas containment, tungsten elements for electrical feedthrough and thermal stability, boron nitride cap and base for thermal efficiency and stainless steel vacuum components and electrical feedthrough to the power supply.

first and last of these are electrically connected to earth, while the middle plate is raised to a high positive voltage. The outcome of this is a significant electric field generated between the middle plate and each of the other plates in the lens. As the ion beam passes into the first electric field it deviates away from the middle of the cylinder. Passing the second electric field — the effect is reversed — the beam converges towards the centre and then leaves the electric field. The Einzel lens can be used to focus or spread the beam.

3.4.1.1.3 Beam Profiling

Beam profiling is provided by two National Electrostatics Corp. rotating beam profilers (RBPM) which give information about the ion beam profile as it leaves the source and again in the beamline (see Figure 3.23). The RBPM consists of a helical wire which rotates at 1080 RPM. As the wire rotates, it sweeps through the beam twice in each rotation, once in each of two orthogonal directions. As the wire passes through the ion beam, it generates secondary electrons which can then be detected in order to gain information about the shape and intensity of the ion beam. The intensity of the (secondary) electrons is displayed on an

oscilloscope. Observing the secondary electron intensity on the oscilloscope is a useful tool during alignment of the ion beam.

3.4.1.1.4 Ion Selection

Ion selection is performed as the beamline curves from the horizontal section into the angled section which allows it to enter the microscope (see figure 3.23). This is performed using an electromagnet, the current of which is varied by the user, and is selected by mass and charge in line with equation 3.5. The magnet itself is a very simple concept, it provides a region of uniform magnetic field in a direction perpendicular to the path of the ions. This causes the ions to follow a circular trajectory, the radius, r, of which is given by:

$$r = \frac{m\,v}{q\,B} \tag{3.5}$$

Where the radius of the curved path of the ions, r, is dependent on the ion's mass, m, its velocity, v, (dependent on its energy), the ion charge, q, and the magnetic field, B. From this, it can be shown that ions of a different mass or of a different charge (1+, 2+ etc.) will be curved through a different path, and thus the magnet allows the user to select the appropriate element and charge for the ion beam. Both mass and energy selection takes place as the ion beam passes through the magnet.

3.4.1.1.5 Double Deflection System

Two pairs of parallel plates are situated between the acceleration tube and the Einzel lens. This allows the beam to be deflected in perpendicular directions for alignment. This is particularly useful for correcting the trajectory of the ion beam between acceleration and focussing by the Einzel lens. There is an additional set of plates (four more plates, eight in total) installed in the beamline to facilitate a shift of the ion beam (rather than a tilt) but it has not been neccessary to use these to date. The ions are deflected in the electric field applied between the two plates, given by equation 3.6:

$$F = qE$$

$$\text{Where, } E = \frac{V_{plates}}{d} \tag{3.6}$$

3.4.1.1.6 Final Deflection

The port chosen to introduce the ion beam to the microscope is the high-takeoff angle EDS port because it allows a small angle between the ion and electron beams. There is no direct line of sight between the port and the sample position which necessitates further deflection within the microscope. This is performed electrostatically using two pairs of plates to deflect the ions in a curved path (obeying equation 3.7 which allows it to reach the sample position). This further reduces the angle between the two beams to 30°. It is worth noting that the path of the ions passing through the final deflection (specifically the vertical component) is determined by their energy and not by mass. Mass selection occurs earlier in the magnet (see section 3.4.1.1.4). The force applied (F) to the ions in the final deflection system is given by:

$$F = \frac{mv^2}{r} = \frac{V_{plates}}{d}q$$

$$\therefore V_{plates} = \frac{dmv^2}{rq}$$

Energy of the ions is given by:

$$E = \frac{mv^2}{2} = qV_{acc}$$

$$v^2 = \frac{2qV_{acc}}{m}$$

Combining equations for force and energy (above):

$$\therefore V_{plates} = \frac{2dV_{acc}}{r} \tag{3.7}$$

3.4.1.1.7 Ion Detection Elements

The MIAMI facility uses a variety of ion current measuring devices in order to gather accurate dosimetry data. The intrinsic difficulty of dosimetry measurements at the sample position is discussed in section 2.4.5. To combat this three ion detection elements have been utilised. Prior to undertaking each experiment an in-house built TEM rod with current measuring abilities has been used at the sample position in order to align the beam to the correct position and intensity. We also use this for dosimetry calculations and monitoring of beam stability. The nature of this device, being at the sample position, means that it cannot be used once the sample is loaded into microscope. The rod is aligned so as to be central in the electron beam prior to each experiment, and the entrance aperture of the rod is designed to be coincident with the sample position. The rod consists of the entrance aperture, followed by a larger secondary aperture which is held at -30 V to provide suppression of secondary electrons. Below the two apertures, a collector plate measures the incoming ion current.

To provide constant monitoring of the ion beam during irradiation steps, a 1.0 mm skimming diaphragm measures the ion current between the second RBPM and the final deflection plates. This system is designed to align the ion beam so as to enter the final deflection close to the zero potential line. This avoids unwanted focusing effects during final deflection but also measures the ions falling onto the diaphragm of the aperture. Ions passing through the aperture continue to the sample position. The skimmer is useful for approximate alignment of the ion beam and provides an indication of flux. In terms of providing dosimetry information this device must be calibrated against another current measuring component.

A third current measuring device has been introduced to provide a measurement which is both close to the sample position (i.e. after the final deflection plates) and able to measure with a sample *in-situ*. A TEM finder grid has been used to position a Faraday cup stalk in the electron beam

reproducibly. The geometry of the positioning is such that the Faraday cup at the end of the stalk is positioned within the ion beam along the trajectory of the ions as they leave the final deflection plates and prior to their striking the sample. This current measurement is unsuppressed (for secondary electron capture) and as a result current readings are higher.

3.4.1.2 JANNuS Facility at CSNSM, Orsay, Paris

The JANNuS facilities [249, 506, 507] at Saclay and Orsay in Paris consist of a triple ion beam system (at Saclay) and a dual ion beam system (at Orsay). The facility at Orsay has the possibility of performing *in-situ* ion-irradiation and TEM. The facility comprises two accelerators, a sample chamber for *ex-situ* irradiation and a Technai G^2 TEM with capabilities for irradiation together with EELS and EDS capabilities. The primary accelerator used in combination with the TEM is a 2 MV van de Graaff (named Aramis) operating in tandem mode. In tandem mode negative ions are sputtered from a solid target. The ions are accelerated to 150 keV. In the centre of the accelerator a nitrogen stripper removes electrons, effectively reversing and multiplying the charge on the ion. Tandem mode is so called because the accelerating voltage is used twice to accelerate the ion. It is capable of producing ion beams of many elements [247] at energies of between 400 keV and 15 MeV. The secondary accelerator (named IRMA) is a Nier-Bernas positive ion source which can generate ions of almost every element. These can be accelerated to energies of between 5 keV and 190 keV (for single charged ions). The angle between the ion and electron beams is 68°.

Unlike the MIAMI facility, direct line of sight is possible from the entry port on the microscope to the sample position. This obviates the need for in-column deflection of the ion beam (see section 3.4.1.1.6). Dosimetry at JANNuS is performed by deflecting the beam onto a Faraday cup several times a second, on which ion beam current is measured. This system means that there is also no requirement for measuring the ion beam current anywhere else within the column, as is the operating procedure at the MIAMI facility.

3.4.2 Ex-Situ

Ex-situ irradiation was performed at Institut Pprime at Université de Poitiers where bulk samples were irradiated using an Eaton NV 3206 ion implanter

which is capable of generating ions of between 20 keV and 200 keV. For our specimens, 160 keV helium ions were implanted in SiC at 400°C to a final fluence of 5 $\times 10^{16}$ ions.cm^{-2}. Post-irradiation anneals were performed at 1400°C for 15 minutes in an argon atmosphere. XTEM samples were subsequently prepared for TEM using the method described in section 3.2.4.

3.4.3 Computer Simulations

3.4.3.1 SRIM

The range of ions in matter and the level of damage created were estimated using SRIM software [158] versions 2008.04 and update 2010. This is a Monte Carlo code which simulates discrete collisions between the ion and atoms within the target. The collisions are statistically weighted both in terms of frequency and collision mechanics based upon stoichiometry of the target material, the density of the material and the scattering cross-section of the target atoms. Between each collision the ion is considered to have taken a straight path. Each ion is followed as it collides with each atom — losing a discrete amount of energy with each collision — in addition to a continuous loss due to electronic stopping. One ion is followed until it falls below the atomic displacement energy threshold at which point it is considered to have stopped, ions are no longer considered when they leave the target. The code then considers each collision within the target and considers each PKA until all the atoms have slowed below the threshold energy. This method allows the simulation of subsequent ion-impacts to generate statistical information about how the species, energy and target material properties combine to provide information about damage formation and ion ranges. SRIM results are presented in sections 4.2.1, 5.2.1 and 5.4.

3.4.3.2 PENELOPE

Penetration and Energy Loss of Positrons and Electrons (PENELOPE) is a Monte Carlo code which simulates the interaction between electrons and materials over the energy range of a few hundred eV up to 1 GeV. Electron interactions with matter cause very small energy losses per interaction event. As a result they travel for long distances into materials and suffer a large number of interactions before being absorbed. The developers of the

PENELOPE code claim that detailed simulations are possible so long as the number of interactions does not exceed a few hundred [508]. The code works in a very similar manner to SRIM, in that individual electrons are simulated until they leave the target or fall below a threshold energy, at which point they are considered to be absorbed. Binary interactions with the atoms in the target are modelled with both elastic and inelastic processes considered. These are statistically weighted by the scattering cross-section of the target atom. The program allows the generation of data such as energy deposition in the target, angle of scattering for electrons leaving the target and range of electrons in a material. Information about the usage of PENELOPE in this project can be found in section 5.4.2.

3.5 Image Analysis

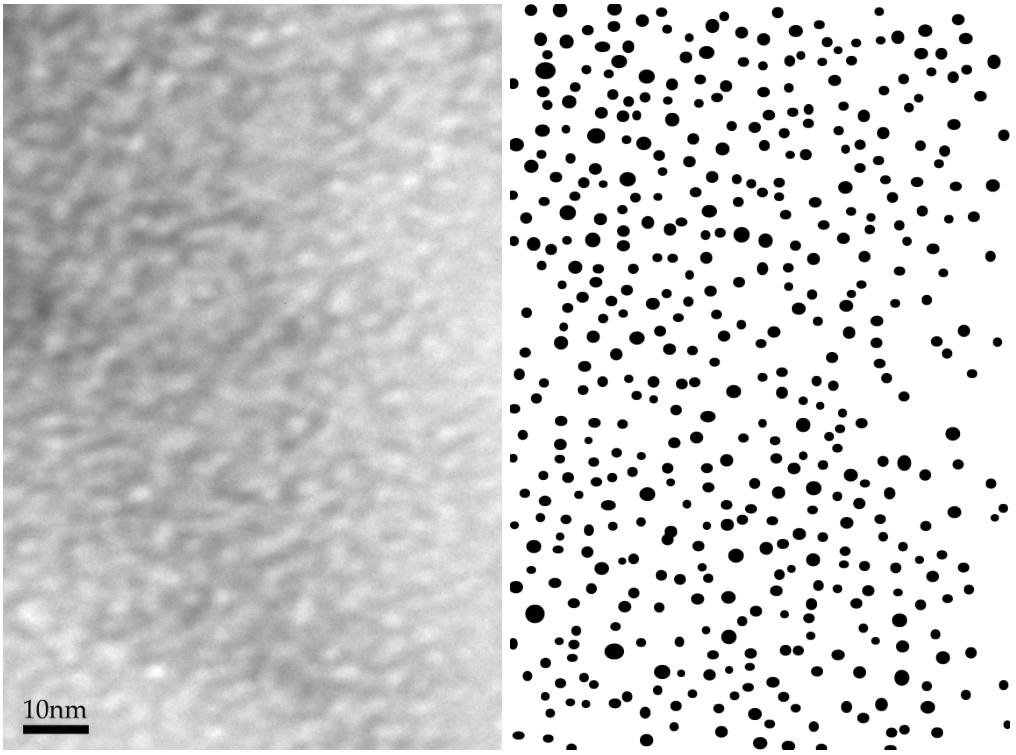

(a) TEM Micrograph **(b)** Photoshop map/Scion Image input

Figure 3.26: Figures to show cropped TEM micrograph and a corresponding Photoshop map of the bubbles for the calculation of mean bubble size. Image shows bubble morphology following an irradiation to 6.26×10^{16} ions/cm^2. Scale bar applies to both panels.

Images collected during these experiments were processed and analysed

digitally. The images were cropped and grey levels were adjusted slightly to optimise contrast for image analysis. In Adobe Photoshop, transparent layers were placed over the images and each bubble was circled. This created a map of the position and size of each bubble. The map was then processed using the Scion Image program which analyses particle sizes using contrast in the map. Figure 3.26 shows an example of a micrograph and its map for mean bubble size calculations. This statistical information was then used to draw conclusions about bubble growth behaviour within the specimen. From the statistical information, several quantities can be determined (these are detailed further in chapter 4). These quantities are then graphed against ion fluence and a line of best fit is added (least squares method) to aid in identification of the relationship between the statistical information and ion fluence. The standard error is calculated for each data point, which is added to the graph as an error bar in the y-axis. The standard error is selected because it is an appropriate representation of the error on the measurements, taking into account the number of bubbles in each image.

For SiC, a linear relationship has been reported between ion fluence and bubble diameter [392], ion fluence and volume occupied by bubbles [392] and between implanted helium and retained helium [509]. A linear relationship is also reported between ion fluence and volume occupied by bubbles in iron [510]. From the information available in the literature review on helium diffusion (see section 2.6.3), we anticipate that the diffusion of helium into bubbles will be low in our experiments. This means that there will be a limited amount of bubble size variation due to diffusion; bubble size variation is more likely to be as a result of incident irradiation. There are some results of high-energy heavy-ion irradiation causing linear decreases in bubble size reported for helium bubbles in aluminium [511, 512]. For these reasons, a linear fit is chosen to be the most appropriate. In some cases, no trend is evident from this fitting, though the best-fit lines have been included on the graphs to demonstrate to the reader where the linear line of best fit lies relative to the data.

Chapter 4

In-situ Analysis of Helium Bubble Nucleation and Growth at the MIAMI Facility

4.1 Introduction

Samples of SiC at 700°C (which avoids amorphisation and simulates conditions similar to those found in proposed Generation IV reactors) were irradiated by 3.5 keV helium ions. Under these conditions, bubbles were observed to form within the samples using TEM. The nucleation and growth of helium bubbles were observed while performing *in-situ* ion-irradiation at the MIAMI facility as described in section 3.4.1.1. It is technologically important to understand these processes due to the expected conditions for nuclear applications of SiC. Helium bubble growth mechanisms will provide information on the behaviour of SiC during helium build up from transmutation reactions (see table 4.1) as well as under alpha particle irradiation.

Product	Transmutation Reaction
Be, He	^{12}C (n,α) ^{9}Be
Mg, He	^{28}Si(n,α) ^{25}Mg , ^{29}Si(n,α) ^{26}Mg
Al	^{28}Si(n,2n) ^{27}Si$\rightarrow$ ^{27}Al
P	^{30}Si(n,γ) ^{31}Si$\rightarrow$ ^{31}P + β

Table 4.1: The most common transmutation reactions in SiC [513].

4.2 Irradiation Conditions

Samples of SiC were prepared by a combination of the tripod and PIPS methods detailed in section 3.2. The experiments were performed at 700°C with samples heated in a Gatan double-tilting heating holder. Samples were irradiated with 3.5 keV helium ions with a flux of $\approx 2.7\times10^{13}$ ions.cm^{-2}.s^{-1}. Samples were irradiated to final fluences of between 8×10^{16} and 10^{17} ions.cm^{-2}. All samples irradiated under these conditions were observed to contain helium bubbles.

4.2.1 Simulation of Irradiation Conducted

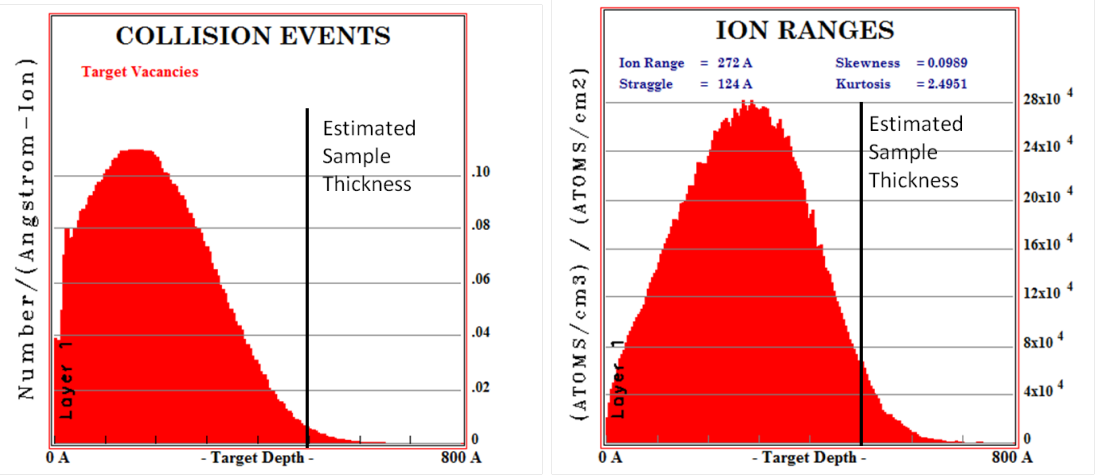

(a) Vacancies produced **(b)** Helium ion range

Figure 4.1: Graphs output from SRIM showing the predicted damage creation and helium ion range in SiC as a result of 3.5 keV helium ion-irradiation at an incident angle of 25° to the surface

Computer simulations were conducted in order to establish the appropriate parameters for implantation into SiC. Version 2003 update 2010 of the SRIM software was used (more details on the SRIM software can be found in section 3.4.3).

Figure 4.1 shows two histograms from the SRIM software for 3.5 keV helium ion implantation into SiC. The energy has been chosen to position the R_P (the midpoint of the ion range) close to the expected middle of the sample. The sample thickness is estimated as 500 Å thick following measurements on the thickness of silicon specimens prepared in a similar fashion [514].

4.3 Experimental Results

Figure 4.2 shows some of the TEM micrographs captured during the irradiation conditions described in section 4.2. The edge of the sample is visible in the bottom right hand corner in each image. Bubbles are clearly visible in each image taken following irradiation above 1.7×10^{16} ions.cm^{-2}.

4.3.1 Observation of Helium Bubbles in SiC

In the experiments conducted utilising the irradiation conditions detailed above (in section 4.2), small bubbles are observed at low fluences throughout the sample. More specifically, this occurred following irradiation to 6.4×10^{15} ions.cm^{-2}. Below this fluence, bubbles are not visible due to the lack of Fresnel contrast generated by bubbles when they are small or do not exist within the specimen. Fresnel contrast relies on a significant difference in inner potential between the substrate and the bubble, when the bubble is small, the contrast created by the bubble is not observable against the surrounding SiC [515]. A limitation in the observation of bubbles by TEM is that the presence of bubbles in the specimen may obscure the part of the sample underneath the bubble. This can result in undercounting of bubbles in the sample because additional bubbles are hidden from view. The extent to which bubble overlap affects the measurements is discussed and quantified in section 6.5.

Bubbles are first observed at a radius of about 0.5 nm. Figures 4.2a and 4.2b show the low fluence bubble morphology in SiC. We expect that the bubbles are at equilibrium pressure due to the high flux of vacancies and helium atoms in the vicinity of each bubble [201, 516]. If a bubble were in either an over- or under-pressurised state, then it would be able to readily absorb either helium atoms or vacancies to enable it to return to equilibrium pressure. Equilibrium conditions for bubbles in solids, are where the pressure of the bubble matches the surface tension of the surrounding lattice. Under these conditions the pressure (P) of a spherical cavity in a solid material is given by equation 4.1:

$$P = \frac{2\gamma}{r} \tag{4.1}$$

Where γ is the surface tension in N.m^{-1} and r is the radius in m.

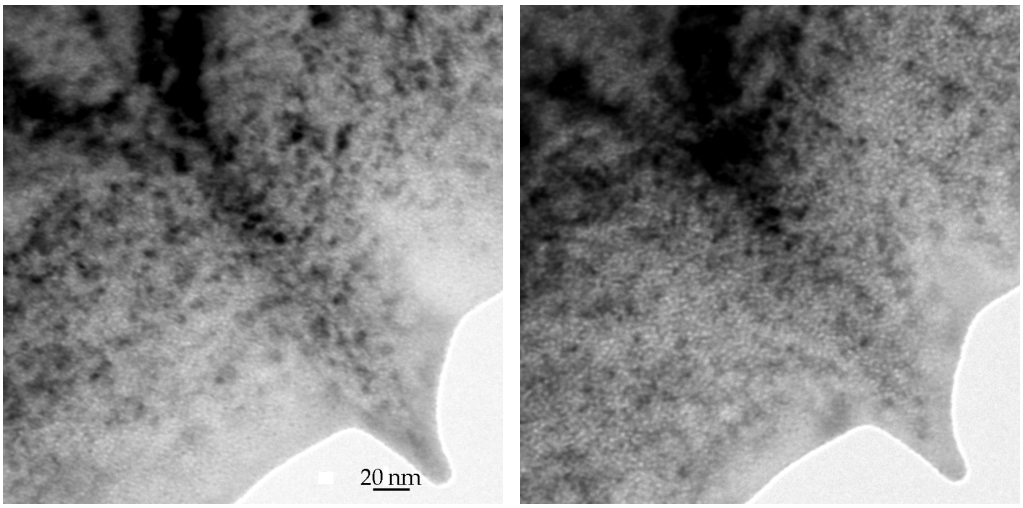

(a) 1.1×10^{16} ions.cm^{-2} **(b)** 1.7×10^{16} ions.cm^{-2}

(c) 2.3×10^{16} ions.cm^{-2} **(d)** 2.8×10^{16} ions.cm^{-2}

Figure 4.2: Bubble development during helium ion-irradiation into SiC. Scale bar in the first image applies to all panels.

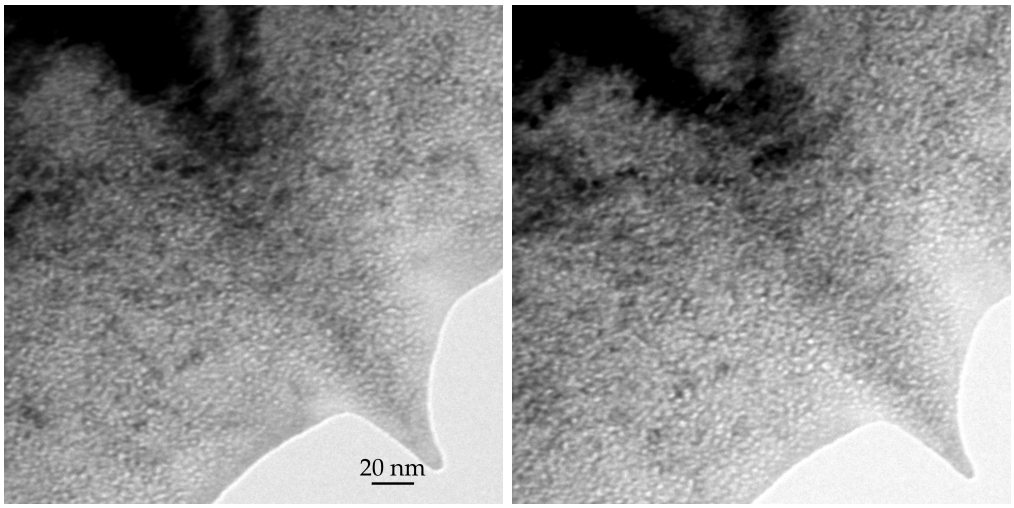

(e) 4.3×10^{16} ions.cm^{-2} **(f)** 6.3×10^{16} ions.cm^{-2}

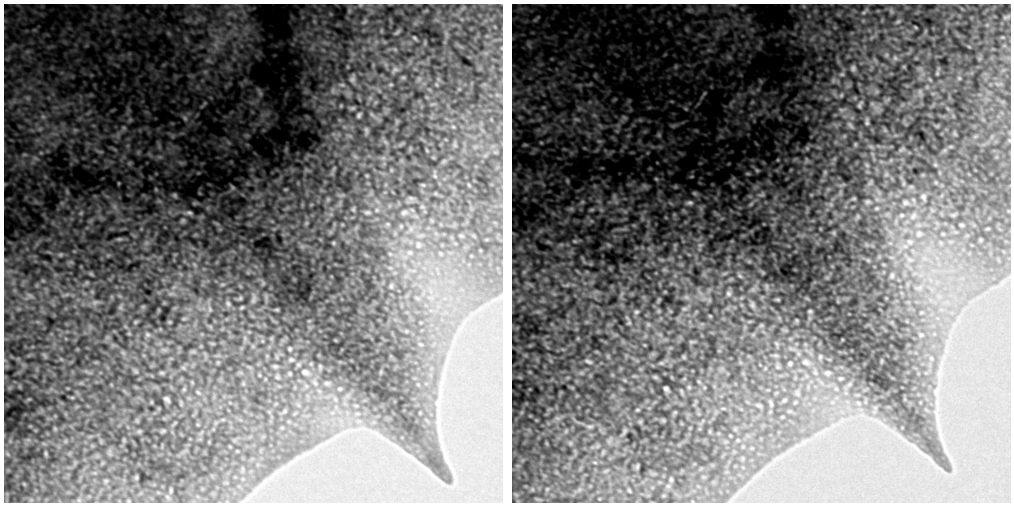

(g) 7.5×10^{16} ions.cm^{-2} **(h)** 9.5×10^{16} ions.cm^{-2}

Figure 4.2: (continued) Bubble development during helium ion-irradiation into SiC. Scale bar in the first image applies to all panels.

4.3.2 Bubble Motion in SiC

During ion-irradiation by helium in the *in-situ* experiments in SiC, there was no observation of significant bubble motion between irradiation steps. This leads to the conclusion that once visible in the TEM, bubbles in SiC are fixed in position. The diffusion of helium bubbles during annealing at 700°C and during these ion-irradiation conditions is found to be negligible.

4.3.3 Size Distribution of Helium Bubbles in SiC

To demonstrate changes within the sample during irradiation the bubble size distribution can be calculated from the measurements taken of each image. This gives a measure of the distribution of sizes within the sample and allows us to draw additional conclusions about bubble growth behaviour. Figure 4.3 shows the evolution of the bubble size distribution with the difference in the distributions due to increasing ion fluence. Bubble size distribution histograms were created by binning the bubble size data using bins of 0.2 nm wide with a maximum radius of 2 nm. The frequency for each graph is normalised to the total number of bubbles in each distribution in order to present the data in a manner which allows graphs to be compared directly.

All of the histograms have an approximately Gaussian-shaped distribution which becomes broader with increasing fluence. This is to be expected as increased helium ion-irradiation is observed to cause both a growth of existing bubbles and the nucleation of new helium bubbles in SiC [207]. At low fluences (TEM micrographs shown in figures 4.2a and 4.2b and distribution shown in figures 4.3a and 4.3b) almost all of the bubbles are <1 nm in radius. At higher fluences a sizable number of bubbles remain below 1 nm in size with the peak of the bubble size distribution remaining below 1 nm in all of the measured distributions. The proportion of bubbles at the smallest sizes rapidly reduces with increasing fluence. The maximum bubble size increases as more helium is implanted in the sample. A graph of maximum bubble size with increasing fluence is shown in figure 4.4. This appears to increase nearly linearly throughout the experiments. A more comprehensive statistical analysis (such as skewness or kurtosis) has not been completed on these results as the error associated with bubble size measurements is not negligible (on the order of $\approx 10\%$). As well as this, there are relatively few bubbles at the larger sizes.

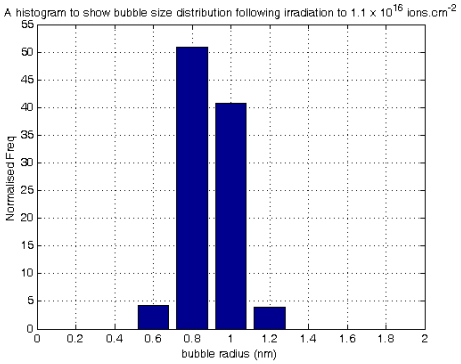

(a) 1.1×10^{16} ions.cm^{-2}. See figure 4.2a.

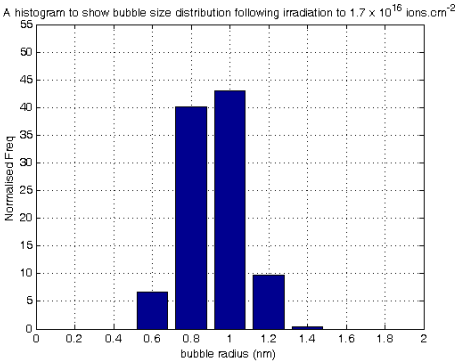

(b) 1.7×10^{16} ions.cm^{-2}. See figure 4.2b.

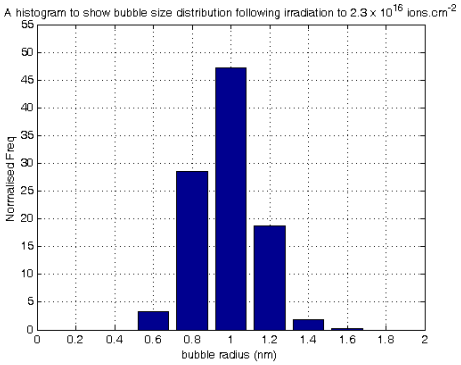

(c) 2.3×10^{16} ions.cm^{-2}. See figure 4.2c.

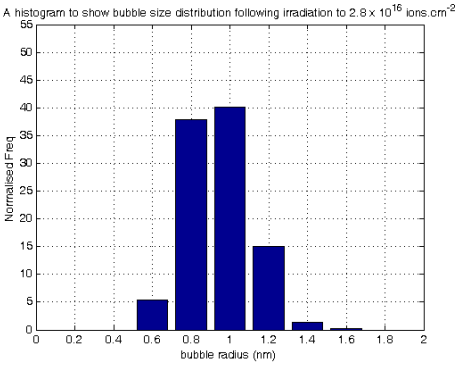

(d) 2.8×10^{16} ions.cm^{-2}. See figure 4.2d.

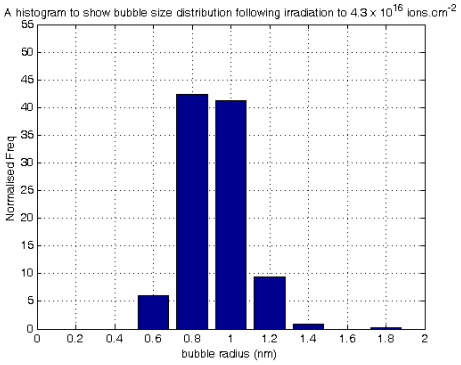

(e) 4.3×10^{16} ions.cm^{-2}. See figure 4.2e.

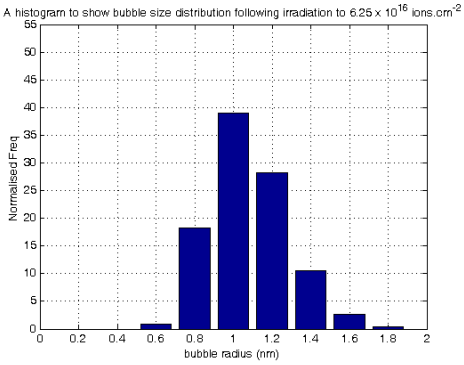

(f) 6.3×10^{16} ions.cm^{-2}. See figure 4.2f.

Figure 4.3: Bubble size distributions of helium bubbles grown by ion-irradiation in SiC.

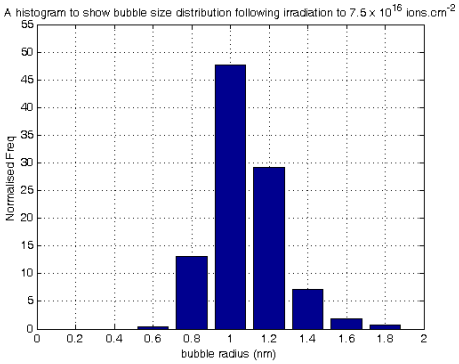

(g) 7.5×10^{16} ions.cm^{-2}. See figure 4.2g.

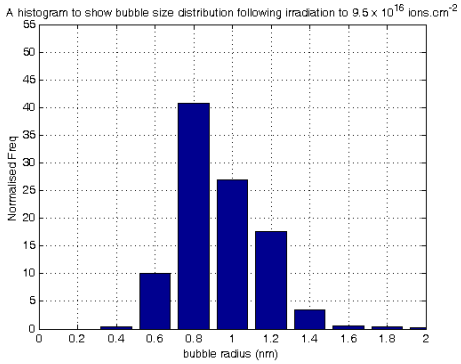

(h) 9.5×10^{16} ions.cm^{-2}. See figure 4.2h.

Figure 4.3: (continued) Bubble size distributions of helium bubbles grown by ion-irradiation in SiC.

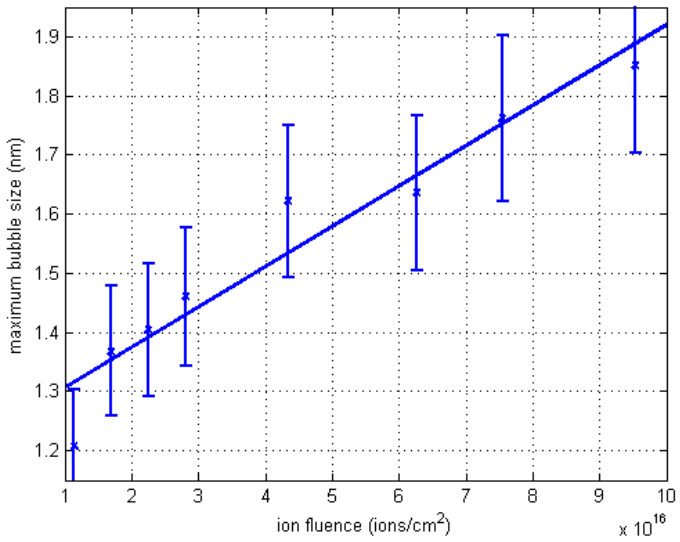

Figure 4.4: Graph showing maximum bubble size against helium ion fluence. The blue line indicates the line of best fit (least squares method).

4.3.4 Mean Bubble Size during Growth

Images were analysed using the method detailed in section 3.5. Figure 4.6 shows the mean bubble size as a function of fluence. The mean bubble size is the average radius of the circles which form when bubbles are projected onto two dimensions. This is measured on the micrograph as the distance between the dark fringe on opposite sides of the bubble. Within the error limits, the mean bubble size does not appear to vary with fluence up to 10^{17} ions.cm^{-2}. That said, when comparing the micrographs in figure 4.2 there is a clear

increase in size in some of the bubbles within the sample as fluence increases. For the mean to remain constant there must be an increase in number of small bubbles. These occurs through the introduction of new, small bubbles to the sample. These are visible by comparing successive images captured during the experiment. An example of this occuring is shown in figure 4.5.

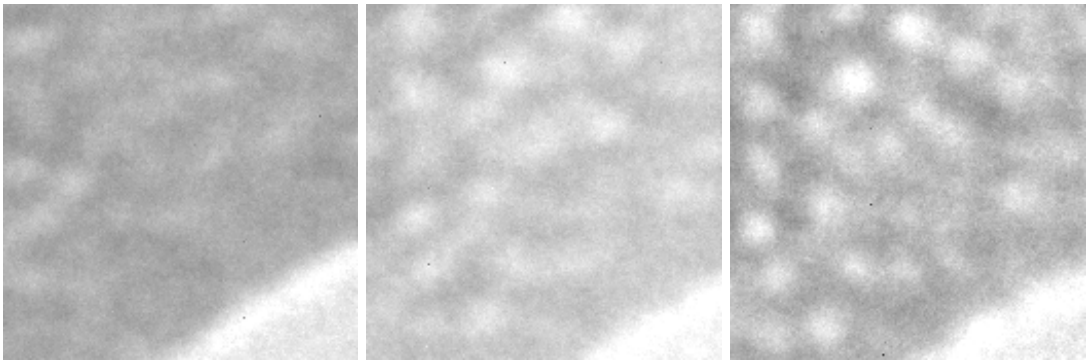

(a) 4.3×10^{16} ions.cm^{-2} **(b)** 6.3×10^{16} ions.cm^{-2} **(c)** 7.5×10^{16} ions.cm^{-2}

Figure 4.5: Three TEM micrographs showing the introduction of small bubbles to the specimen with increasing fluence. The images correspond to the same area (approximately 20 nm $\times$ 20 nm square) of the specimen.

4.3.5 Helium Bubble to SiC ratio

To calculate the increase in the fraction of the sample containing helium bubbles with increasing fluence, the ratio of projected bubble area to sample area has been calculated. This was determined by performing a similar analysis to that described in section 3.5. The bubble area was calculated by summing the area of the each of the bubbles observed on a micrograph. The ratio of bubble area to sample area was determined using equation 4.2:

$$A_{b_i} = \pi \times r_i^2$$

$$Ratio = \frac{Total\,Area\,of\,bubbles}{Area\,of\,\mathrm{SiC}} = \frac{\sum_{i=1}^{N} A_{b_i}}{A_s} \tag{4.2}$$

Where A_{b_i} is the area of the ith bubble with a radius r_i, A_s is the area of the sample in that micrograph and N is the number of the bubbles. The creation of maps containing every bubble within a given area of the

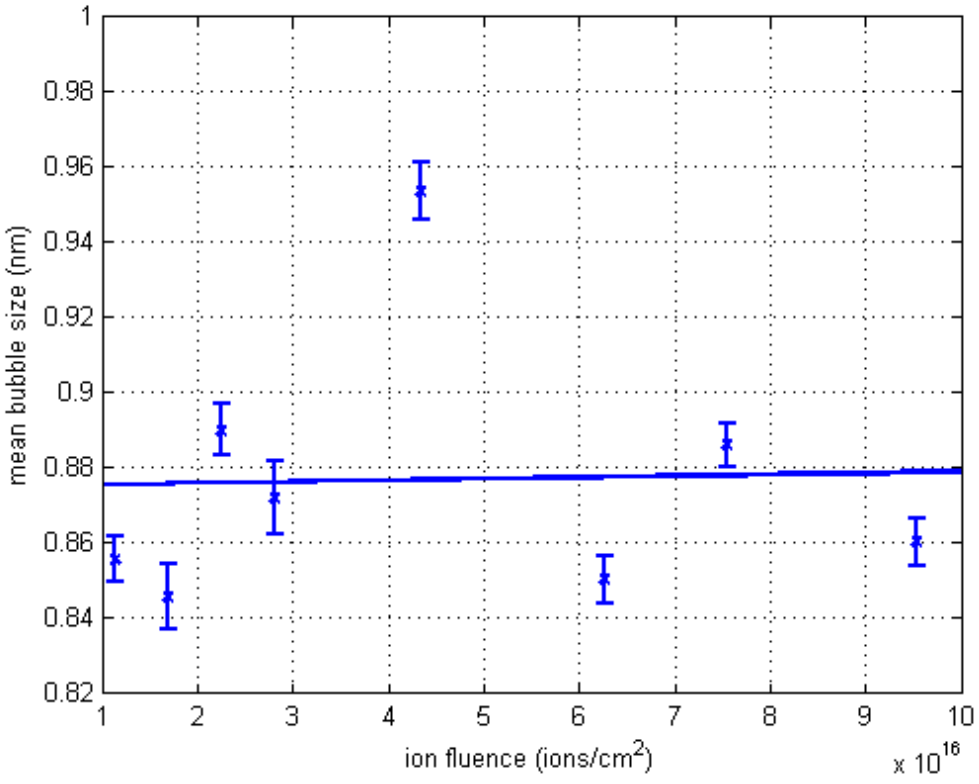

Figure 4.6: Graph showing mean bubble size against helium ion fluence. The blue line indicates the line of best fit (least squares method).

sample is a slight modification to the method detailed in section 3.5. When determining the area occupied by helium bubbles, it is essential to include every bubble which is observable on the TEM micrograph. Critically, for these experiments, this measurement provides more information than the more commonly used calculation of mean bubble size. Figure 4.7 shows a micrograph and corresponding bubble map.

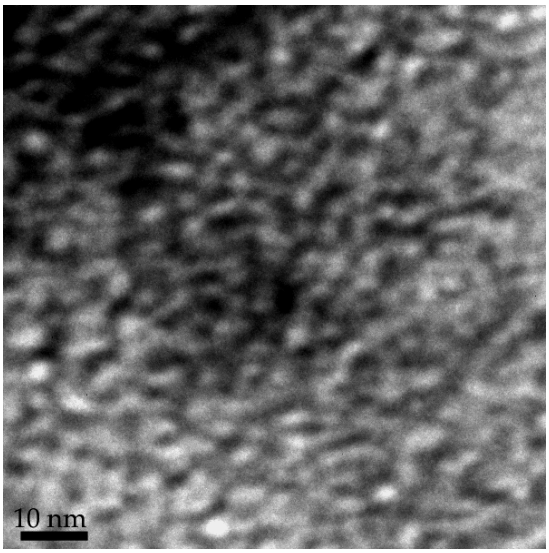

(a) TEM Micrograph

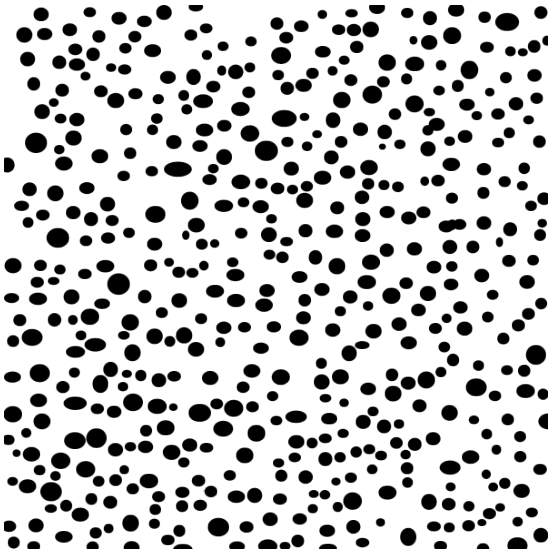

(b) map/Scion input

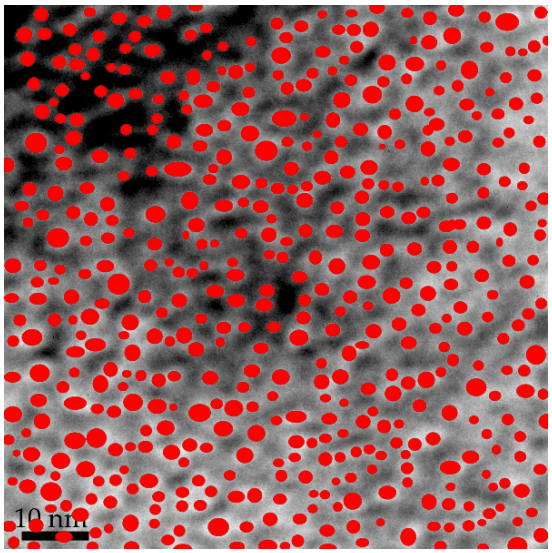

(c) TEM Micrograph and Scion input overlay

Figure 4.7: Figures to show cropped TEM micrograph and a map of the bubbles created in Photoshop for the calculation of ratio of bubble area to sample area. Image shows bubble morphology following irradiation to 6.3×10^{16} ions.cm^{-2}. Scale bar applies to all three panels.

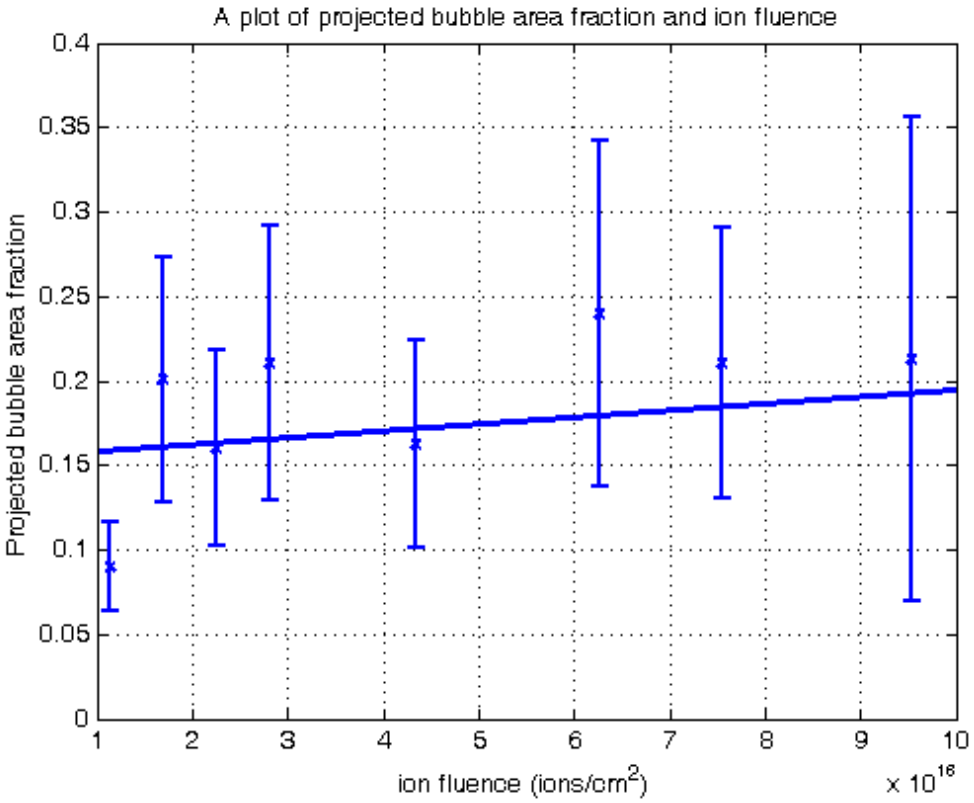

Figure 4.8: Graph showing ratio of projected helium bubble area to sample area with increasing fluence. (Assuming minimal overlap of bubbles.) The blue line indicates the line of best fit (least squares method).

Figure 4.8 shows that the area of the sample containing helium bubbles increases (albeit slowly) as we introduce more helium by ion-irradiation. The error on each data point in the graph is significant due to the high error associated with each individual measurement. Therefore, it is not appropriate to draw significant conclusions about the trend from the data graphed in figure 4.8. Despite this, in the range of ion fluences investigated in this work ($\leq 10^{17}$ ions.cm^{-2}) the increase in fraction of sample containing helium bubbles appears to increase approximately linearly with fluence.

4.3.6 Fraction of Implanted Helium Within Bubbles

Equations of state have been calculated for helium bubbles in SiC based on the comprehensive review of helium bubbles in metals completed by Donnelly in 1985 [201]. Assuming the bubbles observed in our experiments are equilibrium

bubbles, as justified in section 4.3.1, we can use this fact and the equations of state to calculate how much helium is in the bubbles of our specimen. To do this, we calculated the equilibrium pressure (P) of a spherical cavity in a solid material which is given by equation 4.1.

For these calculations the value of γ used was 3.6 N.m^{-1}. This has been reported experimentally by researchers at Jülich [182, 266] which fits estimations of γ using bond and formation energies as well as when compared with scaled values of γ of diamond. Using the equation of state published by Mills, Liebenberg and Bronson (M-L-B) in 1980 [517] we have calculated the molar volume for each bubble in our sample and, thus, the number of helium atoms in each bubble. The authors of the M-L-B equation compared their experimental data (in the range -200°C to 25°C and 2 to 20 kbar) with the M-L-B equation and found that it could predict V_M with an error of $\pm$0.3%. The equation is given as:

$$\begin{aligned} V_M = {} & (22.575 + 0.0064655T - 7.2645T^{-\frac{1}{2}})P^{-\frac{1}{3}} \\ & + (-12.483 - 0.024549T)P^{-\frac{2}{3}} \\ & + (1.0596 + 0.10604T - 19.641T^{-\frac{1}{2}} + 189.84T^{-1})P^{-1} \end{aligned} \tag{4.3}$$

Where V_M is the volume of one mole of helium in cm^3, T is the absolute temperature in Kelvin and P is the pressure in kilobars. The number of helium atoms in a bubble of a given volume, N_i, is given by:

$$\begin{aligned} \frac{V_M}{N_A} &= \frac{V_i}{N_i} \\ \therefore N_i &= V_i \frac{N_A}{V_M} \end{aligned} \tag{4.4}$$

Where N_A is Avagadro's number and the volume of the ith bubble is given as V_i. The bubble maps shown in section 4.3.5 were used to calculate the percentage of helium in M bubbles, given by the equation below:

$$\%\, of\ helium\ in\ bubbles\ = \frac{\sum_{i=1}^{M} N_i}{No.\, of\ He\ atoms\ implanted} \times 100 \tag{4.5}$$

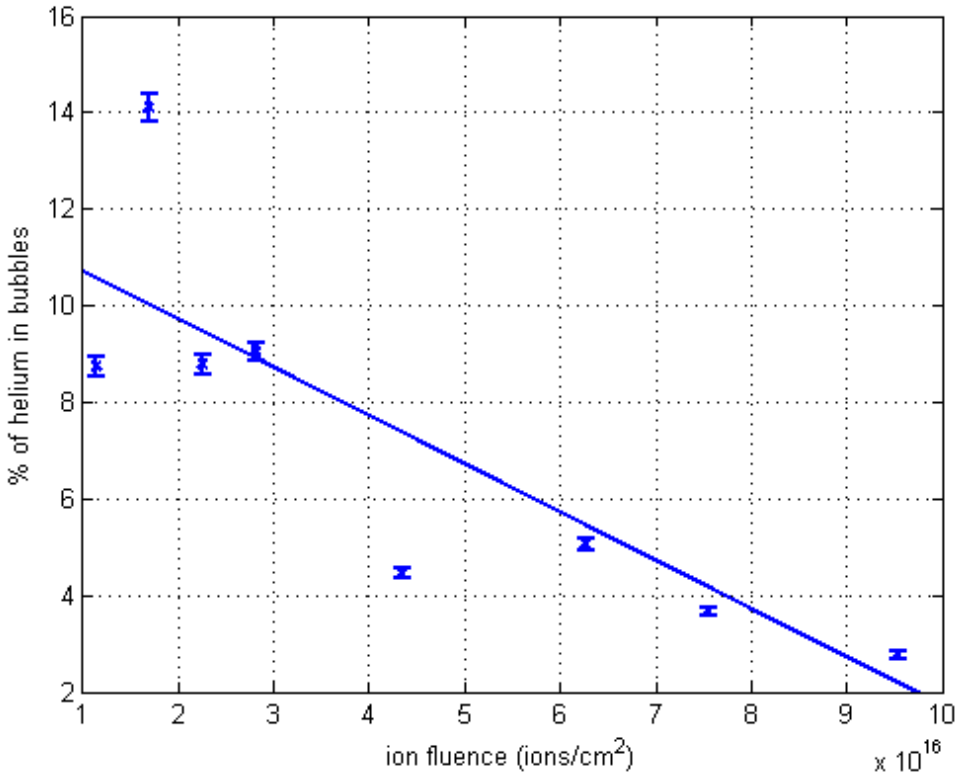

Figure 4.9: Graph showing fraction of helium in bubbles for various fluences. The blue line indicates the line of best fit (least squares method).

Figure 4.9 shows the fraction of helium in bubbles for various fluences. The graph shows that in the early part of the implantation, approximately 9% of the implanted helium forms visible bubbles within the sample. As fluence increases, at around 3×10^{16} ions.cm^{-2}, there is a decrease in fraction of helium within the visible bubbles. This reduction continues up to 10^{17} ions.cm^{-2}.

4.4 Summary

This chapter contains experimental results from *in-situ* 3.5 keV helium ion-irradiation while performing TEM of SiC samples at 700°C. Images were captured regularly throughout the irradiation. Samples were irradiated to a

maximum fluence of 10^{17} ions.cm^{-2}. For the first time, it is possible to state that helium bubbles grown under these conditions in SiC are fixed in position throughout the experiment. Other behaviour such as Ostwald ripening and motion and coalescence have not been observed to occur. Mean bubble size does not appear to increase with increasing fluence; instead, an increase in area occupied by bubbles is observed. Finally, the fraction of implanted helium within the bubbles is calculated using equations of state. These observations indicate that as fluences increases, a smaller fraction of the implanted ions are in observable bubbles. At lower fluences, helium in bubbles accounts for a higher fraction of the total number of implanted ions.

Chapter 5

Behaviour of Helium Bubbles in SiC under High-Energy Gold Ion-Irradiation at the JANNuS Facility

5.1 Introduction

Samples of SiC implanted with 160 keV helium ions (*ex-situ* to the TEM) at 400°C and subsequently annealed to 1400°C (details in section 3.4.2) were prepared for TEM using the technique outlined in section 3.2.4. The purpose of this annealing is to create a population of large, well-defined helium bubbles as has been seen in previous work [207]. These samples were subsequently irradiated at the JANNuS facility in Orsay, Paris by high-energy (4 MeV) gold ions. The purpose of this irradiation was to gain an understanding of the behaviour of SiC under conditions similar to those during high-energy neutron irradiation to which future nuclear materials are predicted to be subjected during their operational life in Generation IV and magnetic confinement fusion reactors. Gold ions were chosen from those available at JANNuS because it offered the highest damage rate. Additionally, they generate PKAs of silicon, which are close to those which will be generated in fusion reactors. (Carbon PKAs are of much lower energy than will be generated in fusion reactors, but it is not possible to generate the appropriate energy of both without using neutrons.) This chapter provides the experimental details for this investigation as well as the observed changes to the bubble population

during the experiments. The final section contains details of simulations performed in order to interpret the experimental results.

5.2 Irradiation Conditions

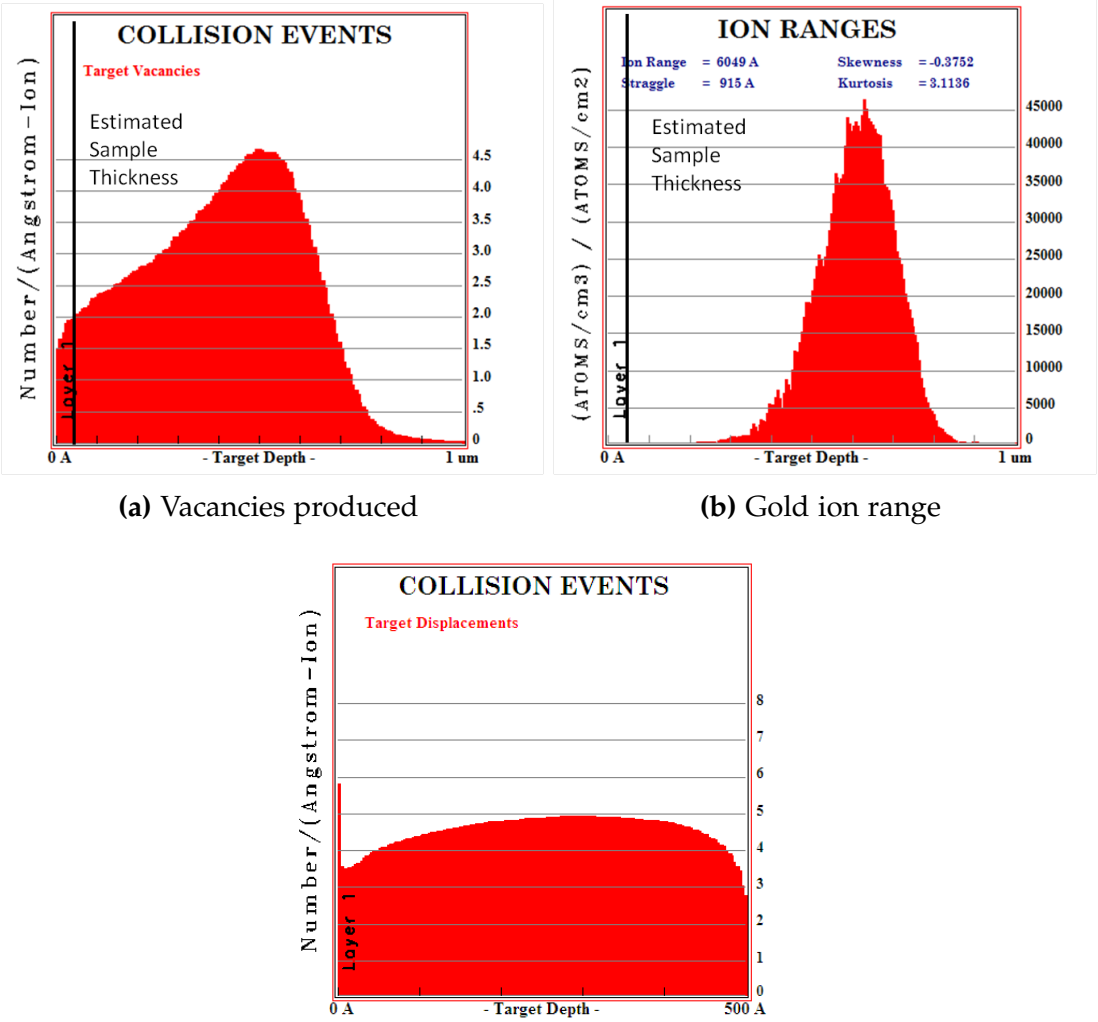

(a) Vacancies produced

(b) Gold ion range

(c) Damage across sample width

Figure 5.1: Graphs output from SRIM showing damage creation and gold ion range in SiC.

At the JANNuS facility, irradiation was conducted using 4 MeV gold ions. The samples were irradiated at 700°C (which avoids amorphisation and simulates conditions similar to those found in proposed Generation IV reactors) in a Gatan model 652 heating holder. The samples had previously been annealed to 1400°C during the sample preparation phase and returned to room temperature (see section 3.2.4). During the experiment, the measured ion

flux was between 3 and 6 $\times$ 10^{11} ions.cm^{-2}.s^{-1}. The highest fluence that the samples were irradiated to was between 5 $\times$ 10^{15} and 10^{16} ions.cm^{-2}. Images of helium bubbles within the sample were captured regularly throughout the experiments using an objective lens defocus of 1000 nm. The microscope was operated at either 80 keV or 200 keV in order to compare the effect of simultaneous ion and electron irradiation of the specimens. Experiments were also carried out with the electron beam off during the irradiation steps, in order to determine the effects, if any, of the electron or ion beam as well as synergistic effects resultant from a combination of electron and ion-irradiation.

5.2.1 Simulation of Irradiation Conducted

Simulations of the ion-irradiations conducted at JANNuS have been performed using the SRIM software. The simulations were performed in order to select the most appropriate ion species and energy for our experimental design. The aim of these experiments was to simulate PKAs generated from fast neutrons using gold ion-irradiation. Details on the SRIM software are provided in section 3.4.3.

Figure 5.1 presents graphs output from SRIM showing target displacements, which are reasonably uniform across the typical thickness of a TEM sample, with some reduction in displacements at surfaces of the sample. The simulation indicates that less than 0.1% of incident ions will come to rest within the sample.

5.3 Experimental Results

5.3.1 Simultaneous 200 keV Electron Beam and Ion-Irradiation

In experiments where the microscope was operated at 200 keV and the electron beam was irradiating part of the sample during the entire experiment while we irradiated with 4 MeV gold ions we observed a marked shrinkage of helium bubbles in the SiC samples. Figure 5.2 shows TEM micrographs captured during these experiments. The thin band of bubbles in the sample is caused by the *ex-situ* irradiation and anneal which results in helium bubbles clustered around R_P of the implanted helium ions. These samples are made in cross-section — so only a small part of the sample contains bubbles — rather than

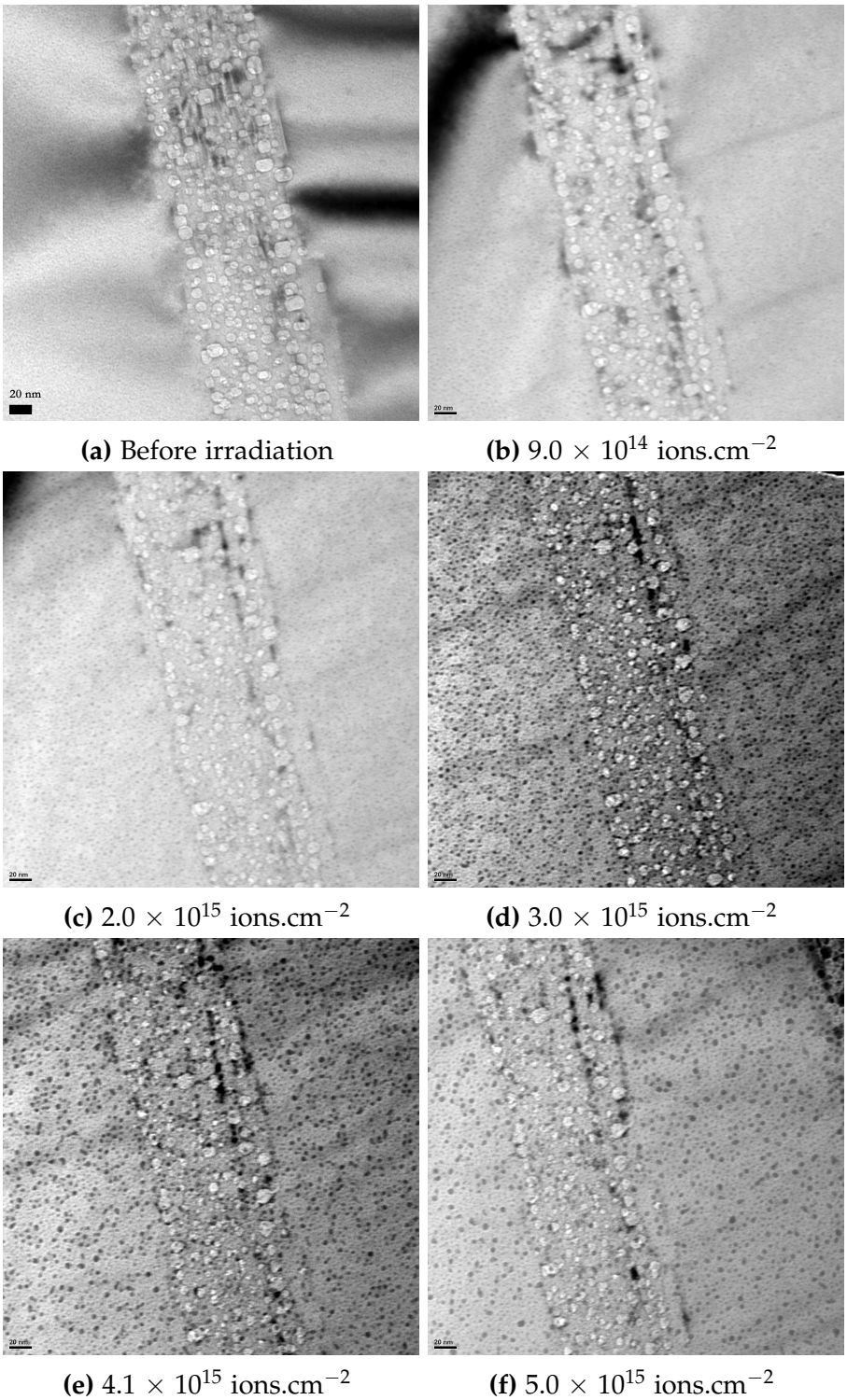

(a) Before irradiation

(b) 9.0×10^{14} ions.cm^{-2}

(c) 2.0×10^{15} ions.cm^{-2}

(d) 3.0×10^{15} ions.cm^{-2}

(e) 4.1×10^{15} ions.cm^{-2}

(f) 5.0×10^{15} ions.cm^{-2}

Figure 5.2: Helium bubble evolution during gold ion-irradiation and continuous 200 keV electron irradiation into SiC at 700°C. Scale bar in the top image corresponds to 20 nm and applies to all images in the figure.

the entire specimen, as we observed in the previous chapter.

Each successive image in figure 5.2 shows the bubble morphology at a higher fluence of gold ion-irradiation on SiC. The bubbles within the sample clearly undergo a reduction in size, which continues with increasing fluence. This carries on for the entire experiment, with some bubbles in the sample in effect 'disappearing' from the micrograph due to the same reasons that small bubbles cannot be seen in the growth phase as described in section 4.3.1. This is where a small bubble is unable to generate sufficient Fresnel contrast to be visible in the image. In addition to size reduction, the bubbles appear to change from spherical-shaped at the beginning of the irradiation to more irregular-shaped following irradiation. To quantify the reduction in bubble size, bubble maps have been produced (as detailed in section 3.5) and the mean bubble size has been calculated. No bubble motion is observed (as during the helium bubble growth reported in section 4.3.2) during these experiments. A small amount of bubble shape modification was observed, as described above. Images in figure 5.2 taken at higher fluences are slightly impaired due to contamination of the sample caused by hydrocarbon cracking on the surface of the sample caused by electron irradiation.

In figure 5.3 the reduction in mean bubble size is noticeable. Apart from an outlying data point the bubble size reduces near-linearly across the entire fluence range investigated in this experiment. As the sample contains relatively well-spaced and well-defined bubbles, it is possible to track individual bubbles through the entire experiment (a unique advantage to performing these experiments *in-situ*). Although it is not possible to present all of this data, each bubble has been tracked and they tend to show the same trend as the mean bubble size in each experiment. An example of this data is presented in figure 5.8.

5.3.2 Use of 80 keV Electron Beam only for Image Capture and Ion-Irradiation

In order to separate effects caused by the electron beam and by the ion-irradiation, we performed experiments with the microscope operating at 80 keV with the electron beam illuminating part of the sample only when required to capture the images. In the previous experiments it was not possible to compare the area inside and outside of the electron beam because of the

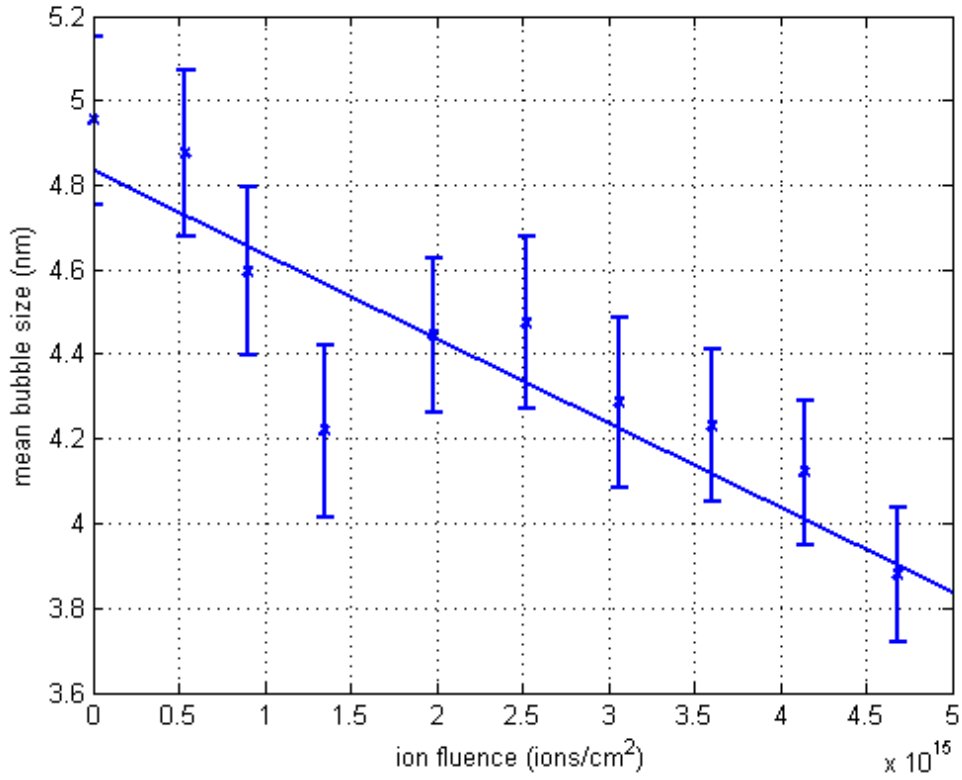

Figure 5.3: Graph showing mean bubble size versus fluence for bubble reduction under gold irradiation. The blue line indicates the line of best fit (least squares method).

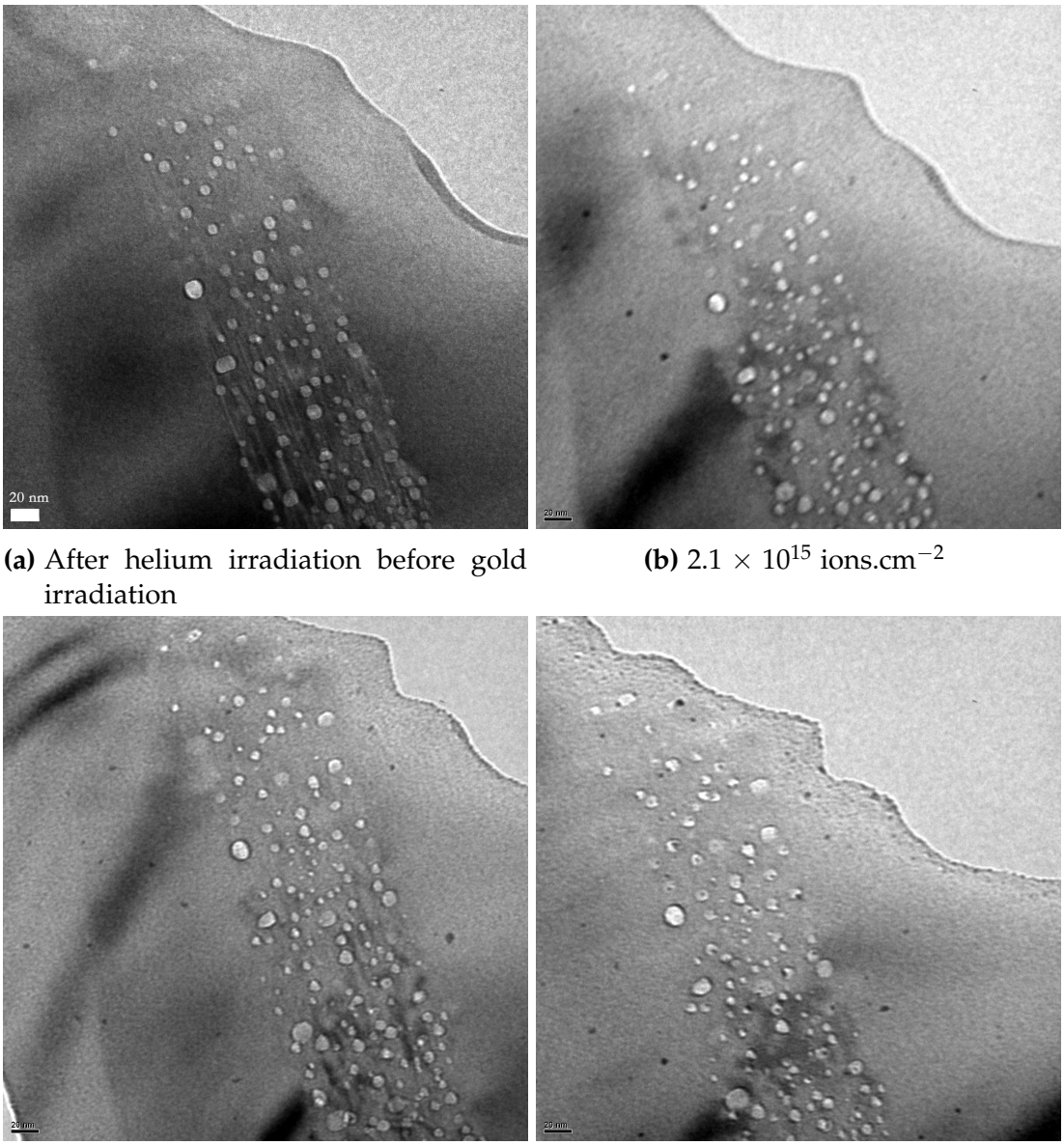

(a) After helium irradiation before gold irradiation

(b) 2.1 $\times$ 10^{15} ions.cm^{-2}

(c) 4.3 $\times$ 10^{15} ions.cm^{-2}

(d) 6.4 $\times$ 10^{15} ions.cm^{-2}

Figure 5.4: Helium bubble evolution during gold ion-irradiation and intermittent 80 keV electron irradiation into SiC at 700°C. Scale bar in the top image corresponds to 20 nm and applies to all images in the figure.

complicated geometry of the sample, electron and ion beams. There is not a sharp interface between areas which have been irradiated by both beams and irradiated by ions only. Additionally, the samples undergo non-neglegable drift during these experiments which makes it difficult to ensure a given area is not exposed to electron irradiation during the experiments. Operating the microscope at a lower voltage is known to avoid displacements in SiC — section 2.5.2 contains a review of the relevant literature — which states that

a theshold energy of 116 keV is required to displace carbon in SiC. This experiment allows an understanding of the effects on the helium bubbles in SiC caused by *only* the high-energy gold irradiation. Micrographs captured during this experiment are shown in figure 5.4.

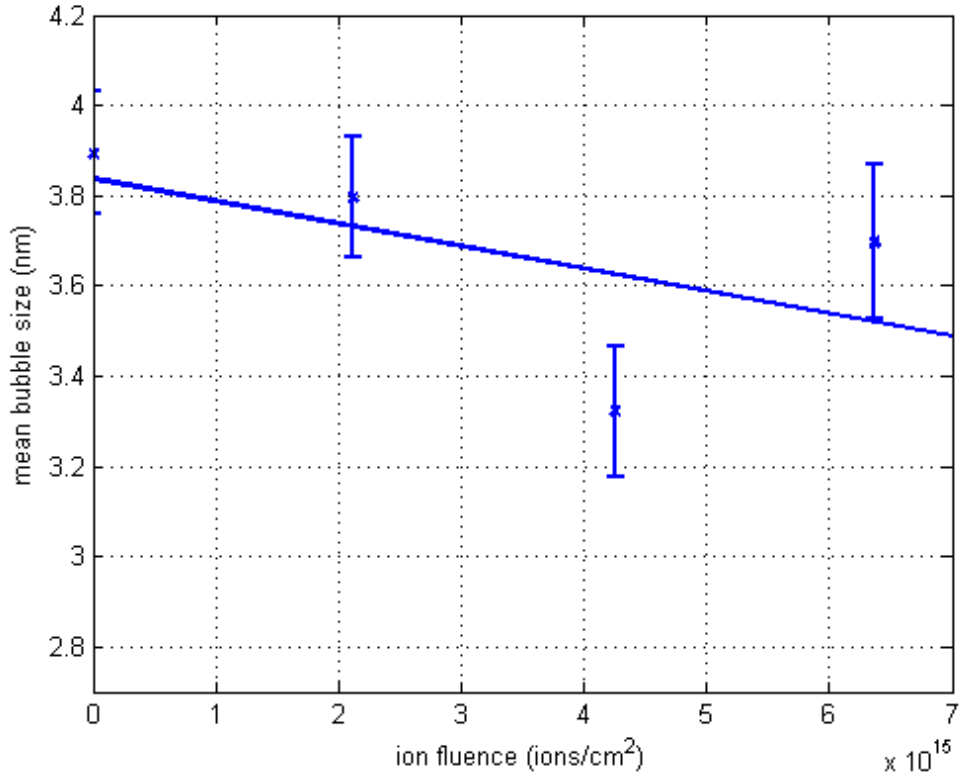

Figure 5.5: Graph showing mean bubble size versus fluence for bubble behaviour under gold irradiation. The blue line indicates the line of best fit (least squares method).

In contrast to the experimental results reported in section 5.3.1, the results from this experiment (with a lower energy electron beam) show a reduced modification to the bubble size within the sample between ion-irradiation steps. As a result, all bubbles visible in the as-prepared sample are visible following irradiation, to a fluence up to and beyond that of experiments where bubble shrinkage was observed. The bubbles appear to undergo a small amount of reshaping while being irradiated, as is observed in the 200 keV electron-beam experiment. There was significantly less contamination of the sample during the experiment, due to reduced cracking of hydrocarbons under the electron beam which is avoided in experiments where the sample is subject to reduced irradiation from the electron beam. With an edge of the sample in view, we are able to monitor the modification of the edge throughout the

experiment. The edge gets sputtered away during the experiments, changing from a smooth continuously curved feature following sample preparation to a jagged, sharp edge of the specimen by the end of the experiment. A similar effect is observed with some of the bubbles within the specimen. Some bubbles appear to become less rounded and the interface between the bubble and the sample becomes less sharp over the course of the experiment. This, we believe, is a result of a continuous flux of vacancies and interstitials in the specimen during the experiment caused by the high-energy gold irradiation. If the bubble absorbs interstitials in one particular area, the bubble deforms slightly and some vacancies are absorbed to return the bubble to equilibrium pressure. The bubbles could appear to be deformed because interstitials and vacancies are absorbed in different parts of the bubble. In addition, some of the bubbles in the sample become craters due to surface sputtering. Bubbles were analysed statistically and their mean size is plotted in figure 5.5.

The data gathered on the mean bubble size for the experiment in which the electron beam was operated at 80 keV and only incident upon the sample for image capture has fewer data points. Fewer images were captured in order to reduce the effect of the electron beam. The graph indicates that the mean bubble size does not decrease significantly following intermittent irradiation by low(er) energy electrons in combination with 4 MeV gold ions. The variation in mean bubble size can be tentatively attributed to underfocus variations in this experiment; this is compounded by having such a low number of data points, which makes it challenging to interpret whether this is a trend or experimental error. The width of the underfocus fringe seen at the edge of the specimen is seen to vary in successive images presented in figure 5.4. However it is not possible to use this information to adjust the data measured.

5.3.3 Intermittent 200 keV Electron Beam and Ion-Irradiation

To confirm the results of the two other experiments in this chapter, an experiment with the TEM operating at 200 keV with the electron beam illuminating part of the sample only for a short period of time between irradiation steps for the purpose of image capture was performed. Figure 5.6 shows TEM micrographs captured during irradiation under these conditions.

Helium bubbles subjected to irradiation by 4 MeV gold ion-irradiation and a

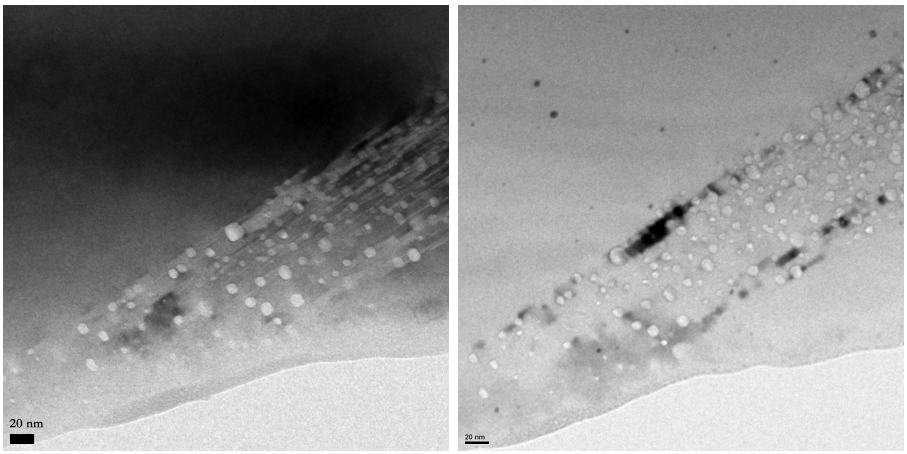

(a) Before irradiation

(b) 2.3×10^{15} ions.cm^{-2}

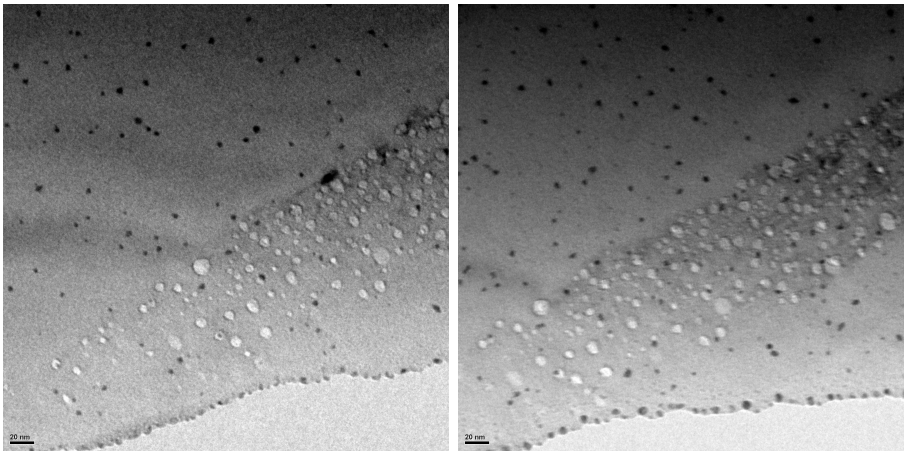

(c) 4.5×10^{15} ions.cm^{-2}

(d) 7.9×10^{15} ions.cm^{-2}

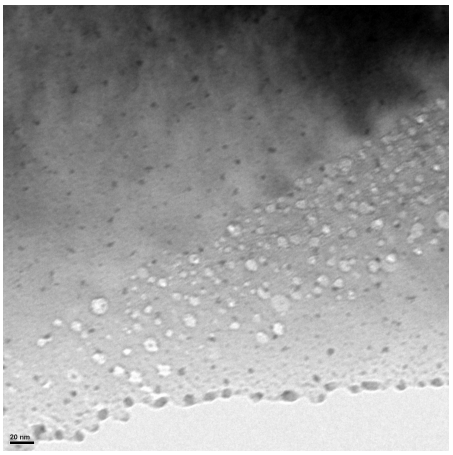

(e) 1.1×10^{16} ions.cm^{-2}

Figure 5.6: Helium bubble evolution during gold ion-irradiation and intermittent 200 keV electron irradiation into SiC at 700°C. Scale bar in the top image corresponds to 20 nm and applies to all images in the figure.

reduced amount of 200 keV electron irradiation (compared to the experiment with continuous electron irradiation) undergo a reduction of size between the results presented in sections 5.3.1 and 5.3.2 over the course of the experiment. There is significant degradation of the edge (more so than in the experiments reported in sections 5.3.1 and 5.3.2). Contamination of the sample is comparable to other experiments with reduced exposure to the electron beam (as reported in section 5.3.2). As reported earlier in this chapter, there is a deformation of the spherical bubbles into an oval or irregular shape during these experiments. This behaviour is observed in the experiments documented in figure 5.6. Bubbles were analysed and the mean bubble radius has been plotted against fluence and is shown in figure 5.7.

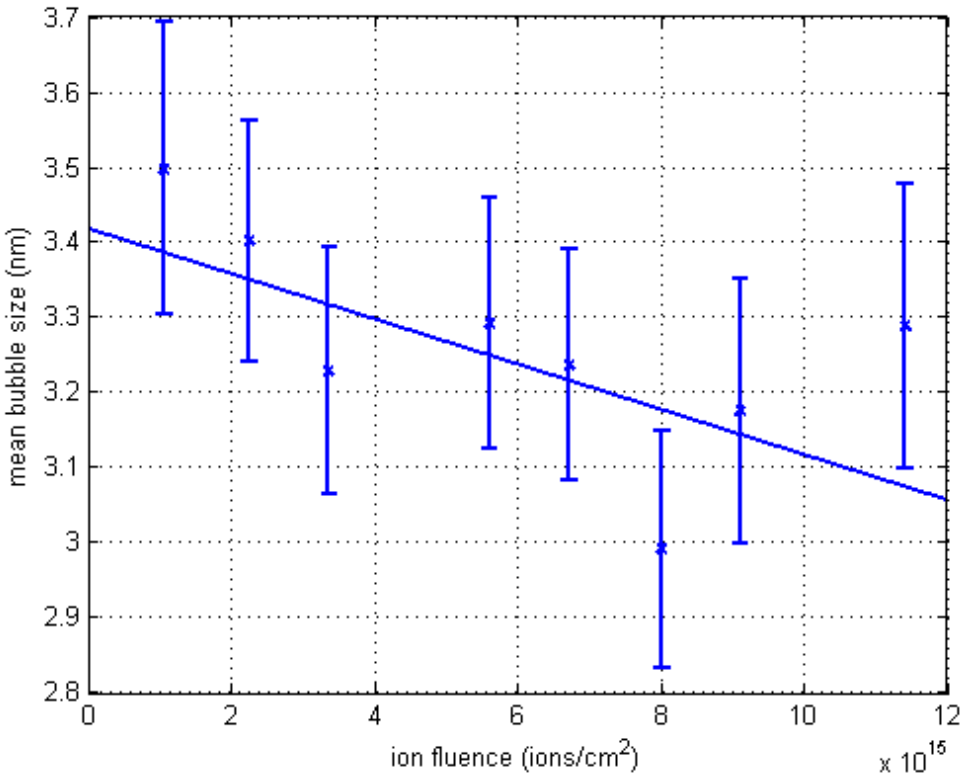

Figure 5.7: Graph showing mean bubble size versus fluence for bubble behaviour under gold irradiation. The blue line indicates the line of best fit (least squares method).

The data for three individual bubbles tracked during this experiment is shown in figure 5.8

The mean bubble size graph shows a small decrease of bubble size in the initial stages of the experiment. Beyond 2.2×10^{15} ions.cm^{-2}, the bubble size

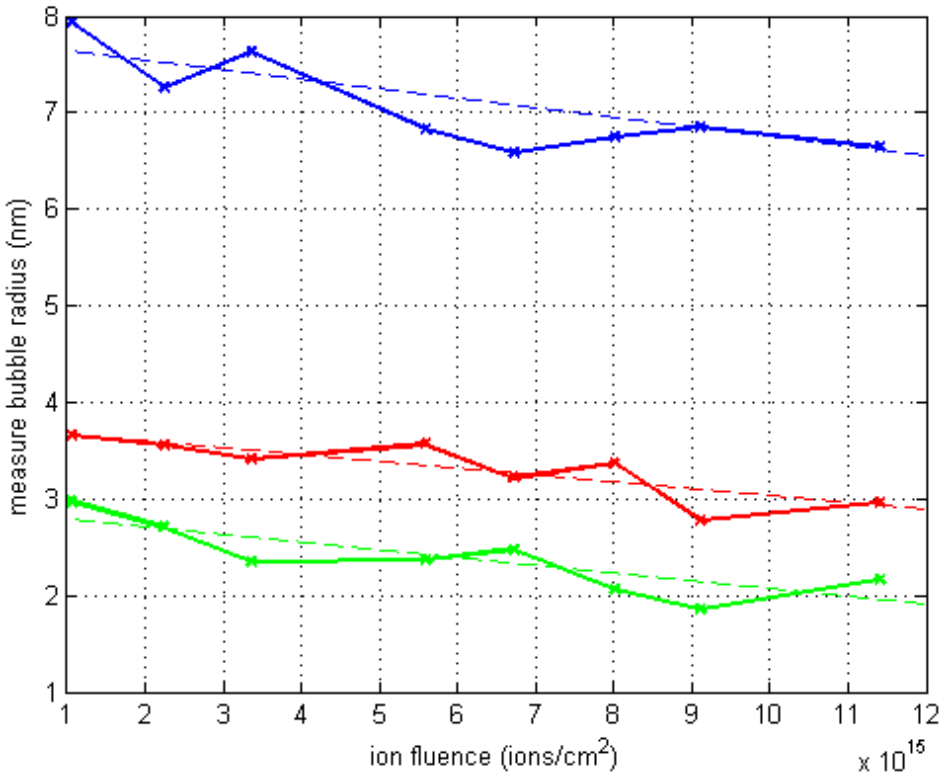

Figure 5.8: Graph showing individual bubble size for three bubbles versus fluence under gold irradiation. Line of best fit (least squares method) is shown with a dashed line for each bubble.

remains reasonably constant, between 3.2 nm and 3.3 nm. The data point associated with the mean bubble radius at 8×10^{15} ions.cm^{-2} sits as an outlier to the trend observed with the other data points. This could be explained in a similar manner, as in the previous section, as an inconsistent underfocus setting during the experiment. Additionally, the edge of the specimen had become more contaminated by the point figure 5.6d was taken than compared to figure 5.4c which could lead to more uncertainty in the measurement. Figure 5.9 shows bubble size variations for each experiment on the same plot. Experiments with intermittent electron irradiation are irradiated to a higher fluence when compared to the 200 keV/continuous irradiation experiments, in order to explore the extent to which bubble size modification is taking place in the experiments.

Figure 5.9 shows the combined results for experiments performed at JANNuS. It shows the clear, rapid decrease in bubble size for experiments performed with the electron beam continuously illuminating the specimen during the

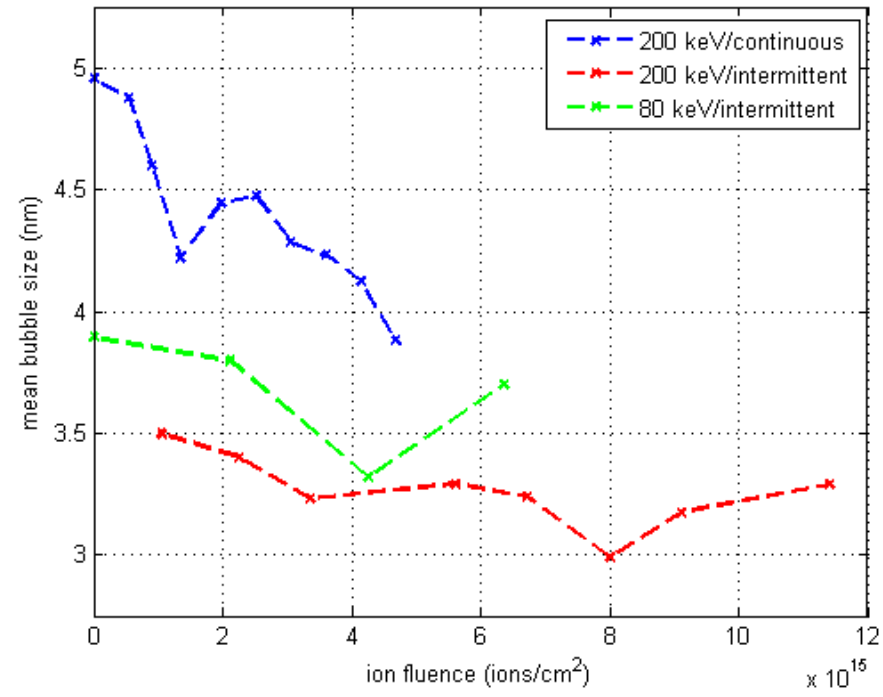

(a) Absolute mean bubble size

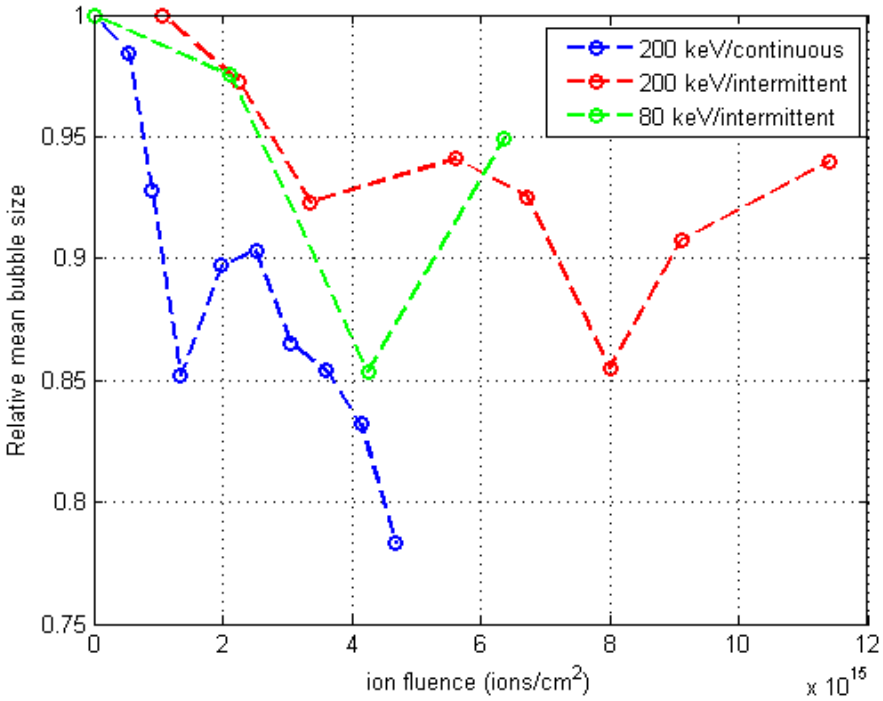

(b) Relative mean bubble size

Figure 5.9: Graph showing both absolute and relative mean bubble size versus fluence for bubble behaviour under gold irradiation for all three experimental conditions.

ion-irradiation. In experiments where a lower energy of electrons is used, or the electron beam illuminates the specimen intermittantly, bubble size is not reduced to the extent as when 200 keV electrons continuously illuminate the specimen, even when ion fluence is doubled.

5.4 Computer Simulations of Helium Bubbles in SiC

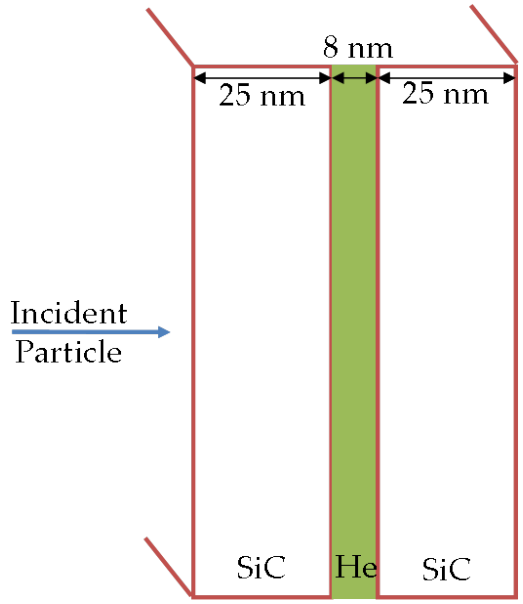

Figure 5.10: Schematic showing layered structure used in simulations. A helium layer is positioned between two layers of SiC. Incident particles have a range beyond the thickness of the target.

In order to understand the results reported in this chapter, computer simulations were performed on a helium layer (8 nm) between two thicker (in the same direction that the irradiation is incident) layers of SiC using SRIM for ion-irradiation simulations and to simulate PKAs in electron beam simulations. (8 nm was chosen as the width of the helium layer as it corresponds to the typical mean bubble diameter at the start of each experiment at JANNuS.) The Penetration and Energy Loss of Positrons and Electrons (PENELOPE) code has been used to simulate electron energy deposition in helium. It is not easy to create a complex model of helium-filled spheres in SiC in the SRIM program. A layered structure is the only possible system which can be created in SRIM, and is therefore used in all of

our simulations in order to generate comparable results. Figure 5.10 shows a schematic of the system generated in both programs for their respective simulations.

5.4.1 SRIM Simulations

SRIM simulations have been used for two different investigations into the behaviour of the helium within the bubbles. Firstly, the relatively simple case of the layered structure shown in figure 5.10 under high-energy gold ion-irradiation. Secondly, SRIM has been used to simulate helium-helium collisions which make up the cascade which forms following the collision between an incident electron and a helium atom in the bubble.

5.4.1.1 Simulation of 4 MeV Gold Ion-Irradiation

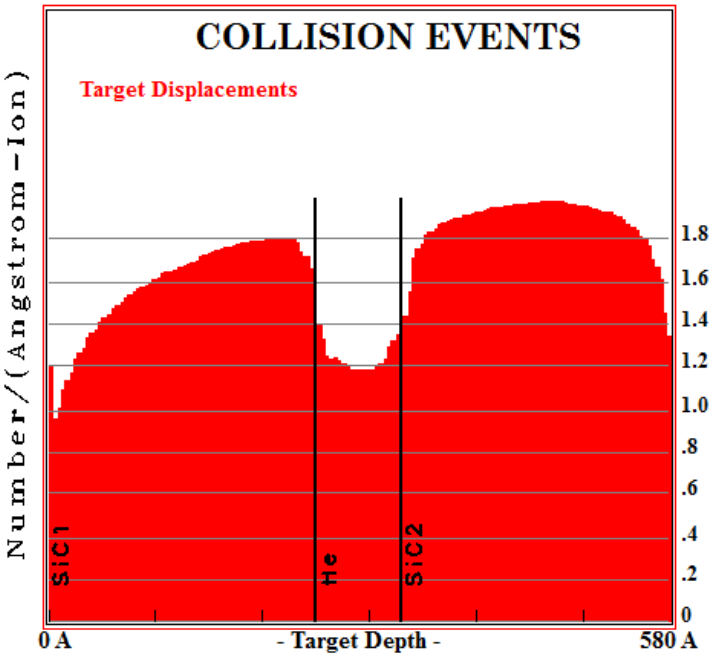

Figure 5.11: Graphical output from SRIM showing displacements caused by gold irradiation on layered model of helium bubbles in SiC.

Ion-irradiation of the layered structure is shown to result in broadly similar results to those reported in section 5.2.1. As well as figures for damage and gold ion distribution within the sample (shown in figure 5.11), a third figure is available which shows helium which is displaced from the helium bubble into the SiC lattice as shown in figure 5.12.

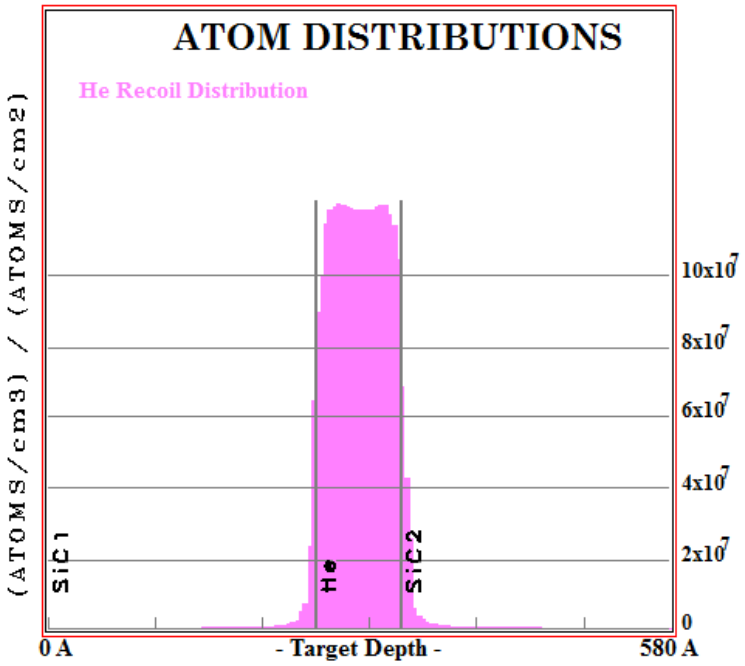

Figure 5.12: Results from SRIM showing helium displaced into the SiC layer.

The final distribution of the helium recoils provides information on the amount of helium displaced from the layer in the simulation. This is normalised to the number of incident ions. From this, the effect of ion-irradiation on helium bubbles in SiC can be calculated.

5.4.1.2 Simulation of Helium Cascades

For each bar on the histogram of the energy deposited in the helium layer by incident electrons (see section 5.4.2), a series of SRIM simulations were performed, in order to calculate whether ions with this kinetic energy would leave the helium bubble and penetrate into the SiC lattice. A collision between an electron and a helium atom (within the bubble) may occur anywhere within the bubble. Therefore, for each energy, seven different layer thicknesses (at one nm intervals from 2 nm to 8 nm inclusive) of helium have been used in order to simulate the effect of helium-helium collisions prior to entry into the SiC layer. The probability of a helium atom being displaced into the SiC lattice is calculated by combining the data for each layer and dividing by the number of layers considered.

The algorithm can be described using a flow chart which demonstrates the stages required for combining the SRIM and PENELOPE simulations to

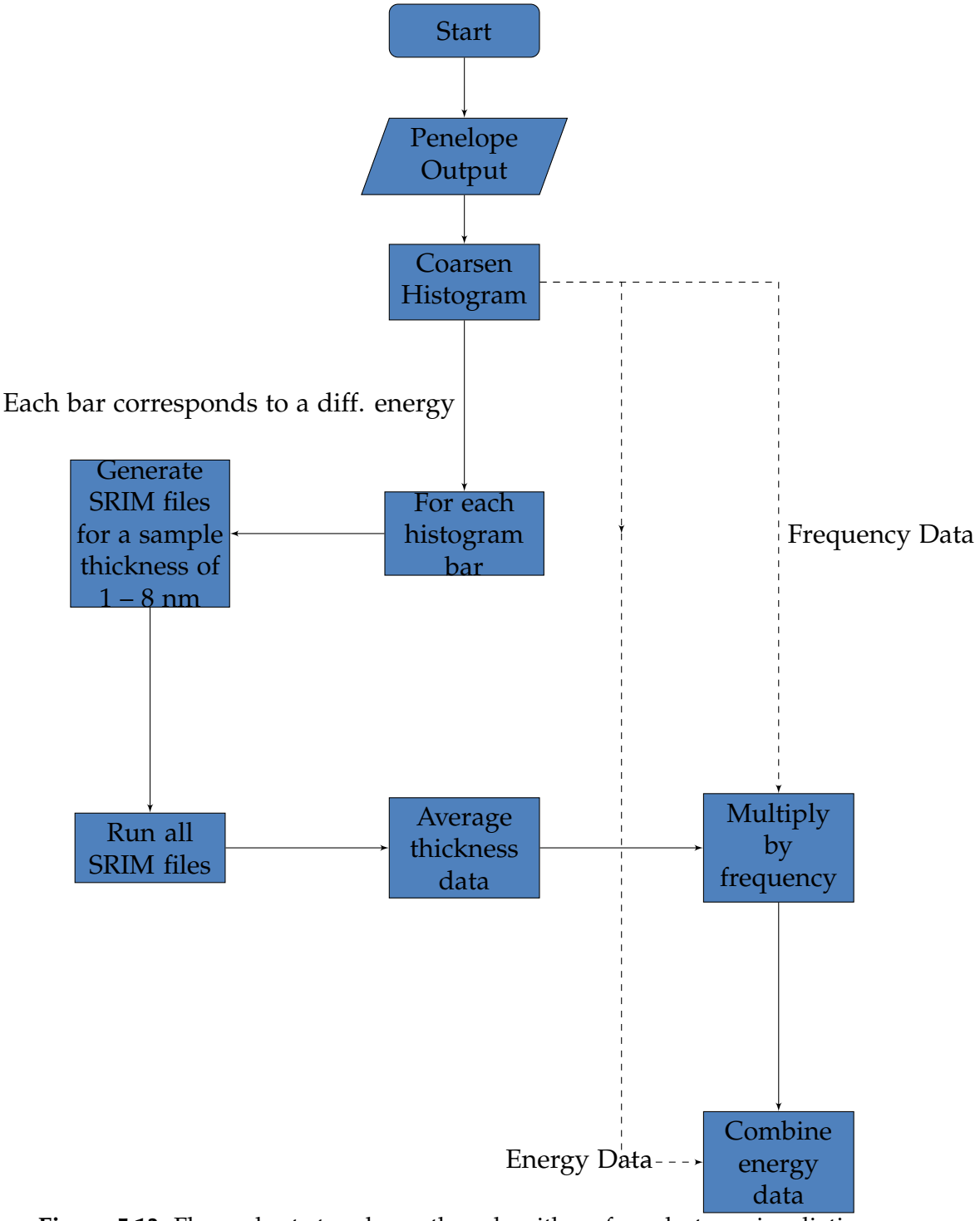

Figure 5.13: Flow chart to show the algorithm for electron irradiation simulations

produce a single value of number for the helium atoms displaced from the bubble per incident electron. The flow chart can be seen in figure 5.13.

5.4.2 PENELOPE Simulations

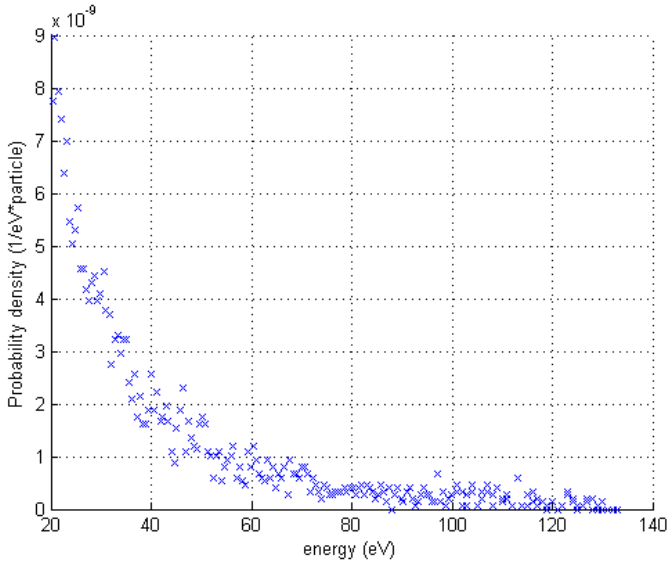

(a) PENELOPE output histogram

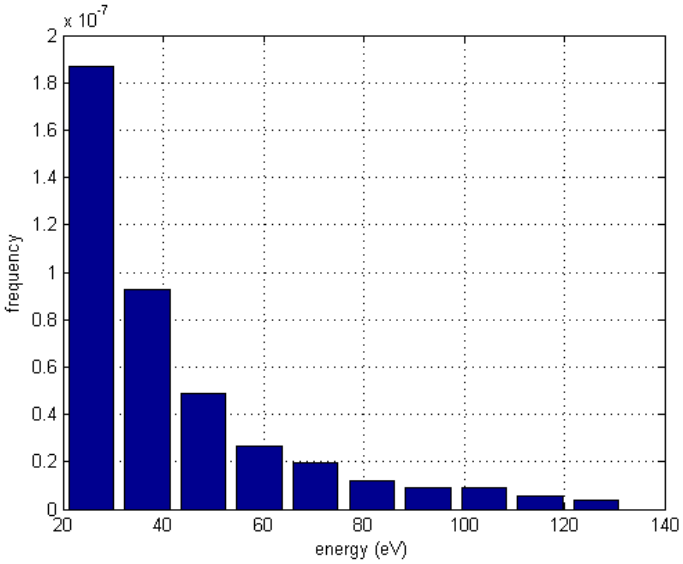

(b) Wider-binned histogram

Figure 5.14: Results from PENELOPE showing energy distribution.

PENELOPE has been used to calculate energy deposition by an incoming electron in the helium layer. This data is combined with data from SRIM simulations which investigate the outcome of helium collision cascades.

Together these provide information about displacement of helium into the SiC layers as a result of electron beam irradiation. Figure 5.14a shows a plot of energy deposited into the helium layer by elastic collisions between the incident electrons and helium atoms in the bubbles.

From the energy deposition information output from PENELOPE (shown in figure 5.14a), a histogram with wider bins is generated and shown in figure 5.14b. For each of the bars in the histogram, a series of SRIM simulations has been completed. The full algorithm followed during these simulations has been detailed in section 5.4.1.2.

5.5 Summary

Three different experiments have been conducted at the JANNuS *in-situ* ion-irradiation/TEM facility in Paris. In experiments where 200 keV electrons were continuously incident on the sample during 4 MeV gold ion-irradiation a significant reduction in bubble size occurred. Under the same ion-irradiation conditions, but differing electron beam conditions (the microscope operating at either 80 or 200 keV with the electron beam on only for image capture) there was a reduced effect on bubble size. In order to begin to investigate the effect of ion-irradiation and electron irradiation on helium bubbles in SiC we ran several simulations using SRIM to simulate 4 MeV gold ion-irradiation and PENELOPE to simulate electron-helium interactions. SRIM was also used to simulate the behaviour of a helium PKA in a helium bubble generated by an electron-helium interaction. The output from these simulations is included in this chapter. Further calculations using these are presented in the following chapter.

Chapter 6

Discussion

6.1 Introduction

The results presented in the previous chapters contain significant new information about the nucleation, growth and evolution of helium bubbles in SiC created by helium ion-irradiation. Additionally, the results from JANNuS provide unique understanding into how helium bubbles in SiC behave under different irradiation conditions. This chapter contains a discussion of the results reported and places them in context within the relevant literature. In the case of electron and ion-irradiation experiments conducted at JANNuS, we use the results of computer simulations to provide an explanation for the experimental observations.

6.2 Helium Bubble Motion in SiC

Bubble motion is determined by surface and bulk diffusion properties of the host material. Thermally-activated bubble motion in metals [518–520] and semiconductors [521, 522] has been reported. Additionally, ion-irradiation has been reported to stimulate bubble motion during irradiation of metals [511, 512, 523–525].

The published literature in this area contains no reported observations of helium bubble motion in SiC at or below 700°C. Our experiments support this; none of our experiments contain noticeable bubble motion during ion-irradiation. We propose that implanted helium diffuses rapidly within the

lattice and becomes trapped on clusters of vacancies which are caused by ion-irradiation. These small clusters of helium and vacancies may be able to diffuse and agglomerate when very small, but will grow to sizes at which they are immobile and they become immediately pinned within the lattice. At this stage they remain subnanoscopic. By the time they are visible in the microscope they have become immobile and therefore no bubble motion is observed. Helium-vacancy clusters then act as nucleation sites for helium bubbles. We can conclude this because of the *in-situ* nature of our experiments, which show that, even in the smallest observable bubbles, no motion is observed.

6.3 Mean Bubble Size During *in-situ* Irradiation

The modest variation in mean bubble size during helium ion implantation is shown in figure 4.6. Despite this, it is clear that the bubbles are growing during these experiments (see TEM micrographs in figure 4.2). The introduction of new, small bubbles (as shown in figure 4.5) counteracts the increase in the mean, which would be caused by existing bubbles growing larger. The mean bubble size therefore does not increase as the oldest, largest bubbles grow.

The fact so many new, small bubbles are introduced is indicative of the high probability of helium-vacancy clusters diffusing into other helium-vacancy clusters within the specimen in comparison to the probability of the helium-vacancy clusters diffusing into existing bubbles. The density of helium-vacancy clusters makes the mean free path to another cluster lower than the mean free path to a bubble. Eventually the helium-vacancy clusters become large enough that they are pinned and these go on to form bubbles. This supports the conclusions made in section 6.2. If the number of helium-vacancy clusters could be reduced by an external treatment (either thermal or ion-induced) then the probability of diffusion and agglomeration within the specimen would result in fewer, larger clusters during the nucleation of helium bubbles. Additionally, it would be more likely that helium-vacancy clusters would diffuse until they became close to or included in existing bubbles rather than nucleating new bubbles within the specimen. This case would result in fewer small bubbles nucleating, and would enhance bubble growth and provide an increase in mean bubble size for increasing fluence which is not observed in these experiments. The lack of variation of mean helium bubble size in SiC during increasing ion fluence has also been reported by Chen [392].

A large number of small (1-2 nm) bubbles has been reported by a number of authors - follow irradiation to a similarly high fluence [119, 222, 387]. Some recent publications have reported that helium-vacancy clusters become pinned in the SiC lattice when they are small, which in our case forms the nucleation of a future bubble [230, 240].

Most materials have a saturation concentration of bubbles, where, on average, as a new bubble tries to nucleate it is likely to be absorbed into an existing bubble. Eventually some bubbles may coalesce, and leave a small amount of material for a new bubble to nucleate in. The introduction of both a large (coalesced) bubble and a small (new) bubble may also result in a negligible change in the mean bubble size as seen in this work.

6.4 Growth Mechanisms for Helium Bubbles in SiC

Bubble growth as a result of ion-irradiation has been reported in the literature to occur through three mechanisms. The first mechanism, motion and coalescence [510, 516], is reliant on bubble motion in the material. (A summary of bubble motion mechanisms is included in section 6.2.) If a bubble intersects with another bubble, they coalesce and form a single larger bubble. The second mechanism, Ostwald ripening [267, 509], is a process where larger bubbles grow at the expense of smaller bubbles, as larger bubbles are thermodynamically favourable. This requires the bubbles to exchange gas atoms (or molecules) and vacancies through the solid. The final mechanism is growth and coalescence, where the bubbles are fixed in position and grow independently by acquisition of gas atoms and vacancies, only coalescing once sufficiently large enough to intersect with adjacent bubbles. Where motion is not observed, but bubble growth occurs, the mechanism is growth and coalescence [266, 511].

As discussed in section 6.2, bubble motion has not been reported in SiC. Additionally, motion and coalescence has not been reported as a mechanism for bubble growth in SiC. But Ostwald ripening has been reported [392, 509, 526]. Despite this, in our experiments, bubbles are seen to increase in number and size throughout the experiments performed. Therefore there is no observation of an Ostwald ripening type process occurring in experiments under these conditions. This leads to a conclusion that the most likely bubble interaction mechanism is through growth and coalescence. Growth

and coalescence has also been reported for experiments performed with neon in SiC [206]. We conclude from our *in-situ* experiments that helium bubbles growth within SiC can be described using the growth and coalescence mechanism.

6.5 Rate of Growth of Helium Bubbles in SiC

Analysis of the *in-situ* TEM experiments has been performed and reported in sections 4.3.5 and 4.3.6. Both sections show a reduction in growth rate with increasing fluence. For lower fluences (less than 3×10^{16} ions.cm^{-2}) the total bubble area increases, and the proportion of implanted helium in bubbles remains constant. At higher fluences (approximately 5×10^{16} ions.cm^{-2}), the proportion of implanted helium in visible bubbles is much lower and the rate of increase of total bubble area is almost constant. The proportion of implanted helium that forms the visible bubbles is always low, the majority of the helium is either in subnanoscopic defects or has diffused out of the specimen. Publications by Oliviero show that implantation in similar conditions to those during these experiments results in very high (over 90%) trapping of implanted helium within the specimen (even though it is not within bubbles) [380, 509]. A THDS study has shown that implanted helium is trapped in SiC up to 1100°C [527] and a mass spectroscopy study has shown helium to be trapped until temperatures exceed 1300°C [389]. Therefore it seems likely that the helium implanted during these experiments is located within the lattice, but not within the visible bubbles.

The reduction in growth rate as ion fluence increases, may be due to either one of two possible reasons. Either, as the number of bubbles increases, the probability of additional bubbles being obscured from view increases, or as the density of bubbles increases the bias for growth of new bubbles may decrease. Bubble overlap has been considered by several workers in the past. In some cases, they simply acknowledge that there is some bubble overlap, but make no attempt to correct for it. This sometimes limits their ability to collect usable data [528]. Other workers [529] simply chose an area of their sample which was thin enough to prevent it from being a problem. The unique nature of these experiments allows us to investigate the statistical likelihood of bubble overlap obscuring a bubble, resulting in undercounting during the analysis. This effect is clearly related to the size and number of bubbles in the specimen. In order to

establish the threshold at which an individual performing analysis is unable to identify whether two overlapping bubbles should be counted as two bubbles or one bubble, some images with typical bubble sizes and densities were created using a random number generator. The position of each of the bubbles was established entirely at random without influence on the location of the existing bubbles. These were then subjected to identical bubble analysis techniques as the TEM micrographs (detailed in section 4.3.5). By analysing the distance between pairs of bubbles that were counted as single bubbles we were able to establish that two bubbles are counted as one bubble if their centres lie within $1.5r$, where r is the radius of the bubbles. Results from simulations have a striking similarity to the TEM micrographs obtained experimentally (see figure 6.1 for an example)

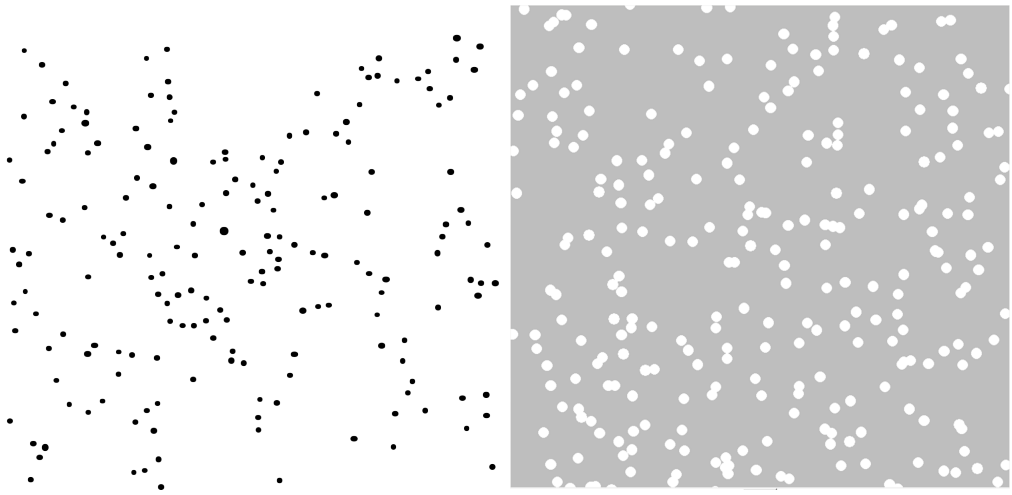

(a) Data collected from experiment **(b)** Image produced by simulation

Figure 6.1: Comparison between simulated spatial bubble distribution and experimental images

Having established the criteria that two bubbles are considered to be one, we are able to perform additional simulations — by generating images with a variety of bubble densities — which represents the increase in number of bubbles observed in our TEM images. We used the information generated by these simulations to perform further calculations, the results of which are visible in figure 6.2. The data from these calculations allows us to correct for undercounting of bubbles due to overlap in the images and establish whether the trends identified from analysis of the images represent the true behavior of helium bubbles in SiC.

Figure 6.2 shows the graphs presented in chapter 4, with a correction applied

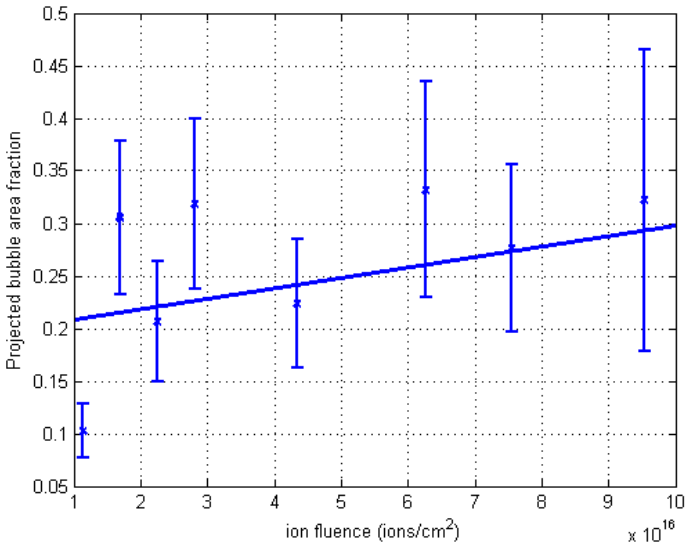

(a) Projected bubble area fraction

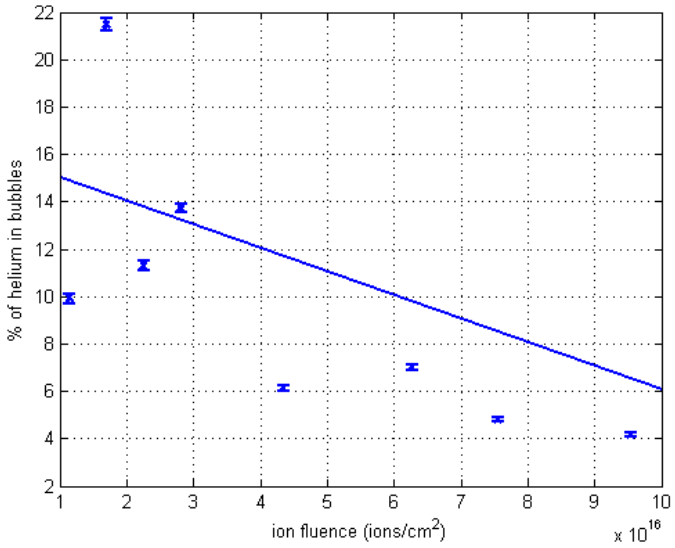

(b) Amount of helium in bubbles

Figure 6.2: Graphs showing data presented in chapter 4, corrected to account for masking due to bubble overlap. The blue lines indicates the lines of best fit (least squares method) for each graph.

to account for the bubbles hidden in the TEM micrograph due to masking by other bubbles. In both cases, the data output by our simulations has higher values than that from our experiments, as is expected, because we have counted more bubbles in our specimen. We conclude that there is a higher percentage of implanted helium in bubbles — most noticable at the lowest fluences. As more helium is implanted into the specimen, the amount that is

found in bubbles increases in absolute terms, but, compared to the amount of helium implanted, this decreases. In addition, despite increasing the amount of helium in the specimen, the rate of growth of bubbles appears to reduce at higher fluences.

From this information we infer that the growth rate of helium bubbles in SiC is slightly hindered by the presence of helium ions (either in bubbles or in clusters with vacancies) in the specimen. The fate of implanted helium is to either join an unresolvable (by TEM) helium-vacancy cluser or diffuse out of the specimen. In order to confirm whether this occurs, an experiment where ion-irradiation is performed to higher fluences is neccessary, in order to observe helium-vacancy cluster evolution. This itself poses problems, as we have shown, observing bubble evolution by TEM can have limitations, as the growth of bubbles results in overlap of underlying bubbles in the specimen. It is worth noting that the calculation of the amount of implanted helium in bubbles is subject to significant errors, mainly due to large error bars when measuring small bubbles but also as a result of overlap and the uncertainty of the degree of pressurisation of the bubbles. However, we are confident that the majority of the implanted helium is not in the bubbles. This is based on the assumption that the bubbles are not highly overpressurised.

6.6 Size Distribution of Helium Bubbles in SiC

The bubble size distributions presented in figure 4.3 provide supporting evidence for the low probability of helium-vacancy clusters moving into existing helium bubbles in SiC. The distributions are broadly symmetrical throughout the experiment, which indicates that as many new bubbles nucleate and are in the early stages of growth as have grown to reach the largest sizes. A relatively small proportion (< 5%) of bubbles reach the largest sizes under these experimental conditions. The maximum bubble size increases throughout an experiment (see figure 4.4). Additionally, the introduction of new small bubbles is observable in the bubble size distributions. This supports the conclusions of section 6.3 and strengthens the argument that above a certain size, helium-vacancy clusters have low mobility in SiC and, thus, it is more likely that a cluster nucleates a new bubble within the specimen rather than diffuses and agglomerates with an existing bubble. When smaller, helium-vacancy clusters have one of two fates. Through

diffusion, they either join other small clusters to form larger clusters or they diffuse into existing bubbles causing the bubble to grow. Large numbers of small helium bubbles have been observed by TEM in *ex-situ* helium ion-irradiation experiments performed at room temperature [222] and at 750°C [241] by Oliviero and Barbot. Based on this, we conclude that this behaviour is typical of helium bubbles in SiC under these conditions and not a result of performing the experiments *in-situ*.

6.7 Electron Beam Effects on Helium Bubbles in SiC

The electron beam effects on helium bubbles in SiC has been simulated using a combination of the computer simulation programs PENELOPE and SRIM. The full method has been described in sections 5.4.2 and 5.4.1.2. The output file generated by PENELOPE provides a distribution of energies transferred to the helium atoms within the bubbles and a probability of that energy transfer occurring for a single incident electron. This output has been combined with data from SRIM in order to simulate the helium-helium cascades which occur following the collision between the incoming electron and the helium atom. The probability of an electron transferring a low amount of energy to the helium atom is quite high. This probability drops rapidly with increasing knock-on energy. Recent MD simulations [530] show that a high percentage of helium atoms with an energy of less than 25 eV do not penetrate the SiC lattice and are backscattered from the surface. We therefore use this as a cutoff and ignore helium atoms with an energy lower than this.

The results, extracted by combining simulations performed using PENELOPE and SRIM, show that on average, for each incident electron, there are on the order of 10^{-7} helium atoms displaced from the bubble. The flux of electrons is many times higher than the ion flux: 2.4×10^{17} electrons.cm^{-2}.s^{-1}. When combined with the SRIM results, and compared with the total number of helium atoms available, over the course of an experiment we conclude that $\approx 0.2\%$ of helium is displaced from the bubble by electron beam irradiation. The removal of such a small percentage does not explain the reduction in bubble size on the scale that has been observed in these experiments and does not explain the experimental results. Frenkel defects, produced by 116 keV

electron irradiation of SiC have been observed to be stable below 425°C [255]. For higher energy electron irradiation the temperature threshold for stability is also observed to increase [244, 257, 260]. For 200 keV electron-irradiation at 700°C there have not been any reports of Frenkel defect production. Most likely, Frenkel defects are produced but these recombine immediately due to the mobility of vacancies and interstitials at this temperature. No reports of TEM-induced bubble shrinkage exist in the current literature. However, electron beams have been reported to cause epitaxial recrystallisation in ion-irradiated SiC [190] and stimulate bubble growth in ion-irradiated SiC [292]. As a result, the conclusion is that electron-beam irradiation on helium bubbles in SiC does not explain the helium bubble shrinkage observed when irradiated with 200 keV electrons simultaneously with 4 MeV gold ions.

6.8 Ion Beam Effect on Helium Bubbles in SiC

The SRIM software has been described in section 3.4.3, specific simulations for this work have been described in section 5.4.1.1. These simulations have been used to assess the energy transferred to the helium atoms and their displacement away from their starting position and into the SiC lattice. Additionally, SRIM provides important information regarding the generation of vacancies during ion-irradiation.

The simulations were performed on a system shown schematically in figure 5.10. The results are presented in section 5.4.1.1. They indicate that over the course of the ion-irradiation experiments at JANNuS, 6.4% of helium ions could be displaced out of the bubble (with 0.8% displaced more than 2 nm from the bubble surface). On average throughout the experiment, SRIM predicts the creation of 900 vacancies per ion (although recombination effects may result in this number being much lower ($\approx$ 200 vacancies/ion) [180]).

Simulation of ion-irradiation using 4 MeV gold ions shows this generates all of the pre-requisites required to cause bubble shrinkage in SiC. The kinetic energy transferred to the helium atoms is sufficient to knock a significant proportion of them from inside the bubble and into the surrounding lattice. This will create under-pressurised bubbles in the lattice. The high density of Frenkel defects generated is sufficient for the (now under-pressurised) bubble to have a close source of interstitials which can be absorbed, causing the bubble to shrink and return to equilibrium pressure [201].

Based on these simulations, we have come to the conclusion that the displacement of helium from within bubbles by the ion-beam has been shown to occur between four and 35 times more frequently than when conducted using electron beam irradiation alone which does not match the observed experimental results. This leads us to believe that either the simulation techniques used do not adequately simulate the behaviour of the system, or there are synergistic phenomina occuring during simultaneous electron and ion beam irradiation, which are difficult to simulate, especially using the tools utilised during this work. There have been several reports of bubble shrinkage during ion-irradiation of helium bubbles in metal substrates. These bubbles shrink and ultimately disappear during this process - similar to that observed during this work [511, 512, 524]. The difference between our work (on SiC) and the work in these publications, is that they're able to isolate the effect of ion-irradiation and the effect of the TEM and we have not been able to do so within this work.

6.9 Conclusion

This chapter contains a summary and discussion of the results chapters in this thesis. Each section summarises a set of significant results and provides supporting evidence in the form of relevant literature and examples from the current work. The work presented complements the existing literature and is generally in agreement with previous work. Apart from the electron beam effect, all of the conclusions are supported by references to previous publications. The work presents, for the first time, results of helium bubble growth observered *in-situ* in the TEM. Several of the conclusions could not be made were it not for this technique.

To summarise, the results are that:

- mean bubble size does not vary during helium bubble growth in these experiments, but maximum bubble size increases. The mean remains static because new small bubbles nucleate;
- when helium bubbles are resolvable by TEM the bubbles are fixed in position and undergo growth and coalescence;
- there is evidence that the rate of observable growth decreases above 6 $\times$ 10^{16} ions.cm^{-2};

- 4 MeV gold ion-irradiation alone could cause a reduction in bubble size due to the kinetic energy transferred to the helium atoms and the introduction of a significant number of interstitials. However, this is not observed during our experiments; and
- simulations of electron beam interaction with helium atoms does not indicate that there is substantial displacement of helium from the bubble due to electron-helium collisions.

Chapter 7

Conclusions and Further Work

7.1 Conclusions

Having conducted *in-situ* ion-irradiation/TEM experiments at the MIAMI and JANNuS facilities and analysed the results, we are able to make the following conclusions:

Helium bubbles grown in SiC at 700°C by ion-irradiation with a flux of $\approx 2.7 \times 10^{13}$ ions.cm^{-2}.s^{-1}, to a final fluence of 10^{17} ions.cm^{-2} do not undergo any observable motion during the *in-situ* experiments.

The mean size of helium bubbles grown in this way does not significantly increase with increasing ion fluence up to an end fluence of 10^{17} ions.cm^{-2}. Instead, new bubbles form and offset the effect on the mean caused by existing bubbles growing.

The growth mechanism for the helium bubbles generated using the conditions in these experiments has been observed to be by growth and coalesence. There is no evidence of Ostwald ripening or motion and coalescence in any of the experiments performed.

Bubble size distributions of helium bubbles during growth in these experiments show that diffusion of clusters of helium atoms and vacancies into existing bubbles is unlikely. Preferential nucleation and growth of new helium bubbles is evident.

For specimens irradiated *in-situ* by 4 MeV gold ions and 200 keV electrons, it has been concluded that there is a significant effect on the helium bubbles attributable to the electron beam. This may be a synergistic effect or an effect caused solely by electron irradiation. We have simulated and compared the

displacements caused by electron irradiation and ion-irradiation in order to attempt to explain the observed behaviour. When comparing the results of the two simulations, the amount of helium displaced from the bubbles is significantly more likely to be caused by ion-irradiation. There are two possible explanations for the disparity between the experimental observations and the results of the simulations performed. There could be a synergistic effect, which would be difficult to investigate using currently available simulation techniques. Alternatively, the simulations do not accurately represent the physical phenomena observed, either due to shortcomings in the simulations or in parameters chosen when modelling the system. We conclude that the results observed by TEM cannot be explained by current simulations and suggest that further experimental and theoretical work be conducted in order to provide a better understanding in this area.

Regardless of the electron beam effect, the effect of high-energy displacing irradiation on helium bubbles in SiC is minimal. Bubble shrinkage is observed following ion-irradiation alone, but is a reduced effect in comparison to ion-irradiation simultaneous with electrons. This matches the previous research overview of SiC — which is that it is a radiation-hard material. This indicates that research focus should shift slightly from neutron irradiation of SiC and focus on other fusion products, such as beta decay where a more significant effect may occur in this material.

7.2 Further Work

In order to ascertain whether helium bubble shrinkage is caused by electron irradiation alone or by a synergistic effect of combined ion and electron irradiation, further *in-situ* experiments should be performed using as similar electron-beam conditions as possible. This should firmly establish the cause of helium bubble shrinkage.

Once the exact conditions for shrinkage are determined, experiments should be performed with different electron energies in order to learn more about the energetics of the displacement of helium from bubbles by the beams. This will provide important information to those performing experiments on helium bubbles in SiC (especially *in-situ*) as to which electron energy can be considered safe to operate the microscope at in order to prevent displacement of atoms from within the bubbles.

It is expected that any future uses of SiC in nuclear reactor construction will be in composite form. In order to further assess the suitability of these composites for use in such applications, similar experiments to those reported in this thesis should be conducted on composite material.

It is already known that helium bubbles form preferentially on grain boundaries in polycrystalline SiC. Investigations as to whether these bubbles can be shrunk by irradiating with ions and/or electrons may be of interest as the mechanical degredation of SiC has been attributed to bubble formation at grain boundaries. If bubble formation can be inhibited or reduced using the mechanism(s) discovered in this work, and, if it can be shown to effect bubbles grown on grain boundaries, then the degredation of polycrystalline SiC could be controlled.

Finally, it is likely that SiC will be used as a structural component because of its extremely good mechanical properties. It will be of interest to the nuclear community to perform ion-irradiation studies in a heating, straining environment in order to ascertain the effect of strain on these results in both single crystal SiC and SiC–SiC composites.

References

[1] S. Saddow and A. Adarwak, eds., *Advances in silicon carbide processing and applications*. Boston: Artech House, 2004.

[2] R. Cheung, "Introduction to Silicon Carbide Microelectromechanical Systems," in *Silicon Carbide Microelectromechanical Systems for Harsh Environments*, ch. Introducti, pp. 1–17, London, UK: Imperial College Press, first ed., 2006.

[3] G. L. Harris, ed., *Properties of Silicon Carbide*. London: INSPEC, 1995.

[4] R. P. Devaty and W. J. Choyke, "Optical Characterization of Silicon Carbide Polytypes," *Physica Status Solidi (a)*, vol. 162, pp. 5–38, July 1997.

[5] J.-H. Boo, K.-S. Yu, M. Lee, and Y. Kim, "Deposition of cubic SiC films on silicon using dimethylisopropylsilane," *Applied Physics Letters*, vol. 66, no. 25, p. 3486, 1995.

[6] H. G. Grimmeiss and J. W. Allen, "Light emitting diodes — How it started," *Journal of Non-Crystalline Solids*, vol. 352, pp. 871–880, June 2006.

[7] Y. Tairov and V. Tsvetkov, "General principles of growing large-size single crystals of various silicon carbide polytypes," *Journal of Crystal Growth*, vol. 52, pp. 146–150, Apr. 1981.

[8] Y. Tairov, "Growth of bulk SiC," *Materials Science and Engineering: B*, vol. 29, pp. 83–89, Jan. 1995.

[9] Y. Tairov and V. Tsvetkov, "Progress in controlling the growth of polytypic crystals," *Progress in Crystal Growth and Characterization*, vol. 7, pp. 111–162, Jan. 1983.

[10] R. Glass, D. Henshall, V. Tsvetkov, and C. Carter, Jr., "SiC Seeded Crystal Growth," *Physica Status Solidi (b)*, vol. 202, pp. 149–162, July 1997.

[11] Cree Scientific, "Timeline (Available at http://www.cree.com/news-and-events/ /media/Files/Cree/News and Events/Media Room/Cree Graphic Timeline.pdf)," 2012.

[12] J. Edmond, H. Kong, A. Suvorov, D. Waltz, and C. Carter, Jr., "6H-Silicon Carbide Light Emitting Diodes and UV Photodiodes," *physica status solidi (a)*, vol. 162, pp. 481–491, July 1997.

[13] W. Choi, I. Lahiri, R. Seelaboyina, and Y. S. Kang, "Synthesis of Graphene and Its Applications: A Review," *Critical Reviews in Solid State and Materials Sciences*, vol. 35, pp. 52–71, Feb. 2010.

[14] N. G. Wright, A. B. Horsfall, and K. Vassilevski, "Prospects for SiC electronics and sensors," *Materials Today*, vol. 11, pp. 16–21, Jan. 2008.

[15] Y. Katoh, L. L. Snead, I. Szlufarska, and W. J. Weber, "Radiation effects in SiC for nuclear structural applications," *Current Opinion in Solid State and Materials Science*, pp. 1–10, Apr. 2012.

[16] F. Eblagon, B. Ehrle, T. Graule, and J. Kuebler, "Development of silicon nitride/silicon carbide composites for wood-cutting tools," *Journal of the European Ceramic Society*, vol. 27, pp. 419–428, Jan. 2007.

[17] R. Johnson, "A study of the pickup of abrasive particles during abrasion of annealed aluminium on silicon carbide abrasive papers," *Wear*, vol. 16, pp. 351–358, Nov. 1970.

[18] M. Mehregany, C. Zorman, and N. Rajan, "Silicon carbide MEMS for harsh environments," *Proceedings of the IEEE*, vol. 86, no. 8, pp. 1594–1609, 1998.

[19] S. Fan, L. Zhang, Y. Xu, L. Cheng, J. Lou, J. Zhang, and L. Yu, "Microstructure and properties of 3D needle-punched carbon/silicon carbide brake materials," *Composites Science and Technology*, vol. 67, pp. 2390–2398, Sept. 2007.

[20] S. Fan, L. Zhang, Y. Xu, L. Cheng, G. Tian, S. Ke, F. Xu, and H. Liu, "Microstructure and tribological properties of advanced carbon/silicon carbide aircraft brake materials," *Composites Science and Technology*, vol. 68, pp. 3002–3009, Nov. 2008.

[21] F. Kennedy, A. Balbahadur, and D. Lashmore, "The friction and wear of Cu-based silicon carbide particulate metaal matrix composites for brake applications," *Wear*, vol. 203-204, pp. 715–721, Mar. 1997.

[22] P. G. Neudeck, "Progress in silicon carbide semiconductor electronics technology," *Journal of Electronic Materials*, vol. 24, pp. 283–288, Apr. 1995.

[23] J. Casady and R. Johnson, "Status of silicon carbide (SiC) as a wide-bandgap semiconductor for high-temperature applications: A review," *Solid-State Electronics*, vol. 39, pp. 1409–1422, Oct. 1996.

[24] C. Weitzel, J. Palmour, C. Carter, K. Moore, K. Nordquist, S. Allen, C. Thero, and M. Bhatnagar, "Silicon carbide high-power devices," *IEEE Transactions on Electron Devices*, vol. 43, no. 10, pp. 1732–1741, 1996.

[25] D. Brown, E. Downey, M. Ghezzo, J. Kretchmer, V. Krishnamurthy, W. Hennessy, and G. Michon, "Silicon carbide MOSFET technology," *Solid-State Electronics*, vol. 39, pp. 1531–1542, Nov. 1996.

[26] D. M. Brown, E. Downey, M. Ghezzo, J. Kretchmer, V. Krishnamurthy, W. Hennessy, and G. Michon, "Silicon Carbide MOSFET Integrated Circuit Technology," *Physica Status Solidi (a)*, vol. 162, pp. 459–479, July 1997.

[27] M. Bhatnagar, P. McLarty, and B. Baliga, "Silicon-carbide high-voltage (400 V) Schottky barrier diodes," *IEEE Electron Device Letters*, vol. 13, pp. 501–503, Oct. 1992.

[28] L. Calcagno, P. Musumeci, F. Roccaforte, C. Bongiorno, and G. Foti, "Crystallisation mechanism of amorphous silicon carbide," *Applied Surface Science*, vol. 184, pp. 123–127, Dec. 2001.

[29] H. Kaneda, T. Onaka, T. Nakagawa, K. Enya, H. Murakami, R. Yamashiro, T. Ezaki, Y. Numao, and Y. Sugiyama, "Cryogenic optical performance of the ASTRO-F SiC telescope.," *Applied optics*, vol. 44, pp. 6823–32, Nov. 2005.

[30] T. T. Saha, D. B. Leviton, and P. Glenn, "Performance of ion-figured silicon carbide SUMER telescope mirror in the vacuum ultraviolet," *Applied Optics*, vol. 35, p. 1742, Apr. 1996.

[31] H. Kaneda, T. Onaka, M. Kawada, and H. Murakami, "Cryogenic Optical Testing of Sandwich-Type Silicon Carbide Mirrors," *Applied Optics*, vol. 42, no. 4, p. 708, 2003.

[32] P. Spanò, F. M. Zerbi, C. J. Norrie, C. R. Cunningham, K. G. Strassmeier, A. Bianco, P. A. Blanche, M. Bougoin, M. Ghigo, P. Hartmann, L. Zago, E. Atad-Ettedgui, B. Delabre, H. Dekker, M. Melozzi, B. Snÿders, R. Takke, and D. D. Walker, "Challenges in optics for Extremely Large Telescope instrumentation," *Astronomische Nachrichten*, vol. 327, pp. 649–673, Aug. 2006.

[33] A. K. Geim, "Graphene: status and prospects.," *Science*, vol. 324, pp. 1530–4, June 2009.

[34] A. K. Geim and K. S. Novoselov, "The rise of graphene.," *Nature materials*, vol. 6, pp. 183–91, Mar. 2007.

[35] C. Soldano, A. Mahmood, and E. Dujardin, "Production, properties and potential of graphene," *Carbon*, vol. 48, pp. 2127–2150, July 2010.

[36] K. V. Emtsev, A. Bostwick, K. Horn, J. Jobst, G. L. Kellogg, L. Ley, J. L. McChesney, T. Ohta, S. A. Reshanov, J. Röhrl, E. Rotenberg, A. K. Schmid, D. Waldmann, H. B. Weber, and T. Seyller, "Towards wafer-size graphene layers by atmospheric pressure graphitization of silicon carbide.," *Nature materials*, vol. 8, pp. 203–7, Mar. 2009.

[37] C. Berger, Z. Song, T. Li, X. Li, A. Y. Ogbazghi, R. Feng, Z. Dai, A. N. Marchenkov, E. H. Conrad, P. N. First, and W. A. de Heer, "Ultrathin Epitaxial Graphite: 2D Electron Gas Properties and a Route toward Graphene-based Nanoelectronics," *The Journal of Physical Chemistry B*, vol. 108, pp. 19912–19916, Dec. 2004.

[38] C. Berger, Z. Song, X. Li, X. Wu, N. Brown, C. Naud, D. Mayou, T. Li, J. Hass, A. N. Marchenkov, E. H. Conrad, P. N. First, and W. a. de Heer, "Electronic confinement and coherence in patterned epitaxial graphene.," *Science (New York, N.Y.)*, vol. 312, pp. 1191–6, May 2006.

[39] T. Angot, "Graphitization of the 6H-SiC (0 0 0 1) surface studied by HREELS," *Surface Science*, vol. 502-503, pp. 81–85, Apr. 2002.

[40] I. Forbeaux, J. Themlin, and J. Debever, "High-temperature graphitization of the 6H-SiC (0001) face," *Surface Science*, vol. 442, pp. 9–18, 1999.

[41] I. Forbeaux, "Solid-state graphitization mechanisms of silicon carbide 6H-SiC polar faces," *Applied Surface Science*, vol. 162-163, pp. 406–412, Aug. 2000.

[42] L. Johansson, F. Owman, and P. Mårtensson, "High-resolution core-level study of 6H-SiC(0001).," *Physical review. B, Condensed matter*, vol. 53, pp. 13793–13802, May 1996.

[43] L. Johansson, F. Owman, P. Mårtensson, C. Persson, and U. Lindefelt, "Electronic structure of 6H-SiC(0001).," *Physical review. B, Condensed matter*, vol. 53, pp. 13803–13807, May 1996.

[44] L. Johansson, P.-A. Glans, and N. Hellgren, "A core level and valence band photoemission study of 6H-SiC," *Surface Science*, vol. 405, pp. 288–297, May 1998.

[45] L. Li, "Atomic structures of 6H-SiC (0001) and (000-1) surfaces," *Surface Science*, vol. 351, pp. 141–148, May 1996.

[46] F. Owman and P. Mårtensson, "STM study of the SiC(0001) $\sqrt{3} \times \sqrt{3}$ surface," *Surface Science*, vol. 330, pp. L639–L645, June 1995.

[47] T. Tsukamoto, "Annealing effect on surfaces of 4H(6H)-SiC(0001)Si face," *Applied Surface Science*, vol. 113-114, pp. 467–471, Apr. 1997.

[48] V. van Elsbergen, T. Kampen, and W. Monch, "Surface analysis of 6HSiC," *Surface Science*, vol. 365, pp. 443–452, Sept. 1996.

[49] A. Charrier, A. Coati, T. Argunova, F. Thibaudau, Y. Garreau, R. Pinchaux, I. Forbeaux, J.-M. Debever, M. Sauvage-Simkin, and J.-M. Themlin, "Solid-state decomposition of silicon carbide for growing ultra-thin heteroepitaxial graphite films," *Journal of Applied Physics*, vol. 92, no. 5, p. 2479, 2002.

[50] A. Mattausch and O. Pankratov, "Ab-Initio Study of Graphene on SiC," *Physical Review Letters*, vol. 99, pp. 1–4, Aug. 2007.

[51] K. Lewotsky, "Graphene Grows Up," *SPIE*, 2010.

[52] K. Yumkella and the Secretary-General's advisory group on energy and climate change (AGECC), "Energy for a sustainable future," Tech. Rep. April 2010, United Nations, New York, NY, 2010.

[53] J. Jacquinot, "Fifty years in fusion and the way forward," *Nuclear Fusion*, vol. 50, p. 014001, Jan. 2010.

[54] L. Snead, "Advanced SiC composites for fusion applications," *Journal of Nuclear Materials*, vol. 219, pp. 3–14, Mar. 1995.

[55] R. Jones, L. Giancarli, A. Hasegawa, Y. Katoh, A. Kohyama, B. Riccardi, L. Snead, and W. Weber, "Promise and challenges of SiCf/SiC composites for fusion energy applications," *Journal of Nuclear Materials*, vol. 307-311, pp. 1057–1072, Dec. 2002.

[56] L. Snead, R. Jones, A. Kohyama, and P. Fenici, "Status of silicon carbide composites for fusion," *Journal of Nuclear Materials*, vol. 233-237, pp. 26–36, Oct. 1996.

[57] B. Riccardi, L. Giancarli, A. Hasegawa, Y. Katoh, A. Kohyama, R. Jones, and L. Snead, "Issues and advances in SiC_f/SiC composites development for fusion reactors," *Journal of Nuclear Materials*, vol. 329-333, pp. 56–65, Aug. 2004.

[58] D. Petti, D. Crawford, and N. Chauvin, "Fuels for Advanced Nuclear Energy Systems," *MRS Bulletin*, vol. 34, pp. 40–45, Jan. 2009.

[59] R. J. Kuhudzai, *Diffusion of ion implanted iodine in 6H-SiC*. Msc dissertation, University of Pretoria, 2010.

[60] G. D. Del Cul, B. B. Spencer, C. W. Forsberg, D. E. Collins, and W. S. Rickman, "TRISO-Coated Fuel Processing to Support High-Temperature Gas-Cooled-Reactors," tech. rep., Oak Ridge National Laboratory, 2002.

[61] S. Ion, D. Nicholls, R. Matzie, and D. Matzner, "Pebble Bed Modular Reactor The First Generation IV Reactor To Be Constructed," *Nuclear Energy*, vol. 43, no. 1, pp. 55–62, 2004.

[62] L. Snead, T. Nozawa, M. Ferraris, Y. Katoh, R. Shinavski, and M. Sawan, "Silicon carbide composites as fusion power reactor structural materials," *Journal of Nuclear Materials*, vol. 417, pp. 330–339, Oct. 2011.

[63] K. Ozawa, Y. Katoh, T. Nozawa, T. Hinoki, and L. L. Snead, "Evaluation of Damage Tolerance of Advanced SiC/SiC Composites after Neutron Irradiation," *IOP Conference Series: Materials Science and Engineering*, vol. 18, p. 162005, Oct. 2011.

[64] A. Kiryushin and N. Kodochigov, "GT-MHR Project," tech. rep., IAEA, Vienna, Austria, 2002.

[65] M. P. Labar, A. S. Shenoy, W. A. Simon, and E. M. Campbell, "Status of the GT-MHR for Electricity Production," in *Proceedings of the world nuclear association annual symposium*, (London, UK), pp. 1–15, 2003.

[66] Z. Wu, D. Lin, and D. Zhong, "The design features of the HTR-10," *Nuclear Engineering and Design*, vol. 218, pp. 25–32, Oct. 2002.

[67] X. Fu, T. Liang, Y. Tang, Z. Xu, and C. Tang, "Preparation of UO_2 Kernel for HTR-10 Fuel Element," *Journal of Nuclear Science and Technology*, vol. 41, pp. 943–948, Sept. 2004.

[68] S. Shiozawa, S. Fujikawa, T. Iyoku, K. Kunitomi, and Y. Tachibana, "Overview of HTTR design features," *Nuclear Engineering and Design*, vol. 233, pp. 11–21, Oct. 2004.

[69] K. Sawa and S. Ueta, "Research and development on HTGR fuel in the HTTR project," *Nuclear Engineering and Design*, vol. 233, pp. 163–172, Oct. 2004.

[70] K. Minato, T. Ogawa, K. Fukuda, M. Shimizu, Y. Tayama, and I. Takahashi, "Fission product behavior in Triso-coated UO2 fuel particles," *Journal of Nuclear Materials*, vol. 208, pp. 266–281, Feb. 1994.

[71] G. K. Miller, D. a. Petti, J. T. Maki, and D. L. Knudson, "An evaluation of the effects of SiC layer thinning on failure of TRISO-coated fuel particles," *Journal of Nuclear Materials*, vol. 355, pp. 150–162, Sept. 2006.

[72] E. López-Honorato, J. Tan, P. Meadows, G. Marsh, and P. Xiao, "TRISO coated fuel particles with enhanced SiC properties," *Journal of Nuclear Materials*, vol. 392, pp. 219–224, July 2009.

[73] W.-J. Kim, J. N. Park, M. S. Cho, and J. Y. Park, "Effect of coating temperature on properties of the SiC layer in TRISO-coated particles," *Journal of Nuclear Materials*, vol. 392, pp. 213–218, July 2009.

[74] T. Nozawa, L. Snead, Y. Katoh, and J. Miller, "Shear properties at the PyC/SiC interface of a TRISO-coating," *Journal of Nuclear Materials*, vol. 371, pp. 304–313, Sept. 2007.

[75] L. L. Snead, T. Nozawa, Y. Katoh, T.-S. Byun, S. Kondo, and D. a. Petti, "Handbook of SiC properties for fuel performance modeling," *Journal of Nuclear Materials*, vol. 371, pp. 329–377, Sept. 2007.

[76] R. Matheny, J. Corelli, and G. Trantina, "Radiation damage in silicon carbide and graphite for fusion reactor first wall applications," *Journal of Nuclear Materials*, vol. 83, pp. 313–321, Sept. 1979.

[77] P. Rocco, H. Scholz, and M. Zucchetti, "Silicon carbide and the new low activation requirements for a fusion reactor first wall," *Journal of Nuclear Materials*, vol. 191-194, pp. 1474–1479, Sept. 1992.

[78] T. Hinoki, L. Snead, Y. Katoh, A. Hasegawa, T. Nozawa, and A. Kohyama, "The effect of high dose/high temperature irradiation on high purity fibers and their silicon carbide composites," *Journal of Nuclear Materials*, vol. 307-311, pp. 1157–1162, Dec. 2002.

[79] F. Najmabadi, W. Conn, R, and T. A. Team, "The ARIES-I Tokamak Reactor Study," *Fusion Technology*, vol. 19, pp. 783–790, 1991.

[80] S. Sharafat, R. Jones, A. Kohyama, and P. Fenici, "Status and prospects for SiC-SiC composite materials development for fusion applications," *Fusion Engineering and Design*, vol. 29, pp. 411–420, Mar. 1995.

[81] E. Bloom, S. Zinkle, and F. Wiffen, "Materials to deliver the promise of fusion power — progress and challenges," *Journal of Nuclear Materials*, vol. 329-333, pp. 12–19, Aug. 2004.

[82] R. Toschi, "Nuclear fusion, an energy source," *Fusion Engineering and Design*, vol. 36, pp. 1–8, Apr. 1997.

[83] K. Tokimatsu, J. Fujino, S. Konishi, Y. Ogawa, and K. Yamaji, "Role of nuclear fusion in future energy systems and the environment under future uncertainties," *Energy Policy*, vol. 31, pp. 775–797, June 2003.

[84] J. A. Paisner, E. M. Campbell, and W. J. Hogan, "The national ignition facility project," in *Proceedings of the American Nuclear Society*, (New Orleans, LA), 1994.

[85] J. Alvarez, A. Rivera, E. Río, K. Mima, and J. M. Perlado, "Key paramaters in the design of HiPER reaction chamber," tech. rep., IAEA, Vienna, Austria, 2010.

[86] P. Rebut, R. Bickerton, and B. Keen, "The Joint European Torus: installation, first results and prospects," *Nuclear Fusion*, vol. 25, pp. 1011–1022, Sept. 1985.

[87] M. Mayer, R. Behrisch, P. Andrew, and A. Peacock, "Erosion at the vessel walls of JET," *Journal of Nuclear Materials*, vol. 241-243, pp. 469–475, Feb. 1997.

[88] M. Keilhacker and the JET team, "Fusion physics progress on the Joint European Torus (JET)," *Plasma Physics and Controlled Fusion*, vol. 41, pp. B1–B23, Dec. 1999.

[89] A. Gibson, "Deuterium-tritium plasmas in the Joint European Torus (JET): Behavior and implications," *Physics of Plasmas*, vol. 5, no. 5, p. 1839, 1998.

[90] F. Sartori, G. de Tommasi, and F. Piccolo, "The Joint European Torus," *IEEE Control Systems Magazine*, vol. 26, pp. 64–78, Apr. 2006.

[91] G. H. Miller, E. I. Moses, and C. R. Wuest, "The National Ignition Facility," *Optical Engineering*, vol. 43, no. 12, p. 2841, 2004.

[92] E. I. Moses, "The National Ignition Facility (NIF): A path to fusion energy," *Energy Conversion and Management*, vol. 49, pp. 1795–1802, July 2008.

[93] E. I. Moses, E. Panarella, and R. Raman, "Plans for Ignition Experiments on the National Ignition Facility," *AIP Conference Proceedings*, pp. 53–59, 2009.

[94] A. T. Anderson, A. K. Burnham, M. T. Tobin, and P. F. Peterson, "Modeling and experiments of x-ray ablation of national ignition facility first wall materials," in *Proceedings of the American Nuclear Society*, (Reno, NV), 1996.

[95] L. T. Summers, J. R. Miller, and J. R. Heim, "The International Thermonuclear Experimental Reactor (ITER); Design and Materials Selection," *Advanced Cryogenic Engineering*, vol. 36, p. 769, 1990.

[96] R. Aymar, "ITER R&D: Executive Summary: Design Overview," *Fusion Engineering and Design*, vol. 55, pp. 107–118, July 2001.

[97] D. J. Campbell, "The physics of the International Thermonuclear Experimental Reactor FEAT," *Physics of Plasmas*, vol. 8, no. 5, p. 2041, 2001.

[98] Y. Shimomura, "The present status and future prospects of the ITER project," *Journal of Nuclear Materials*, vol. 329-333, pp. 5–11, Aug. 2004.

[99] V. Barabash, A. Peacock, S. Fabritsiev, G. Kalinin, S. Zinkle, A. Rowcliffe, J.-W. Rensman, A. Tavassoli, P. Marmy, P. Karditsas, F. Gillemot, and M. Akiba, "Materials challenges for ITER — Current status and future activities," *Journal of Nuclear Materials*, vol. 367-370, pp. 21–32, Aug. 2007.

[100] H. Bolt, V. Barabash, W. Krauss, J. Linke, R. Neu, S. Suzuki, and N. Yoshida, "Materials for the plasma-facing components of fusion reactors," *Journal of Nuclear Materials*, vol. 329-333, pp. 66–73, Aug. 2004.

[101] D. Clery, "ITER wall materials pass strict test," *Physics World*, Oct. 2012.

[102] G. Wright, J. Westerhout, R. Al, E. Alves, L. Alves, N. Barradas, M. van den Berg, D. Borodin, S. Brezinsek, S. Brons, H. van Eck, B. de Groot, a.W. Kleyn, W. Koppers, O. Kruijt, J. Linke, N. Lopes Cardozo, M. Mayer, H. van der Meiden, P. Prins, G. van Rooij, J. Scholten, a.E. Shumack, P. Smeets, G. De Temmerman, W. Vijvers, and J. Rapp, "Materials research under ITER-like divertor conditions at FOM Rijnhuizen," *Journal of Nuclear Materials*, vol. 417, pp. 457–462, Oct. 2011.

[103] C. Wong, V. Chernov, a. Kimura, Y. Katoh, N. Morley, T. Muroga, K. Song, Y. Wu, and M. Zmitko, "ITER-Test blanket module functional materials," *Journal of Nuclear Materials*, vol. 367-370, pp. 1287–1292, Aug. 2007.

[104] F. Dobran, "Fusion energy conversion in magnetically confined plasma reactors," *Progress in Nuclear Energy*, vol. 60, pp. 89–116, Sept. 2012.

[105] P. J. Paul, P. J. Manuel, and T. Martin, "Target manufacturing and delivery for HiPER," *Journal of Physics: Conference Series*, vol. 112, p. 032070, May 2008.

[106] B. J. L. Garrec, C. Hernandez-Gomez, T. Winstone, and J. Collier, "HiPER laser architecture principles," *Journal of Physics: Conference Series*, vol. 244, p. 032020, Aug. 2010.

[107] S. Konishi, S. Nishio, and K. Tobita, "DEMO plant design beyond ITER," *Fusion Engineering and Design*, vol. 63-64, pp. 11–17, Dec. 2002.

[108] D. Maisonnier, I. Cook, S. Pierre, B. Lorenzo, D. P. Luigi, G. Luciano, N. Prachai, and P. Aldo, "DEMO and fusion power plant conceptual studies in Europe," *Fusion Engineering and Design*, vol. 81, pp. 1123–1130, Feb. 2006.

[109] D. Maisonnier, "European DEMO design and maintenance strategy," *Fusion Engineering and Design*, vol. 83, pp. 858–864, Dec. 2008.

[110] R. Lässer, N. Baluc, J.-L. Boutard, E. Diegele, S. Dudarev, M. Gasparotto, a. Möslang, R. Pippan, B. Riccardi, and B. van der Schaaf, "Structural materials for DEMO: The EU development, strategy, testing and modelling," *Fusion Engineering and Design*, vol. 82, pp. 511–520, Oct. 2007.

[111] K. Ehrlich, E. Bloom, and T. Kondo, "International strategy for fusion materials development," *Journal of Nuclear Materials*, vol. 283-287, pp. 79–88, Dec. 2000.

[112] K. Ehrlich, "Materials research towards a fusion reactor," *Fusion Engineering and Design*, vol. 56-57, pp. 71–82, Oct. 2001.

[113] W. N. Association, "Nuclear Power in the United Kingdom http://www.world-nuclear.org/info/inf84.html(accessed 25/10/2012)," 2012.

[114] EDF Energy, "Our Nuclear Power Stations. Available from http://www.edfenergy.com/about-us/energy-generation/nuclear-generation/nuclear-power-stations/ (Accessed 12/12/2012)," 2012.

[115] C. Patchett and The Office of Nuclear Regulation, "Chief Nuclear Inspector's Annual Report 2013," Tech. Rep. 2013, Office of Nuclear Regulation, Bootle, Liverpool, UK, 2013.

[116] S. Grover and M. Metcalfe, "Graphite Materials Testing in the ATR for Lifetime Management of Magnox Reactors," *... of the Conference on High Temperature Reactors ...*, 2002.

[117] C. Bataille and C. Birraux, "Lifetime of Nuclear Power Plants and New Designs of Reactors," Tech. Rep. 832, Parliamentary office for scientific and technological assessment, Paris, France, 2003.

[118] J. Jowit, "Nuclear reactor reprieve puts UK energy plans in doubt," May 2012.

[119] A. Hasegawa, M. Saito, S. Nogami, K. Abe, R. Jones, and H. Takahashi, "Helium-bubble formation behavior of SiCf/SiC composites after helium implantation," *Journal of Nuclear Materials*, vol. 264, pp. 355–358, Jan. 1999.

[120] G. S. Was, *Fundamentals of Radiation Materials Science*. New York: Springer, 1st ed., 2007.

[121] G. Pensl, F. Ciobanu, T. Frank, M. Kreiger, S. Reshanov, F. Schmid, and M. Weidner, "SiC Material Properties," *International Journal of High Speed Electronics and Systems*, vol. 15, no. 4, pp. 705–745, 2005.

[122] F. Bechstedt, P. Käckell, A. Zywietz, K. Karch, B. Adolph, K. Tenelsen, and J. Furthmüller, "Polytypism and Properties of Silicon Carbide," *physica status solidi (b)*, vol. 202, pp. 35–62, July 1997.

[123] K. Karch, P. Pavone, W. Windl, O. Schütt, and D. Strauch, "Ab initio calculation of structural and lattice-dynamical properties of silicon carbide," *Physical Review B*, vol. 50, pp. 17054–17063, Dec. 1994.

[124] C. Park, B.-h. Cheong, K.-h. Lee, and K. Chang, "Structural and electronic properties of cubic, 2H, 4H, and 6H SiC," *Physical Review B*, vol. 49, pp. 4485–4493, Feb. 1994.

[125] D. N. Talwar and J. C. Sherbondy, "Thermal expansion coefficient of 3C-SiC," *Applied Physics Letters*, vol. 67, no. 22, p. 3301, 1995.

[126] Z. Li and R. C. Bradt, "Thermal expansion of the hexagonal (4H) polytype of SiC," *Journal of Applied Physics*, vol. 60, no. 2, p. 612, 1986.

[127] G. L. DesAutels, P. Powers, C. Brewer, M. Walker, M. Burky, and G. Anderson, "Optical temperature sensor and thermal expansion measurement using a femtosecond micromachined grating in 6H-SiC.," *Applied optics*, vol. 47, pp. 3773–7, July 2008.

[128] Y. Tairov and V. Tsvetkov, "Semiconductor Compounds AIV BIV," in *Handbook on Electrotechnical Materials* (Y. Koritskii, V. Pasynkov, and B. Tareev, eds.), pp. 446–471, Leningrad: Energomashizdat, 1988.

[129] R. Han, X. Xu, X. Hu, N. Yu, J. Wang, Y. Tian, and W. Huang, "Development of bulk SiC single crystal grown by physical vapor transport method," *Optical Materials*, vol. 23, pp. 415–420, July 2003.

[130] R. Stein and P. Lanig, "Control of polytype formation by surface energy effects during the growth of SiC monocrystals by the sublimation method," *Journal of Crystal Growth*, vol. 131, pp. 71–74, July 1993.

[131] R. Yakimova, M. Syväjärvi, T. Iakimov, H. Jacobsson, R. Rå back, A. Vehanen, and E. Janzén, "Polytype stability in seeded sublimation growth of 4H-SiC boules," *Journal of Crystal Growth*, vol. 217, pp. 255–262, Aug. 2000.

[132] M. Kanaya, J. Takahashi, Y. Fujiwara, and A. Moritani, "Controlled sublimation growth of single crystalline 4H-SiC and 6H-SiC and identification of polytypes by x-ray diffraction," *Applied Physics Letters*, vol. 58, no. 1, p. 56, 1991.

[133] D. Hofmann, E. Schmitt, M. Bickermann, M. Kölbl, P. Wellmann, and A. Winnacker, "Analysis on defect generation during the SiC bulk growth process," *Materials Science and Engineering: B*, vol. 61-62, pp. 48–53, July 1999.

[134] M. Dudley, S. Wang, W. Huang, C. H. Carter, V. F. Tsvetkov, and C. Fazi, "White-beam synchrotron topographic studies of defects in 6H-SiC single crystals," *Journal of Physics D: Applied Physics*, vol. 28, pp. A63–A68, Apr. 1995.

[135] D. Barrett, J. McHugh, H. Hobgood, R. Hopkins, P. McMullin, R. Clarke, and W. Choyke, "Growth of large SiC single crystals," *Journal of Crystal Growth*, vol. 128, pp. 358–362, Mar. 1993.

[136] S. Wang and J. He, "Defects analysis in single crystalline 6H-SiC at different PVT growth stages," *Materials Science and Engineering: B*, vol. 83, pp. 8–12, June 2001.

[137] L. N. Zhu, H. Li, B. Q. Hu, X. Wu, and X. L. Chen, "New type of defects in SiC grown by the PVT method," *Journal of Physics: Condensed Matter*, vol. 17, pp. L85–L91, Mar. 2005.

[138] H. S. Kong, J. T. Glass, and R. F. Davis, "Epitaxial growth of β-SiC thin films on 6H α-SiC substrates via chemical vapor deposition," *Applied Physics Letters*, vol. 49, no. 17, p. 1074, 1986.

[139] C. R. Eddy and D. K. Gaskill, "Materials science. Silicon carbide as a platform for power electronics.," *Science (New York, N.Y.)*, vol. 324, pp. 1398–400, June 2009.

[140] C. R. Stoldt, C. Carraro, W. Ashurst, D. Gao, R. T. Howe, and R. Maboudian, "A low-temperature CVD process for silicon carbide MEMS," *Sensors and Actuators A: Physical*, vol. 97-98, pp. 410–415, Apr. 2002.

[141] R. Rupp, Y. Makarov, H. Behner, and A. Wiedenhofer, "Silicon Carbide Epitaxy in a Vertical CVD Reactor: Experimental Results and Numerical Process Simulation," *Physica Status Solidi (b)*, vol. 202, pp. 281–304, July 1997.

[142] J. Chin, P. Gantzel, and R. Hudson, "The structure of chemical vapor deposited silicon carbide," *Thin Solid Films*, vol. 40, pp. 57–72, Jan. 1977.

[143] J. Powell and D. Larkin, "Process-Induced Morphological Defects in Epitaxial CVD Silicon Carbide," *Physica Status Solidi (b)*, vol. 202, pp. 529–548, July 1997.

[144] A. Henry, J. ul Hassan, J. P. Bergman, C. Hallin, and E. Janzén, "Thick Silicon Carbide Homoepitaxial Layers Grown by CVD Techniques," *Chemical Vapor Deposition*, vol. 12, pp. 475–482, Sept. 2006.

[145] C. A. Zorman, A. J. Fleischman, A. S. Dewa, M. Mehregany, C. Jacob, S. Nishino, and P. Pirouz, "Epitaxial growth of 3C-SiC films on 4 in. diam (100) silicon wafers by atmospheric pressure chemical vapor deposition," *Journal of Applied Physics*, vol. 78, no. 8, p. 5136, 1995.

[146] H. Nagasawa and Y. Yamaguchi, "Atomic level epitaxy of 3C-SiC by low pressure vapour deposition with alternating gas supply," *Thin Solid Films*, vol. 225, pp. 230–234, Mar. 1993.

[147] I. Golecki, F. Reidinger, and J. Marti, "Single-crystalline, epitaxial cubic SiC films grown on (100) Si at 750 ÂřC by chemical vapor deposition," *Applied Physics Letters*, vol. 60, no. 14, p. 1703, 1992.

[148] S. Saddow, M. Mazzola, S. Rendakova, and V. Dmitriev, "Silicon carbide CVD homoepitaxy on wafers with reduced micropipe density," *Materials Science and Engineering: B*, vol. 61-62, pp. 158–160, July 1999.

[149] D.-J. Kim, D.-J. Choi, and Y.-W. Kim, "Effect of reactant depletion on the microstructure and preferred orientation of polycrystalline SiC films by chemical vapor deposition," *Thin Solid Films*, vol. 266, pp. 192–197, Oct. 1995.

[150] X.-A. Fu, R. Jezeski, C. a. Zorman, and M. Mehregany, "Use of deposition pressure to control residual stress in polycrystalline SiC films," *Applied Physics Letters*, vol. 84, no. 3, p. 341, 2004.

[151] M. Nastasi, J. W. Mayer, and J. K. Hirvonen, *Ion-Solid interactions: Fundementals and applications*. Cambridge, UK: Cambridge University Press, first ed., 1996.

[152] J. F. Ziegler, J. Biersack, and M. Ziegler, *SRIM: The stopping and range of ions in matter*. Chester, MD, USA: SRIM Co., 2008.

[153] R. Simonton and A. F. Tasch, "Channeling effects in ion implantation," in *Handbook of ion implantation technology* (J. F. Ziegler, ed.), pp. 119–221, Amsterdam: Elsevier B.V., 1992.

[154] E. Morvan, P. Godignon, M. Vellvehi, a. HalleÌĄn, M. Linnarsson, and a. Y. Kuznetsov, "Channeling implantations of Al[sup +] into 6H silicon carbide," *Applied Physics Letters*, vol. 74, no. 26, p. 3990, 1999.

[155] I. Chakarov and M. Temkin, "Modelling of ion implantation in SiC crystals," *Nuclear Instruments and Methods in Physics Research Section B: Beam Interactions with Materials and Atoms*, vol. 242, pp. 690–692, Jan. 2006.

[156] M. T. Robinson, "Basic physics of radiation damage production," *Journal of Nuclear Materials*, vol. 216, pp. 1–28, 1994.

[157] J. Williams and J. Poate, eds., *Ion Implantation and Beam Processing*. New York: Academic Press, 1984.

[158] J. F. Ziegler, "SRIM-2003," *Nuclear Instruments and Methods in Physics Research Section B: Beam Interactions with Materials and Atoms*, vol. 219-220, pp. 1027–1036, June 2004.

[159] H. H. Andersen and H. L. Bay, "Sputtering yield measurements," *Topics in Applied Physics*, vol. 47, pp. 145–218, 1981.

[160] J. J. Ayache, L. Beaunier, J. Boumendil, G. Ehret, and D. D. Laub, *Sample Preparation Handbook for Transmission Electron Microscopy*. New York: Springer, 2010.

[161] C. Khare, J. Gerlach, C. Patzig, and B. Rauschenbach, "Ion beam sputter deposition of epitaxial Ag films on native oxide covered Si(100) substrates," *Applied Surface Science*, vol. 258, pp. 9617–9622, Oct. 2012.

[162] H. Le-Quoc, A. Lacoste, S. Béchu, a. Bès, D. Bourgault, and D. Fruchart, "Deposition of thin films of $Mg_2Si_{1-x}Sn_x$ solid solution by plasma-assisted co-sputtering," *Journal of Alloys and Compounds*, vol. 538, pp. 73–78, Oct. 2012.

[163] J. Roth, J. Bohdansky, W. Poschenrieder, and M. Sinha, "Physical and chemical sputtering of graphite and SiC by hydrogen and helium in the energy range of 600 to 7500 eV," *Journal of Nuclear Materials*, vol. 63, pp. 222–229, Dec. 1976.

[164] K. Sone, M. Saidoh, K. Nakamura, R. Yamada, Y. Murakami, T. Shikama, M. Fukutomi, M. Kitajima, and M. Okada, "Sputtering of silicon carbide coatings by low-energy hydrogen ions," *Journal of Nuclear Materials*, vol. 98, pp. 270–278, June 1981.

[165] R. Menzel, T. Bachmann, F. Machalett, W. Wesch, U. Lang, M. Wendt, C. Musil, and R. Mühle, "Surface smoothing and patterning of SiC by focused ion beams," *Applied Surface Science*, vol. 136, pp. 1–7, Oct. 1998.

[166] L. Bischoff, J. Teichert, and V. Heera, "Focused ion beam sputtering investigations on SiC," *Applied Surface Science*, vol. 184, pp. 372–376, Dec. 2001.

[167] K. Wittmaack, "Reliability of a popular simulation code for predicting sputtering yields of solids and ranges of low-energy ions," *Journal of Applied Physics*, vol. 96, no. 5, p. 2632, 2004.

[168] G. Ecke, R. Kosiba, V. Kharlamov, Y. Trushin, and J. Pezoldt, "The estimation of sputtering yields for SiC and Si," *Nuclear Instruments and Methods in Physics Research Section B: Beam Interactions with Materials and Atoms*, vol. 196, pp. 39–50, Nov. 2002.

[169] H. J. Queisser, "Defects in Semiconductors: Some Fatal, Some Vital," *Science*, vol. 281, pp. 945–950, Aug. 1998.

[170] A. Kelly, G. Groves, and P. Kidd, *Crystallography and crystal defects*. Chichester: John Wiley and Sons, first ed., 2000.

[171] A. Mattausch, *Ab initio-Theory of Point Defects and Defect Complexes in SiC*. PhD thesis, University of Erlangen-Nurnberg, 2005.

[172] C. Kittel, *Introduction to Solid State Physics*. New York: John Wiley and Sons, seventh ed., 1996.

[173] J. Bergman, L. Storasta, F. Carlsson, S. Sridhara, B. Magnusson, and E. Janzen, "Defects in 4H silicon carbide," *Physica B: Condensed Matter*, vol. 308-310, pp. 675–679, Dec. 2001.

[174] T. Dalibor, G. Pensl, H. Matsunami, T. Kimoto, W. J. Choyke, A. Schöner, and N. Nordell, "Deep Defect Centers in Silicon Carbide Monitored with Deep Level Transient Spectroscopy," *Physica Status Solidi (a)*, vol. 162, pp. 199–225, July 1997.

[175] F. Gao, W. Weber, M. Posselt, and V. Belko, "Atomistic study of intrinsic defect migration in 3C-SiC," *Physical Review B*, vol. 69, pp. 2–6, June 2004.

[176] N. Son, P. Hai, and E. Janzén, "Carbon vacancy-related defect in 4H and 6H SiC," *Physical Review B*, vol. 63, pp. 4–7, Apr. 2001.

[177] N. Son, P. Hai, and E. Janzén, "Silicon Antisite in 4H SiC," *Physical Review Letters*, vol. 87, pp. 2–5, July 2001.

[178] A. Gali, P. Deák, E. Rauls, N. Son, I. Ivanov, F. Carlsson, E. Janzén, and W. Choyke, "Anti-site pair in SiC: a model of the DI center," *Physica B: Condensed Matter*, vol. 340-342, pp. 175–179, Dec. 2003.

[179] F. Gao and W. J. Weber, "Computer simulation of disordering and amorphization by Si and Au recoils in 3C-SiC," *Journal of Applied Physics*, vol. 89, no. 8, p. 4275, 2001.

[180] Y. Gao, S. I. Soloviev, and T. S. Sudarshan, "Investigation of boron diffusion in 6H-SiC," *Applied Physics Letters*, vol. 83, no. 5, p. 905, 2003.

[181] G. Lucas and L. Pizzagalli, "Theoretical study of the recombination of Frenkel pairs in irradiated silicon carbide," *Journal of Physics: Condensed Matter*, vol. 19, p. 086208, Feb. 2007.

[182] J. Chen, P. Jung, and H. Trinkaus, "Evolution of Helium Platelets and Associated Dislocation Loops in α-SiC," *Physical Review Letters*, vol. 82, pp. 2709–2712, Mar. 1999.

[183] P. O. a. Persson, L. Hultman, M. S. Janson, a. HalleÌĄn, R. Yakimova, D. Panknin, and W. Skorupa, "On the nature of ion implantation induced dislocation loops in 4H-silicon carbide," *Journal of Applied Physics*, vol. 92, no. 5, p. 2501, 2002.

[184] R. Price, "Neutron irradiation-induced voids in β-silicon carbide," *Journal of Nuclear Materials*, vol. 48, pp. 47–57, Aug. 1973.

[185] T. YANO, "Structures of Dislocation Loops in Some Ceramics Induced by Fast Neutron Irradiation.," *Journal of the Ceramic Society of Japan*, vol. 111, no. 1291, pp. 155–161, 2003.

[186] A. Hallén, M. Janson, A. Kuznetsov, D. Å berg, M. Linnarsson, B. Svensson, P. Persson, F. Carlsson, L. Storasta, J. Bergman, S. Sridhara, and Y. Zhang, "Ion implantation of silicon carbide," *Nuclear Instruments and Methods in Physics Research Section B: Beam Interactions with Materials and Atoms*, vol. 186, pp. 186–194, Jan. 2002.

[187] M. Dudley, X. R. Huang, W. Huang, A. Powell, S. Wang, P. Neudeck, and M. Skowronski, "The mechanism of micropipe nucleation at inclusions in silicon carbide," *Applied Physics Letters*, vol. 75, no. 6, p. 784, 1999.

[188] J. Takahashi, M. Kanaya, and Y. Fujiwara, "Sublimation growth of SiC single crystalline ingots on faces perpendicular to the (0001) basal plane," *Journal of Crystal Growth*, vol. 135, pp. 61–70, Jan. 1994.

[189] H. Tanaka, Y. Uemura, and Y. Inomata, "Observations of holes around dislocation core in SiC crystal," *Journal of Crystal Growth*, vol. 53, pp. 630–632, June 1981.

[190] E. Oliviero, M. L. David, M. F. Beaufort, J. Nomgaudyte, L. Pranevicius, A. Declemy, and J. F. Barbot, "Formation of bubbles by high dose He implantation in 4H-SiC," *Journal of Applied Physics*, vol. 91, no. 3, p. 1179, 2002.

[191] U. Lindefelt, H. Iwata, S. Öberg, and P. Briddon, "Stacking faults in 3C-, 4H-, and 6H-SiC polytypes investigated by an ab initio supercell method," *Physical Review B*, vol. 67, pp. 1–12, Apr. 2003.

[192] T. A. Kuhr, J. Liu, H. J. Chung, M. Skowronski, and F. Szmulowicz, "Spontaneous formation of stacking faults in highly doped 4H-SiC during annealing," *Journal of Applied Physics*, vol. 92, no. 10, p. 5863, 2002.

[193] H. J. Chung, J. Q. Liu, and M. Skowronski, "Stacking fault formation in highly doped 4H-SiC epilayers during annealing," *Applied Physics Letters*, vol. 81, no. 20, p. 3759, 2002.

[194] J. Q. Liu, H. J. Chung, T. Kuhr, Q. Li, and M. Skowronski, "Structural instability of 4H-SiC polytype induced by n-type doping," *Applied Physics Letters*, vol. 80, no. 12, p. 2111, 2002.

[195] G. Foti, "Silicon carbide: from amorphous to crystalline material," *Applied Surface Science*, vol. 184, pp. 20–26, Dec. 2001.

[196] S. Harada, M. Ishimaru, T. Motooka, T. Nakata, T. Yoneda, and M. Inoue, "Recrystallization of MeV Si implanted 6H-SiC," *Applied Physics Letters*, vol. 69, no. 23, p. 3534, 1996.

[197] V. Heera, R. Kögler, W. Skorupa, and J. Stoemenos, "Complete recrystallization of amorphous silicon carbide layers by ion irradiation," *Applied Physics Letters*, vol. 67, no. 14, p. 1999, 1995.

[198] P. Neudeck and J. Powell, "Performance limiting micropipe defects in silicon carbide wafers," *IEEE Electron Device Letters*, vol. 15, pp. 63–65, Feb. 1994.

[199] T. A. Kuhr, E. K. Sanchez, M. Skowronski, W. M. Vetter, and M. Dudley, "Hexagonal voids and the formation of micropipes during SiC sublimation growth," *Journal of Applied Physics*, vol. 89, no. 8, p. 4625, 2001.

[200] N. Ghoniem, S. Sharafat, J. Williams, and L. Mansur, "Theory of helium transport and clustering in materials under irradiation," *Journal of Nuclear Materials*, vol. 117, pp. 96–105, July 1983.

[201] S. E. Donnelly, "The density and pressure of helium in bubbles in implanted metals: A critical review," *Radiation Effects*, vol. 90, pp. 1–47, Sept. 1985.

[202] L. Mansur and W. Coghlan, "Mechanisms of helium interaction with radiation effects in metals and alloys: A review," *Journal of Nuclear Materials*, vol. 119, pp. 1–25, Nov. 1983.

[203] L. Di Cioccio, F. Letertre, Y. Le Tiec, A. Papon, C. Jaussaud, and M. Bruel, "Silicon carbide on insulator formation by the Smart-Cut process," *Materials Science and Engineering: B*, vol. 46, pp. 349–356, Apr. 1997.

[204] D. Senor, G. Youngblood, L. Greenwood, D. Archer, D. Alexander, M. Chen, and G. Newsome, "Defect structure and evolution in silicon carbide irradiated to 1 dpa-SiC at 1100 ÂřC," *Journal of Nuclear Materials*, vol. 317, pp. 145–159, May 2003.

[205] S. Leclerc, a. DecleÌĄmy, M. F. Beaufort, C. Tromas, and J. F. Barbot, "Swelling of SiC under helium implantation," *Journal of Applied Physics*, vol. 98, no. 11, p. 113506, 2005.

[206] J. Aihara, K. Hojou, S. Furuno, M. Ishihara, and K. Hayashi, "Amorphization with ion irradiation and recrystallization by annealing of SiC crystals," *Nuclear Instruments and Methods in Physics Research Section B: Beam Interactions with Materials and Atoms*, vol. 166-167, pp. 379–384, May 2000.

[207] J. Barbot, M. Beaufort, M. Texier, and C. Tromas, "Swelling and stacking fault formation in helium implanted SiC," *Journal of Nuclear Materials*, vol. 413, pp. 162–165, June 2011.

[208] I.-T. Bae, W. J. Weber, and Y. Zhang, "Direct measurement of local volume change in ion-irradiated and annealed SiC," *Journal of Applied Physics*, vol. 106, no. 12, p. 123525, 2009.

[209] A. Benyagoub, "Irradiation effects induced in silicon carbide by low and high energy ions," *Nuclear Instruments and Methods in Physics Research Section B: Beam Interactions with Materials and Atoms*, vol. 266, pp. 2766–2771, June 2008.

[210] H. Scholz, a.J. Frias Rebelo, D. Rickerby, P. Krogul, W. Lee, J. Evans, and P. Fenici, "Swelling behaviour and TEM studies of SiCf/SiC composites after fusion relevant helium implantation," *Journal of Nuclear Materials*, vol. 258-263, pp. 1572–1576, Oct. 1998.

[211] C. Tromas, V. Audurier, S. Leclerc, M. Beaufort, a. Declémy, and J. Barbot, "Evolution of mechanical properties of SiC under helium implantation," *Journal of Nuclear Materials*, vol. 373, pp. 142–149, Feb. 2008.

[212] T. Iseki, T. Maruyama, T. Yano, T. Suzuki, and T. Mori, "Effects of neutron irradiation and subsequent annealing on strength and toughness of SiC ceramics," *Journal of Nuclear Materials*, vol. 170, pp. 95–100, Jan. 1990.

[213] D. B. Williams and C. B. Carter, *Transmission Electron Microscopy : A textbook for Materials Science*. New York: Springer, 2nd ed., 2009.

[214] S. Klepeis, J. Benedict, and R. Anderson, "A grinding/polishing tool for TEM sample preparation," in *Materials research society symposium proceedings* (J. Bravman, R. Anderson, and M. McDonald, eds.), (Pittsburgh, Pennsylvania), pp. 179–184, 1987.

[215] T. Ishitani, H. Tsuboi, and T. Yaguchi, "Transmission electron microscope sample preparation using a focused ion beam," *Journal of Electron Microscopy*, vol. 326, pp. 322–326, 1994.

[216] F. A. Stevie, C. B. Vartuli, L. A. Giannuzzi, T. L. Shofner, S. R. Brown, B. Rossie, F. Hillion, R. H. Mills, M. Antonell, R. B. Irwin, and B. M. Purcell, "Application of focused ion beam lift-out specimen preparation to TEM, SEM, STEM, AES and SIMS analysis," *Surface and Interface Analysis*, vol. 31, pp. 345–351, May 2001.

[217] J. McCaffrey, M. Phaneuf, and L. Madsen, "Surface damage formation during ion-beam thinning of samples for transmission electron microscopy," *Ultramicroscopy*, vol. 87, pp. 97–104, Apr. 2001.

[218] S. Walck, "The small angle cleavage technique applied to coatings and thin films," *Thin solid films*, vol. 309, pp. 399–405, 1997.

[219] M. Ishimaru, I.-T. Bae, A. Hirata, Y. Hirotsu, J. Valdez, and K. Sickafus, "Volume swelling of amorphous SiC during ion-beam irradiation," *Physical Review B*, vol. 72, pp. 1–7, July 2005.

[220] W. Jiang, Y. Zhang, M. H. Engelhard, W. J. Weber, G. J. Exarhos, J. Lian, and R. C. Ewing, "Behavior of Si and C atoms in ion amorphized SiC," *Journal of Applied Physics*, vol. 101, no. 2, p. 023524, 2007.

[221] S. Leclerc, M. F. Beaufort, a. DecleÌĄmy, and J. F. Barbot, "Evolution of defects upon annealing in He-implanted 4H-SiC," *Applied Physics Letters*, vol. 93, no. 12, p. 122101, 2008.

[222] E. Oliviero, M. Beaufort, F. Pailloux, and J. Barbot, "Damage formation in high energy helium implanted 4H-SiC," *Nuclear Instruments and Methods in Physics Research Section B: Beam Interactions with Materials and Atoms*, vol. 218, pp. 391–395, June 2004.

[223] Y. Zhang, W. J. Weber, W. Jiang, C. M. Wang, A. HalleÌĄn, and G. Possnert, "Effects of implantation temperature and ion flux on damage accumulation in Al-implanted 4H-SiC," *Journal of Applied Physics*, vol. 93, no. 4, p. 1954, 2003.

[224] Y. Zhang, I.-t. Bae, K. Sun, C. Wang, M. Ishimaru, Z. Zhu, W. Jiang, and W. Weber, "Damage profile and ion distribution of slow heavy ions in compounds," *Journal of Applied Physics*, vol. 105, no. 10, p. 104901, 2009.

[225] S. Ha, H. Chung, N. Nuhfer, and M. Skowronski, "Dislocation nucleation in 4H silicon carbide epitaxy," *Journal of Crystal Growth*, vol. 262, pp. 130–138, Feb. 2004.

[226] L. Snead, S. Zinkle, J. Hay, and M. Osborne, "Amorphization of SiC under ion and neutron irradiation," *Nuclear Instruments and Methods in Physics Research Section B: Beam Interactions with Materials and Atoms*, vol. 141, pp. 123–132, May 1998.

[227] L. Snead and J. C. Hay, "Neutron irradiation induced amorphization of silicon carbide," *Journal of Nuclear Materials*, vol. 273, pp. 213–220, 1999.

[228] D. Rao and K. Muraleedharan, "TEM specimen preparation techniques," *Microscopy: Science, Technology, Applications and Education*, no. 320, pp. 1232–1244, 2010.

[229] Y. Katoh, H. Kishimoto, and A. Kohyama, "Low Temperature Swelling in Beta-SiC Associated with Point Defect Accumulation," *Materials Transactions*, vol. 43, no. 4, pp. 612–616, 2002.

[230] C. Zhang, S. Donnelly, V. Vishnyakov, J. Evans, T. Shibayama, and Y. Sun, "A study of the formation of nanometer-scale cavities in helium-implanted 4H-SiC," *Nuclear Instruments and Methods in Physics Research Section B: Beam Interactions with Materials and Atoms*, vol. 218, pp. 53–60, June 2004.

[231] R. C. Birtcher, M. Kirk, K. Furuya, G. Lumpkin, and M.-O. Ruault, "In situ Transmission Electron Microscopy Investigation of Radiation Effects," *Journal of Materials Research*, vol. 20, pp. 1654–1683, Mar. 2005.

[232] N. Frangis, J. van Landuyt, M. Grimaldi, and L. Calcagno, "Electron microscopy and Rutherford backscattering spectrometry characterisation of 6H SiC samples implanted with He+," *Nuclear Instruments and Methods in Physics Research Section B: Beam Interactions with Materials and Atoms*, vol. 120, pp. 186–189, Dec. 1996.

[233] Y. Pacaud, W. Skorupa, and J. Stoemenos, "Microstructural characterization of amorphized and recrystallized 6H-SiC," *Nuclear Instruments and Methods in Physics Research Section B: Beam Interactions with Materials and Atoms*, vol. 120, pp. 181–185, Dec. 1996.

[234] W. Weber, "Temperature and dose dependence of ion-beam-induced amorphization in α-SiC," *Journal of Nuclear Materials*, vol. 244, pp. 258–265, Apr. 1997.

[235] W. Weber, "Structure and properties of ion-beam-modified (6H) silicon carbide," *Materials Science and Engineering A*, vol. 253, pp. 62–70, Sept. 1998.

[236] M. Ishimaru, S. Harada, T. Motooka, T. Nakata, T. Yoneda, and M. Inoue, "Amorphization and solid phase epitaxy of high-energy ion implanted 6H-SiC," *Nuclear Instruments and Methods in Physics Research Section B: Beam Interactions with Materials and Atoms*, vol. 127-128, pp. 195–197, May 1997.

[237] M. Ishimaru, R. M. Dickerson, and K. E. Sickafus, "High-dose oxygen ion implantation into 6H-SiC," *Applied Physics Letters*, vol. 75, no. 3, p. 352, 1999.

[238] J. Chen and P. Jung, "Effect of helium on radiation damage in a SiC/C composite," *Ceramics International*, vol. 26, pp. 513–516, June 2000.

[239] H. Kishimoto, Y. Katoh, and A. Kohyama, "Microstructural stability of SiC and SiC/SiC composites under high temperature irradiation environment," *Journal of Nuclear Materials*, vol. 307-311, pp. 1130–1134, Dec. 2002.

[240] C. H. Zhang, S. E. Donnelly, V. M. Vishnyakov, and J. H. Evans, "Dose dependence of formation of nanoscale cavities in helium-implanted 4H-SiC," *Journal of Applied Physics*, vol. 94, no. 9, 2003.

[241] J. F. Barbot, S. Leclerc, M.-L. David, E. Oliviero, R. Montsouka, F. Pailloux, D. Eyidi, M.-F. Denanot, M.-F. Beaufort, A. Declémy, V. Audurier, and C. Tromas, "Helium implantation into 4H-SiC," *Physica Status Solidi (a)*, vol. 206, pp. 1916–1923, Aug. 2009.

[242] N. Asaoka, "Formation of Si clusters in electron-irradiated SiC studied by electron energy-loss spectroscopy," *Diamond and Related Materials*, vol. 10, pp. 1251–1254, July 2001.

[243] S. Muto, T. Tanabe, T. Shibayama, and H. Takahashi, "Damaging process of α-SiC under electron irradiation studied with electron microscopy and spectroscopy," *Nuclear Instruments and Methods in Physics Research Section B: Beam Interactions with Materials and Atoms*, vol. 191, pp. 519–523, May 2002.

[244] I.-T. Bae, W. J. Weber, M. Ishimaru, and Y. Hirotsu, "Effect of ionization rates on dynamic recovery processes during electron-beam irradiation of 6H-SiC," *Applied Physics Letters*, vol. 90, no. 12, p. 121910, 2007.

[245] W. Weber, L. Wang, Y. Zhang, W. Jiang, and I. Bae, "Effects of dynamic recovery on amorphization kinetics in 6H-SiC," *Nuclear Instruments and Methods in Physics Research Section B: Beam Interactions with Materials and Atoms*, vol. 266, pp. 2793–2796, June 2008.

[246] I.-T. Bae, M. Ishimaru, and Y. Hirotsu, "Structural changes of SiC under electron-beam irradiation: Temperature dependence," *Nuclear Instruments and Methods in Physics Research B*, vol. 250, pp. 315–319, 2006.

[247] J. Hinks, "A review of transmission electron microscopes with in situ ion irradiation," *Nuclear Instruments and Methods in Physics Research Section B: Beam Interactions with Materials and Atoms*, vol. 267, pp. 3652–3662, Dec. 2009.

[248] C. W. Allen and E. A. Ryan, "In situ transmission electron microscopy employed for studies of effects of ion and electron irradiation on materials," *Microscopy Research and Technique*, vol. 42, no. 4, pp. 255–259, 1998.

[249] Y. Serruys, M.-O. Ruault, P. Trocellier, S. Henry, O. Kaïtasov, and P. Trouslard, "Multiple ion beam irradiation and implantation: JANNUS project," *Nuclear Instruments and Methods in Physics Research Section B: Beam Interactions with Materials and Atoms*, vol. 240, pp. 124–127, Oct. 2005.

[250] J. A. Hinks, J. A. van den Berg, and S. E. Donnelly, "MIAMI: Microscope and ion accelerator for materials investigations," *Journal of Vacuum Science & Technology A: Vacuum, Surfaces, and Films*, vol. 29, no. 2, p. 021003, 2011.

[251] K. Hattar, P. Rossi, G. Vizkelethy, and B. Doyle, "The Feasibility and Development of an In situ Ion Irradiation TEM at Sandia National Laboratories," *Microscopy and Microanalysis*, vol. 17, pp. 498–499, Oct. 2011.

[252] E. Salonen, K. Nordlund, J. Keinonen, and C. Wu, "Chemical sputtering of amorphous silicon carbide under hydrogen bombardment," *Applied Surface Science*, vol. 184, pp. 387–390, Dec. 2001.

[253] M. Balden, S. Picarle, and J. Roth, "Mechanism of the chemical erosion of SiC under hydrogen irradiation," *Journal of Nuclear Materials*, vol. 290-293, pp. 47–51, Mar. 2001.

[254] H. Plank, R. Schwörer, and J. Roth, "Erosion behaviour and surface composition modifications of SiC under D+ ion bombardment," *Nuclear*

Instruments and Methods in Physics Research Section B: Beam Interactions with Materials and Atoms, vol. 111, pp. 63–69, Apr. 1996.

[255] K. Danno and T. Kimoto, "Investigation of deep levels in n-type 4H-SiC epilayers irradiated with low-energy electrons," *Journal of Applied Physics*, vol. 100, no. 11, p. 113728, 2006.

[256] A. A. Barry, B. Lehmann, D. Fritsch, and D. Braunig, "Energy dependence of electron damage and displacement threshold energy in 6H silicon carbide," *IEEE Transactions on Nuclear Science*, vol. 38, no. 6, pp. 1111–1115, 1991.

[257] L. Storasta, J. P. Bergman, E. JanzeÌĄn, A. Henry, and J. Lu, "Deep levels created by low energy electron irradiation in 4H-SiC," *Journal of Applied Physics*, vol. 96, no. 9, p. 4909, 2004.

[258] K. Saiki, H. Tanaka, and S. Tanaka, "Surface composition change of TiC and SiC under hydrogen ion bombardment," *Journal of Nuclear Materials*, vol. 128-129, pp. 744–748, Dec. 1984.

[259] Y. Oya, Y. Onishi, T. Takeda, H. Kimura, K. Okuno, and S. Tanaka, "Interaction between hydrogen isotopes and damaged structures produced by He+ implantation in SiC," *Fusion Engineering and Design*, vol. 81, pp. 987–992, Feb. 2006.

[260] J. Steeds, G. Evans, L. Danks, S. Furkert, W. Voegeli, M. Ismail, and F. Carosella, "Transmission electron microscope radiation damage of 4H and 6H SiC studied by photoluminescence spectroscopy," *Diamond and Related Materials*, vol. 11, pp. 1923–1945, Dec. 2002.

[261] M. Aboelfotoh and J. Doyle, "Defect energy levels in electron-irradiated and deuterium-implanted 6H silicon carbide," *Physical Review B*, vol. 59, pp. 10823–10829, Apr. 1999.

[262] M. Ishimaru, I.-t. Bae, and Y. Hirotsu, "Electron-beam-induced amorphization in SiC," *Physical Review B*, vol. 68, pp. 1–4, Oct. 2003.

[263] H. Hanchen, N. Ghoniem, and H. Huang, "Neutron displacement damage cross sections for SiC," *Journal of Nuclear Materials*, vol. 199, pp. 221–230, Feb. 1993.

[264] K. Hojou, S. Furuno, K. Kushita, H. Otsu, and K. Izui, "In-situ observation of damage evolution in SiC crystals during He+ and H2+ dual-ion beam irradiation," *Journal of Nuclear Materials*, vol. 191-194, pp. 583–587, Sept. 1992.

[265] K. Hojou, S. Furuno, K. Kushita, H. Otsu, Y. Furuya, and K. Izui, "In situ EELS and TEM observation of silicon carbide irradiated with helium ions at low temperature and successively annealed," *Nuclear Instruments and Methods in Physics Research Section B: Beam Interactions with Materials and Atoms*, vol. 116, pp. 382–388, Aug. 1996.

[266] K. Hojou, S. Furuno, K. Kushita, N. Sasajima, and K. Izui, "EELS analysis of SiC crystals under hydrogen and helium dual-ion beam irradiation," *Nuclear Instruments and Methods in Physics Research Section B: Beam Interactions with Materials and Atoms*, vol. 141, pp. 148–153, May 1998.

[267] W. Hua, S.-D. Yao, N. D. Theodore, X.-M. Wang, W.-K. Chu, M. Martin, and L. Shao, "Ion-irradiation-induced athermal annealing of helium bubbles in SiC," *Nuclear Instruments and Methods in Physics Research Section B: Beam Interactions with Materials and Atoms*, vol. 268, pp. 2325–2328, July 2010.

[268] W. Weber, W. Jiang, Y. Zhang, and A. Hallén, "Damage evolution and recovery in 4H and 6H silicon carbide irradiated with aluminum ions," *Nuclear Instruments and Methods in Physics Research Section B: Beam Interactions with Materials and Atoms*, vol. 191, pp. 514–518, May 2002.

[269] C. Dutto, E. Fogarassy, D. Mathiot, D. Muller, P. Kern, and D. Ballutaud, "Long-pulse duration excimer laser annealing of Al+ ion implanted 4H-SiC for pn junction formation," *Applied Surface Science*, vol. 208-209, pp. 292–297, Mar. 2003.

[270] S. Ahmed, C. J. Barbero, T. W. Sigmon, and J. W. Erickson, "Boron and aluminum implantation in α-SiC," *Applied Physics Letters*, vol. 65, no. 1, p. 67, 1994.

[271] M. Ishimaru, I.-T. Bae, Y. Hirotsu, S. Matsumura, and K. Sickafus, "Structural Relaxation of Amorphous Silicon Carbide," *Physical Review Letters*, vol. 89, pp. 3–6, July 2002.

[272] R. Vardiman, "Temperature-induced phase development in titanium-implanted silicon carbide," *Materials Science and Engineering: A*, vol. 177, pp. 209–215, Apr. 1994.

[273] Y. Pacaud, J. Stoemenos, G. Brauer, R. Yankov, V. Heera, M. Voelskow, R. Kögler, and W. Skorupa, "Radiation damage and annealing behaviour of Ge+-implanted SiC," *Nuclear Instruments and Methods in Physics Research Section B: Beam Interactions with Materials and Atoms*, vol. 120, pp. 177–180, Dec. 1996.

[274] T. Gorelik, U. Kaiser, C. Schubert, W. Wesch, and U. Glatzel, "Transmission electron microscopy study of Ge implanted into SiC," *Journal of Materials Research*, vol. 17, pp. 479–486, Jan. 2002.

[275] A. Audren, A. Benyagoub, L. Thome, and F. Garrido, "Ion implantation of iodine into silicon carbide: Influence of temperature on the produced damage and on the diffusion behaviour," *Nuclear Instruments and Methods in Physics Research Section B: Beam Interactions with Materials and Atoms*, vol. 266, pp. 2810–2813, June 2008.

[276] J. J. Li, C. Zhang, C. Xu, X. Jia, Y. Song, and Y. Jin, "Lattice damage and nanohardness in 6H-SiC implanted with multiple-energy Xe ions," *Nuclear Instruments and Methods in Physics Research Section B: Beam Interactions with Materials and Atoms*, vol. 286, pp. 124–128, Nov. 2011.

[277] E. Friedland, N. van der Berg, T. Hlatshwayo, R. Kuhudzai, J. Malherbe, E. Wendler, and W. Wesch, "Diffusion behavior of cesium in silicon carbide at T>1000°C," *Nuclear Instruments and Methods in Physics Research Section B: Beam Interactions with Materials and Atoms*, vol. 286, pp. 102–107, Dec. 2011.

[278] S. Arpiainen, K. Saarinen, P. Hautojärvi, L. Henry, M.-F. Barthe, and C. Corbel, "Optical transitions of the silicon vacancy in 6H-SiC studied by positron annihilation spectroscopy," *Physical Review B*, vol. 66, pp. 1–10, Aug. 2002.

[279] H. Itoh, M. Yoshikawa, I. Nashiyama, H. Okumura, S. Misawa, and S. Yoshida, "Photoluminescence of radiation induced defects in 3C-SiC epitaxially grown on Si," *Journal of Applied Physics*, vol. 77, no. 2, p. 837, 1995.

[280] H. Itoh, N. Hayakawa, I. Nashiyama, and E. Sakuma, "Electron spin resonance in electron-irradiated 3C-SiC," *Journal of Applied Physics*, vol. 66, no. 9, p. 4529, 1989.

[281] H. Itoh, M. Yoshikawa, I. Nashiyama, S. Misawa, H. Okumura, and S. Yoshida, "Radiation induced defects in CVD-grown 3C-SiC," *IEEE Transactions on Nuclear Science*, vol. 37, no. 6, pp. 1732–1738, 1990.

[282] A. Polity, S. Huth, and M. Lausmann, "Defect characterization in electron-irradiated 6H-SiC by positron annihilation," *Physical Review B*, vol. 59, pp. 10603–10606, Apr. 1999.

[283] X. D. Chen, S. Fung, C. C. Ling, C. D. Beling, and M. Gong, "Deep level transient spectroscopic study of neutron-irradiated n-type 6H-SiC," *Journal of Applied Physics*, vol. 94, no. 5, p. 3004, 2003.

[284] S. Orlinski, J. Schmidt, E. Mokhov, and P. Baranov, "Silicon and carbon vacancies in neutron-irradiated SiC: A high-field electron paramagnetic resonance study," *Physical Review B*, vol. 67, pp. 1–8, Mar. 2003.

[285] D. Åberg, A. Hallén, and B. Svensson, "Low-dose ion implanted epitaxial 4H-SiC investigated by deep level transient spectroscopy," *Physica B: Condensed Matter*, vol. 273-274, pp. 672–676, Dec. 1999.

[286] A. Kawasuso, H. Itoh, T. Ohshima, K. Abe, and S. Okada, "Vacancy production by 3 MeV electron irradiation in 6H-SiC studied by positron lifetime spectroscopy," *Journal of Applied Physics*, vol. 82, no. 7, p. 3232, 1997.

[287] A. Castaldini, A. Cavallini, L. Rigutti, F. Nava, S. Ferrero, and F. Giorgis, "Deep levels by proton and electron irradiation in 4H-SiC," *Journal of Applied Physics*, vol. 98, no. 5, p. 053706, 2005.

[288] T. Ohshima, A. Uedono, K. Abe, H. Itoh, Y. Aoki, M. Yoshikawa, S. Tanigawa, and I. Nashiyama, "Characterization of vacancy-type defects and phosphorus donors introduced in 6H-SiC by ion implantation," *Applied Physics A: Materials Science & Processing*, vol. 67, pp. 407–412, Oct. 1998.

[289] S. Kondo, Y. Katoh, and L. Snead, "Microstructural defects in SiC neutron irradiated at very high temperatures," *Journal of Nuclear Materials*, vol. 382, pp. 160–169, Dec. 2008.

[290] J. Grisolia, B. de Mauduit, J. Gimbert, T. Billon, G. Ben Assayag, C. Bourgerette, and A. Claverie, "TEM studies of the defects introduced by ion implantation in SiC," *Nuclear Instruments and Methods in Physics Research Section B: Beam Interactions with Materials and Atoms*, vol. 147, pp. 62–67, Jan. 1999.

[291] K. Hojou, S. Furuno, and K. Izui, "In-situ Observation of Structural Damage in SiC Crystals Induced by Hydrogen Ion Irradiation and Successive Electron Irradiation," *Journal of Electron Microscopye*, vol. 40, pp. 157–161, 1991.

[292] J. Aihara, K. Hojou, S. Furuno, and M. Ishihara, "Bubble formation with electron irradiation in SiC implanted with hydrogen or deuterium," *Nuclear Instruments and Methods in Physics Research Section B: Beam Interactions with Materials and Atoms*, vol. 191, pp. 540–543, May 2002.

[293] K. Hojou and K. Izui, "Bubbles in SiC crystals formed by helium ion irradiation at high temperatures," *Journal of Nuclear Materials*, vol. 160, pp. 147–152, Dec. 1988.

[294] K. Hojou, S. Furuno, H. Otsu, K. Izui, and T. Tsukamoto, "In-situ observation system of the dynamic process of structual changes during ion irradiation and its application to SiC and TiC crystals," *Journal of Nuclear Materials*, vol. 155-157, pp. 298–302, July 1988.

[295] T. Taguchi, N. Igawa, S. Miwa, E. Wakai, S. Jitsukawa, L. Snead, and A. Hasegawa, "Synergistic effects of implanted helium and hydrogen and the effect of irradiation temperature on the microstructure of SiC/SiC composites," *Journal of Nuclear Materials*, vol. 335, pp. 508–514, Dec. 2004.

[296] P. Jung, "A comparison of defects in helium implanted α- and β-SiC," *Journal of Nuclear Materials*, vol. 283-287, pp. 806–810, Dec. 2000.

[297] V. Heera, W. Skorupa, B. Pécz, and L. Dobos, "Ion beam synthesis of graphite and diamond in silicon carbide," *Applied Physics Letters*, vol. 76, no. 20, p. 2847, 2000.

[298] M. Ishimaru, M. Naito, Y. Hirotsu, and K. E. Sickafus, "Amorphous structures of silicon carbonitride formed by high-dose nitrogen ion implantation into silicon carbide," *Nuclear Instruments and Methods in Physics Research Section B: Beam Interactions with Materials and Atoms*, vol. 206, pp. 994–998, May 2003.

[299] S. Miyagawa, S. Nakao, K. Saitoh, M. Ikeyama, H. Niwa, S. Tanemura, Y. Miyagawa, and K. Baba, "Formation of β-Si_3N_4 by nitrogen implantation into SiC," *Journal of Applied Physics*, vol. 78, no. 12, p. 7018, 1995.

[300] W. M. Tsang, S. P. Wong, and J. K. N. Lindner, "Effect of tungsten implantation on electron field emission properties of ion-beam-synthesized SiC layers," *Applied Physics Letters*, vol. 84, no. 16, p. 3193, 2004.

[301] H. Weishart, H. Steffen, W. Matz, M. Voelskow, and W. Skorupa, "Ion beam synthesis by tungsten-implantation into 6H-silicon carbide," *Nuclear Instruments and Methods in Physics Research Section B: Beam Interactions with Materials and Atoms*, vol. 112, pp. 338–341, May 1996.

[302] T. Licht, N. Achtziger, D. Forkel-Wirth, K. Freitag, J. Grillenberger, M. Kaltenhäuser, U. Reislöhner, M. Rüb, M. Uhrmacher, and W. Witthuhn, "Hafnium, cadmium and indium impurities in 4H-SiC observed by perturbed angular correlation spectroscopy," *Diamond and Related Materials*, vol. 6, pp. 1436–1439, Aug. 1997.

[303] V. Heera, H. Reuther, J. Stoemenos, and B. Pécz, "Phase formation due to high dose aluminum implantation into silicon carbide," *Journal of Applied Physics*, vol. 87, no. 1, p. 78, 2000.

[304] J. Stoemenos, B. Pécz, and V. Heera, "Epitaxial aluminum carbide formation in 6H-SiC by high-dose Al^+ implantation," *Applied Physics Letters*, vol. 74, no. 18, p. 2602, 1999.

[305] L. Bischoff and J. Teichert, "Writing cobalt FIB implantation into 6H:SiC," *Applied Surface Science*, vol. 184, pp. 336–339, Dec. 2001.

[306] R. Zimmerman, D. Ila, E. Williams, B. Gasic, A. Elsamadicy, A. Evelyn, D. Poker, D. Hensley, and D. J. Larkin, "Gold, silver and copper nanocrystal formation in SiC by MeV implantation," *Nuclear Instruments and Methods in Physics Research Section B: Beam Interactions with Materials and Atoms*, vol. 166-167, pp. 892–896, May 2000.

[307] N. Achtziger, G. Pasold, R. Sielemann, C. Hülsen, J. Grillenberger, and W. Witthuhn, "Tungsten in silicon carbide: Band-gap states and their polytype dependence," *Physical Review B*, vol. 62, pp. 12888–12895, Nov. 2000.

[308] J. Grillenberger, U. Grossner, B. Svensson, F. Albrecht, W. Witthuhn, and R. Sielemann, "Deep acceptor states of platinum and iridium in 4H-silicon carbide," *Physical Review B*, vol. 70, pp. 1–8, Nov. 2004.

[309] K. Danno and T. Kimoto, "Deep level transient spectroscopy on as-grown and electron-irradiated p-type 4H-SiC epilayers," *Journal of Applied Physics*, vol. 101, no. 10, p. 103704, 2007.

[310] T. Kimoto, K. Danno, and J. Suda, "Lifetime-killing defects in 4H-SiC epilayers and lifetime control by low-energy electron irradiation," *Physica Status Solidi (B)*, vol. 245, pp. 1327–1336, July 2008.

[311] H. von Bardeleben, J. Cantin, L. Henry, and M. Barthe, "Vacancy defects in p-type 6H-SiC created by low-energy electron irradiation," *Physical Review B*, vol. 62, pp. 10841–10846, Oct. 2000.

[312] X. Chen, C. Yang, M. Gong, W. Ge, S. Fung, C. Beling, J. Wang, M. Lui, and C. Ling, "Low Energy Electron Irradiation Induced Deep Level Defects in 6H-SiC: The Implication for the Microstructure of the Deep Levels E1/E2," *Physical Review Letters*, vol. 92, pp. 10–13, Mar. 2004.

[313] A. Matsunaga, C. Kinoshita, K. Nakai, and Y. Tomokiyo, "Radiation-induced amorphization and swelling in ceramics," *Journal of Nuclear Materials*, vol. 179-181, pp. 457–460, Mar. 1991.

[314] M. Gong, S. Fung, C. D. Beling, and Z. You, "A deep level transient spectroscopy study of electron irradiation induced deep levels in p-type 6H-SiC," *Journal of Applied Physics*, vol. 85, no. 10, p. 7120, 1999.

[315] T. Egilsson, A. Henry, I. Ivanov, J. Lindström, and E. Janzén, "Photoluminescence of electron-irradiated 4H-SiC," *Physical Review B*, vol. 59, pp. 8008–8014, Mar. 1999.

[316] A. Kawasuso, F. Redmann, R. Krause-Rehberg, T. Frank, M. Weidner, G. Pensl, P. Sperr, and H. Itoh, "Vacancies and deep levels in electron-irradiated 6H SiC epilayers studied by positron annihilation and deep level transient spectroscopy," *Journal of Applied Physics*, vol. 90, no. 7, p. 3377, 2001.

[317] H. Inui, H. Mow, and H. Fujita, "Electron irradiation induced crystalline-amorphous transition in ceramics," *Acta Metallurgica*, vol. 37, pp. 1337–1342, May 1989.

[318] H. Ohyama, K. Takakura, K. Uemura, K. Shigaki, T. Kudou, M. Arai, S. Kuboyama, S. Matsuda, C. Kamezawa, E. Simoen, and C. Claeys, "Radiation-induced defects in SiC-MESFETs after 2-MeV electron irradiation," *Physica B: Condensed Matter*, vol. 376-377, pp. 382–384, Apr. 2006.

[319] S. Dannefaer and D. Kerr, "Positron annihilation investigation of electron irradiation-produced defects in 6H-SiC," *Diamond and Related Materials*, vol. 13, pp. 157–165, Jan. 2004.

[320] N. T. Son, E. Sörman, W. M. Chen, M. Singh, C. Hallin, O. Kordina, B. Monemar, E. Janzén, and J. L. Lindström, "Dominant recombination center in electron-irradiated 3C SiC," *Journal of Applied Physics*, vol. 79, no. 7, p. 3784, 1996.

[321] N. Son, E. Sörman, M. Singh, W. Chen, C. Hallin, O. Kordina, B. Monemar, J. Lindström, and E. Janzén, "Deep luminescent centres in electron-irradiated 6H SiC," *Diamond and Related Materials*, vol. 6, pp. 1378–1380, Aug. 1997.

[322] N. T. N. Son, E. Sörman, W. M. Chen, C. Hallin, O. Kordina, B. Monemar, E. Janzén, and J. L. Lindström, "Optically detected magnetic resonance studies of defects in electron-irradiated 3C SiC layers," *Physical Review B*, vol. 55, pp. 2863–2866, Feb. 1997.

[323] S. Dannefaer, D. Craigen, and D. Kerr, "Carbon and silicon vacancies in electron-irradiated 6H-SiC.," *Physical review. B, Condensed matter*, vol. 51, pp. 1928–1930, Jan. 1995.

[324] H. Matsuura, K. Aso, S. Kagamihara, H. Iwata, T. Ishida, and K. Nishikawa, "Decrease in Al acceptor density in Al-doped 4H-SiC by irradiation with 4.6 MeV electrons," *Applied Physics Letters*, vol. 83, no. 24, p. 4981, 2003.

[325] A. Taylor, "A second target station for ISIS," *Physica B: Condensed Matter*, vol. 276-278, pp. 36–37, Mar. 2000.

[326] "ILL Annual Report 1996," tech. rep., ILL, Grenoble, France, 1996.

[327] L. Snead, Y. Katoh, and S. Connery, "Swelling of SiC at intermediate and high irradiation temperatures," *Journal of Nuclear Materials*, vol. 367-370, pp. 677–684, Aug. 2007.

[328] T. Suzuki, T. Maruyama, T. Iseki, T. Mori, and M. Ito, "Recovery behavior in neutron irradiated β-sic," *Journal of Nuclear Materials*, vol. 149, pp. 334–340, Aug. 1987.

[329] C. Wu, J. Bonal, and B. Kryger, "The effect of high-dose neutron irradiation on the properties of graphite and silicon carbide," *Journal of Nuclear Materials*, vol. 208, pp. 1–7, Jan. 1994.

[330] L. Snead, Y. Katoh, A. Kohyama, J. Bailey, N. Vaughn, and R. Lowden, "Evaluation of neutron irradiated near-stoichiometric silicon carbide fiber composites," *Journal of Nuclear Materials*, vol. 283-287, pp. 551–555, Dec. 2000.

[331] M. Osborne, C. Hubbard, L. Snead, and D. Steiner, "Neutron irradiation effects on the density, tensile properties and microstructural changes in Hi-Nicalon^{TM} and Sylramic^{TM} SiC fibers," *Journal of Nuclear Materials*, vol. 253, pp. 67–77, Mar. 1998.

[332] K. Ozawa, T. Nozawa, Y. Katoh, T. Hinoki, and A. Kohyama, "Mechanical properties of advanced SiC/SiC composites after neutron irradiation," *Journal of Nuclear Materials*, vol. 367-370, pp. 713–718, Aug. 2007.

[333] R. Blackstone and E. E. Voice, "The expansion of silicon carbide by neutron irradiation at high temperature," *Journal of Nuclear Materials*, vol. 39, pp. 319–322, June 1971.

[334] R. Price, "Effects of fast-neutron irradiation on pyrolytic silicon carbide," *Journal of Nuclear Materials*, vol. 33, pp. 17–22, Oct. 1969.

[335] R. Matthews, "Irradiation damage in reaction-bonded silicon carbide," *Journal of Nuclear Materials*, vol. 51, pp. 203–208, June 1974.

[336] K. Okamura, T. Matsuzawa, M. Sato, Y. Higashiguchi, and S. Morozumi, "Effects of neutron irradiation on SiC fiber," *Journal of Nuclear Materials*, vol. 133-134, pp. 705–708, Aug. 1985.

[337] K. Okamura, T. Matsuzawa, M. Sato, H. Kayano, S. Morozumi, H. Tezuka, and A. Kohyama, "Effects of neutron irradiation on fine structure and strength of SiC fibers," *Journal of Nuclear Materials*, vol. 157, pp. 329–333, July 1988.

[338] S. Harrison and J. Corelli, "Microstructure of polycrystalline SiC containing excess Si after neutron and ion irradiation," *Journal of Nuclear Materials*, vol. 99, pp. 203–212, Sept. 1981.

[339] V. Nagesh, J. W. Farmer, R. F. Davis, and H. S. Kong, "Defects in neutron irradiated SiC," *Applied Physics Letters*, vol. 50, no. 17, p. 1138, 1987.

[340] S. Seshadri, A. Dulloo, F. Ruddy, J. Seidel, and L. Rowland, "Demonstration of an SiC neutron detector for high-radiation environments," *IEEE Transactions on Electron Devices*, vol. 46, pp. 567–571, Mar. 1999.

[341] K. Sasaki, T. Yano, T. Maruyama, and T. Iseki, "Helium release and microstructure of neutron-irradiated SiC ceramics," *Journal of Nuclear Materials*, vol. 179-181, pp. 407–410, Mar. 1991.

[342] L. Leblanc and G. Ross, "Measurements and Monte Carlo calculations of hydrogen and deuterium depth distributions into silicon carbide implanted in the energy range from 0.25 to 1.75 keV," *Nuclear Instruments and Methods in Physics Research Section B: Beam Interactions with Materials and Atoms*, vol. 114, pp. 203–207, July 1996.

[343] N. Huang, Q. Xiong, and D. Wang, "Study in chemical bonding states of SiC films before and after hydrogen ion irradiation," *Journal of Nuclear Materials*, vol. 321, pp. 152–157, Sept. 2003.

[344] J. M. Lannon, J. S. Gold, and C. D. Stinespring, "Hydrogen ion interactions with silicon carbide and the nucleation of diamond thin films," *Journal of Applied Physics*, vol. 77, no. 8, p. 3823, 1995.

[345] H. Ning-Kang, W. De-Zhi, Z. Ping, and X. Qi, "X-Ray Photoelectron Spectroscopy Analysis of the Electron Beam Treated SiC Films Before and After Hydrogen Ion Irradiation," *Chinese Physics Letters*, vol. 21, pp. 61–64, Jan. 2004.

[346] W. Jiang, W. Weber, S. Thevuthasan, and R. Grötzschel, "Irradiation effects and thermal annealing behavior in H_2^+-implanted 6H-SiC," *Nuclear Instruments and Methods in Physics Research Section B: Beam Interactions with Materials and Atoms*, vol. 166-167, pp. 374–378, May 2000.

[347] D. Davydov, A. Lebedev, V. Kozlovski, N. Savkina, and A. Strel'chuk, "DLTS study of defects in 6H- and 4H-SiC created by proton irradiation," *Physica B: Condensed Matter*, vol. 308-310, pp. 641–644, Dec. 2001.

[348] G. Alfieri, E. V. Monakhov, B. G. Svensson, and A. Hallén, "Defect energy levels in hydrogen-implanted and electron-irradiated n-type 4H silicon carbide," *Journal of Applied Physics*, vol. 98, no. 11, p. 113524, 2005.

[349] M. L. David, "Electrically active defects in irradiated 4H-SiC," *Journal of Applied Physics*, vol. 95, no. 9, p. 4728, 2004.

[350] G. Chollon, J. Vallerot, D. Helary, and S. Jouannigot, "Structural and textural changes of CVD-SiC to indentation, high temperature creep and irradiation," *Journal of the European Ceramic Society*, vol. 27, pp. 1503–1511, Jan. 2007.

[351] A. A. Lebedev, A. M. Strel'chuk, V. V. Kozlovski, N. Savkina, D. V. Davydov, and V. V. Solov'ev, "Studies of the effect of proton irradiation on 6H-SiC pn junction properties," *Materials Science and Engineering: B*, vol. 61-62, pp. 450–453, July 1999.

[352] A. Strel'chuk, V. Kozlovski, N. Savkina, M. Rastegaeva, and A. Andreev, "Influence of proton irradiation on recombination current in 6H-SiC PN structures," *Materials Science and Engineering: B*, vol. 61-62, pp. 441–445, July 1999.

[353] A. M. Strel'chuk, A. A. Lebedev, V. V. Kozlovski, N. S. Savkina, D. V. Davydov, V. V. Solov'ev, and M. G. Rastegaeva, "Doping of 6H-SiC PN structures by proton irradiation," *Nuclear Instruments and Methods in Physics Research Section B: Beam Interactions with Materials and Atoms*, vol. 147, pp. 74–78, Jan. 1999.

[354] A. A. Lebedev, A. I. Veinger, D. V. Davydov, V. V. Kozlovski, N. S. Savkina, and A. M. Strel'chuk, "Doping of n-type 6H-SiC and 4H-SiC with defects created with a proton beam," *Journal of Applied Physics*, vol. 88, no. 11, p. 6265, 2000.

[355] A. A. Lebedev, A. I. Veinger, D. V. Davydov, V. V. Kozlovskii, N. S. Savkina, and A. M. Strel'chuk, "Radiation defects in n-4H-SiC irradiated with 8-MeV protons," *Semiconductors*, vol. 34, pp. 1016–1020, Sept. 2000.

[356] A. Kuznetsov, M. Janson, A. Hallén, B. Svensson, and A. Nylandsted Larsen, "Boron diffusion in Si and SiC during 2.5 MeV proton irradiation at 500-850^{circ}C," *Nuclear Instruments and Methods in Physics Research Section B: Beam Interactions with Materials and Atoms*, vol. 148, pp. 279–283, Jan. 1999.

[357] H. von Bardeleben, J. Cantin, I. Vickridge, and G. Battistig, "Proton-implantation-induced defects in n-type 6H- and 4H-SiC: An electron paramagnetic resonance study," *Physical Review B*, vol. 62, pp. 10126–10134, Oct. 2000.

[358] L. Henry, M.-F. Barthe, C. Corbel, P. Desgardin, G. Blondiaux, S. Arpiainen, and L. Liszkay, "Silicon vacancy-type defects in as-received and 12-MeV proton-irradiated 6H-SiC studied by positron annihilation spectroscopy," *Physical Review B*, vol. 67, pp. 1–10, Mar. 2003.

[359] O. Plaksin, V. Stepanov, H. Amekura, and N. Kishimoto, "Conductivity of SiC during neutron and proton irradiation," *Journal of Nuclear Materials*, vol. 307-311, pp. 1146–1151, Dec. 2002.

[360] Z. Luo, T. Chen, A. Ahyi, A. Sutton, B. Haugerud, J. Cressler, D. Sheridan, J. Williams, P. Marshall, and R. Reed, "Proton radiation effects in 4H-SiC diodes and MOS capacitors," *IEEE Transactions on Nuclear Science*, vol. 51, pp. 3748–3752, Dec. 2004.

[361] Z. Luo, T. Chen, J. Cressler, D. Sheridan, J. Williams, R. Reed, and P. Marshall, "Impact of proton irradiation on the static and dynamic characteristics of high-voltage 4H-SiC JBS switching diodes," *IEEE Transactions on Nuclear Science*, vol. 50, pp. 1821–1826, Dec. 2003.

[362] S. Nigam, J. Kim, F. Ren, G. Y. Chung, M. F. MacMillan, R. Dwivedi, T. N. Fogarty, R. Wilkins, K. K. Allums, C. R. Abernathy, S. J. Pearton, and J. R. Williams, "High energy proton irradiation effects on SiC Schottky rectifiers," *Applied Physics Letters*, vol. 81, no. 13, p. 2385, 2002.

[363] S. Lazanu, I. Lazanu, E. Borchi, and M. Bruzzi, "Theoretical calculations of the primary defects induced by pions and protons in SiC," *Nuclear Instruments and Methods in Physics Research Section A: Accelerators, Spectrometers, Detectors and Associated Equipment*, vol. 485, pp. 768–773, June 2002.

[364] R. Harris, A. Frasca, and M. Patton, "Displacement damage effects on the forward bias characteristics of SiC Schottky barrier power diodes," *IEEE Transactions on Nuclear Science*, vol. 52, pp. 2408–2412, Dec. 2005.

[365] R. Harris and A. Frasca, "Proton Irradiation of Silicon Schottky Barrier Power Diodes," *IEEE Transactions on Nuclear Science*, vol. 53, pp. 1995–2003, Aug. 2006.

[366] S. Sciortino, F. Hartjes, S. Lagomarsino, F. Nava, M. Brianzi, V. Cindro, C. Lanzieri, M. Moll, and P. Vanni, "Effect of heavy proton and neutron irradiations on epitaxial 4H-SiC Schottky diodes," *Nuclear Instruments and Methods in Physics Research Section A: Accelerators, Spectrometers, Detectors and Associated Equipment*, vol. 552, pp. 138–145, Oct. 2005.

[367] A. Ivanov, N. Strokan, D. Davydov, N. Savkina, A. Lebedev, Y. Mironov, G. Riabov, and E. Ivanov, "Radiation hardness of SiC based ions detectors for influence of the relative protons," *Applied Surface Science*, vol. 184, pp. 431–436, Dec. 2001.

[368] V. Kažukauskas, R. Jasiulionis, V. Kalendra, and J.-V. Vaitkus, "Influence of irradiation by 24 GeV protons on the properties of 4H-SiC radiation detectors," *Diamond and Related Materials*, vol. 16, pp. 1058–1061, Apr. 2007.

[369] M. Balden and J. Roth, "Comparison of the chemical erosion of Si, C and SiC under deuterium ion bombardment," *Journal of Nuclear Materials*, vol. 279, pp. 351–355, June 2000.

[370] N. Almqvist, M. Rubel, and E. Franconi, "Surface characterization of SiC composites exposed to deuterium ions, using atomic force microscopy," *Materials Science and Engineering: A*, vol. 201, pp. 277–285, Oct. 1995.

[371] Y. Oya, H. Suzuki, K. Morita, K. Iinuma, S. Uchida, Y. Makide, and S. Tanaka, "Retention and replacement of hydrogen isotopes and isotope effect in SiC by H+ and D+ ion irradiation," *Fusion Engineering and Design*, vol. 61-62, pp. 705–710, Nov. 2002.

[372] M. Kitajima, M. Fukutomi, and M. Okada, "Deuterium ion irradiation of SiC and SiC-Al-O compound films on molybdenum," *Thin Solid Films*, vol. 87, pp. 297–311, Jan. 1982.

[373] M. Mohri, S. Kato, S. Shinada, K. Watanabe, and T. Yamashina, "Analysis of secondary ion species sputtered from SiC surface during He+ and D+

ion irradiation," *Journal of Nuclear Materials*, vol. 93-94, pp. 692–696, Oct. 1980.

[374] S. Kato, T. Satake, M. Mohri, and T. Yamashina, "Energy analysis of secondary ion species sputtered from silicon carbide surface during deuterium ion irradiation," *Journal of Nuclear Materials*, vol. 103, pp. 351–355, Jan. 1981.

[375] E. Oliviero, C. Tromas, F. Pailloux, a. Declémy, M. Beaufort, C. Blanchard, and J. Barbot, "Damage formation and recovery in temperature helium implanted 4H-SiC," *Materials Science and Engineering: B*, vol. 102, pp. 289–292, Sept. 2003.

[376] T. Sugiyama, Y. Morimoto, K. Iguchi, K. Okuno, M. Miyamoto, H. Iwakiri, and N. Yoshida, "Effects of helium irradiation on chemical behavior of energetic deuterium in SiC," *Journal of Nuclear Materials*, vol. 307-311, pp. 1080–1083, Dec. 2002.

[377] S. Igarashi, S. Muto, and T. Tanabe, "Surface blistering of ion irradiated SiC studied by grazing incidence electron microscopy," *Journal of Nuclear Materials*, vol. 307-311, pp. 1126–1129, Dec. 2002.

[378] K. Hojou, "Structural changes induced by helium ion irradiation in silicon carbide crystals," *Journal of Nuclear Materials*, vol. 133-134, pp. 709–713, Aug. 1985.

[379] W. Jiang, S. Thevuthasan, W. Weber, and R. Grötzschel, "Deuterium channeling analysis for He^+-implanted 6H-SiC," *Nuclear Instruments and Methods in Physics Research Section B: Beam Interactions with Materials and Atoms*, vol. 161-163, pp. 501–504, Mar. 2000.

[380] E. Oliviero, M. F. Beaufort, J. F. Barbot, A. van Veen, and a. Fedorov, "Helium implantation defects in SiC: A thermal helium desorption spectrometry investigation," *Journal of Applied Physics*, vol. 93, no. 1, p. 231, 2003.

[381] W. Jiang, W. Weber, S. Thevuthasan, and D. McCready, "Accumulation and recovery of irradiation damage in He+ implanted α-SiC," *Journal of Nuclear Materials*, vol. 257, pp. 295–302, Dec. 1998.

[382] W. Jiang, W. J. Weber, S. Thevuthasan, and D. E. McCready, "Rutherford backscattering spectrometry channeling study of ion-irradiated 6H-SiC," *Surface and Interface Analysis*, vol. 27, pp. 179–184, Apr. 1999.

[383] W. Weber, W. Jiang, and S. Thevuthasan, "Defect annealing kinetics in irradiated 6H-SiC," *Nuclear Instruments and Methods in Physics Research Section B: Beam Interactions with Materials and Atoms*, vol. 166-167, pp. 410–414, May 2000.

[384] W. Jiang, W. Weber, S. Thevuthasan, and D. McCready, "Displacement energy measurements for ion-irradiated 6H-SiC," *Nuclear Instruments and Methods in Physics Research Section B: Beam Interactions with Materials and Atoms*, vol. 148, pp. 557–561, Jan. 1999.

[385] K. Nakata, S. Kasahara, S. Shimanuki, Y. Katano, H. Ohno, and J. Kuniya, "Damage structure obtained by cross-sectional observation in silicon carbide irradiated with helium ions," *Journal of Nuclear Materials*, vol. 179-181, pp. 403–406, Mar. 1991.

[386] L. Rovner and K. Chen, "MeV He+ bombardment of silicon carbide and carbon," *Journal of Nuclear Materials*, vol. 63, pp. 307–312, Dec. 1976.

[387] M. Beaufort, E. Oliviero, M. David, J. Nomgaudyte, L. Pranevicius, A. Declémy, and J. Barbot, "Defects induced by high energy helium implantation in 4H-SiC," *Nuclear Instruments and Methods in Physics Research Section B: Beam Interactions with Materials and Atoms*, vol. 186, pp. 218–222, Jan. 2002.

[388] S. Nogami, A. Hasegawa, K. Abe, T. Taguchi, and R. Yamada, "Effect of dual-beam-irradiation by helium and carbon ions on microstructure development of SiC/SiC composites," *Journal of Nuclear Materials*, vol. 283-287, pp. 268–272, Dec. 2000.

[389] A. Hasegawa, B. Oliver, S. Nogami, K. Abe, and R. Jones, "Study of helium effects in SiC/SiC composites under fusion reactor environment," *Journal of Nuclear Materials*, vol. 283-287, pp. 811–815, Dec. 2000.

[390] M. Sasase, Y. Ito, K. Yasuda, R. Ishigami, S. Hatori, and A. Yamamoto, "Defect formation in 6H-SiC irradiated by 3 MeV He ions," *Nuclear Instruments and Methods in Physics Research Section B: Beam Interactions with Materials and Atoms*, vol. 209, pp. 179–183, Aug. 2003.

[391] N. Khánh, Z. Zolnai, T. Lohner, L. Tóth, L. Dobos, and J. Gyulai, "He ion beam density effect on damage induced in SiC during Rutherford backscattering measurement," *Nuclear Instruments and Methods in Physics Research Section B: Beam Interactions with Materials and Atoms*, vol. 161-163, pp. 424–428, Mar. 2000.

[392] J. Chen, P. Jung, and H. Trinkaus, "Microstructural evolution of helium-implanted α-SiC," *Physical Review B*, vol. 61, pp. 12923–12932, May 2000.

[393] A. Hasegawa, M. Saito, K. Abe, and R. Jones, "Helium implantation effects on mechanical properties of SiCf/SiC composites," *Journal of Nuclear Materials*, vol. 253, pp. 31–35, Mar. 1998.

[394] S. Nogami, A. Hasegawa, L. L. Snead, R. H. Jones, and K. Abe, "Effect of He pre-implantation and neutron irradiation on mechanical properties of

SiC/SiC composite," *Journal of Nuclear Materials*, vol. 329-333, pp. 577–581, Aug. 2004.

[395] M. Kokkoris, S. Kossionides, A. Kyriakis, K. Zachariadou, G. Fanourakis, R. Vlastou, and T. Paradellis, "Study of the irradiation damage in SiC by ion channeling," *Nuclear Instruments and Methods in Physics Research Section B: Beam Interactions with Materials and Atoms*, vol. 188, pp. 78–83, Apr. 2002.

[396] N. Ramungul, V. Khemka, Y. Zheng, R. Patel, and T. Chow, "6H-SiC P^+N junctions fabricated by beryllium implantation," *IEEE Transactions on Electron Devices*, vol. 46, pp. 465–470, Mar. 1999.

[397] T. Henkel, Y. Tanaka, N. N. Kobayashi, H. Tanoue, M. M. Gong, X. D. Chen, S. Fung, and C. D. Beling, "Structural and electrical properties of beryllium implanted silicon carbide," in *MRS Proceedings*, vol. 572, (San Fransisco, USA), pp. 117 – 122, Materials Research Society, Feb. 1999.

[398] X. Chen, S. Fung, C. Beling, Y. Huang, Q. Li, S. Xu, M. Gong, T. Henkel, H. Tanoue, and N. Kobayashi, "Photoluminescence characterization of beryllium-implanted 6HâĂŞsilicon carbide," *Solid State Communications*, vol. 121, pp. 67–71, Jan. 2002.

[399] S. Fung, X. Chen, C. Beling, Y. Huang, Q. Li, S. Xu, M. Gong, T. Henkel, H. Tanoue, and N. Kobayashi, "Photoluminescence study of beryllium implantation induced intrinsic defects in 6H-silicon carbide," *Physica B: Condensed Matter*, vol. 308-310, pp. 710–713, Dec. 2001.

[400] D. Panknin, H. Wirth, A. Mücklich, and W. Skorupa, "Electrical and microstructural properties of highly boron-implantation doped 6H-SiC," *Journal of Applied Physics*, vol. 89, no. 6, p. 3162, 2001.

[401] N. S. Saks, A. K. Agarwal, S.-H. Ryu, and J. W. Palmour, "Low-dose aluminum and boron implants in 4H and 6H silicon carbide," *Journal of Applied Physics*, vol. 90, no. 6, p. 2796, 2001.

[402] M. Ghezzo, D. M. Brown, E. Downey, J. Kretchmer, and J. J. Kopanski, "Boron-implanted 6H-SiC diodes," *Applied Physics Letters*, vol. 63, no. 9, p. 1206, 1993.

[403] M. Gong, C. V. Reddy, C. D. Beling, S. Fung, G. Brauer, H. Wirth, and W. Skorupa, "Deep level traps in the extended tail region of boron-implanted n-type 6H-SiC," *Applied Physics Letters*, vol. 72, no. 21, p. 2739, 1998.

[404] T. Troffer, M. Schadt, T. Frank, H. Itoh, G. Pensl, J. Heindl, H. P. Strunk, and M. Maier, "Doping of SiC by Implantation of Boron and Aluminum," *Physica Status Solidi (a)*, vol. 162, pp. 277–298, July 1997.

[405] M. V. Rao, J. A. Gardner, P. H. Chi, O. W. Holland, G. Kelner, J. Kretchmer, and M. Ghezzo, "Phosphorus and boron implantation in 6HâĂŞSiC," *Journal of Applied Physics*, vol. 81, no. 10, p. 6635, 1997.

[406] C. Peppermüller, R. Helbig, K. Rottner, and A. Schöner, "Low temperature photoluminescence measurements on boron- and hydrogen-implanted 6H-SiC," *Applied Physics Letters*, vol. 70, no. 8, p. 1014, 1997.

[407] T. Kimoto, O. Takemura, H. Matsunami, T. Nakata, and M. Inoue, "Al+ and B+ implantations into 6H-SiC epilayers and application to pn junction diodes," *Journal of Electronic Materials*, vol. 27, pp. 358–364, Apr. 1998.

[408] L. Storasta and H. Tsuchida, "Reduction of traps and improvement of carrier lifetime in 4H-SiC epilayers by ion implantation," *Applied Physics Letters*, vol. 90, no. 6, p. 062116, 2007.

[409] Y. Nakano, R. K. Malhan, T. Kachi, and H. Tadano, "Effect of C and B sequential implantation on the B acceptors in 4H-SiC," *Journal of Applied Physics*, vol. 89, no. 11, p. 5961, 2001.

[410] G. Compagnini and G. Foti, "1430 cm^{-1} Raman line in ion implanted carbon rich amorphous silicon carbide," *Nuclear Instruments and Methods in Physics Research Section B: Beam Interactions with Materials and Atoms*, vol. 127-128, pp. 639–642, May 1997.

[411] T. Kimoto and N. Inoue, "Nitrogen Ion Implantation into α-SiC Epitaxial Layers," *physica status solidi (a)*, vol. 162, pp. 263–276, July 1997.

[412] D. Åberg, A. Hallén, P. Pellegrino, and B. G. Svensson, "Nitrogen deactivation by implantation-induced defects in 4H-SiC epitaxial layers," *Applied Physics Letters*, vol. 78, no. 19, p. 2908, 2001.

[413] D. Dwight, M. V. Rao, O. W. Holland, G. Kelner, P. H. Chi, J. Kretchmer, and M. Ghezzo, "Nitrogen and aluminum implantation in high resistivity silicon carbide," *Journal of Applied Physics*, vol. 82, no. 11, p. 5327, 1997.

[414] C. Uslu, D. Lee, Y. Berta, B. Park, D. Poker, and L. Riester, "Enhanced surface hardness in nitrogen-implanted silicon carbide," *Nuclear Instruments and Methods in Physics Research Section B: Beam Interactions with Materials and Atoms*, vol. 118, pp. 693–697, Sept. 1996.

[415] F. Moscatelli, A. Poggi, S. Solmi, and R. Nipoti, "Nitrogen Implantation to Improve Electron Channel Mobility in 4H-SiC MOSFET," *IEEE Transactions on Electron Devices*, vol. 55, pp. 961–967, Apr. 2008.

[416] M. Ghezzo, D. Brown, E. Downey, J. Kretchmer, W. Hennessy, D. Polla, and H. Bakhru, "Nitrogen-implanted SiC diodes using high-temperature implantation," *IEEE Electron Device Letters*, vol. 13, pp. 639–641, Dec. 1992.

[417] M. Ishimaru and K. E. Sickafus, "Dose dependence of microstructural evolution in oxygen-ion-implanted silicon carbide," *Applied Physics Letters*, vol. 75, no. 10, p. 1392, 1999.

[418] J. Aihara, M. Ishihara, K. Hojou, and S. Furuno, "Influence of Thermal History on Crystal Nucleation in Silicon Carbide Amorphized with Neon Irradiation," *Journal of the American Ceramic Society*, vol. 87, pp. 1146–1148, June 2004.

[419] C. Xu, C. Zhang, J. J. Li, L. Zhang, Y. Yang, Y. Song, X. Jia, and K. Chen, "A HRXRD and nano-indentation study on Ne-implanted 6H-SiC," *Nuclear Instruments and Methods in Physics Research Section B: Beam Interactions with Materials and Atoms*, vol. 286, pp. 129–133, Sept. 2012.

[420] V. Heera, K. Madhusoodanan, A. Mücklich, D. Panknin, and W. Skorupa, "Institute of ion beam physics and materials research," tech. rep., 2003.

[421] H. Wirth, D. Panknin, W. Skorupa, and E. Niemann, "Efficient p-type doping of 6H-SiC: Flash-lamp annealing after aluminum implantation," *Applied Physics Letters*, vol. 74, no. 7, p. 979, 1999.

[422] S. Fung, M. Gong, C. D. Beling, G. Brauer, H. Wirth, and W. Skorupa, "Aluminum-implantation-induced deep levels in n-type 6H-SiC," *Journal of Applied Physics*, vol. 84, p. 1152, May 1998.

[423] V. Heera, A. Mücklich, C. Dubois, M. Voelskow, and W. Skorupa, "Layer morphology and Al implant profiles after annealing of supersaturated, single-crystalline, amorphous, and nanocrystalline SiC," *Journal of Applied Physics*, vol. 96, no. 5, p. 2841, 2004.

[424] E. M. Handy, M. V. Rao, O. W. Holland, K. A. Jones, M. A. Derenge, and N. Papanicolaou, "Variable-dose (10^{17}-10^{20} cm^{-3}) phosphorus ion implantation into 4H-SiC," *Journal of Applied Physics*, vol. 88, no. 10, p. 5630, 2000.

[425] M. A. Capano, J. A. Cooper, M. R. Melloch, A. Saxler, and W. C. Mitchel, "Ionization energies and electron mobilities in phosphorus- and nitrogen-implanted 4H-silicon carbide," *Journal of Applied Physics*, vol. 87, no. 12, p. 8773, 2000.

[426] Y. Negoro, N. Miyamoto, T. Kimoto, and H. Matsunami, "Remarkable lattice recovery and low sheet resistance of phosphorus-implanted 4H-SiC (110)," *Applied Physics Letters*, vol. 80, no. 2, p. 240, 2002.

[427] S. Nakashima, T. Mitani, J. Senzaki, H. Okumura, and T. Yamamoto, "Deep ultraviolet Raman scattering characterization of ion-implanted SiC crystals," *Journal of Applied Physics*, vol. 97, no. 12, p. 123507, 2005.

[428] T. Troffer, C. Peppermüller, G. Pensl, K. Rottner, and A. Schöner, "Phosphorus-related donors in 6H-SiC generated by ion implantation," *Journal of Applied Physics*, vol. 80, no. 7, p. 3739, 1996.

[429] S. A. Reshanov, G. Pensl, H. Nagasawa, and A. Schöner, "Identification of sulfur double donors in 4H-, 6H-, and 3C-silicon carbide," *Journal of Applied Physics*, vol. 99, no. 12, p. 123717, 2006.

[430] D. Alok and B. Baliga, "SiC device edge termination using finite area argon implantation," *IEEE Transactions on Electron Devices*, vol. 44, pp. 1013–1017, June 1997.

[431] D. Morrison, N. Wright, A. Horsfall, C. Johnson, A. O'Neill, A. Knights, K. Hilton, and M. Uren, "Effect of post-implantation anneal on the electrical characteristics of Ni 4H-SiC Schottky barrier diodes terminated using self-aligned argon ion implantation," *Solid-State Electronics*, vol. 44, pp. 1879–1885, Nov. 2000.

[432] I. Singer, "Surface chemistry and mechanical behavior of silicon carbide and silicon nitride implanted with titanium to high fluences and high temperatures," *Surface and Coatings Technology*, vol. 33, pp. 487–499, Dec. 1987.

[433] T. Kimoto, T. Nakajima, H. Matsunami, T. Nakata, and M. Inoue, "Formation of semi-insulating 6H-SiC layers by vanadium ion implantations," *Applied Physics Letters*, vol. 69, no. 8, p. 1113, 1996.

[434] W. Chao, Z. Yi-Men, Z. Yu-Ming, M. Ge-Lin, G. Hui, and X. Da-Qing, "Dopant diffusion and surface morphology of vanadium implanted 4H-silicon carbide," *Chinese Physics*, vol. 16, pp. 2455–2461, Aug. 2007.

[435] F. Takano, W. Wang, H. Akinaga, H. Ofuchi, S. Hishiki, and T. Ohshima, "Characterization of Mn-doped 3C-SiC prepared by ion implantation," *Journal of Applied Physics*, vol. 101, no. 9, p. 09N510, 2007.

[436] F. Takano, W. Wang, H. Ofuchi, T. Ohshima, H. Akinaga, M. Caldas, and N. Studart, "Structural And Magnetic Properties Of Mn-Doped SiC," pp. 443–444, 2010.

[437] U. Kaiser, "Nanocrystal formation in hexagonal SiC after Ge+ ion implantation.," *Journal of electron microscopy*, vol. 50, pp. 251–63, Jan. 2001.

[438] M. W. Dashiell, G. Xuan, E. Ansorge, X. Zhang, J. Kolodzey, G. C. DeSalvo, J. R. Gigante, W. J. Malkowski, R. C. Clarke, J. Liu, and M. Skowronski, "Pseudomorphic SiC alloys formed by Ge ion implantation," *Applied Physics Letters*, vol. 85, no. 12, p. 2253, 2004.

[439] C.-L. Xu, C.-H. Zhang, Y. Zhang, L.-Q. Zhang, Y.-T. Yang, X.-J. Jia, X.-B. Liu, P. Huang, and R.-S. Wang, "Mechanical Properties and Defect Evolution of Kr-Implanted 6H-SiC," *Chinese Physics Letters*, vol. 28, p. 106103, Oct. 2011.

[440] C. I. Muntele, D. Ila, and R. Zimmerman, "Low Energy Palladium Implantation in Silicon Carbide: Solid State Gas Sensors," in *AIP Conference Proceedings*, vol. 680, pp. 621–624, AIP, 2003.

[441] H. MacLean and R. Ballinger, "Silver ion implantation and annealing in CVD Silicon Carbide: The effect of temperature on silver migration," in *Proceedings of the 2nd international topical meeting of high temperature reactor technology*, (Beijing), pp. 1–20, 2004.

[442] H. MacLean, R. Ballinger, L. Kolaya, S. Simonson, N. Lewis, and M. Hanson, "The effect of annealing at 1500^{circ}C on migration and release of ion implanted silver in CVD silicon carbide," *Journal of Nuclear Materials*, vol. 357, pp. 31–47, Oct. 2006.

[443] E. Wendler, T. Bierschenk, W. Wesch, E. Friedland, and J. Malherbe, "Institut für Festkörperphysik Annual Report," tech. rep., Jena, 2009.

[444] N. Papanicolaou, M. Rao, B. Molnar, J. Tucker, A. Edwards, O. Holland, and M. Ridgway, "Ion-implantation in SiC and GaN," *Nuclear Instruments and Methods in Physics Research Section B: Beam Interactions with Materials and Atoms*, vol. 148, pp. 416–420, Jan. 1999.

[445] M. Levalois, I. Lhermitte-Sebire, P. Marie, E. Paumier, and J. Vicens, "Optical and electrical properties of 6H α-SiC irradiated by swift xenon ions," *Nuclear Instruments and Methods in Physics Research Section B: Beam Interactions with Materials and Atoms*, vol. 107, pp. 239–241, Feb. 1996.

[446] J. Grillenberger, N. Achtziger, R. Sielemann, and W. Witthuhn, "Radiotracer identification of a Ta-related deep level in 4H-SiC," *Journal of Applied Physics*, vol. 88, no. 6, p. 3260, 2000.

[447] C. Muntele, R. Ichou, I. Muntele, S. Sarkisov, and D. Ila, "Surface characterization of silicon carbide following shallow implantation of platinum ions," *Surface and Coatings Technology*, vol. 201, pp. 8339–8342, Aug. 2007.

[448] W. Jiang and W. Weber, "Multiaxial channeling study of disorder accumulation and recovery in gold-irradiated 6H-SiC," *Physical Review B*, vol. 64, pp. 1–11, Sept. 2001.

[449] W. Jiang, W. J. Weber, J. Lian, and N. M. Kalkhoran, "Disorder accumulation and recovery in gold-ion irradiated 3C-SiC," *Journal of Applied Physics*, vol. 105, no. 1, p. 013529, 2009.

[450] S. Miwa, A. Hasegawa, T. Taguchi, N. Igawa, and K. Abe, "Cavity Formation in a SiC/SiC Composite under Simultaneous Irradiation of Hydrogen, Helium and Silicon Ions," *Materials Transactions*, vol. 46, no. 3, pp. 536–542, 2005.

[451] A. Hasegawa, S. Miwa, S. Nogami, A. Taniguchi, T. Taguchi, and K. Abe, "Study of hydrogen effects on microstructural development of SiC base materials under simultaneous irradiation with He- and Si-ion irradiation conditions," *Journal of Nuclear Materials*, vol. 329-333, pp. 582–586, Aug. 2004.

[452] Y. Katoh, H. Kishimoto, and A. Kohyama, "The influences of irradiation temperature and helium production on the dimensional stability of silicon carbide," *Journal of Nuclear Materials*, vol. 307-311, pp. 1221–1226, Dec. 2002.

[453] K. Park, Y. Katoh, H. Kishimoto, and A. Kohyama, "Evaluation of dual-ion irradiated β-SiC by means of indentation methods," *Journal of Nuclear Materials*, vol. 307-311, pp. 1187–1190, Dec. 2002.

[454] W. Jiang, W. Weber, S. Thevuthasan, and V. Shutthanandan, "Accumulation and recovery of disorder on silicon and carbon sublattices in ion-irradiated 6H-SiC," *Journal of Nuclear Materials*, vol. 289, pp. 96–101, Feb. 2001.

[455] W. Skorupa, V. Heera, Y. Pacaud, and H. Weishart, "Ion beam processing of single crystalline silicon carbide," *Nuclear Instruments and Methods in Physics Research Section B: Beam Interactions with Materials and Atoms*, vol. 120, pp. 114–120, Dec. 1996.

[456] I. A. Salama, N. R. Quick, and A. Kar, "Laser doping of silicon carbide substrates," *Journal of Electronic Materials*, vol. 31, pp. 200–208, Mar. 2002.

[457] M. Willander, M. Friesel, Q.-U. Wahab, and B. Straumal, "Silicon carbide and diamond for high temperature device applications," *Journal of Materials Science: Materials in Electronics*, vol. 17, pp. 1–25, Jan. 2006.

[458] K. Rüschenschmidt, H. Bracht, N. A. Stolwijk, M. Laube, G. Pensl, and G. R. Brandes, "Self-diffusion in isotopically enriched silicon carbide and its correlation with dopant diffusion," *Journal of Applied Physics*, vol. 96, no. 3, p. 1458, 2004.

[459] R. Ghoshtagore and R. Coble, "Self-Diffusion in Silicon Carbide," *Physical Review*, vol. 143, pp. 623–626, Mar. 1966.

[460] J. Hong, M. Hon, and R. Davis, "Self-diffusion in alpha and beta silicon carbide," *Ceramurgia International*, vol. 5, pp. 155–160, Oct. 1979.

[461] M. K. Linnarsson, "Self-diffusion of ^{12}C and ^{13}C in intrinsic 4H-SiC," *Journal of Applied Physics*, vol. 95, no. 12, p. 8469, 2004.

[462] Y. Sun, T. Miyasato, and N. Sonoda, "Outdiffusion of the excess carbon in SiC films into Si substrate during film growth," *Journal of Applied Physics*, vol. 84, no. 11, p. 6451, 1998.

[463] K. Verghese, L. Zumwalt, C. Feng, and E. T.S., "Hydrogen permeation through non-metallic solids," *Journal of Nuclear Materials*, vol. 85-86, pp. 1161–1164, Dec. 1979.

[464] F. Demichelis, C. Pirri, E. Tresso, V. Rigato, and G. DellaMea, "Hydrogen diffusion and related defects in hydrogenated amorphous silicon carbide," *Journal of Non-Crystalline Solids*, vol. 128, pp. 133–138, Apr. 1991.

[465] M. Janson, *Hydrogen diffusion and ion implantation in silicon carbide*. PhD thesis, KTH, Institute of Technology, 2003.

[466] B. Aradi, P. Deák, a. Gali, N. Son, and E. Janzén, "Diffusion of hydrogen in perfect, p-type doped, and radiation-damaged 4H-SiC," *Physical Review B*, vol. 69, pp. 2–5, June 2004.

[467] P. Jung, "Diffusion and retention of helium in graphite and silicon carbide," *Journal of Nuclear Materials*, vol. 191-194, pp. 377–381, Sept. 1992.

[468] Y. Pramono, K. Sasaki, and T. Yano, "Release and Diffusion Rate of Helium in Neutron- Irradiated SiC," *Journal of nuclear science and technology*, vol. 41, no. 7, pp. 751–755, 2004.

[469] J. Bernholc, S. Kajihara, C. Wang, A. Antonelli, and R. Davis, "Theory of native defects, doping and diffusion in diamond and silicon carbide," *Materials Science and Engineering: B*, vol. 11, pp. 265–272, Jan. 1992.

[470] M. Linnarsson, M. Janson, S. Karlsson, A. Schöner, N. Nordell, and B. Svensson, "Diffusion of light elements in 4H- and 6H-SiC," *Materials Science and Engineering: B*, vol. 61-62, pp. 275–280, July 1999.

[471] T. Henkel, Y. Tanaka, N. Kobayashi, H. Tanoue, and S. Hishita, "Diffusion of implanted beryllium in silicon carbide studied by secondary ion mass spectrometry," *Applied Physics Letters*, vol. 78, no. 2, p. 231, 2001.

[472] H. Bracht, N. A. Stolwijk, M. Laube, and G. Pensl, "Diffusion of boron in silicon carbide: Evidence for the kick-out mechanism," *Applied Physics Letters*, vol. 77, no. 20, p. 3188, 2000.

[473] M. Laube, G. Pensl, and H. Itoh, "Suppressed diffusion of implanted boron in 4H-SiC," *Applied Physics Letters*, vol. 74, no. 16, p. 2292, 1999.

[474] M. S. Janson, M. K. Linnarsson, a. HalleÌĄn, B. G. Svensson, N. Nordell, and H. Bleichner, "Transient enhanced diffusion of implanted boron in 4H-silicon carbide," *Applied Physics Letters*, vol. 76, no. 11, p. 1434, 2000.

[475] K. Rüschenschmidt, H. Bracht, M. Laube, N. Stolwijk, and G. Pensl, "Diffusion of boron in silicon carbide," *Physica B: Condensed Matter*, vol. 308-310, pp. 734–737, Dec. 2001.

[476] M. Linnarsson, U. Zimmermann, J. Wong-Leung, A. Schöner, M. Janson, C. Jagadish, and B. Svensson, "Solubility limits of dopants in 4HâĂŞSiC," *Applied Surface Science*, vol. 203-204, pp. 427–432, Jan. 2003.

[477] I. G. Atabaev, "Nonequilibrium Diffusion of Boron in SiC at Low Temperatures," *Materials Sciences and Applications*, vol. 01, no. 02, pp. 53–58, 2010.

[478] M. Bockstedte, A. Mattausch, and O. Pankratov, "Different roles of carbon and silicon interstitials in the interstitial-mediated boron diffusion in SiC," *Physical Review B*, vol. 70, pp. 1–13, Sept. 2004.

[479] Z. Tian, N. Quick, and A. Kar, "Laser-enhanced diffusion of nitrogen and aluminum dopants in silicon carbide," *Acta Materialia*, vol. 54, pp. 4273–4283, Sept. 2006.

[480] L. Kroko and A. Milnes, "Diffusion of nitrogen into silicon carbide single crystals doped with aluminum," *Solid-State Electronics*, vol. 9, pp. 1125–1134, Nov. 1966.

[481] G. J. Phelps, N. G. Wright, E. G. Chester, C. M. Johnson, A. G. O'Neill, S. Ortolland, A. Horsfall, K. Vassilevski, R. M. Gwilliam, P. G. Coleman, and C. P. Burrows, "Enhanced nitrogen diffusion in 4H-SiC," *Applied Physics Letters*, vol. 80, no. 2, p. 228, 2002.

[482] A. Hofgen, V. Heera, F. Eichhorn, and W. Skorupa, "Annealing and recrystallization of amorphous silicon carbide produced by ion implantation," *Journal of Applied Physics*, vol. 84, no. 9, p. 4769, 1998.

[483] A. Hofgen, V. Heera, F. Eichhorn, W. Skorupa, and W. Moller, "Annealing and recrystallization of amorphous silicon carbide produced by ion implantation," *Materials Science and Engineering*, vol. 62, pp. 353–357, 1999.

[484] V. Heera, J. Stoemenos, R. KoÌĹgler, M. Voelskow, and W. Skorupa, "Crystallization and surface erosion of SiC by ion irradiation at elevated temperatures," *Journal of Applied Physics*, vol. 85, no. 3, p. 1378, 1999.

[485] E. Wendler, a. Heft, and W. Wesch, "Ion-beam induced damage and annealing behaviour in SiC," *Nuclear Instruments and Methods in Physics Research Section B: Beam Interactions with Materials and Atoms*, vol. 141, pp. 105–117, May 1998.

[486] W. Weber and L. Wang, "The temperature dependence of ion-beam-induced amorphization in β-SiC," *Nuclear Instruments and Methods in Physics Research Section B: Beam Interactions with Materials and Atoms*, vol. 106, pp. 298–302, Dec. 1995.

[487] R. Devanathan, F. Gao, and W. J. Weber, "Amorphization of silicon carbide by carbon displacement," *Applied Physics Letters*, vol. 84, no. 19, p. 3909, 2004.

[488] S. Zinkle and N. Ghoniem, "Operating temperature windows for fusion reactor structural materials," *Fusion Engineering and Design*, vol. 51-52, pp. 55–71, Nov. 2000.

[489] W. Wesch, A. Heft, E. Wendler, T. Bachmann, and E. Glaser, "High temperature ion implantation of silicon carbide," *Nuclear Instruments and Methods in Physics Research Section B: Beam Interactions with Materials and Atoms*, vol. 96, pp. 335–338, Mar. 1995.

[490] M. Bolen, S. Harrison, L. Biedermann, and M. Capano, "Graphene formation mechanisms on 4H-SiC(0001)," *Physical Review B*, vol. 80, Sept. 2009.

[491] K. Konishi and K. Yoh, "Transport characteristics of a single-layer graphene field-effect transistor grown on 4H-silicon carbide," *Physica E: Low-dimensional Systems and Nanostructures*, vol. 42, pp. 2792–2795, Sept. 2010.

[492] E. Oliviero, "High energy N+ ion implantation in 4H-SiC," *Nuclear Instruments and Methods in Physics Research Section B: Beam Interactions with Materials and Atoms*, vol. 257, pp. 265–269, Apr. 2007.

[493] I. A. Salama, N. R. Quick, and A. Kar, "Laser synthesis of carbon-rich SiC nanoribbons," *Journal of Applied Physics*, vol. 93, no. 11, p. 9275, 2003.

[494] S. Tongay, M. Lemaitre, J. Fridmann, a. F. Hebard, B. P. Gila, and B. R. Appleton, "Drawing graphene nanoribbons on SiC by ion implantation," *Applied Physics Letters*, vol. 100, no. 7, p. 073501, 2012.

[495] J. Hass, J. Millán-Otoya, P. First, and E. Conrad, "Interface structure of epitaxial graphene grown on 4H-SiC(0001)," *Physical Review B*, vol. 78, pp. 1–10, Nov. 2008.

[496] I. Forbeaux, J.-M. Themlin, and J.-M. Debever, "Heteroepitaxial graphite on 6H-SiC(0001): Interface formation through conduction-band electronic structure," *Physical Review B*, vol. 58, pp. 16396–16406, Dec. 1998.

[497] E. Ruska, "The development of the electron microscope and of electron microscopy," *Bioscience Reports*, vol. 7, pp. 607–629, Aug. 1987.

[498] E. Rutherford, "LXXIX. The scattering of α and β particles by matter and the structure of the atom," *Philosophical Magazine Series 6*, vol. 21, pp. 669–688, May 1911.

[499] K. Furuya, K. Mitsuishi, M. Song, and T. Saito, "In-situ, analytical, high-voltage and high-resolution transmission electron microscopy of Xe ion implantation into Al," *Journal of electron microscopy*, vol. 48, no. 5, pp. 511–518, 1999.

[500] R. F. Egerton, P. Li, and M. Malac, "Radiation damage in the TEM and SEM.," *Micron (Oxford, England : 1993)*, vol. 35, pp. 399–409, Jan. 2004.

[501] T. M. Smeeton, C. J. Humphreys, J. S. Barnard, and M. J. Kappers, "The impact of electron beam damage on the detection of indium-rich localisation centres in InGaN quantum wells using transmission electron microscopy," *Journal of Materials Science*, vol. 41, pp. 2729–2737, Apr. 2006.

[502] L. W. Hobbs, "Radiation effects in analysis of inorganic specimens by TEM," in *An Introduction to Analytical Electron Microscopy* (J. J. Hren, J. Goldstein, and D. Joy, eds.), pp. 437–476, New York: Plenum Press, 1st ed., 1979.

[503] J. A. Hinks, A. N. Jones, A. Theodosiou, J. A. V. D. Berg, and S. E. Donnelly, "Transmission Electron Microscopy Study of Graphite under in situ Ion Irradiation," in *Proceedings of Ion Irradiations workshop, Oxford*, vol. 29, 2011.

[504] S. Howell, *Handbook of CCD Astronomy*. Cambridge, UK: Cambridge University Press, 1 ed., 2000.

[505] J. A. Hinks, A. N. Jones, A. Theodosiou, J. a. van den Berg, and S. E. Donnelly, "Transmission Electron Microscopy Study of Graphite under in situ Ion Irradiation," *Journal of Physics: Conference Series*, vol. 371, p. 012046, July 2012.

[506] Y. Serruys, M.-O. Ruault, P. Trocellier, S. Miro, A. Barbu, L. Boulanger, O. Kaïtasov, S. Henry, O. Leseigneur, P. Trouslard, S. Pellegrino, and S. Vaubaillon, "JANNUS: experimental validation at the scale of atomic modelling," *Comptes Rendus Physique*, vol. 9, pp. 437–444, Apr. 2008.

[507] Y. Serruys, P. Trocellier, S. Miro, E. Bordas, M. Ruault, O. Kaïtasov, S. Henry, O. Leseigneur, T. Bonnaillie, S. Pellegrino, S. Vaubaillon, and D. Uriot, "JANNUS: A multi-irradiation platform for experimental validation at the scale of the atomistic modelling," *Journal of Nuclear Materials*, vol. 386-388, pp. 967–970, Apr. 2009.

[508] F. Salvat, J. M. Fernandez-Varea, and J. Sempau, "PENELOPE , a code system for Monte Carlo simulation of electron and photon," in *Workshop Proceedings*, (Issy-les-Moulineaux, France), Nuclear Energy Agency, 2011.

[509] E. Oliviero, A. van Veen, A. Fedorov, M. Beaufort, and J. Barbot, "Helium implantation defects in SiC studied by thermal helium desorption

spectrometry," *Nuclear Instruments and Methods in Physics Research Section B: Beam Interactions with Materials and Atoms*, vol. 186, pp. 223–228, Jan. 2002.

[510] K. Ono, K. Arakawa, and K. Hojou, "Formation and migration of helium bubbles in Fe and Fe-9Cr ferritic alloy," *Journal of Nuclear Materials*, vol. 307-311, pp. 1507–1512, Dec. 2002.

[511] R. Birtcher, S. Donnelly, and C. Templier, "Evolution of helium bubbles in aluminum during heavy-ion irradiation.," *Physical review. B, Condensed matter*, vol. 50, pp. 764–769, July 1994.

[512] S. Donnelly, R. Birtcher, and C. Templier, "The effect of dense and dilute collision cascades on helium bubbles in metals," *Nuclear Instruments and Methods in Physics Research Section B: Beam Interactions with Materials and Atoms*, vol. 106, pp. 583–588, Dec. 1995.

[513] H. Heinisch, "Transmutations in SiC irradiated in ARIES-IV first wall," tech. rep., Pacific NorthWest National Laboratory, 2001.

[514] K. J. Abrams, J. A. Hinks, C. J. Pawley, G. Greaves, J. A. van den Berg, D. Eyidi, M. B. Ward, and S. E. Donnelly, "Helium irradiation effects in polycrystalline Si, silica, and single crystal Si," *Journal of Applied Physics*, vol. 111, no. 8, p. 083527, 2012.

[515] H. Iwakiri, K. Yasunaga, K. Morishita, and N. Yoshida, "Microstructure evolution in tungsten during low-energy helium ion irradiation," *Journal of Nuclear Materials*, vol. 283-287, pp. 1134–1138, 2000.

[516] S. Sharafat, A. Takahashi, Q. Hu, and N. Ghoniem, "A description of bubble growth and gas release of helium implanted tungsten," *Journal of Nuclear Materials*, vol. 386-388, pp. 900–903, Apr. 2009.

[517] R. L. Mills, D. H. Liebenberg, and J. C. Bronson, "Equation of state and melting properties of ^{4}He from measurements to 20 kbar," *Physics Review B*, vol. 21, pp. 5137–5148, Jun 1980.

[518] H. Yamaguchi, I. Hashimoto, H. Mitsuya, K. Nakamura, E. Yagi, and M. Iwaki, "The random motion of bubbles in krypton-implanted aluminum," *Journal of Nuclear Materials*, vol. 161, pp. 164–168, Feb. 1989.

[519] J. Evans and A. van Veen, "An electron microscope study of helium bubble diffusion in gold," *Journal of Nuclear Materials*, vol. 168, pp. 12–18, Oct. 1989.

[520] C. Van Siclen, R. Wright, and S. Usmar, "Anomalous helium bubble diffusion in dilute aluminum alloys," *Physical Review Letters*, vol. 68, pp. 3892–3895, June 1992.

[521] V. Chkuaseli and H. Matzke, "Fission gas bubble behaviour in uranium dioxide," *Journal of Nuclear Materials*, vol. 201, pp. 92–96, May 1993.

[522] J. Evans, "Bubble diffusion to grain boundaries in UO2 and metals during annealing: a new approach," *Journal of Nuclear Materials*, vol. 210, pp. 21–29, June 1994.

[523] D. E. Alexander and R. Birtcher, "The effect of ion irradiation on inert gas bubble mobility," *Journal of Nuclear Materials*, vol. 191-194, pp. 1289–1294, Sept. 1992.

[524] S. Donnelly, R. Birtcher, C. Templier, and V. Vishnyakov, "Response of helium bubbles in gold to displacement-cascade damage.," *Physical review. B, Condensed matter*, vol. 52, pp. 3970–3975, Aug. 1995.

[525] K. Ono, K. Arakawa, and R. Birtcher, "Intermittent rapid motion of helium bubbles in Cu during irradiation with high energy self-ions," *Nuclear Instruments and Methods in Physics Research Section B: Beam Interactions with Materials and Atoms*, vol. 206, pp. 114–117, May 2003.

[526] J. Grisolia, F. Cristiano, B. De Mauduit, G. B. Assayag, F. Letertre, B. Aspar, L. Di Cioccio, and A. Claverie, "Kinetic aspects of the growth of hydrogen induced platelets in SiC," *Journal of Applied Physics*, vol. 87, no. 12, p. 8415, 2000.

[527] S. Miro, J. Costantini, J. Haussy, L. Beck, S. Vaubaillon, S. Pellegrino, C. Meis, J. Grob, Y. Zhang, and W. Weber, "Nuclear reaction analysis of helium migration in silicon carbide," *Journal of Nuclear Materials*, vol. 415, pp. 5–12, Aug. 2011.

[528] A. Jostsons, C. DuBose, G. Copeland, and J. Stiegler, "Defect structure of neutron irradiated boron carbide," *Journal of Nuclear Materials*, vol. 49, pp. 136–150, 1974.

[529] K. Nogita and K. Une, "Radiation-induced microstructural change in high burnup UO2 fuel pellets," *Nuclear Instruments and Methods in Physics Research B*, vol. 91, pp. 301–306, 1994.

[530] R. Webb, "Energy and penetration of helium in sic." Private Communication, 2013.